Repurposing quinoline-based (metallo) drug leads for the treatment of *Leishmania major*-induced cutaneous leishmaniasis

Takudzwa Emmanuel Murwira

Department of Molecular and Cell Biology

University of Cape Town

February 2025

Repurposing quinoline-based (metallo) drug leads for the treatment of *Leishmania major*-induced cutaneous leishmaniasis

A dissertation submitted to the University of Cape Town in fulfilment of the degree of

Master of Science

by

Takudzwa Emmanuel Murwira

Supervisor: Dr Ramona Hurdayal

Co-supervisor: Professor Gregory Smith

Department of Molecular and Cell Biology

University of Cape Town

Rondebosch, 7701

Cape Town

February 2025

Plagiarism Declaration

I know the meaning of plagiarism and declare that all of the work in the document, "**Repurposing quinoline-based (metallo) drug leads for the treatment of *Leishmania major*-induced cutaneous leishmaniasis**" is my own work and, to the best of my knowledge, has not been previously submitted for examination for any degree, at any university. All sources of information are cited and fully referenced at the end of each chapter.

Signature: Signed by candidate

Date: 10 February 2025

Acknowledgements

First, I would like to express my utmost gratitude to my supervisors, Dr Ramona Hurdayal and Professor Gregory Smith. Conducting this MSc research would not have been possible for me without the Faculty of Science funding and fellowship they secured for me to do so. I am greatly appreciative of all their support and guidance these past two years, especially Prof. Smith with regard to the synthesis and advanced chemistry aspects of this research, which were relatively foreign to me.

Secondly, I would like to thank the University of Cape Town and the Faculty of Science for providing the financial support to conduct this research study.

Thirdly, I want to thank the members of the GS Organometallic Research Group and Leishmaniasis Research Group (a.k.a. SA Leishmaniacs), past and present, for their guidance, assistance and companionship. An honourable mention goes to Ghannish Soogary, who not only helped me better understand advanced chemistry along with other GS Group members but also shares an appreciation for dark humour like me (thanks for the endless exchange of memes and Instagram reels!). Another honourable mention goes to Rebeng Maine, who took time off her busy schedule to help Ghannish and me become more familiar with mouse experimental procedures and BSL2 lab work.

Fourthly, I wish to thank several members of the Department of Chemistry, Department of Molecular and Cell Biology (MCB) and Research Animal Facility (RAF). Chemistry Department: My thanks go to Dr Marwaan Rylands and Dr Stephen De Doncker for running NMR analyses on my samples and Dr Hong Su for performing X-ray crystallography experiments. MCB: I give my thanks to Ms Shakiera Sattar and Ms Bronwyn Arendze-Bailey for the BSL2 training and support, as well as Ms Maureen Jacobs for the autoclave runs and assisting with lab cleanups. RAF: A massive thanks to Mr Rodney Lucas for the training in mouse handling techniques, which ultimately helped me secure the relevant authorisation to perform animal experiments.

Lastly, I want to thank friends and family. To Tamika Moonsamy, thank you for giving me a ride from the airport when I landed in the country after being away for three years. To Sharoné Van Eck, thank you for all the chats we had on the MCB balcony and for sharing your life experiences with me. Finally, to my parents, thank you for helping me obtain a university education at UCT despite the unfavourable economic conditions in Zimbabwe. Special thanks go to my mother, whose encouragement helped me get through my lowest point before getting the chance to pursue this MSc degree, and whose prayers likely kept me safe while far away from home. I hope that obtaining this degree will lead me to a path in life that will allow me to give back to you and make you proud of me.

Abstract

Leishmaniasis is a vector-borne neglected tropical disease, of which cutaneous leishmaniasis is the most common form. There is a crucial need to develop new drugs for cutaneous leishmaniasis, as current drugs are sub-optimal due to parasite-specific drug resistance, drug-induced host toxicity and lengthy treatment. Repurposing existing drugs and/or compounds with established biological activity provides an attractive measure for antileishmanial drug development. For instance, *N*-heterocyclic molecules, such as quinolines and aminoquinolines, are commonly used as privileged scaffolds for developing antimalarial and anticancer drugs, which show enhanced activity when combined with metal complexes. This is exemplified by the iron-containing compound ferrocene, which has been shown to amplify the efficacy of several quinoline-based drug candidates. Accordingly, this study investigates the potential of repurposing ferrocenyl-quinoline compounds as potential drug candidates for the treatment of cutaneous leishmaniasis caused by *Leishmania major* LV39, focusing on *in vitro* antiparasitic activity and cytotoxicity, using murine and cell-based models of the disease.

Four ferrocenyl-quinoline compounds consisting of the quinoline scaffold bonded to ferrocene via varying linkers (imino-alkyl, amino-alkyl, triazole amine and phenyl-alkene) were synthesised. The synthetic routes used to generate these compounds and their precursors consisted of nucleophilic aromatic substitution, Schiff base condensation, copper(I)-catalysed azide-alkyne cycloaddition and Mizoroki-Heck coupling. All the compounds were fully characterised using standard spectroscopic (^{1}H, ^{13}C{^{1}H} NMR and FT-IR spectroscopy) and analytical (mass spectrometry, melting point and elemental analysis) techniques.

The four compounds and their precursors were assessed for their antileishmanial activity against the promastigote form of *L. major* LV39. The amino-alkyl and triazole amine-linked compounds were the most active (IC_{50} = 0.50 and 4.04 µg/ml, respectively), with the former being more active than the control drug amphotericin B (IC_{50} = 1.94 µg/ml). Generally, the four ferrocenyl-quinoline compounds had higher antileishmanial activity than their respective precursors. The cytotoxicity of the compounds was also assessed against the murine RAW 264.7 macrophage cell line, and all four compounds were observed to be more cytotoxic than amphotericin B (CC_{50} < 50 µg/ml). Although the amino-alkyl and triazole amine-linked compounds had the highest cytotoxicities (CC_{50} = 0.86 and 8.55 µg/ml, respectively), both compounds were more selective toward *L. major* promastigotes than their imino-alkyl and phenyl-amine counterparts (SI > 1), making them promising antileishmanial agents worthy of further investigation. This study not only delineates structure-based trends on antileishmanial activity but also demonstrates the significance of incorporating metals in drug design to enhance potency.

Abbreviations, Symbols and Units

°C	Degree(s) Celsius
ν	Wavenumber
λ_{ex}	Excitation wavelength
λ_{em}	Emission wavelength
δ	Chemical shift
µg	Microgram (10^{-6} g)
µM	Micro molar (10^{-6} M)
Å	Angstrom (10^{-10} m)
AmpB	Amphotericin B
ATR	Attenuated total reflection
BALB/c	*Leishmania*-susceptible mouse strain
br s	Broad singlet
C57BL/6	*Leishmania*-resistant mouse strain
CC_{50}	Half-maximal cytotoxic concentration
$CDCl_3$	Deuterated chloroform
CL	Cutaneous leishmaniasis
cm^{-1}	Reciprocal centimetres
COSY	Homonuclear correlation spectroscopy
CuAAC	Copper(I)-catalysed azide-alkyne cycloaddition
d	Doublet
dd	Doublet of doublets
DCM	Dichloromethane

DMEM	Dulbecco's Modified Eagle Medium
DMF	Dimethylformamide
DMSO	Dimethyl sulfoxide
DMSO (d_6)	Deuterated dimethyl sulfoxide
ESI-MS	Electrospray ionisation mass spectrometry
EtOAc	Ethyl acetate
EtOH	Ethanol
FACS	Fluorescence-activated cell sorting
FBS	Fetal bovine serum
FT-IR	Fourier-transform infrared spectroscopy
g	Gram(s)
HPLC	High-performance liquid chromatography
h	Hour(s)
IC_{50}	Half-maximal inhibitory concentration
J	Coupling constant
LC-MS	Liquid chromatography-mass spectrometry
m	Multiplet
M199	Medium 199
MCL	Mucocutaneous leishmaniasis
MeOD	Deuterated methanol
MeOH	Methanol
MHz	Megahertz
ml	Millilitre(s)
mmol	Millimole(s) (10^{-3} mol)
M.p.	Melting point

m/z	Mass to charge ratio
NMR	Nuclear magnetic resonance
nm	Nanometre(s) (10^{-9} m)
PBS	phosphate-buffered saline
ppm	Parts per million
RAW 264.7	Mouse macrophage cell line
ROS	Reactive oxygen species
r.t.	Room temperature
s	Singlet
SD	Standard deviation
SI	Selectivity index
t	Triplet
TFA	Trifluoroacetic acid
TLC	Thin layer chromatography
TMS	Tetramethylsilane
t_R	Retention time (minutes)
VL	Visceral leishmaniasis
v/v%	Volume percentage
w/v%	Weight percentage

Table of Contents

CHAPTER 1

Introduction and Literature Review

1.1. Leishmaniasis

1.1.1. Epidemiology and prevalence

Leishmaniasis is a spectrum of vector-borne parasitic diseases caused by several species of the protozoan parasite *Leishmania*. There are mainly three forms of leishmaniasis: cutaneous leishmaniasis (CL), mucocutaneous leishmaniasis (MCL), and visceral leishmaniasis (VL). [1] Cutaneous leishmaniasis is the most common form of the disease, characterised by ulcer-like lesions that appear on the skin at the site of infection. When these lesions appear in the nose, mouth and throat mucous membranes, the disease is classified as mucocutaneous. Visceral leishmaniasis is the deadliest form of the disease, with a mortality rate of 100% if untreated, characterised by weight loss, irregular bouts of fever, anaemia, and enlargement of the spleen and liver. [2–4] The most common causative agents of CL are *L. major*, *L. mexicana* and *L. tropica*, those of MCL are *L. (Viannia) braziliensis* and *L. panamensis*, while VL is typically caused by *L. donovani* and *L. infantum*. [5–9] All the parasite species are transmitted by sandfly vectors of either the *Phlebotomus* or *Lutzomyia* genus, depending on whether the species are in the Old World (Asia, Africa and Europe) or the New World (the Americas, particularly South America). [3,6,7,9]

Approximately between a million and 2 million cases of leishmaniasis are reported annually. [3,4,6] Despite being a risk to up to 1 billion people worldwide, leishmaniasis is classified as a neglected tropical disease (NTD) as it is endemic in economically disadvantaged regions, namely the Middle East, South America, the Mediterranean Basin and northern and western Africa. The incidence of the disease also coincides with the high presence of *Phlebotomus*/*Lutzomyia* sandflies in these regions. [3–6] Sandflies are also present in southern Africa, particularly Botswana and Namibia. However, the species that mostly occupy this region belong to the genus *Sergentomyia* and are not known to be vectors of *Leishmania* parasites, though *Phlebotomus rodhaini* has been identified in Botswana recently. [10,11] Furthermore, relatively few CL cases have been reported in northern parts of Namibia since the 1970s, but the true identity of the responsible *Leishmania* and *Phlebotomus* species remains unclear. [12]

1.1.2. Leishmania life cycle and immunology of leishmaniasis in mice

Leishmania infection is transmitted via a bite from infected female *Phlebotomus* or *Lutzomyia* sandflies. [3,6] The parasite exists in two distinct forms. It is in its flagellated promastigote form (**Figure 1.1B**) while in the gut of a sandfly and transforms into the aflagellated amastigote form (**Figure 1.1C**) when taken up by macrophages of the mammalian host. As illustrated in **Figure 1.1A**, when an infected sandfly bites a mammalian organism for a blood meal, it regurgitates promastigotes into the bloodstream. These promastigotes then enter the macrophages via immunoglobulin-mediated phagocytosis. While inside the macrophages' phagolysosomes, the parasites differentiate into amastigotes, which then multiply before lysing the host cells and being released to either infect other cells or be ingested by another sandfly taking a blood meal. In the latter scenario, the amastigotes transform back into their promastigote form in the sandfly gut. [5,13]

In order to study and understand all forms of leishmaniasis, mammalian animal models, such as rodents, dogs, and monkeys, have been used. In the case of cutaneous leishmaniasis, murine models have been the most commonly used for the past 40 years to investigate the cell types, cytokines, signal transduction cascades and antileishmanial effector mechanisms necessary for parasite control. [14] Two types of mice are used in cutaneous leishmaniasis research as models for the disease: BALB/c and C57BL/6 (**Figure 1.2A**). Infected BALB/c mice are more susceptible to the disease and showcase a non-healing phenotype. On the other hand, C57BL/6 mice are more resistant, resulting in them displaying a healing phenotype. [15] For studies on cutaneous leishmaniasis, these phenotypes are typically exhibited after an eight-week footpad infection with *Leishmania* parasites, where BALB/c mice show continuous footpad swelling and C57BL/6 show a lesser degree of swelling that subsides over time (**Figure 1.2B**).

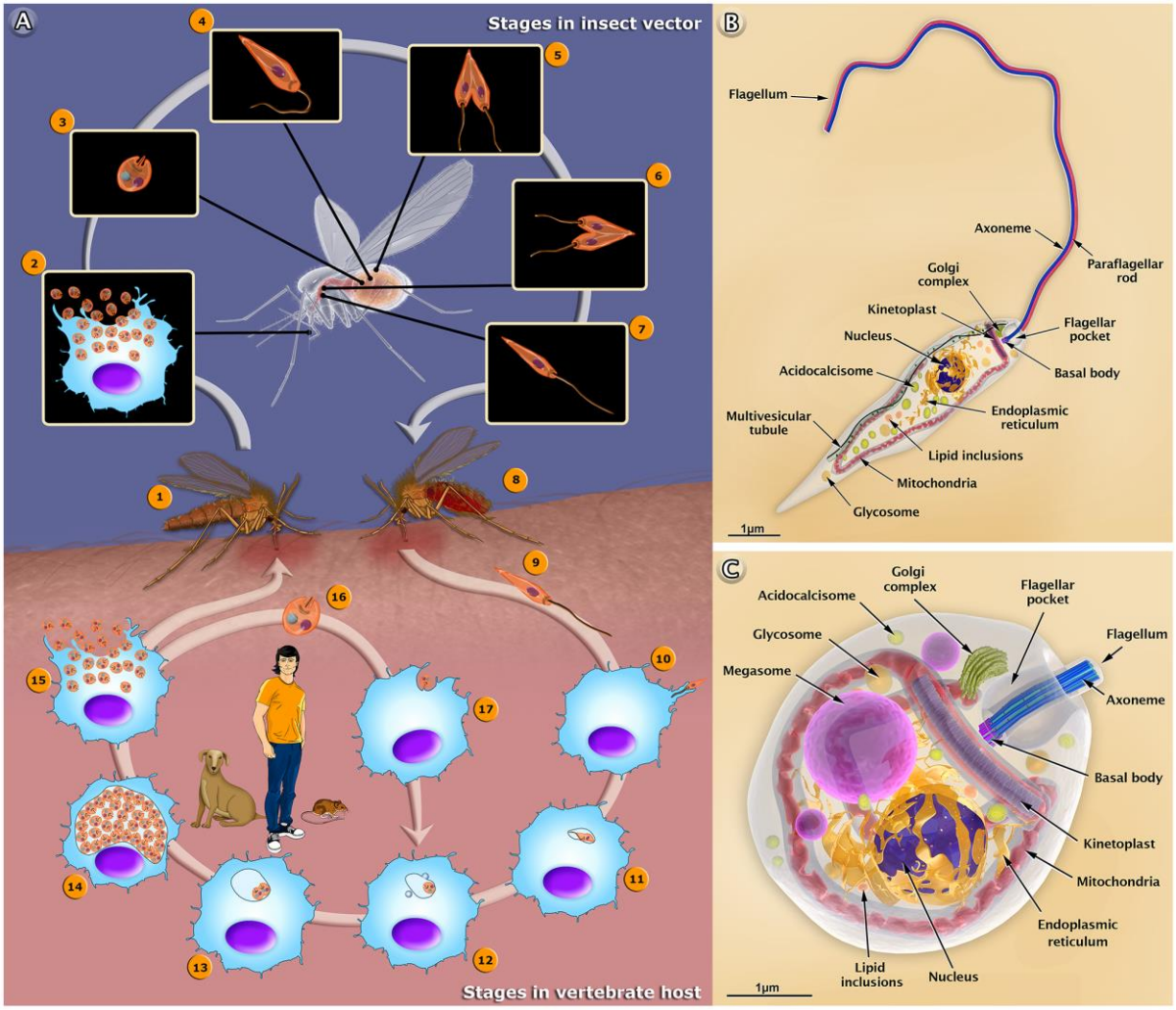

Figure 1.1: *Life cycle and structure of the Leishmania parasite**.** (A) The multiple stages of the parasite's life cycle in the sandfly vector and the vertebrate host. The sandfly releases Leishmania promastigotes into the host's bloodstream, where they are taken up by macrophages and transform into amastigotes. Amastigotes either infect nearby macrophages or revert back into the promastigote stage after being released from infected macrophages ingested by another sandfly during a blood meal. (B) Structure of the parasite's promastigote form. (C) Structure of the parasite's amastigote form.* [13]

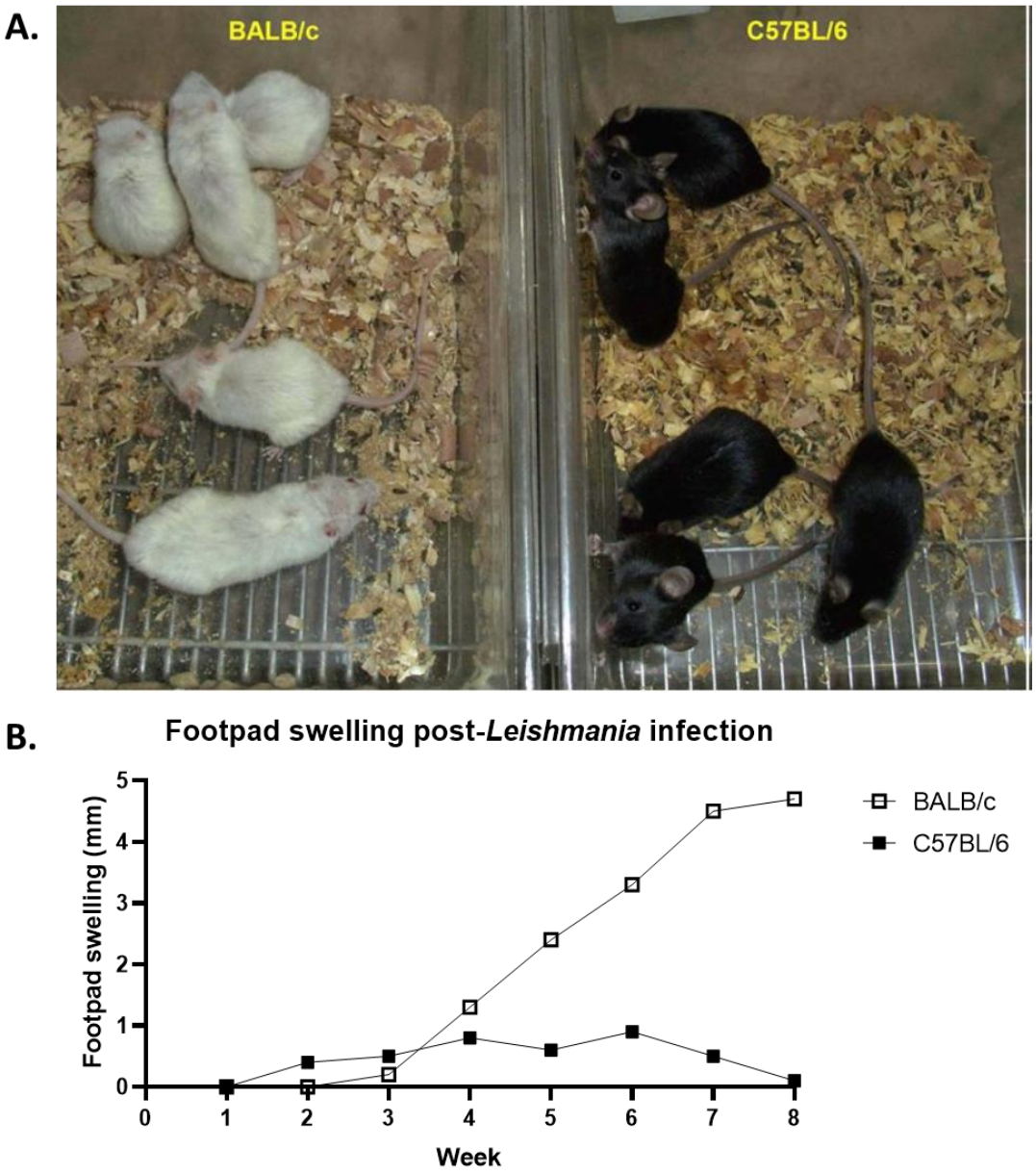

Figure 1.2: *Mouse breeds used in leishmaniasis research and footpad swelling in Leishmania-infected mice. (A) BALB/c (left) and C57BL/6 mice (right), which are commonly used to study Leishmania infection in vivo;* [16] *(B) Footpad swelling in a BALB/c and C57BL/6 mouse infected with L. major. L. major promastigotes were injected subcutaneously into the hind footpad of the mice, and the footpad swelling was monitored over eight weeks.*

Through the use of BALB/c and C57BL/6 mouse models for cutaneous leishmaniasis infection and progression, multiple studies have shown that the host genetic background, *Leishmania* species, and different parasite isolates can influence immune response. [8] It is now known that the disease's progression is dependent on which cytokines are produced by T helper cells upon infection and whether they activate a proinflammatory Type-1/Th1 or anti-inflammatory Type-2/Th2 response in

macrophages, with the susceptible BALB/c strain displaying a Th2 response and the resistant C57BL/6 strain showcasing a Th1 response.

The mechanisms by which each type of response Is evoked are summarised in **Figure 1.3**. In the initial stage of *Leishmania* infection, 90% of the parasites that penetrate the skin are eliminated by the complement system, a complex network of activators, regulators and signals that enhance the activities of antibodies and phagocytic cells. [17] The surviving parasites, which can still cause infection, are phagocytosed by dendritic cells (DCs) that present *Leishmania* antigens to CD4 T cells. At the same time, neutrophils also use neutrophil extracellular traps (NETs) to immobilise and phagocytose the parasites, subsequently generating reactive oxygen species (ROS) and nitric oxide (NO) to kill them. [7,8,17] DCs also produce the cytokines IL-12 and IL-4, which drive the T cells to differentiate into either Type-1 (Th1) or Type-2 (Th2) cells, respectively. The activated T cells then produce cytokines that activate macrophages into a form that either promotes parasite-killing (M1) or promotes conditions for parasite survival (M2). The cytokines IL-4, IL-6, IL-9, IL-10, IL-13 and TGF-β produced by Th2 and T reg cells induce a response that lead to an M2 macrophage phenotype, while the cytokines IL-2, IL-12, IFN-γ and TNF-α made by Th1 cells activate the M1 phenotype. M1 macrophage activation results in the production of parasite-killing NO via inducible nitric oxide synthase (iNOS). M2 macrophage activation induces polyamine and urea production by arginase, favouring parasite proliferation. [7,8,16–18] Both iNOS and arginase utilise L-arginine as a substrate for their respective functions, meaning that induction of M1 activation inhibits M2 activation and vice-versa. [8,15]

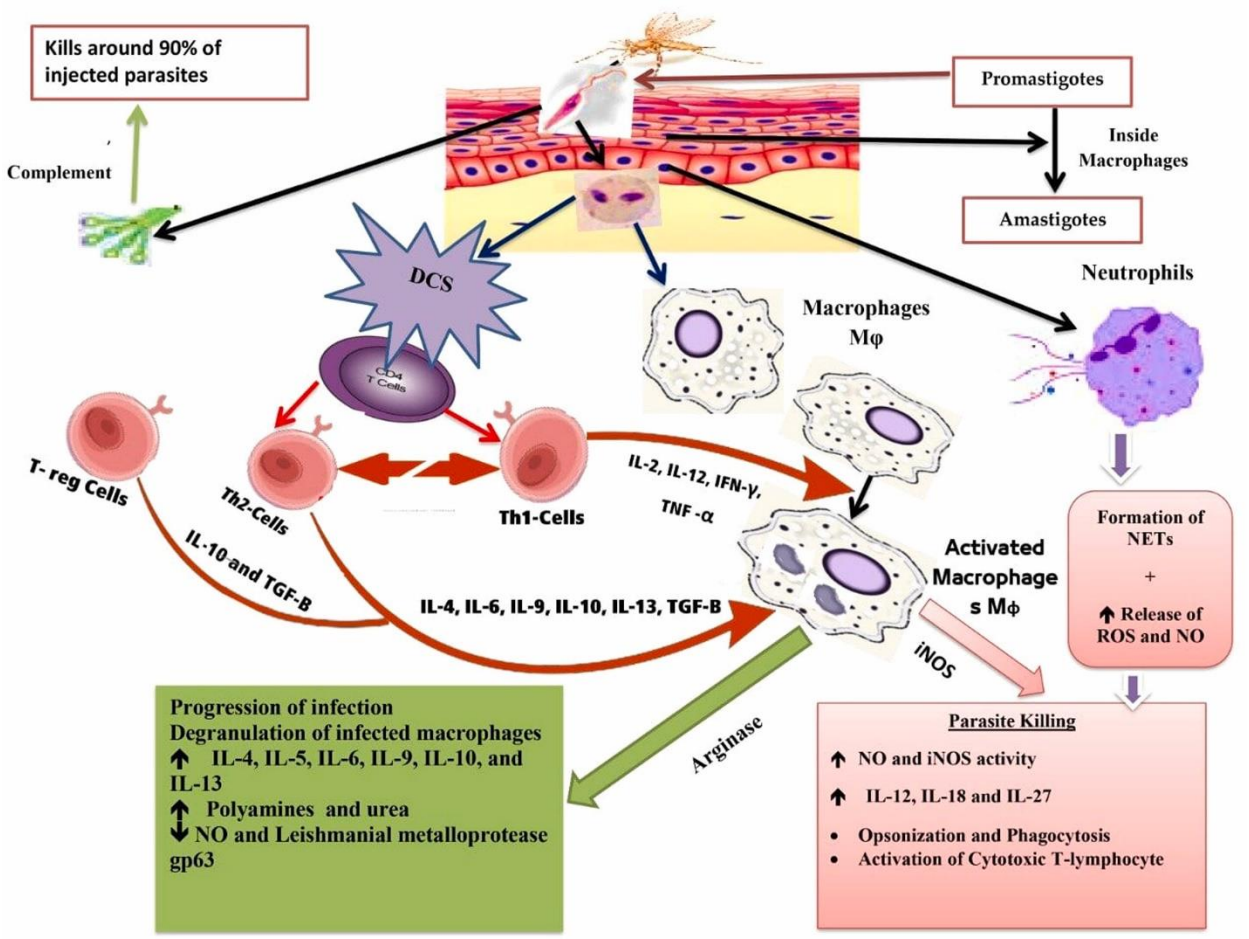

Figure 1.3: *Immune response mechanisms against Leishmania infection. Initial parasite elimination is carried out by the complement system, with surviving parasites being either killed by neutrophils or taken up by antigen-presenting DCs. Polarisation of T cells into Th1 or Th2 cells via the production of IL-12 or IL-4 by DCs eventually leads to cytokine-mediated macrophage activation for either parasite-killing or infection progression.* [17]

1.1.3. Available drugs and treatment

The primary drugs used for treating all forms of leishmaniasis are antimony-based compounds collectively known as pentavalent antimonials. These are meglumine antimoniate (Glucantim) (**Figure 1.4A**) and sodium stibogluconate (Pentostam) (**Figure 1.4B**), first introduced in the 1940s. [2,19] Despite being in use for over half a century, their mechanism of action is still poorly understood, with proposed models suggesting that they activate host immune responses, act as prodrugs, or inhibit metabolic pathways in amastigotes. [19] In particular, the prodrug model links the activity of pentavalent antimonials to their reduction from Sb(V) to the more toxic Sb(III) by amastigotes and, to a lesser extent, host macrophages. [19] Pentavalent antimonials are administered parenterally over 28-30 days at daily doses of between 10 and 60 mg/kg, with patients required to be hospitalised to receive

treatment. [6,19] While effective against non-resistant forms of *Leishmania*, the use of these drugs in endemic regions has been limited due to the emergence of resistant strains. [2,19,20] Additionally, pentavalent antimonials can cause severe side effects like anaemia, cardiotoxicity, nausea, vomiting and pancreatitis. [6,21]

Amphotericin B (**Figure 1.4C**) is one of the alternative drugs that is also currently being used for leishmaniasis treatment. This compound is an antifungal drug with nearly 100% efficacy against antimony-resistant *Leishmania* strains, and this has been attributed to its ability to form pores in the cell membranes of fungi and parasites by binding to ergosterol. [2,22] The drug is administered intravenously at 1 mg/kg daily for 20 to 30 days, but most people who receive it experience infusion reactions and potentially fatal side effects, such as nephrotoxicity and myocarditis. [2,6,19,23] Liposomal amphotericin B, a lipid formulation of the drug, is a more favoured and less toxic option than the free drug and is administered at a dose of 3 mg/kg per day over 10 to 20 days. [6,23] Unfortunately, there have been recent reports of several *Leishmania* species exhibiting resistance to the drug. [24–26]

Miltefosine (**Figure 1.4D**), originally created as an anticancer drug, was found to be effective against all forms of leishmaniasis and has the benefit of being suitable for oral administration, reducing the need for hospitalisation. [2] Miltefosine is typically administered daily at 50 to 100 mg for 28 days, with its mechanism of action believed to be an induction of cell apoptosis. [2,19,23] However, it also causes gastrointestinal side effects, and there have been recent reports of resistance to this drug. [2,19]

The abovementioned issues associated with antimonials, amphotericin B and miltefosine have also been observed with other drug options like pentamidine and paromomycin. Therefore, it is crucial to develop newer and more effective drugs against CL with no or fewer severe side effects and less invasive administration routes. An attractive option for finding more reliable antileishmanial agents is the repurposing of known antiparasitic drugs or biologically active compounds.

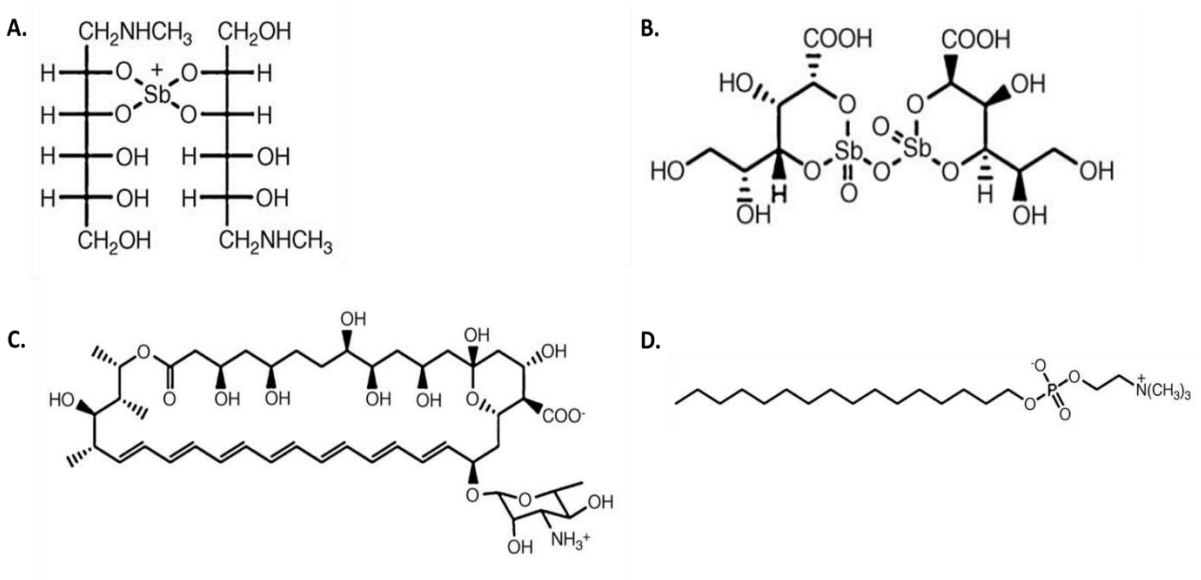

***Figure 1.4**: Structures of drugs currently in use to treat leishmaniasis. The first-line drugs used against non-resistant Leishmania strains are the sugar-based pentavalent antimonials meglumine antimoniate (A) and sodium stibogluconate (B), which both contain atoms of the metalloid antimony in their structures. Amphotericin B (C) consists of a polyhydroxyl chain and polyene chain bound to a mycosamine group, while miltefosine (D) is a phospholipid-based drug.* [21]

1.2. Approaches to new antileishmanial drug design

1.2.1. Drug repurposing

Drug repurposing, also sometimes known as drug repositioning, is the finding of new uses for drugs or pharmaceutical ingredients in diseases other than what they were originally developed for. [27–29] The use of amphotericin B and miltefosine indicated earlier are examples of drug repurposing for leishmaniasis treatment, despite the negative effects of these drugs. While developing new leishmanicidal drugs remains an option, progress in this regard has been slow because of the hesitance of pharmaceutical companies to invest in their development, as they believe that the market for these drugs will be too low to produce significant returns. [2]

There are several advantages to repurposing existing drugs and bioactive compounds. One of the major benefits is that it significantly reduces the costs and time required for novel drug development. The cost of developing a new drug may go up to 1.8 billion dollars and take over a decade to complete. [2,30] Another advantage is that some of the clinical trial phases associated with *de novo* drug development can be bypassed, and there is a lower probability of clinical failure since the safety profiles and efficacy of the repurposed drugs are already documented. As a consequence, the time

taken for the drugs to reach their new market is also decreased. [30] It is, therefore, more reasonable to repurpose existing drugs whose pharmacokinetic and safety profiles are well-known.

Repurposed drugs have been shown to have high efficacy in a variety of disease settings. [27] For example, thalidomide, which was banned in 1962 by the WHO as anxiety and morning sickness medication due to its teratogenicity, was successfully repurposed for leprosy treatment and later cancer treatment. [29] Aspirin, a well-known analgesic, currently has the potential of being repurposed as an anticancer agent due to its recently discovered ability to inhibit metastasis. [30] At present, the success rate of FDA-approved repurposed drugs and vaccines sits at approximately 30%. [30]

1.2.2. Quinoline and antimalarial properties.

One compound that has been a candidate for the drug repurposing strategy is quinoline (**Figure 1.5A**). Quinoline is an *N*-heterocyclic aromatic organic compound, which is known to possess antimalarial, antibacterial, antiviral and antifungal activity. [31–33] It is for this reason that it is commonly used as a pharmacophoric scaffold for the design and synthesis of multiple drugs targeting these microorganisms. The most well-known quinoline-based drug is the antimalarial drug chloroquine (**Figure 1.5B**), a derivative of 4-aminoquinoline that has been in use for decades. Other quinoline-based drugs used to combat malaria include primaquine (**Figure 1.5C**), hydroxychloroquine (**Figure 1.5D**) and mefloquine (**Figure 1.5E**). [21,34]

One aspect of drug repurposing involves investigating the efficacies of existing drugs against pathogens with one or more similar traits. While the malaria-causing *Plasmodium* parasite and the *Leishmania* parasite are distinct organisms with different survival mechanisms, the common characteristic between them is that they are both intracellular protozoan parasites that infect blood cells, albeit different blood cells. Due to the success of quinoline-based compounds as antimalarials, many researchers have sought to repurpose the quinoline scaffold to create compounds that possess antileishmanial properties.

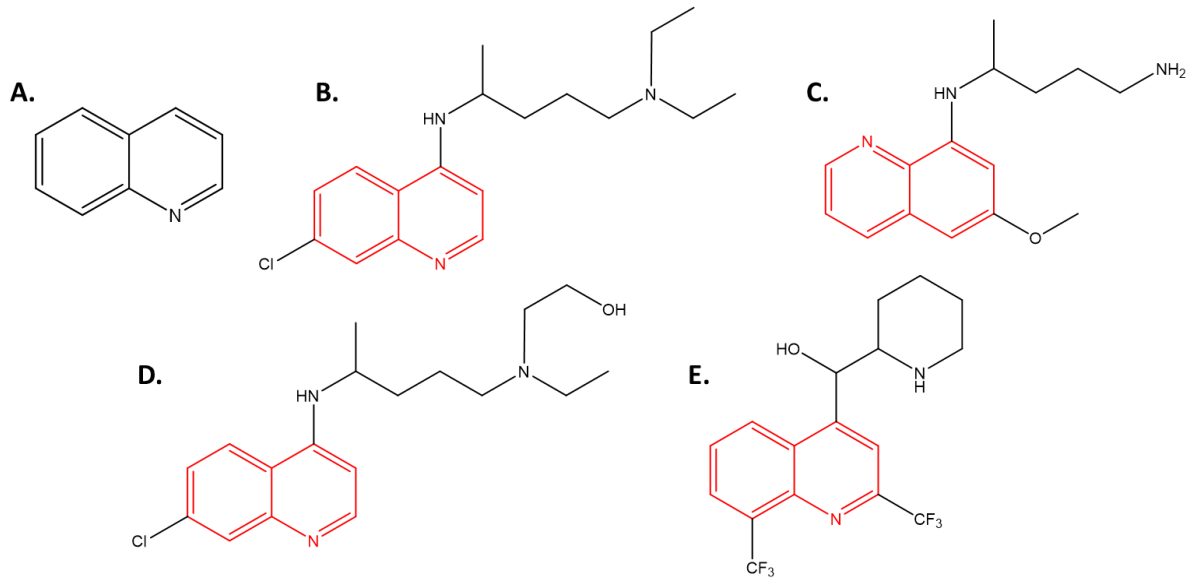

Figure 1.5: *Structures of quinoline and quinoline-derived antimalarial drugs. Quinoline (A) is the main component of the currently available antimalarial drugs chloroquine (B), primaquine (C), hydroxychloroquine (D) and mefloquine (E). The quinoline moiety in the chemical structures of the drugs is highlighted in red.* [21,35]

1.2.3. Use of quinolines in antileishmanial drug design

In a recent study by Sabt *et al*., twenty quinoline-isatin hybrids were synthesised and showed higher *in vitro* activity against both the promastigote and amastigote forms of *L. major* compared to miltefosine (IC_{50} < 8.00 µM). [36] The three most active compounds (**Figure 1.6**) were found to be non-cytotoxic to green monkey kidney cells (CC_{50} > 100.00 µM). Through molecular docking experiments, the authors also linked the three compounds' activity to their ability to bind to pteridine reductase 1, a crucial enzyme required by *Leishmania* species for folate metabolism and DNA biosynthesis. [36]

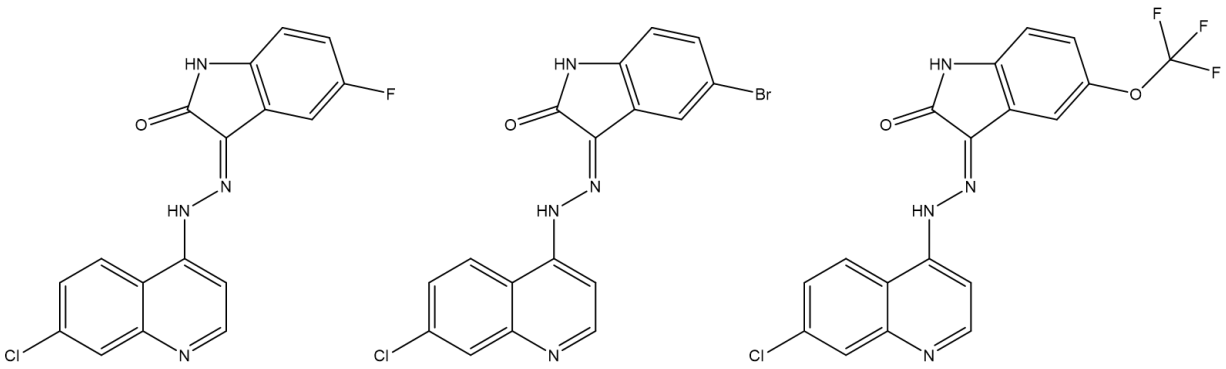

Figure 1.6*: The three most active quinoline-isatin hybrid compounds synthesised by Sabt et al.* [36]

Another study by Tavares *et al*. reported the activity of clioquinol (**Figure 1.7**), a derivative of 8-hydroxyquinoline, against *L. amazonensis* and *L. infantum* in 2018. [37] The compound was less potent than amphotericin B against the promastigotes and amastigotes of both species (IC_{50} > 0.10 μg/ml), but it was significantly less cytotoxic to red blood cells and murine macrophages (CC_{50} >> 1.00 μg/ml) and reduced the parasites' ability to infect macrophages. Furthermore, they showed that this reduction in infectivity was a result of a disruption in the parasites' plasma membrane, changes in the mitochondrial membrane potential and elevated production of ROS. [37]

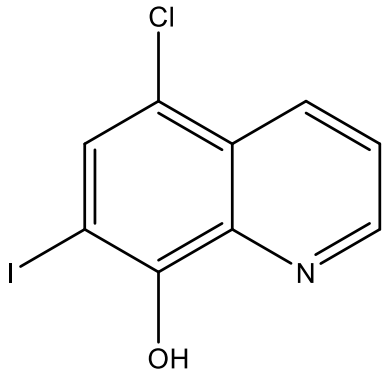

***Figure 1.7**: Structure of clioquinol.* [37]

Tafenoquine and sitamaquine (**Figure 1.8**), compounds based on 8-aminoquinoline that were originally intended to be antimalarial agents, have also demonstrated high inhibitory activity against antimony-sensitive and antimony-resistant strains of *L. donovani* in a mouse model and *in vitro*. [38,39] In the case of sitamaquine, its exact molecular targets remain unknown. Sitamaquine was also considered to be a potential oral treatment option for VL. Unfortunately, after reaching phase 2-b clinical trials and exhibiting severe side effects, its development as an antileishmanial drug was stopped in 2017. [2] Garnier *et al.* attempted to develop formulations of sitamaquine dihydrochloride for topical application, but while these formulations showed reasonable activity against the parasite *in vitro*, *in vivo* experiments ultimately did not show reduced parasite burden or slowed lesion progression. [40]

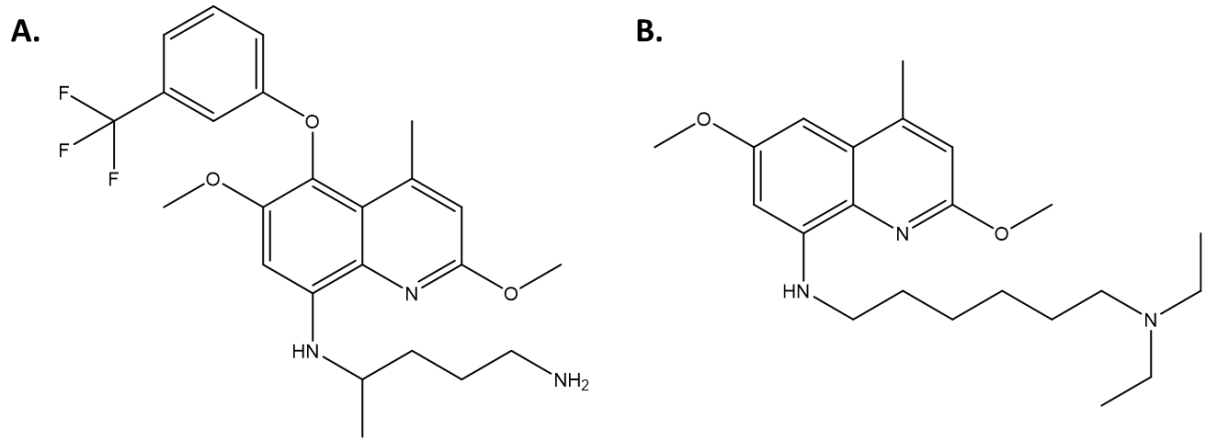

***Figure 1.8**: Structures of tafenoquine (A) and sitamaquine (B).* [38]

Quinoline-based compounds found in nature also appear to be promising drug leads. In 2020, Torres Suarez *et al.* synthesised eight analogues of a naturally occurring quinoline alkaloid found in the plant *Raputia heptaphylla* and tested their antileishmanial activity against *L. (V.) panamensis*. [41] Only two compounds were found to be non-cytotoxic to human monocyte-derived macrophages (hMDMs) while having high antiparasitic activity against both promastigotes and amastigotes. In addition to this, the authors observed that the compounds altered the amastigote cellular structure, with the parasites having vacuolated cytoplasm and abnormal chromatin distribution after treatment. [41]

From the examples given above, it is evident that quinoline-based compounds have the potential to be utilised as reliable antileishmanial agents. Nevertheless, researchers around the world have also been exploring other classes of compounds to aid drug development, specifically transition metal-based compounds.

1.3. Metals in medicine

1.3.1. Historical usage

Since ancient history, metals and metal-based drugs have had a major role as chemotherapeutic and anti-infective agents. For example, the use of copper and lead compounds to treat eye infections and as an antiseptic is detailed in the Ebers Papyrus, an Egyptian record of herbal medicine written in 1550 BC. [42,43] In more recent history, we have seen the development of metal-based drugs such as the organometallic compound arsphenamine/Salvarsan for syphilis treatment, the anticancer drug cisplatin (**Figure 1.9A**) and the rheumatoid arthritis drug auranofin (**Figure 1.9B**). [21,43,44] There is now

an increased interest in metal-based agents as remedies for various diseases. This is because scientists recognised that by choosing suitable ligands, it is possible to fine-tune the reactivity of metal compounds toward target biomolecules and counter the systemic toxicity of some metals. [21]

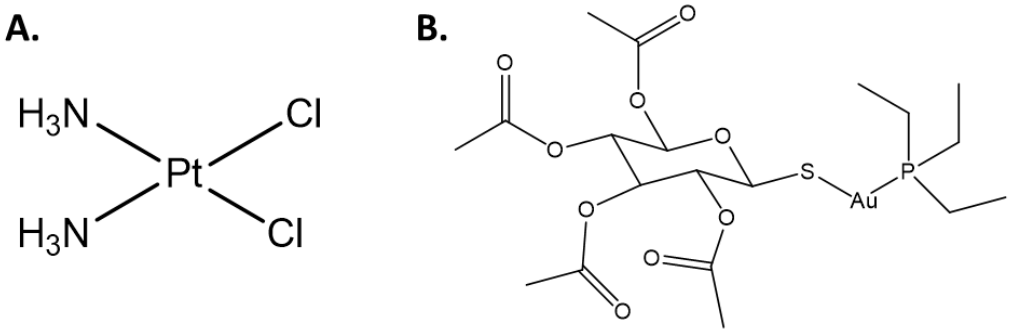

***Figure 1.9**: Structures of cisplatin (A) and auranofin (B).* [21]

1.3.2. Use of metals in antiparasitic drug design

Metal-based compounds have been used as antiparasitics since they show a pronounced selectivity for selected parasites' biomolecules compared to the host's biomolecules. [21] It is worth noting that while it is not considered a metallic element in the strictest sense, the p-block metalloid antimony, which has a mixture of both metallic and non-metallic properties, is still an essential component in the structures of first-line antileishmanial drugs. Antimony itself has a history of being used as a general panacea during the 16th century. [19] This indicates the value of having metallic or metal-like elements in antiparasitic drug design.

In support of this, a study by Fricker *et al*. investigated the inhibitory effects of metal complexes against the cysteine proteases of trypanosomatids, which are essential proteins in the life cycles of parasites in this order. [45] The researchers synthesised a series of gold(III), palladium(II) and oxorhenium(V) complexes (**Figure 1.10**), and two of the rhenium complexes exhibited the greatest inhibition of cruzain and cpB, the cysteine proteases found in *Trypanosoma* and *Leishmania* species, respectively. An additional two rhenium complexes and one palladium complex were observed to inhibit the growth of *T. cruzi*, with the palladium compound also showing high antileishmanial activity against *L. major*, *L. mexicana* and *L. donovani*. [45]

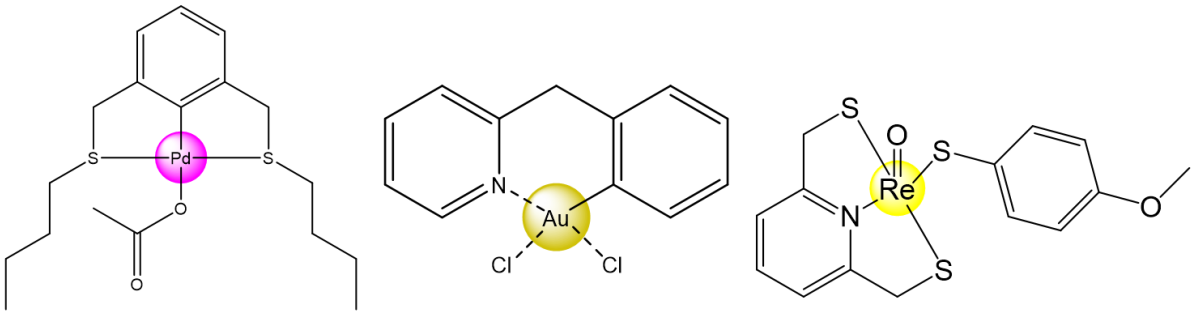

***Figure 1.10**: Examples of the palladium, gold and rhenium complexes synthesised by Fricker et al.* [45]

Copper, although generally known for its good electrical conductivity and use in electric wires today, is another metal that has interestingly found a use in the development of enhanced antiparasitic agents. In 2023, de Azevedo-França and colleagues reported the synthesis of six hybrid compounds consisting of copper(II) complexes bonded to three known antifungal and antiparasitic azole drugs (clotrimazole, fluconazole and ketoconazole) (**Figure 1.11**). [46] They observed that all six hybrids had lower IC_{50} values than the standalone drugs against both the promastigote and amastigote forms of *L. amazonensis* (IC_{50} < 2.00 µM). In addition to that, when compared to the free azole drugs, the hybrids were generally equally or more selective towards the parasite than murine macrophages. [46]

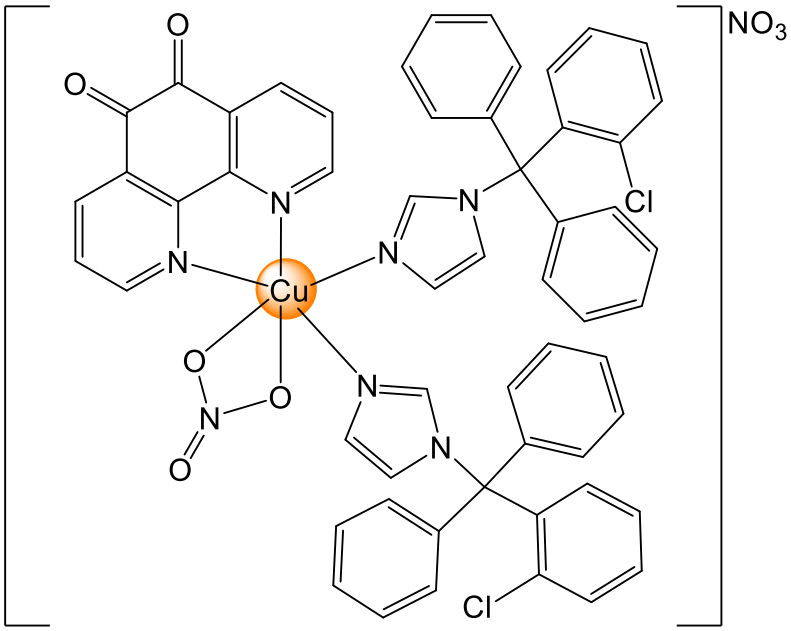

***Figure 1.11**: One of the clotrimazole-containing copper(II) complexes synthesised by de Azevedo-França et al.* [46]

Duffin and Andrews demonstrated the potential use of gallium as an antileishmanial metal, inspired by success stories of its use in anticancer treatments. [47] In their 2023 study, the authors synthesised and assessed six gallium-quinolinol complexes with various alkyl chains to enhance lipophilicity, a feature that pentavalent antimonials lack. Two of the complexes were found to be the most active and selective against *L. major*, *L. amazonensis* and *L. donovani*, with one outcompeting amphotericin B (**Figure 1.12**), making them promising candidates for future *in vivo* testing. [47]

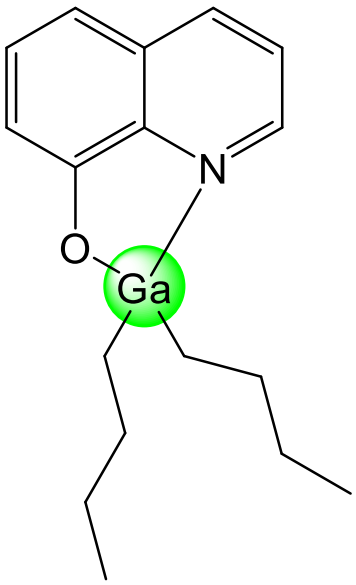

***Figure 1.12**: The most biologically active gallium-quinolinol complex synthesised by Duffin and Andrews.* [47]

In the field of malaria research, multiple studies have shown how coupling the quinoline scaffold to metal complexes can lead to compounds that possess enhanced antimalarial properties. [48–54] Metals that have been used to this effect include platinum group metals, such as platinum, iridium, rhodium and ruthenium, as well as iron. Iron, in particular, has gained much interest and seen extensive use in the form of its organometallic complex ferrocene.

1.3.3. Ferrocene: General properties and uses

Ferrocene consists of an iron atom bonded to two cyclopentadienyl rings (**Figure 1.13A**). This compound was combined with chloroquine to create the more potent antimalarial drug ferroquine (**Figure 1.13B**) to overcome chloroquine resistance in *Plasmodium* parasites, making ferroquine the

most advanced organometallic drug candidate to date, currently undergoing clinical trials. [21,35,49,51,55] Ferroquine's success has motivated malaria researchers to also incorporate ferrocene in a variety of quinoline-derived scaffolds, for instance, scaffolds containing branched polyamine linkers to accommodate multiple ferrocene cores. [50] Its use has also been extended to cancer treatment. The antitumoral compound ferrocifen (**Figure 1.13C**) was developed by combining ferrocene with the antitumoral drug tamoxifen and has had a similar level of success to that of ferroquine. [35,56] This showcases the versatility of ferrocene as it can be used in conjunction with a range of medicinally active organic compounds.

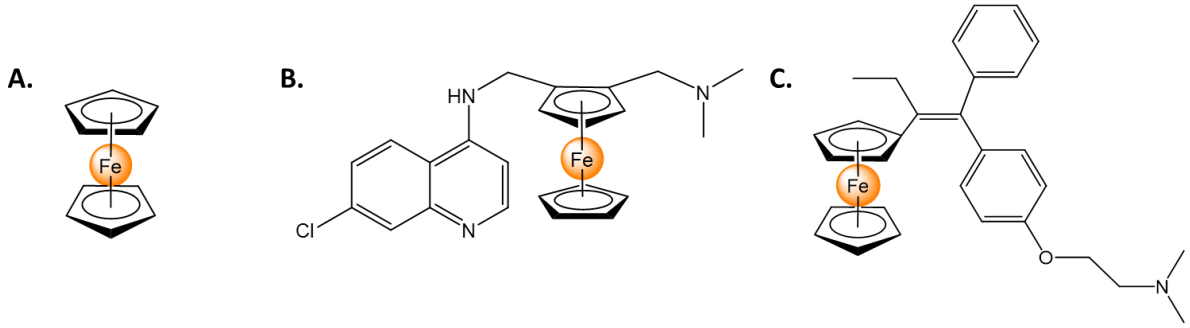

Figure 1.13: *Structures of ferrocene and derivatives. (A) Ferrocene; (B) Ferroquine; (C) Ferrocifen.* [55,56]

The successful use of ferrocene in drug design has been attributed to several characteristics. The first is the complex's reversible redox properties. Oxidation of Fe(II) to Fe(III) results in the production of ROS, which are known to cause cellular damage. [21,35,57,58] Secondly, ferrocene is relatively easy to functionalise, thus allowing for a variety of chemical entities to be coupled to it. [35,52] Thirdly, the complex is lipophilic in nature, which enhances the cell permeability of drug compounds and increases their bioavailability. [51] Lastly, ferrocene is generally non-toxic compared to other metals and metal complexes as well as stable in aqueous and aerobic media. [52,56]

1.3.4. Use of ferrocene in antileishmanial drug design

The use of ferrocene with regard to leishmaniasis is still in its infancy and has been documented in relatively fewer studies compared to the work done in researching ferrocenyl antimalarials. These few studies, however, have provided promising outcomes through diverse approaches to new antileishmanial drug design. They also showcase the ability of ferrocene to combine with a wide range of biologically active organic compounds.

In 2003, the *in vitro* activity of ten synthesised *N*-ferrocenylmethyl, *N'*-methyl-2-substituted benzimidazoles and benzimidazolium iodide salts against *L. infantum* was reported by Howarth and Hanlon. [59] One of the salts is illustrated in **Figure 1.14**. Benzimidazole is another privileged heterocyclic pharmacophoric scaffold that has seen extensive use in a number of disease settings. [60,61] However, while these salts were effective against the parasite, it is unclear whether they were tested on the promastigote or amastigote form, and there was no mention of their cytotoxicity in host cells.

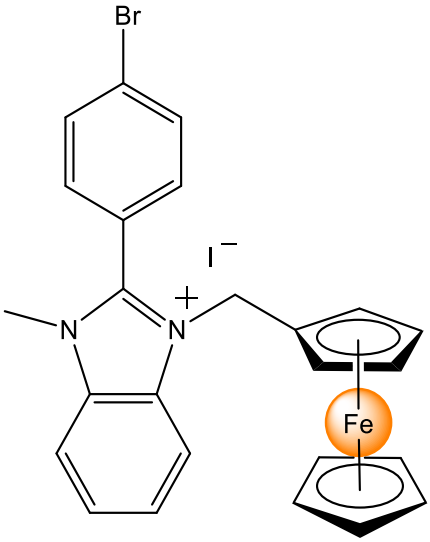

***Figure 1.14**: One of the N-ferrocenylmethyl, N'-methyl-2-substituted benzimidazolium iodide salts synthesised by Howarth and Hanlon.* [59]

The antileishmanial properties of benzimidazole-based ferrocenyl compounds were assessed by Quintal *et al*. as well, who synthesised a series of ferrocenyl-quinoline and imidazole compounds. [62] All the 12 compounds synthesised consisted of the ferrocene moiety bonded to either a quinoline, benzimidazole, pyridine or imidazole derivative via an amide bridge (**Figure 1.15**), the rationale being that the amide bond could be hydrolysed in infected macrophages, thus allowing for drug release. Only three were found to be active against *L. infantum*, surpassing miltefosine in antiamastigote activity, cytotoxicity and selectivity. [62]

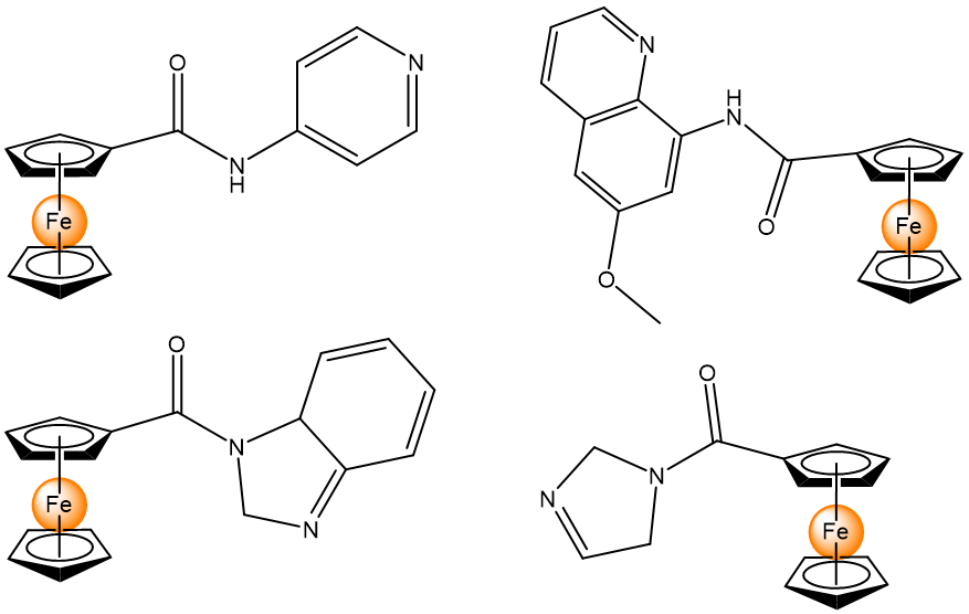

***Figure 1.15**: Examples of the ferrocenyl compounds synthesised by Quintal et al.* [62]

Yousuf and colleagues reported on the synthesis of ferrocenyl-quinoline compounds for use against *L. donovani* and *L. major*. [63,64] Their first report in 2015 described the synthesis of a triazole-containing ferrocenyl-quinoline compound using click chemistry (**Figure 1.16**). The compound had higher potency against *L. donovani* (IC_{50} = 15.26 µM), outcompeting miltefosine, chloroquine and ferroquine. This potency was marked by elevated ROS and NO production as well as changes in parasite morphology. [63] The authors followed up on their work the subsequent year by synthesising 13 5-aryl substituted derivatives of their ferrocenyl-quinoline compound. The three most active derivatives had comparable activity to miltefosine and also induced NO production. [64]

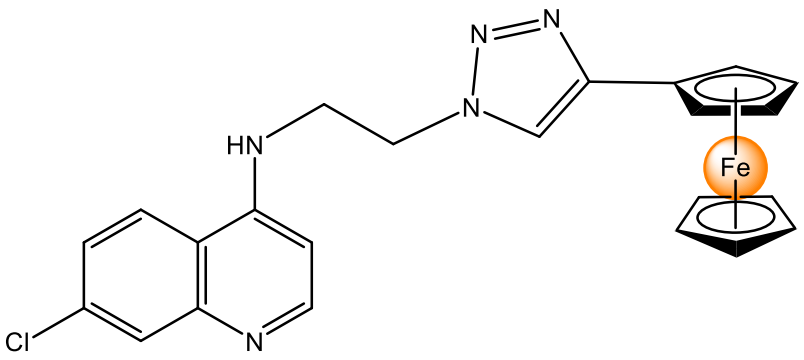

***Figure 1.16**: The ferrocenyl-quinoline compound first synthesised by Yousuf et al.* [63]

Recently, Moller *et al.* synthesised a series of 17 ferrocenyl-azines (such as the one illustrated in **Figure 1.17**) and assessed their activity against *L. major* and two *L. donovani* strains. [65] Only five were biologically active against the promastigotes of the *L. donovani* strains (IC_{50} = 0.69 – 2.72 µM), with one compound being active against the antimonial-resistant strain. The five compounds were further tested against the amastigote form of *L. donovani*, and only two were found to be significantly selective toward the parasite with reference to THP-1 macrophages. [65]

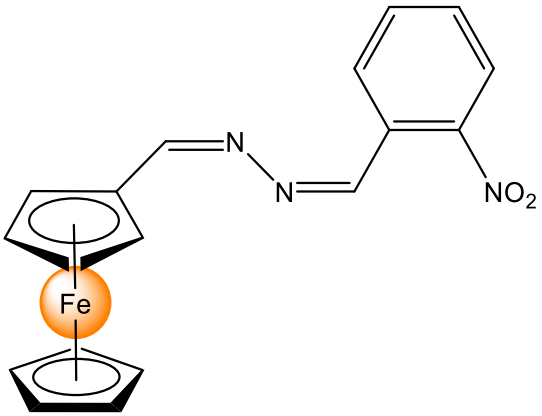

***Figure 1.17**: One of the ferrocenyl-azines synthesised by Moller et al.* [65]

Coupling antimicrobial peptides to the ferrocene moiety also shows promise. Costa *et al.* demonstrated this when they conjugated ferrocene to an antimicrobial peptide derived from the human chemokine CXCL4. They found that it was more active against *L. amazonensis* than the peptide alone and amphotericin B (IC_{50} < 0.63 µM). However, it was also more cytotoxic than the sole peptide (CC_{50} < 100 µM), thus resulting in a lower selectivity index. [66]

1.4. Rationale and motivation

Drug resistance has been a major problem when it comes to treating parasitic diseases, and cutaneous leishmaniasis is no exception. In the case of leishmaniasis, this problem is worsened by the fact that the drugs currently in use are severely toxic to patients. It is clear that safer and more potent drug candidates are needed to overcome this problem. Additionally, the possibility of potential vectors of the disease entering South Africa's borders cannot be completely ignored, given that some cases have been reported in Namibia over the decades, though fewer than those in Africa's central and northern regions. [12]

As developing novel antileishmanial drugs is costly, the next best and significantly more affordable alternative is to repurpose biologically active compounds that have proven their effectiveness against other parasitic illnesses in the past and recent years. The success stories of using metallo *N*-heterocyclic compounds to overcome drug resistance in malaria, another parasitic disease that affects the African continent, hold promise in the search for new antileishmanial drug candidates. Furthermore, the use of ferrocenyl heterocyclic compounds to treat cutaneous leishmaniasis has not been explored extensively. Given the above, this study investigated the potential of repurposing quinoline-based ferrocenyl drug leads to treat cutaneous leishmaniasis, specifically caused by *L. major*.

1.5. Aims and objectives

1.5.1. Overall aim

The overall aim of this study was to determine the antileishmanial activity of repurposed ferrocenyl-quinoline compounds in cell-based models of murine cutaneous leishmaniasis caused by *L. major*.

1.5.2. Specific objectives

The specific objectives were as follows:

1) Synthesise a series of ferrocenyl-quinoline compounds with varying linkers. The proposed linkers are as follows: imino-alkane (**Figure 1.18A**), amino-alkane (**Figure 1.18B**), triazole-amine (**Figure 1.18C**) phenyl-amine (**Figure 1.18D**) and phenyl-alkene (**Figure 1.18E**).

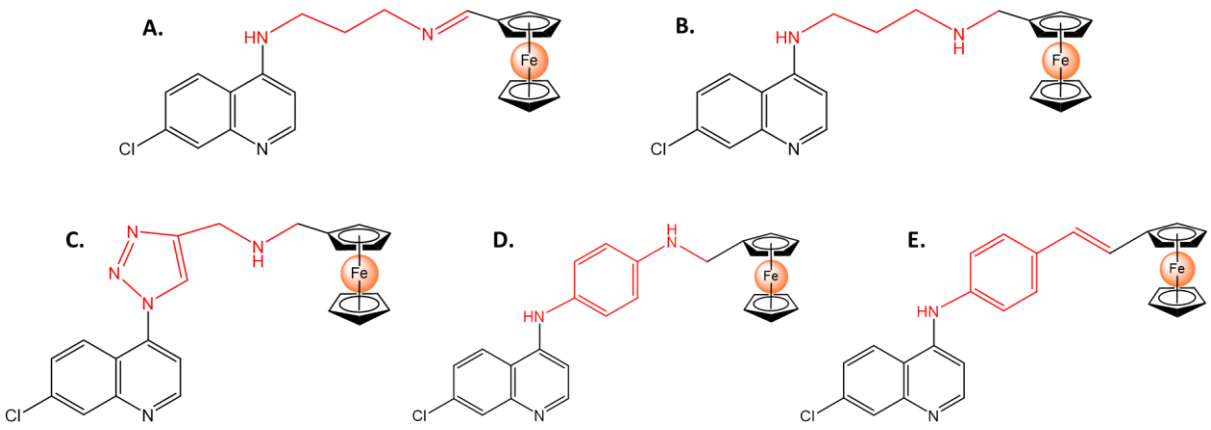

Figure 1.18: *Structures of proposed ferrocenyl-quinoline compounds. Variable linkers highlighted in red are as follows: imino-alkane (A), amino-alkane (B), triazole-amine (C), phenyl-amine (D) and phenyl-alkene (E).*

2) Characterise the synthesised ferrocenyl-quinoline compounds using various spectroscopic and analytical techniques, including nuclear magnetic resonance spectroscopy (NMR), Fourier-transform infrared spectroscopy (FT-IR), high-performance liquid chromatography (HPLC), high-resolution electrospray ionisation (ESI) mass spectrometry and melting point analysis.
3) Determine the *in vitro* antileishmanial activity (IC_{50}) of the synthesised compounds against promastigotes of *L. major* (LV39).
4) Determine the *in vitro* cytotoxicity (CC_{50}) of the compounds in murine RAW 264.7 macrophages.

REFERENCES

1 World Health Organisation, Leishmaniasis, https://www.who.int/news-room/fact-sheets/detail/leishmaniasis, (accessed 30 April 2023).

2 A. C. Pinheiro and M. V. N. de Souza, Current leishmaniasis drug discovery, *RSC Medicinal Chemistry*, 2022, **13**, 1029–1043.

3 H. F. Tamiru, Y. J. Mashalla, R. Mohammed and G. T. Tshweneagae, Cutaneous leishmaniasis a neglected tropical disease: Community knowledge, attitude and practices in an endemic area, Northwest Ethiopia, *BMC Infectious Diseases*, 2019, **19**, 1–10.

4 D. A. Boakye, M. Wilson and M. Kweku, A review of leishmaniasis in west Africa., *Ghana medical journal*, 2005, **39**, 94–7.

5 A. Tabbabi, Review of leishmaniasis in the middle east and North Africa, *African Health*

Sciences, 2019, **19**, 1329–1337.

6 R. Arenas, E. Torres-Guerrero, M. R. Quintanilla-Cedillo and J. Ruiz-Esmenjaud, Leishmaniasis: A review, *F1000Research*, 2017, **6**, 1–15.

7 G. Volpedo, T. Pacheco-Fernandez, E. A. Holcomb, N. Cipriano, B. Cox and A. R. Satoskar, Mechanisms of immunopathogenesis in cutaneous leishmaniasis and post Kala-azar dermal leishmaniasis (PKDL), *Frontiers in Cellular and Infection Microbiology*, 2021, **11**, 1–16.

8 Á. Gabriel, A. Valério-Bolas, J. Palma-Marques, P. Mourata-Gonçalves, P. Ruas, T. Dias-Guerreiro and G. Santos-Gomes, Cutaneous leishmaniasis: The complexity of host's effective immune response against a polymorphic parasitic disease, *Journal of Immunology Research*, 2019, **2019**, 1–16.

9 I. Abadías-Granado, A. Diago, P. A. Cerro, A. M. Palma-Ruiz and Y. Gilaberte, Cutaneous and Mucocutaneous Leishmaniasis, *Actas Dermo-Sifiliograficas*, 2021, **112**, 601–618.

10 A. Krüger, First collection records of phlebotomine sandflies (Diptera: Psychodidae) in Botswana, *African Invertebrates*, 2015, **56**, 645–649.

11 A. Krüger, Phlebotomine sandflies of Botswana: a taxonomic review and a faunistic update with the first record of genus Phlebotomus, *Acta Tropica*, 2017, **171**, 96–100.

12 B. H. Noden and B. E. Van Der Colf, Neglected tropical diseases of Namibia: Unsolved mysteries, *Acta Tropica*, 2013, **125**, 1–17.

13 D. E. Teixeira, M. Benchimol, J. C. F. Rodrigues, P. H. Crepaldi, P. F. P. Pimenta and W. de Souza, The Cell Biology of Leishmania: How to Teach Using Animations, *PLoS Pathogens*, 2013, **9**, 8–11.

14 E. N. Loría-Cervera and F. J. Andrade-Narváez, Review: Animal models for the study of leishmaniasis immunology, *Revista do Instituto de Medicina Tropical de Sao Paulo*, 2014, **56**, 1–11.

15 C. M. Restrepo, A. Llanes, L. Herrera, E. Ellis, R. Lleonart and P. L. Fernández, Gene expression patterns associated with leishmania panamensis infection in macrophages from BALB/c and C57BL/6 mice, *PLoS Neglected Tropical Diseases*, 2021, **15**, 1–20.

16 M. Amini, H. Nahrevanian, M. Farahmand, S. Khatami, S. Javadian and F. Mirkhani, Immuno-biochemical variation in susceptible BALB/c and resistant C57BL/6 mice infected with Iranian strain of cutaneous leishmaniasis; Leishmania major MRHO/IR/75/ER, *Internet Journal of*

Infectious Diseases, 2009, **7**, 1–4.

17 E. K. Elmahallawy, A. A. M. Alkhaldi and A. A. Saleh, Host immune response against leishmaniasis and parasite persistence strategies: A review and assessment of recent research, *Biomedicine and Pharmacotherapy*, 2021, **139**, 111671.

18 R. Hurdayal and F. Brombacher, Interleukin-4 Receptor Alpha: From innate to adaptive immunity in murine models of cutaneous leishmaniasis, *Frontiers in Immunology*, 2017, **8**, 1–15.

19 A. K. Haldar, P. Sen and S. Roy, Use of Antimony in the Treatment of Leishmaniasis: Current Status and Future Directions, *Molecular Biology International*, 2011, **2011**, 1–23.

20 L. L. G. Ferreira and A. D. Andricopulo, Chemoinformatics strategies for leishmaniasis drug discovery, *Frontiers in Pharmacology*, 2018, **9**, 1–11.

21 M. Navarro, C. Gabbiani, L. Messori and D. Gambino, Metal-based drugs for malaria, trypanosomiasis and leishmaniasis: Recent achievements and perspectives, *Drug Discovery Today*, 2010, **15**, 1070–1078.

22 F. Frézard, M. M. G. Aguiar, L. A. M. Ferreira, G. S. Ramos, T. T. Santos, G. S. M. Borges, V. M. R. Vallejos and H. L. O. De Morais, Liposomal Amphotericin B for Treatment of Leishmaniasis: From the Identification of Critical Physicochemical Attributes to the Design of Effective Topical and Oral Formulations, *Pharmaceutics*, 2022, **15**, 99.

23 S. Sundar and J. Chakravarty, Liposomal amphotericin B and leishmaniasis: Dose and response, *Journal of Global Infectious Diseases*, 2010, **2**, 159.

24 B. A. Ferreira, E. M. Coser, S. de la Roca, J. I. Aoki, N. Branco, G. H. C. Soares, M. I. S. Lima and A. C. Coelho, Amphotericin B resistance in Leishmania amazonensis: In vitro and in vivo characterization of a Brazilian clinical isolate, *PLoS Neglected Tropical Diseases*, 2024, **18**, 1–18.

25 E. A. Alpizar-Sosa, N. R. B. Ithnin, W. Wei, A. W. Pountain, S. K. Weidt, A. M. Donachie, R. Ritchie, E. A. Dickie, R. J. S. Burchmore, P. W. Denny and M. P. Barrett, Amphotericin B resistance in Leishmania mexicana: Alterations to sterol metabolism and oxidative stress response, *PLOS Neglected Tropical Diseases*, 2022, **16**, e0010779.

26 C. Mano, A. Kongkaew, P. Tippawangkosol, P. Somboon, S. Roytrakul, P. Pescher, G. F. Späth, C. Uthaipibull, A. Tantiworawit, P. Siriyasatien and N. Jariyapan, Amphotericin B resistance correlates with increased fitness in vitro and in vivo in Leishmania (Mundinia) martiniquensis,

Frontiers in Microbiology, 2023, **14**, 1–12.

27 N. C. Baker, S. Ekins, A. J. Williams and A. Tropsha, A bibliometric review of drug repurposing, *Drug Discovery Today*, 2018, **23**, 661–672.

28 P. Ayyar and U. Subramanian, Repurposing – second life for drugs, *Pharmacia*, 2022, **69**, 51–59.

29 J. P. Jourdan, R. Bureau, C. Rochais and P. Dallemagne, Drug repositioning: a brief overview, *Journal of Pharmacy and Pharmacology*, 2020, **72**, 1145–1151.

30 T. Pillaiyar, S. Meenakshisundaram, M. Manickam and M. Sankaranarayanan, A medicinal chemistry perspective of drug repositioning: Recent advances and challenges in drug discovery, *European Journal of Medicinal Chemistry*, 2020, **195**, 112275.

31 S. M. Prajapati, K. D. Patel, R. H. Vekariya, S. N. Panchal and H. D. Patel, Recent advances in the synthesis of quinolines: A review, *RSC Advances*, 2014, **4**, 24463–24476.

32 K. M. Al-Ahmary, M. S. Alenezi and M. M. Habeeb, Synthesis, spectroscopic and DFT theoretical studies on the hydrogen bonded charge transfer complex of 4-aminoquinoline with chloranilic acid, *Journal of Molecular Liquids*, 2016, **220**, 166–182.

33 P. Yadav and K. Shah, Quinolines, a perpetual, multipurpose scaffold in medicinal chemistry, *Bioorganic Chemistry*, 2021, **109**, 104639.

34 T. M. Belete, Recent progress in the development of new antimalarial drugs with novel targets, *Drug Design, Development and Therapy*, 2020, **14**, 3875–3889.

35 D. Gambino and L. Otero, Design of prospective antiparasitic metal-based compounds including selected organometallic cores, *Inorganica Chimica Acta*, 2018, **472**, 58–75.

36 A. Sabt, W. M. Eldehna, T. M. Ibrahim, A. A. Bekhit and R. Z. Batran, New antileishmanial quinoline linked isatin derivatives targeting DHFR-TS and PTR1: Design, synthesis, and molecular modeling studies, *European Journal of Medicinal Chemistry*, 2023, **246**, 114959.

37 G. de S. V. Tavares, D. V. C. Mendonça, D. P. Lage, J. da T. Granato, F. M. Ottoni, F. Ludolf, M. A. Chávez-Fumagalli, M. C. Duarte, C. A. P. Tavares, R. J. Alves, E. S. Coimbra and E. A. F. Coelho, Antileishmanial Activity, Cytotoxicity and Mechanism of Action of Clioquinol Against Leishmania infantum and Leishmania amazonensis Species, *Basic and Clinical Pharmacology and Toxicology*, 2018, **123**, 236–246.

38 V. Yardley, F. Gamarro and S. L. Croft, Antileishmanial and antitrypanosomal activities of the 8-

aminoquinoline tafenoquine, *Antimicrobial Agents and Chemotherapy*, 2010, **54**, 5356–5358.

39 P. M. Loiseau, S. Cojean and J. Schrével, Sitamaquine as a putative antileishmanial drug candidate: From the mechanism of action to the risk of drug resistance, *Parasite*, 2011, **18**, 115–119.

40 T. Garnier, M. B. Brown, M. J. Lawrence and S. L. Croft, In-vitro and in-vivo studies on a topical formulation of sitamaquine dihydrochloride for cutaneous leishmaniasis, *Journal of Pharmacy and Pharmacology*, 2010, **58**, 1043–1054.

41 E. Torres Suarez, D. S. Granados-Falla, S. M. Robledo, J. Murillo, Y. Upegui and G. Delgado, Antileishmanial activity of synthetic analogs of the naturally occurring quinolone alkaloid N-methyl-8-methoxyflindersin, *PLOS ONE*, 2020, **15**, e0243392.

42 A. M. Metwaly, M. M. Ghoneim, I. H. Eissa, I. A. Elsehemy, A. E. Mostafa, M. M. Hegazy, W. M. Afifi and D. Dou, Traditional ancient Egyptian medicine: A review, *Saudi Journal of Biological Sciences*, 2021, **28**, 5823–5832.

43 K. J. Franz and N. Metzler-Nolte, Introduction: Metals in Medicine, *Chemical Reviews*, 2019, **119**, 727–729.

44 K. J. Williams, The introduction of 'chemotherapy' using arsphenamine - The first magic bullet, *Journal of the Royal Society of Medicine*, 2009, **102**, 343–348.

45 S. P. Fricker, R. M. Mosi, B. R. Cameron, I. Baird, Y. Zhu, V. Anastassov, J. Cox, P. S. Doyle, E. Hansell, G. Lau, J. Langille, M. Olsen, L. Qin, R. Skerlj, R. S. Y. Wong, Z. Santucci and J. H. McKerrow, Metal compounds for the treatment of parasitic diseases, *Journal of Inorganic Biochemistry*, 2008, **102**, 1839–1845.

46 J. A. de Azevedo-França, V. Feliciano dos Santos Ramos, L. Messori, F. Santanni, L. Sorace, L. Pereira Borba-Santos, S. Rozental, J. Cola Fernandes Rodrigues and M. Navarro, Synthesis, characterization, and biological evaluation of hybrid copper(ii) complexes containing azole drugs and planar ligands against neglected diseases, *New Journal of Chemistry*, 2023, **48**, 2515–2526.

47 R. N. Duffin and P. C. Andrews, Structure-activity effects in the anti-leishmanial activity of di-alkyl gallium quinolin-8-olates, *Dalton Transactions*, 2023, **52**, 15848–15858.

48 M. Mbaba, T. M. Golding and G. S. Smith, Recent Advances in the Biological Investigation of Organometallic Platinum-Group Metal (Ir, Ru, Rh, Os, Pd, Pt) Complexes as Antimalarial Agents, *Molecules*, 2020, **25**, 5276.

49 N. Baartzes, T. Stringer and G. S. Smith, in *Advances in Bioorganometallic Chemistry*, Elsevier Inc., 2018, pp. 193–213.

50 T. Stringer, C. De Kock, H. Guzgay, J. Okombo, J. Liu, S. Kanetake, J. Kim, C. Tam, L. W. Cheng, P. J. Smith, D. T. Hendricks, K. M. Land, T. J. Egan and G. S. Smith, Mono- and multimeric ferrocene congeners of quinoline-based polyamines as potential antiparasitics, *Dalton Transactions*, 2016, **45**, 13415–13426.

51 J. Aksić, M. Genčić, N. Stojanović, N. Radulović, D. Zlatković, M. Dimitrijević, Z. Stojanović-Radić, J. Srbljanović, T. Štajner and L. Jovanović, New Iron Twist to Chloroquine–Upgrading Antimalarials with Immunomodulatory and Antimicrobial Features, *Journal of Medicinal Chemistry*, 2023, **66**, 2084–2101.

52 P. Govender, H. Lemmerhirt, A. T. Hutton, B. Therrien, P. J. Bednarski and G. S. Smith, First- and Second-Generation Heterometallic Dendrimers Containing Ferrocenyl–Ruthenium(II)–Arene Motifs: Synthesis, Structure, Electrochemistry, and Preliminary Cell Proliferation Studies, *Organometallics*, 2014, **33**, 5535–5545.

53 D. D. N'Da and P. J. Smith, Synthesis, in vitro antiplasmodial and antiproliferative activities of a series of quinoline-ferrocene hybrids, *Medicinal Chemistry Research*, 2014, **23**, 1214–1224.

54 D. R. Melis, C. B. Barnett, L. Wiesner, E. Nordlander and G. S. Smith, Quinoline-triazole half-sandwich iridium(iii) complexes: Synthesis, antiplasmodial activity and preliminary transfer hydrogenation studies, *Dalton Transactions*, 2020, **49**, 11543–11555.

55 C. Biot, G. Glorian, L. A. Maciejewski, J. S. Brocard, O. Domarle, G. Blampain, P. Millet, A. J. Georges and J. Lebibi, Synthesis and antimalarial activity in vitro and in vivo of a new ferrocene-chloroquine analogue, *Journal of Medicinal Chemistry*, 1997, **40**, 3715–3718.

56 C. C. Albertyn, A. van Niekerk, S. Duffy, V. M. Avery, E. Strauss and P. Chellan, Investigation of bioorganometallic artemisinins as antiplasmodials, *Journal of Organometallic Chemistry*, 2023, **987**–**988**, 122633.

57 Y. Na, J. S. Lee, J. Woo, S. Ahn, E. Lee, W. Il Choi and D. Sung, Reactive oxygen species (ROS)-responsive ferrocene-polymer-based nanoparticles for controlled release of drugs, *Journal of Materials Chemistry B*, 2020, **8**, 1906–1913.

58 B. S. Ludwig, S. Tomassi, S. Di Maro, F. S. Di Leva, A. Benge, F. Reichart, M. Nieberler, F. E. Kühn, H. Kessler, L. Marinelli, U. Reuning and S. Kossatz, The organometallic ferrocene exhibits amplified anti-tumor activity by targeted delivery via highly selective ligands to αvβ3, αvβ6, or

α5β1 integrins, *Biomaterials*, 2021, **271**, 120754.

59 J. Howarth and K. Hanlon, N-ferrocenylmethyl, N'-methyl-2-substituted benzimidazolium iodide salts with in vitro activity against the Leishmania infantum parasite strain L1, *Bioorganic and Medicinal Chemistry Letters*, 2003, **13**, 2017–2020.

60 M. Gaba and C. Mohan, Development of drugs based on imidazole and benzimidazole bioactive heterocycles: recent advances and future directions, *Medicinal Chemistry Research*, 2016, **25**, 173–210.

61 S. Tahlan, S. Kumar, K. Ramasamy, S. M. Lim, S. A. A. Shah, V. Mani, R. Pathania and B. Narasimhan, Design, synthesis and biological profile of heterocyclic benzimidazole analogues as prospective antimicrobial and antiproliferative agents, *BMC Chemistry*, 2019, **13**, 1–15.

62 S. Quintal, T. S. Morais, C. P. Matos, M. Paula Robalo, M. F. M. Piedade, M. J. Villa De Brito, M. Helena Garcia, M. Marques, C. Maia, L. Campino and J. Madureira, Synthesis, structural characterization and leishmanicidal activity evaluation of ferrocenyl N-heterocyclic compounds, *Journal of Organometallic Chemistry*, 2013, **745**–**746**, 299–311.

63 M. Yousuf, D. Mukherjee, A. Pal, S. Dey, S. Mandal, C. Pal and S. Adhikari, Synthesis and biological evaluation of ferrocenylquinoline as a potential antileishmanial agent, *ChemMedChem*, 2015, **10**, 546–554.

64 M. Yousuf, D. Mukherjee, S. Dey, C. Pal and S. Adhikari, Antileishmanial ferrocenylquinoline derivatives: Synthesis and biological evaluation against Leishmania donovani, *European Journal of Medicinal Chemistry*, 2016, **124**, 468–479.

65 J. Möller, C. Kannigadu, J. Aucamp, M. C. Joseph, A. J. Swarts and D. D. N'Da, Synthesis, electrochemistry, and in vitro antileishmanial efficacy of novel ferrocenylazines, *Applied Organometallic Chemistry*, 2023, **37**, 1–13.

66 N. C. S. Costa, J. P. Piccoli, N. A. Santos-Filho, L. C. Clementino, A. M. Fusco-Almeida, S. R. De Annunzio, C. R. Fontana, J. B. M. Verga, S. F. Eto, J. M. Pizauro-Junior, M. A. S. Graminha and E. M. Cilli, Antimicrobial activity of RP-1 peptide conjugate with ferrocene group, *PLoS ONE*, 2020, **15**, 1–22.

CHAPTER 2

Materials and Methods

2.1. Chemical synthesis methods

2.1.1. Reagents and general details

Unless stated otherwise, all synthetic procedures were carried out under an inert argon atmosphere using standard Schlenk line techniques. All solvents and reagents were of reagent grade and used as received (Sigma-Aldrich, Merck and KIMIX), and anhydrous solvents were degassed with argon before use. Reactions were monitored by thin-layer chromatography (TLC) using aluminium-backed Merck precoated silica-gel 60 F_{254} plates, and compounds were visualised under ultraviolet (UV) light. Column chromatography was performed using 60 Å silica gel (70-230 mesh).

2.1.2. Spectroscopic and analytical techniques

Nuclear magnetic resonance (NMR) spectra were recorded on either a Varian Mercury 300 spectrometer (^{1}H: 300.08 MHz, ^{13}C {^{1}H}: 75.46 MHz), a Bruker Top-spin GmbH 400 Plus spectrometer (^{1}H: 399.95 MHz; ^{13}C{^{1}H}: 100.65 MHz) or a Bruker 600 FT spectrometer (^{1}H: 600.10 MHz, ^{13}C {^{1}H}: 150.60 MHz). Chemical shift values (δ) and *J*-coupling constants are reported in ppm and Hz, respectively, relative to tetramethylsilane (TMS) as an internal standard (δ 0.00). Infrared spectra were recorded using a Perkin-Elmer Spectrum 100 FT-IR spectrometer equipped with an Attenuated Total Reflectance Infrared Unit (ATR-IR). Melting points were obtained using a Büchi Melting Point Apparatus B-540. High-resolution mass spectrometry determinations were carried out using Electrospray Ionisation (ESI) on a Waters Cyclic IMS QTOF mass spectrometer coupled to a Waters UPLC, equipped with an ESI probe and with data recorded using the positive mode. Purity was determined using an Agilent HPLC 1260 equipped with an Agilent 1260 UV/Vis diode array detector (DAD) and an Agilent Pursuit 5 C18 column (5 µM, 150 mm ×4.6 mm). The compounds were eluted using a mixture of solvent A (0.1 % TFA in H_2O) and solvent B (MeOH) at a flow rate of 0.5 ml/min. The gradient elution conditions were as follows: 90 % solvent A between 0 and 2 min, 90 – 10 % solvent A from 2 to 8 min, and 10 %

solvent A from 8 to 25 min. Elemental analysis was done using a Perkin-Elmer 2400 CHN Elemental Analyser.

2.2. Synthesis of compounds

2.2.1. N'-(7-Chloroquinolin-4-yl)-propane-1,3-diamine (Compound 1) [1]

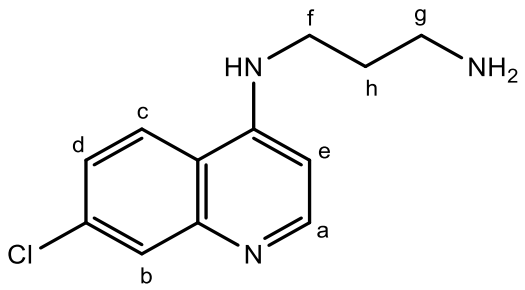

1,3-Diaminopropane (1.06 ml, 12.6 mmol) was slowly added to 4,7-dichloroquinoline (0.501 g, 2.53 mmol), and the resulting mixture was heated for 30 minutes at 80 °C without stirring. The temperature was then raised to 140 °C with stirring. After 22 hours, the yellow reaction mixture was cooled to room temperature before adding 1M NaOH (30 ml). The resulting mixture was stirred for 2 - 3 hours and extracted with hot EtOAc (3 x 40 ml). The organic layers were combined, washed with distilled H_2O (2 x 30 ml), brine (1 x 30 ml), and dried over anhydrous Na_2SO_4. Following filtration, the solvent of the filtrate was removed, leaving the precursor compound **1** as an off-white/pale yellow powder.

Yield: 0.343 g, 58%. **^{1}H NMR** (300 MHz, MeOD): (δ, ppm) 8.35 (d, *J* = 5.1 Hz, 1H, H_a), 8.08 (d, *J* = 8.7 Hz, 1H, H_c), 7.77 (s, 1H, H_b), 7.39 (d, *J* = 9.1 Hz, 1H, H_d), 6.54 (d, *J* = 5.4 Hz, 1H, H_e), 3.43 (t, *J* = 6.9 Hz, 2H, H_f), 2.81 (t, *J* = 6.5 Hz, 2H, H_g), 1.97 – 1.83 (m, 2H, H_h). **^{13}C {^{1}H} NMR** (101 MHz, MeOD): (δ, ppm) 152.69, 152.45, 149.68, 136.31, 127.61, 125.99, 124.26, 118.78, 99.66, 41.65, 40.16, 31.75. **IR**: (ν_{max}/cm^{-1}) 3247 (N-H), 2931 (C-H), 2861 (C-H), 1579 (C=N). **M.p.:** 135 – 139 °C. **LC-MS:** Calculated for $C_{12}H_{15}ClN_3^+$: 236.09. Found: 236.10 $[M+H]^+$. **Purity** (HPLC): 88% (t_R = 3.34 min).

2.2.2. (E)-N-(3-(Ferrocenylideneamino)propyl)-7-chloroquinolin-4-amine (Compound 2) [2]

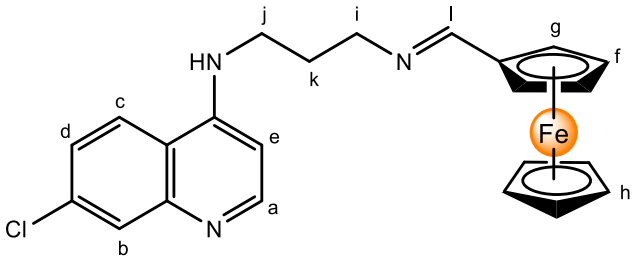

To a suspension of the precursor compound **1** (0.204 g, 0.863 mmol) in diethyl ether (30 ml), a solution of ferrocenecarboxaldehyde (0.205 g, 0.955 mmol) in diethyl ether (5 ml) was added, and the mixture was stirred for 72 hours at room temperature (25 °C). An orange precipitate was filtered, washed with diethyl ether to remove excess aldehyde, and dried *in vacuo*, leaving compound **2** as an orange/brown powder.

Yield: 0.270 g, 72%. **^{1}H NMR** (300 MHz, $CDCl_3$): (δ, ppm) 8.50 (br s, 1H, H_a), 8.20 (s, 1H, H_l), 7.96 (s, 1H, H_b), 7.83 (d, J = 7.9 Hz, 1H, H_c), 7.26 (br s, 1H, H_d), 6.38 (br s, 1H, H_e), 4.69 (br s, 2H, H_f), 4.48 (br s, 2H, H_g), 4.19 (s, 5H, H_h), 3.72 (br s, 2H, H_i), 3.50 (br s, 2H, H_j), 2.17 (br s, 2H, H_k). **^{13}C {^{1}H} NMR** (150 MHz, $CDCl_3$): (δ, ppm) 162.04, 152.08, 150.29, 149.07, 134.68, 128.50, 124.83, 122.09, 117.44, 98.53, 80.21, 70.80, 69.16, 68.49, 61.29, 43.54, 29.63. **IR**: (ν_{max}/cm^{-1}) 3228 (N-H), 1578 (C=N). **M.p.:** 104 – 108 °C. **ESI-MS:** Calculated for $C_{23}H_{23}ClN_3Fe^+$: 432.0800. Found: 432.0930 $[M+H]^+$. **Purity** (HPLC): 88% (t_R = 3.11 min).

2.2.3. N-(7-Chloro-4-quinolinyl)-N'-ferrocenyl-propane-1,3-diamine (Compound 3) [3]

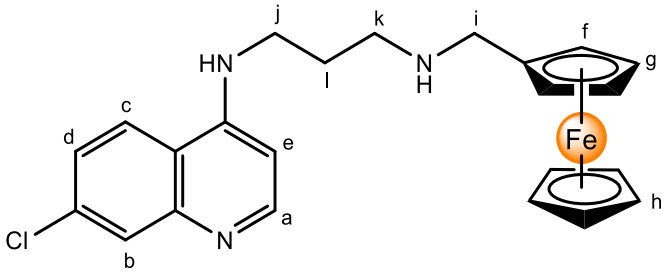

Ferrocenecarboxaldehyde (0.217 g, 1.01 mmol) and the precursor compound **1** (0.263 g, 1.12 mmol) were dissolved in anhydrous methanol (20 ml). The mixture was stirred at room temperature (25 °C) for 24 hours. Sodium borohydride (0.114 g, 3.00 mmol) was added slowly, and the resulting mixture was stirred for an additional two hours. The reaction mixture was quenched with the addition of 5% w/v $NaHCO_3$ solution (20 ml), and the resulting mixture was extracted with diethyl ether (3 × 20 ml).

The combined organic fractions were dried over anhydrous Na_2SO_4, and the solvent was removed under reduced pressure. Purification of the desired product was done by column chromatography using silica with a mixture of ethyl acetate/methanol/Et_3N in increasing polarity, 100:0:0 to 94:4:2 ratios. The solvent mixture was removed from the fractions containing compound **3**, and this was crystallised into an orange solid using solvent diffusion/layering with DCM and hexane.

Yield: 0.160 g, 36%. **^{1}H NMR** (300 MHz, $CDCl_3$): (δ, ppm) 8.42 (d, 1H, H_a), 7.88 (s, 1H, H_b), 7.65 (d, *J* = 9.0 Hz, 1H, H_c), 7.21 (d, *J* = 8.8 Hz, 1H, H_d), 6.24 (d, 1H, H_e), 4.24 (br s, 2H, H_f), 4.20 (br s, 2H, H_g), 4.14 (s, 5H, H_h), 3.65 (br s, 2H, H_i), 3.39 (br s, 2H, H_j), 2.99 (br s, 2H, H_k), 2.24 (br s, NH) 1.94 (br s, 2H, H_l). **^{13}C {^{1}H} NMR** (150 MHz, $CDCl_3$): (δ, ppm) 152.05, 150.77, 149.00, 134.74, 128.29, 125.06, 122.73, 117.63, 98.19, 85.71, 68.92, 68.67, 68.37, 49.61, 49.58, 44.31, 27.14. **IR**: (ν_{max}/cm^{-1}) 3220 (N-H), 2830 (C-H), 1576 (C=N). **M.p.:** 118 – 122 °C. **ESI-MS:** Calculated for $C_{23}H_{25}ClN_3Fe^+$: 434.1000. Found: 434.1088 $[M+H]^+$. **Purity** (HPLC): 97% (t_R = 3.12 min).

2.2.4. 4-Azido-7-chloroquinoline (Compound 4) [4]

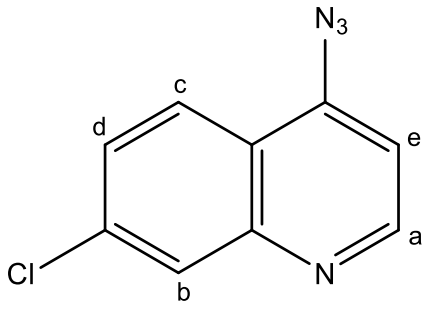

4,7-Dichloroquinoline (2.04 g, 10.3 mmol) was dissolved in 5 ml anhydrous DMF. NaN_3 (1.34 g, 20.6 mmol) was then added in one portion, and the resulting mixture was stirred at 65 °C overnight, whereupon TLC indicated reaction completion. The reaction mixture was then allowed to cool to ambient temperature, after which it was diluted in DCM (100 ml), washed with water (3 x 30 ml), dried over anhydrous Na_2SO_4, and evaporated to dryness. The residue was crystallised from a DCM/hexane mixture to yield the precursor compound **4** as a grey powder.

Yield: 0.582 g, 28%. **^{1}H NMR** (300 MHz, $CDCl_3$): (δ, ppm) 8.81 (br s, 1H, H_a), 8.04 (s, 1H, H_b), 7.98 (d, *J* = 8.8 Hz, 1H, H_c), 7.47 (d, *J* = 8.8 Hz, 1H, H_d), 7.12 (d, *J* = 3.5 Hz, 1H, H_e). **^{13}C {^{1}H} NMR** (101 MHz, $CDCl_3$): (δ, ppm) 151.44, 149.70, 146.50, 136.71, 128.30, 127.72, 123.92, 120.09, 108.90. **IR**: (ν_{max}/cm^{-1}) 2125 (N=N=N), 1608 (C=N). **M.p.:** 116 – 118 °C. **LC-MS:** Calculated for $C_9H_6ClN_4^+$: 205.02. Found: 205.10 $[M+H]^+$. **Purity** (HPLC): 97% (t_R = 8.44 min).

2.2.5. Ferrocene methyl amino N-prop-2-yne (Compound 5) [5]

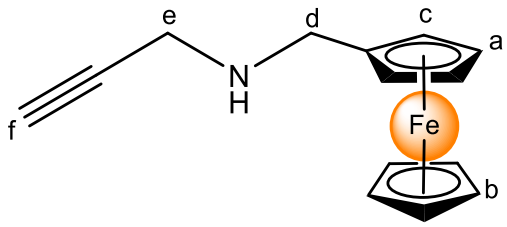

Ferrocenecarboxaldehyde (0.401 g, 1.87 mmol) was dissolved in methanol (5 ml). Propargylamine (143 µl, 2.25 mmol) was added to the solution. The reaction mixture was allowed to stir at room temperature (25 °C) in the dark (covered flask in foil) for 24 hours. All solvent was removed from the reaction mixture under reduced pressure. The crude mixture was extensively dried under reduced pressure at 40 °C to remove residual unreacted amine. The crude imine was re-dissolved in methanol (5 ml) and cooled to 0 °C. While stirring, sodium borohydride (0.213 g, 3.51 mmol) was added stepwise in small amounts over 15 minutes to the reaction mixture, which was left to stir for one hour. After all the methanol was evaporated under reduced pressure, the mixture was suspended in distilled H_2O (20 ml) and extracted with DCM (3 × 15 ml). The combined organic layer was washed with brine (25 ml) and saturated sodium bicarbonate (25 ml). The organic layer was dried over $MgSO_4$, filtered, and the solvent evaporated under reduced pressure until dryness. The dark orange-red oil crude product mixture was purified by silica column chromatography, solvent system: 10:01:90 (EtOAc:Et_3N:DCM). The precursor compound **5** was obtained as an orange-brown powder.

Yield: 0.396 g, 84%. **^{1}H NMR** (300 MHz, $CDCl_3$): (δ, ppm) 4.21 (br s, 2H, H_a), 4.14 (s, 5H, H_b), 4.11 (br s, 2H, H_c), 3.60 (s, 2H, H_d), 3.45 (s, 2H, H_e), 2.27 (s, 1H, H_f). **^{13}C {^{1}H} NMR** (101 MHz, $CDCl_3$): (δ, ppm) 86.10, 82.29, 71.63, 68.51, 68.08, 67.92, 47.47, 37.64. **IR**: (ν_{max}/cm^{-1}) 3301 (N-H), 3092 (C-H), 2848 (C-H), 2092 (C≡C). **M.p.:** 38 – 40 °C. **ESI-MS:** Calculated for $C_{14}H_{15}NFe^+$: 253.0500. Found: 253.0554 $[M]^+$. **Elemental analysis** for $C_{14}H_{15}NFe$ (253.619 g.mol^{-1}): Calculated (%) C, 66.43%; H, 5.97%; N, 5.53. Found (%) C, 67.25%; H, 4.05%; N, 4.45%. (Purity determined by elemental analysis; could not be determined by LC or HPLC).

2.2.6. N-Ferrocenyl-1-(1-(7-chloroquinolin-4-yl)-1H-1,2,3-triazol-4-yl)methanamine (Compound 6)

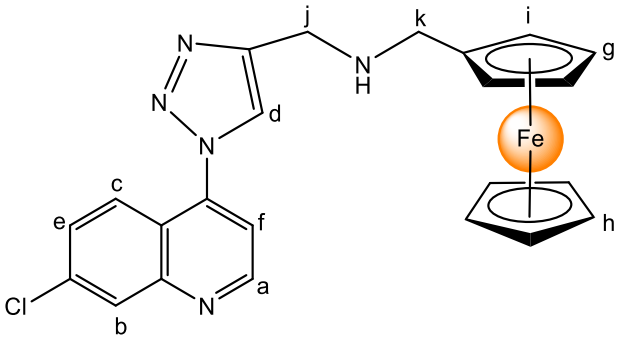

A freshly prepared 5 ml solution of sodium ascorbate (0.0830 g, 0.419 mmol.) and $CuSO_4.5H_2O$ (0.0520 g, 0.209 mmol) in water was added to a 5 ml solution of compound **4** (0.143 g, 0.698 mmol) and compound **5** (0.177 g, 0.698 mmol) in DCM. The mixture was allowed to stir at 30 °C for 72 h and stopped when the reaction was completed, as shown by thin layer chromatography analysis. To the resulting reaction mixture, DCM (30 ml) was added, which was then washed with a saturated NH_4Cl solution (3 × 30 ml) to remove Cu^{2+} ions and subsequently washed with water (3 × 30 ml). The solution was then dried using anhydrous Na_2SO_4, filtered, and the solvent was thereafter removed from the filtrate. Purification was achieved via column chromatography using silica gel and a DCM/methanol mixture (100:0 to 96:4). Compound **6** was crystallised as a dark yellow solid by layering ethyl acetate or DCM with hexane/pentane.

Yield: 0.054 g, 17%. **^{1}H NMR** (400 MHz, $CDCl_3$): (δ, ppm) 9.05 (d, *J* = 4.6 Hz, 1H, H_a), 8.24 (d, *J* = 2.0 Hz, 1H, H_b), 8.01 (d, *J* = 9.1 Hz, 1H, H_c), 7.96 (s, 1H, H_d), 7.59 (dd, *J* = 9.1 Hz, 2.0 Hz, 1H, H_e), 7.48 (d, *J* = 4.6 Hz, 1H, H_f), 4.23 (m, 2H, H_g), 4.15 (s, 5H, H_h), 4.13 (m, 2H, H_i), 4.09 (s, 2H, H_j), 3.68 (s, 2H, H_k). **^{13}C {^{1}H} NMR** (101 MHz, $CDCl_3$): (δ, ppm) 151.55, 150.37, 148.01, 141.23, 137.05, 129.54, 129.14, 124.84, 123.64, 120.76, 116.05, 86.21, 68.69, 68.63, 68.15, 48.97, 44.31. **IR**: (ν_{max}/cm^{-1}) 3330 (N-H), 3125 (C-H), 3085 (C-H), 2923 (C-H), 2849 (C-H), 1593 (C=N). **M.p.:** 95 – 98 °C. **ESI-MS:** Calculated for $C_{23}H_{20}ClN_5Fe^+$: 457.0800. Found: 457.0762 $[M]^+$. **Purity** (HPLC): 93% (t_R = 19.97 min).

2.2.7. N-(7-Chloro-quinolin-4-yl)-benzene-1,4-diamine (Compound 7) [6]

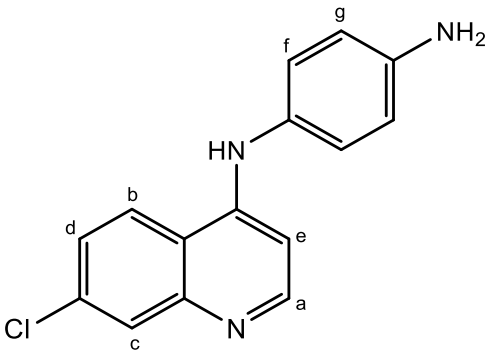

A mixture of 4,7-dichloroquinoline (0.426 g, 2.15 mmol) and *p*-phenylenediamine (0.465 g, 4.30 mmol) in absolute ethanol (10 ml) was heated for eight hours at 75 ˚C with continued stirring. An evident orange precipitate formed. The solvent was then reduced under vacuum to a minimum (~ 5 ml), and the precipitate was filtered and washed with ethanol, followed by EtOAc. This yielded the precursor compound **7** as a bright yellow/orange powder.

Yield: 0.560 g, 96%. **^{1}H NMR** (400 MHz, DMSO): (δ, ppm) 10.75 (br s, NH, NH_2), 8.73 (d, *J* = 9.1 Hz, 1H, H_b), 8.43 (d, *J* = 6.4 Hz, 1H, H_a), 8.06 (d, *J* = 1.8 Hz, 1H, H_c), 7.82 (dd, *J* = 9.0 Hz, 2.0 Hz, 1H, H_d), 7.07 (d, *J* = 8.6 Hz, 2H, H_f), 6.70 (d, *J* = 8.6 Hz, 2H, H_g), 6.60 (d, *J* = 6.6 Hz, 1H, H_e). **^{13}C {^{1}H} NMR** (101 MHz, DMSO): (δ, ppm) 155.15, 148.52, 143.33, 139.48, 138.02, 126.98, 126.57, 125.75, 124.50, 119.55, 115.68, 114.47, 99.93. **IR**: (ν_{max}/cm^{-1}) 3429 (N-H), 3319 (N-H), 1604 (C=N). **M.p.:** Decomposes at 250 °C. **LC-MS:** Calculated for $C_{15}H_{13}ClN_3^+$: 270.07. Found: 270.10 $[M+H]^+$. (No purity data as compound was not selected for biological testing).

2.2.8. N'-Ferrocenylbenzene-1,4-diamine (Compound 8) [7]

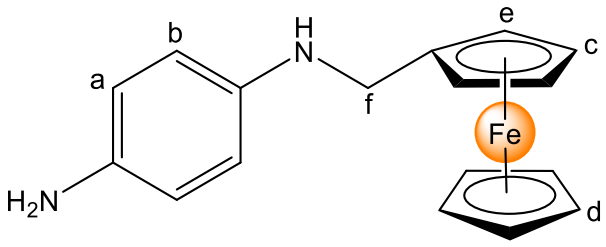

A 40 ml solution of ferrocenecarboxaldehyde (0.278 g, 1.30 mmol) in anhydrous methanol was added dropwise to a 10 ml solution of *p*-phenylenediamine (0.140 g, 1.30 mmol) in anhydrous methanol containing five drops of glacial acetic acid. The reaction mixture was stirred for 24 hours at room temperature (25 °C), after which sodium borohydride (0.196 g, 5.19 mmol.) was added portion-wise.

After stirring for an additional two hours at room temperature, the mixture was quenched with saturated $NaHCO_3$ (40 ml) before extraction with DCM (3 x 100 ml). The organic layer was washed with distilled water and then dried over Na_2SO_4. After removing the solvent under vacuum, the brown residue was purified by column chromatography using silica gel with hexane/EtOAc as the eluant, first eluting a red band (bis-ferrocenyl methyl-phenylenediamine) with a 4:1 mixture and then a reddish-brown band with a 1:1 mixture. The second band was the precursor compound **8**, which was obtained as either orange-red granules or a fine dark-red powder after recrystallisation/precipitation using a DCM/Hexane/Pentane mixture.

Yield: 0.059 g, 15%. **^{1}H NMR** (400 MHz, $CDCl_3$): (δ, ppm) 6.64 (d, *J* = 8.6 Hz, 2H, H_a), 6.57 (d, *J* = 8.6 Hz, 2H, H_b), 4.23 (t, *J* = 1.8 Hz, 2H, H_c), 4.17 (s, 5H, H_d), 4.13 (t, *J* = 1.8 Hz, 2H, H_e), 3.90 (s, 2H, H_f), 3.39 (br s, NH, NH_2). **^{13}C {^{1}H} NMR** (101 MHz, $CDCl_3$): (δ, ppm) 141.72, 138.05, 117.03, 114.80, 86.98, 68.57, 68.22, 67.92, 44.77. **IR**: (ν_{max}/cm^{-1}) 3424 (N-H), 3347 (N-H). **M.p.:** 99 – 103 °C **ESI-MS:** Calculated for $C_{17}H_{18}N_2Fe^+$: 306.0800. Found: 306.0803 $[M]^+$. (No purity data as compound was not selected for biological testing).

2.2.9. 7-chloro-N-(4-iodophenyl)quinolin-4-amine (Compound 9) [8]

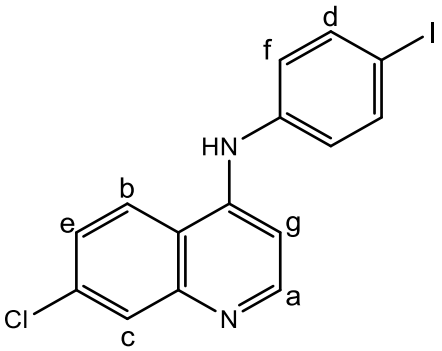

4,7-Dichloroquinoline (0.416 g, 2.10 mmol) and 4-iodoaniline (0.919 g, 4.20 mmol) were dissolved in 10 ml of absolute ethanol. The solution was refluxed for 24 hours, after which a yellow-green precipitate was formed. After cooling the solution to room temperature, the precipitate was filtered and washed with cold ethanol followed by acetone to yield the precursor compound **9** as a yellow-green powder.

Yield: 0.721 g, 90%. **^{1}H NMR** (400 MHz, MeOD): (δ, ppm) 8.54 (d, *J* = 9.1 Hz, 1H, H_b), 8.41 (d, *J* = 7.0 Hz, 1H, H_a), 7.96 (d, *J* = 2.0 Hz, 1H, H_c), 7.94 (d, 2H, H_d), 7.81 (dd, *J* = 9.1, 2.0 Hz, 1H, H_e), 7.28 (d, *J* = 8.6 Hz, 2H, H_f), 6.93 (d, *J* = 7.0 Hz, 1H, H_g). **^{13}C {^{1}H} NMR** (101 MHz, MeOD): (δ, ppm) 156.95, 144.73, 141.45, 140.92, 140.58, 138.16, 129.33, 128.46, 126.16, 120.76, 117.60, 101.67, 93.46. **IR**: (ν_{max}/cm^{-1}) 1607

(C=N). **M.p.:** Decomposes at 250 °C. **LC-MS:** Calculated for $C_{15}H_{11}ClN_2I^+$: 380.96. Found: 381.10 $[M+H]^+$. **Purity** (LC): 99% (t_R = 0.752 min).

2.2.10. (E)-(2-(4-aminophenyl)ethenyl)-ferrocene (Compound 10) [9]

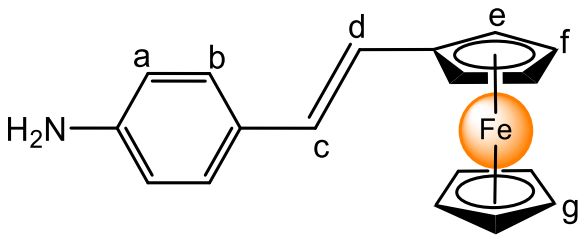

A mixture of vinylferrocene (0.508 g, 2.39 mmol), 4-iodoaniline (0.525 g, 2.39 mmol), $Pd(OAc)_2$ (0.0430 g, 8 mol%), K_2CO_3 (0.662 g, 4.79 mmol) and β-CD (0.272 g, 10 mol%) in ~ 5 ml of DMF was stirred for 18 hours at 110 °C under an Ar atmosphere. Upon cooling to room temperature, the mixture was diluted with EtOAc (50 ml), filtered through a silica pad (~ 2 cm in height) and then washed with distilled H_2O (4 x 100 ml). The organic layer was dried over Na_2SO_4 before filtering it and removing the solvent under a vacuum to produce an orange residue. This residue was then purified by column chromatography using silica gel and a petroleum ether/EtOAc mixture (70:30). Finally, the precursor compound **10** was precipitated from the eluted factions as an orange solid using ice-cold petroleum ether.

Yield: 0.224 g, 31%. **^{1}H NMR** (400 MHz, DMSO): (δ, ppm) 7.15 (d, *J* = 8.4 Hz, 2H, H_a), 6.58 (s, NH_2), 6.52 (d, *J* = 8.4 Hz, 2H, H_b), 5.16 (br s, 2H, H_c & H_d), 4.46 (t, *J* = 1.7 Hz, 2H, H_e), 4.23 (t, *J* = 1.7 Hz, 2H, H_f), 4.10 (s, 5H, H_g). **^{13}C {^{1}H} NMR** (150 MHz, DMSO): (δ, ppm) 147.98, 126.77, 126.64, 125.49, 120.78, 113.98, 84.70, 68.85, 68.24, 66.07. **IR**: (ν_{max}/cm^{-1}) 3364 (N-H), 1606 (C=C). **M.p.:** 165 – 169 °C. **ESI-MS:** Calculated for $C_{18}H_{18}NFe^+$: 304.0700. Found: 304.0771 $[M+H]^+$. **Elemental analysis** for $C_{18}H_{17}NFe$ (303.1826 g.mol^{-1}): Calculated (%) C, 71.31%; H, 5.65%; N, 4.62. Found (%) C, 73.57%; H, 6.02%; N, 3.67%. (Purity determined by elemental analysis; could not be determined by LC or HPLC).

2.2.11. (E)-7-chloro-N-(4-(ferrocene-ethenyl)phenyl)quinolin-4-amine (Compound 11)

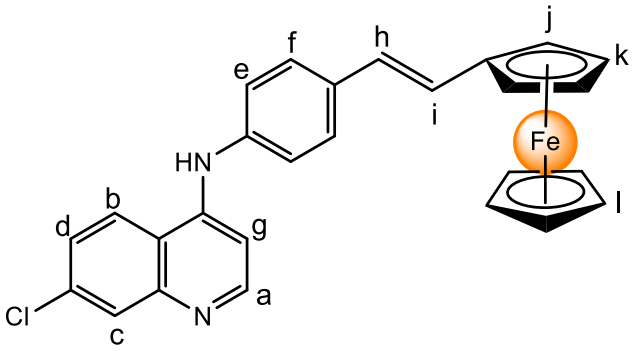

4,7-Dichloroquinoline (0.230 g, 1.16 mmol) and compound **10** (0.176 g, 0.580 mmol) were stirred in 10 ml of heated anhydrous methanol (45 °C) for 24 hours. The orange solution was diluted with 40 ml EtOAc and then washed with distilled H_2O before drying the organic layer over Na_2SO_4. After filtration, the solvent was removed under vacuum to leave an orange residue, which was then purified by column chromatography using silica gel and a DCM/EtOAc/Et_3N mixture (90:10:1) to afford compound **11** as an orange powder after removal of the solvent.

Yield: 0.0468 g, 17%. **^{1}H NMR** (400 MHz, DMSO): (δ, ppm) 9.13 (s, NH), 8.48 (d, *J* = 5.3 Hz, 1H, H_a), 8.43 (d, *J* = 9.1 Hz, 1H, H_b), 7.90 (d, *J* = 2.2 Hz, 1H, H_c), 7.57 (dd, 1H, H_d), 7.54 (d, *J* = 8.5 Hz, 2H, H_e), 7.33 (d, *J* = 8.5 Hz, 2H, H_f), 6.97 (d, *J* = 5.3 Hz, 1H, H_g), 6.93 (d, *J* = 16.2 Hz, 1H, H_h), 6.78 (d, *J* = 16.2 Hz, 1H, H_i), 4.56 (t, *J* = 1.8 Hz, 2H, H_j), 4.31 (m, 2H, H_k), 4.15 (s, 5H, H_l). **^{13}C {^{1}H} NMR** (101 MHz, DMSO): (δ, ppm) 152.05, 149.65, 147.79, 138.79, 133.99, 133.51, 127.71, 126.73, 126.08, 125.23, 125.02, 124.52, 122.63, 118.43, 102.11, 83.46, 69.04, 68.88, 66.72. **IR**: (ν_{max}/cm^{-1}) 1570 (C=N). **M.p.:** Decomposes at 220 °C. **ESI-MS:** Calculated for $C_{27}H_{22}ClN_2Fe^+$: 465.0700. Found: 465.0822 $[M+H]^+$. **Elemental analysis** for $C_{27}H_{21}ClN_2Fe$ (464.7728 g.mol^{-1}): Calculated (%) C, 69.77%; H, 4.55%; N, 6.03. Found (%) C, 71.87%; H, 4.15%; N, 5.38%. (Purity determined by elemental analysis; could not be determined by LC or HPLC).

2.3. X-ray crystallography

Single-crystal X-ray diffraction data were collected on a Bruker D8 Venture diffractometer using graphite-monochromated Mo-Kα radiation (χ = 0.71073 Å). Data collection was carried out at 173 (2) K. Temperature was controlled by an Oxford Cryostream cooling system (Oxford Cryostat). Cell refinement and data reduction were performed using the program SAINT. [10] The data were scaled, and absorption correction was performed using SADABS. [11]

The structure was solved by direct methods using SHELXS-97 and refined by full-matrix least-squares methods based on F^2 using SHELXL-2014 and the graphics interface program X-Seed. [11–13] The programs X-Seed and POV-Ray were used to prepare molecular graphic images. [12–14]

All non-hydrogen atoms were refined anisotropically. All hydrogen atoms, except the amino hydrogen atoms, were placed in idealised positions and refined in riding models with U_{iso} assigned 1.2 times U_{eq} of their parent atoms and the C-H bond distances were constrained to 0.95 Å and 0.99 Å respectively. The amino hydrogens were located in the difference density maps and refined independently. The structure was refined to R factor of 0.0362.

2.4. Biological methods

2.4.1. Ethics statement

This study was performed in strict accordance with the recommendations of the South African national guidelines and the University of Cape Town of practice for laboratory animal procedures. All mouse experiments were performed according to protocols approved by the Animal Research Ethics Committee of the Health Sciences Faculty, University of Cape Town (**AEC Number**: 022/017) and Institutional Biosafety Committee (IBC005-2022). All efforts were made to minimise the suffering of the animals.

2.4.2. Parasite culture [15,16]

Leishmania major LV39 (MRHO/SV/59/P) promastigotes were stored in liquid nitrogen or at -80 °C in 2 ml cryovials (Corning) containing 92% fetal bovine serum (FBS) (Gibco) and 8% v/v dimethyl sulfoxide (DMSO) (Sigma-Aldrich) at 2 x 10^8 parasites/ml. One cryovial of *L. major* LV39 was thawed at room temperature, and the parasites were resuspended in 8 ml of 1 x phosphate-buffered saline (PBS), pH 7.4, before being centrifuged at room temperature at 3000 rpm for 10 minutes. The resulting pellet containing the parasites was resuspended in 10 ml of 1 x PBS and centrifuged once more, as before. The parasite pellet was then resuspended in 5 ml of complete medium 199 (M199) (M199 (Gibco) supplemented with 10% FBS, 50 units/ml penicillin and 50 µg/ml streptomycin (Gibco)), transferred to a 25 cm^3 tissue culture flask (Corning) and incubated at 26 °C. When the parasites had reached confluency, an additional 5 ml of complete M199 was added to the flask. The parasite culture was maintained by sub-culturing every seven days when the parasites reached confluency. This was done

by transferring confluent parasites into a 25 cm^3 tissue culture flask containing complete M199 at a ratio of 1:50 (parasite suspension: medium volume) and incubating the flask at 26 °C.

2.4.3. Leishmania major infection [15,16]

To prepare *L. major* LV39 promastigotes for infection, a confluent parasite culture was transferred from a tissue culture flask to a 50 ml centrifuge tube and centrifuged at 500 rpm for 10 minutes to remove cell debris. The supernatant was collected and centrifuged at 3000 rpm for 10 minutes to pellet the parasites. The parasite pellet was washed twice by centrifugation in 1 x PBS at 3000 rpm for 10 minutes, and then the parasites were resuspended in 1 ml of 1 x PBS, fixed in 4% v/v paraformaldehyde and counted using a Neubauer haemocytometer. A new parasite culture was initiated by transferring 1 x 10^7 parasites to a 25 cm^3 tissue culture flask containing 10 ml of complete M199 and incubating the flask at 26 °C for five to six days. The parasite number was counted daily and plotted graphically on GraphPad Prism 8 (GraphPad Software, USA, https://www.graphpad.com) to monitor growth to stationary phase.

Once the parasites had reached stationary phase, they were centrifuged, washed and counted as described above, and a parasite solution was then prepared in 1 x PBS for footpad infection at a concentration of 2 x 10^6/50 µl. Prior to infection, the weights and footpad sizes of BALB/c mice were measured, and the mice were anaesthetised with 12% v/v ketamine (Anaket-V; Centaur Labs) and 8% v/v xylazine (Rompun; Bayer) in 1 x PBS by intraperitoneal injection at a dose or 10 µl/gram. Anaesthetised mice were then inoculated subcutaneously in the left hind footpad with 50 µl of the parasite solution. The body weights of infected animals were monitored weekly. The swelling of infected footpads was also monitored weekly and measured using a Mitutoyo micrometre calliper (Brütsch) relative to baseline footpad measurements.

At eight weeks post-infection, the infected mice were euthanised by halothane inhalation and cervical dislocation, and *L. major* amastigotes were aspirated from infected footpads using a syringe containing 200 µl of 1 x PBS. The aspirated parasites were transferred to a 15 ml centrifuge tube containing 5 ml of 1 x PBS, and the tube was centrifuged at 4000 rpm for five minutes. The pelleted parasites were resuspended in 5 ml of complete M199 before being transferred to a 25 cm^3 tissue culture flask for incubation at 26 °C to allow for differentiation into promastigotes.

2.4.4. Antipromastigote activity assay [22–24]

Stock solutions of compounds **1**, **2**, **3**, **4**, **5**, **6**, **9**, **10** and **11**, were prepared in DMSO (Sigma-Aldrich) at 10 mg/ml and stored at -20 °C. Compound **9** was partially soluble and was tested as a suspension. On the day of the assay, the compounds were diluted down to either 100 µg/ml or 10 µg/ml and then serially diluted (1:2) in complete M199 in flat-bottomed 96-well plates (SPL) (100 µg/ml – 0.8 µg/ml for **1**, **2**, **4**, **5**, **9**, **10** and **11**; 10 µg/ml – 0.08 µg/ml for **3** and **6**) along with amphotericin B (Sigma-Aldrich) (10 µg/ml – 0.08 µg/ml) and DMSO (0.10% - 0.0008% and 1% - 0.008% v/v). All dilutions were made in triplicate. *L. major* LV39 promastigotes, which had been grown to stationary phase (as described in *Section 2.3.3*), were transferred to fresh medium and then added to the plates at 2.5 x 10^6 parasites/well in 100 µl. The plates were incubated at 26 °C for 48 hours, after which 50 µl of resazurin (Sigma-Aldrich) (0.0125% w/v in 1 x PBS) was added to the wells. After an additional incubation of 24 hours, the fluorescence of the wells was recorded using a FLUOstar Omega spectrofluorometer (BMG) (λ_{ex} 520 nm; λ_{em} 620 nm). GraphPad Prism 8 (GraphPad Software, USA, https://www.graphpad.com) was used to calculate IC_{50} values via non-linear dose-response curve-fitting analysis.

2.4.5. RAW 264.7 cell culture [20,21]

A cryovial containing 2 x 10^6/ml frozen RAW 264.7 cells (ATCC TIB-71) was rapidly thawed at 37 °C, and the cells were transferred to a centrifuge tube containing 15 ml complete complete Dulbecco's Modified Eagle Medium (DMEM) (DMEM (Gibco) supplemented with 10% FBS, 50 units/ml penicillin and 50 µg/ml streptomycin (Gibco)). The tube was centrifuged at 1200 rpm for 10 minutes at room temperature to pellet the cells before resuspending them in 5 ml of complete DMEM and transferring them to a 25 cm^3 culture flask. The cells were incubated in a 5% CO_2 incubator at 37 °C until they reached 60 – 80% confluency, after which they were treated with 0.05% v/v trypsin before adding 10 ml of complete DMEM to the flask. The cells were then gently scraped off the flask surface using a cell scraper, and 4 ml of the resulting cell suspension was diluted in 16 ml complete DMEM and transferred to a 75 cm^3 culture flask. Alternatively, 10 ml of the suspension was diluted in 40 ml of complete DMEM and transferred to a 175 cm^3 culture flask to grow a higher number of cells. The culture flasks were incubated for three days in a 5% CO_2 incubator at 37 °C, with the cells being sub-cultured into a new flask on the third day.

2.4.6. Flow cytometry and extracellular staining [15]

RAW 264.7 cells were seeded in 96-well V-bottom plates (Greiner Bio-One) at 1 x 10^6 cells/well and centrifuged at 1500 rpm for five minutes. The supernatant was discarded, and the cells were resuspended in 50 µl antibody cocktail containing CD11b-BV421 (clone, M1/70) and F4/80-PE-Cy7 (clone, BM8) antibodies prepared in FACS buffer (1% v/v FBS in 1 x PBS, pH 7.4) supplemented with 10 µg/ml anti-FcγR (2.4G2) and 1% v/v heat inactivated rat serum. The plates were then covered in foil and incubated at 4 °C for 30 minutes. After the incubation period, the cells were washed with 150 µl FACS buffer and centrifuged at 1500 rpm for five minutes to remove unbound antibodies. The supernatant was discarded, and then the cells were fixed using 200 µl of 2% v/v paraformaldehyde in 1 x PBS for 20 minutes at 4 °C. After centrifuging the plates for five minutes at 1500 rpm, the cells were washed with 200 µl of PBS and centrifuged as before. Finally, the cells were resuspended in 200 µl of cold FACS buffer, transferred to foil-covered tubes and stored at 4 °C until time for acquisition. Acquisition was performed using a BD LSRFortessa flow cytometer (BD Biosciences, USA), and data was analysed on FlowJo v.10.10.0 (Treestar, USA).

2.4.7. Cytotoxicity assay [23–25]

RAW 264.7 macrophages were seeded in flat-bottomed 96-well plates (SPL) at 2 x 10^4 cells/well in complete DMEM and incubated at 37 °C in 5% CO_2 overnight to allow for adherence. On the day of the assay, the culture medium in the 96-well plates was removed and replaced with serial dilutions (1:2) of compounds **1** - **11**, amphotericin B and DMSO. Dilutions were done in complete DMEM for a concentration range of 50 – 0.4 µg/ml (25 – 0.2 µg/ml for compound **3**), with each compound being added in triplicate. DMSO was diluted to a range of 0.5 – 0.004% v/v. The plates were then incubated at 37 °C in 5% CO_2 for 48 hours, after which 50 µl of resazurin (0.0125% w/v in 1 x PBS) was added to the wells. After an additional incubation of 24 hours, the fluorescence of the wells was recorded using a FLUOstar Omega spectrofluorometer (λ_{ex} 520 nm; λ_{em} 620 nm). GraphPad Prism 8 was used to calculate CC_{50} values via non-linear dose-response curve-fitting analysis. The selectivity index (SI) of each compound was calculated by dividing the CC_{50} value by the IC_{50} value.

References

1 C. C. Musonda, S. Little, V. Yardley and K. Chibale, Application of multicomponent reactions to antimalarial drug discovery. Part 3: Discovery of aminoxazole 4-aminoquinolines with potent antiplasmodial activity in vitro, *Bioorganic and Medicinal Chemistry Letters*, 2007, **17**, 4733–

4736.

2 T. Stringer, C. De Kock, H. Guzgay, J. Okombo, J. Liu, S. Kanetake, J. Kim, C. Tam, L. W. Cheng, P. J. Smith, D. T. Hendricks, K. M. Land, T. J. Egan and G. S. Smith, Mono- and multimeric ferrocene congeners of quinoline-based polyamines as potential antiparasitics, *Dalton Transactions*, 2016, **45**, 13415–13426.

3 P. F. Salas, C. Herrmann, J. F. Cawthray, C. Nimphius, A. Kenkel, J. Chen, C. de Kock, P. J. Smith, B. O. Patrick, M. J. Adam and C. Orvig, Structural Characteristics of Chloroquine-Bridged Ferrocenophane Analogues of Ferroquine May Obviate Malaria Drug-Resistance Mechanisms, *Journal of Medicinal Chemistry*, 2013, **56**, 1596–1613.

4 E. M. Guantai, K. Ncokazi, T. J. Egan, J. Gut, P. J. Rosenthal, P. J. Smith and K. Chibale, Design, synthesis and in vitro antimalarial evaluation of triazole-linked chalcone and dienone hybrid compounds, *Bioorganic and Medicinal Chemistry*, 2010, **18**, 8243–8256.

5 C. C. Albertyn, A. van Niekerk, S. Duffy, V. M. Avery, E. Strauss and P. Chellan, Investigation of bioorganometallic artemisinins as antiplasmodials, *Journal of Organometallic Chemistry*, 2023, **987**–**988**, 122633.

6 K. V. Sashidhara, M. Kumar, R. K. Modukuri, R. K. Srivastava, A. Soni, K. Srivastava, S. V. Singh, J. K. Saxena, H. M. Gauniyal and S. K. Puri, Antiplasmodial activity of novel keto-enamine chalcone-chloroquine based hybrid pharmacophores, *Bioorganic and Medicinal Chemistry*, 2012, **20**, 2971–2981.

7 R. Arancibia, A. H. Klahn, G. E. Buono-Core, E. Gutierrez-Puebla, A. Monge, M. E. Medina, C. Olea-Azar, J. D. Maya and F. Godoy, Synthesis, characterization and anti-Trypanosoma cruzi evaluation of ferrocenyl and cyrhetrenyl imines derived from 5-nitrofurane, *Journal of Organometallic Chemistry*, 2011, **696**, 3238–3244.

8 A. S. Ressurreição, D. Gonçalves, A. R. Sitoe, I. S. Albuquerque, J. Gut, A. Góis, L. M. Gonçalves, M. R. Bronze, T. Hanscheid, G. A. Biagini, P. J. Rosenthal, M. Prudeîncio, P. O'Neill, M. M. Mota, F. Lopes and R. Moreira, Structural optimization of quinolon-4(1 H)-imines as dual-stage antimalarials: Toward increased potency and metabolic stability, *Journal of Medicinal Chemistry*, 2013, **56**, 7679–7690.

9 K. Kanagaraj and K. Pitchumani, The aminocyclodextrin/Pd(OAc)2 complex as an efficient catalyst for the Mizoroki-Heck cross-coupling reaction, *Chemistry - A European Journal*, 2013, **19**, 14425–14431.

10 SAINT, Bruker AXS Inc., Madison, WI, USA, v2019.1-0.

11 G. M. Sheldrick, SHELXS-97, SHELXL-2014 and SADABS, *Acta Crystallographica Section C: Structural Chemistry*, 1997, **71**, 3–8.

12 L. J. Barbour, X-Seed — A Software Tool for Supramolecular Crystallography, *Journal of Supramolecular Chemistry*, 2001, **1**, 189–191.

13 J. L. Atwood and L. J. Barbour, Molecular Graphics: From Science to Art, *Crystal Growth & Design*, 2003, **3**, 3–8.

14 Persistance of Vision Private Ltd, Persistance of Vision Raytracer (Version 3.6), http://www.povray.org/, (accessed 23 December 2024).

15 B. O. Osero, Z. Cele, R. T. Aruleba, R. A. Maine, M. Ozturk, M. B. Lutz, F. Brombacher and R. Hurdayal, Interleukin-4 Responsive Dendritic Cells Are Dispensable to Host Resistance Against Leishmania mexicana Infection, *Frontiers in Immunology*, 2022, **12**, 1–15.

16 R. Hurdayal, N. E. Nieuwenhuizen, R. Khutlang and F. Brombacher, Inflammatory Dendritic Cells, Regulated by IL-4 Receptor Alpha Signaling, Control Replication, and Dissemination of Leishmania major in Mice, *Frontiers in Cellular and Infection Microbiology*, 2020, **9**, 1–15.

17 R. E. Heap, J. L. Marín-Rubio, J. Peltier, T. Heunis, A. Dannoura, A. Moore and M. Trost, Proteomics characterisation of the L929 cell supernatant and its role in BMDM differentiation, *Life Science Alliance*, 2021, **4**, 1–10.

18 O. Tamgue, L. Gcanga, M. Ozturk, L. Whitehead, S. Pillay, R. Jacobs, S. Roy, S. Schmeier, M. Davids, Y. A. Medvedeva, K. Dheda, H. Suzuki, F. Brombacher and R. Guler, Differential targeting of c-Maf, Bach-1, and Elmo-1 by microRNA-143 and microRNA-365 promotes the intracellular growth of mycobacterium tuberculosis in alternatively IL-4/IL-13 activated macrophages, *Frontiers in Immunology*, 2019, **10**, 1–16.

19 S. P. Parihar, M. A. Hartley, R. Hurdayal, R. Guler and F. Brombacher, Topical Simvastatin as Host-Directed Therapy against Severity of Cutaneous Leishmaniasis in Mice, *Scientific Reports*, 2016, **6**, 1–10.

20 T. T. Lucy, A. N. M. Mamun-Or-Rashid, M. Yagi and Y. Yonei, Serial Passaging of RAW 264.7 Cells Modulates Intracellular AGE Formation and Downregulates RANKL-Induced In Vitro Osteoclastogenesis, *International Journal of Molecular Sciences*, 2022, **23**, 2371.

21 B. Taciak, M. Białasek, A. Braniewska, Z. Sas, P. Sawicka, Ł. Kiraga, T. Rygiel and M. Król,

Evaluation of phenotypic and functional stability of RAW 264.7 cell line through serial passages, *PLoS ONE*, 2018, **13**, 1–13.

22 A. Badirzadeh, M. Heidari-Kharaji, V. Fallah-Omrani, H. Dabiri, A. Araghi and A. Salimi Chirani, Antileishmanial activity of Urtica dioica extract against zoonotic cutaneous leishmaniasis, *PLOS Neglected Tropical Diseases*, 2020, **14**, e0007843.

23 J. Möller, C. Kannigadu, J. Aucamp, M. C. Joseph, A. J. Swarts and D. D. N'Da, Synthesis, electrochemistry, and in vitro antileishmanial efficacy of novel ferrocenylazines, *Applied Organometallic Chemistry*, 2023, **37**, 1–13.

24 A. Kulshrestha, V. Bhandari, R. Mukhopadhyay, V. Ramesh, S. Sundar, L. Maes, J. C. Dujardin, S. Roy and P. Salotra, Validation of a simple resazurin-based promastigote assay for the routine monitoring of miltefosine susceptibility in clinical isolates of Leishmania donovani, *Parasitology Research*, 2013, **112**, 825–828.

25 L. Jamalzadeh, H. Ghafoori, R. Sariri, H. Rabuti, J. Nasirzade, H. Hasani and M. R. Aghamaali, Cytotoxic Effects of Some Common Organic Solvents on MCF-7, RAW-264.7 and Human Umbilical Vein Endothelial Cells, *Avicenna Journal of Medical Biochemistry*, 2016, **4**, 10–33453.

CHAPTER 3

Results and Discussion

3.1. Introduction

There is a crucial need to develop newer and more effective drugs for the treatment of leishmaniasis due to the shortcomings of currently available drugs. The search for new drug candidates has led some researchers to create various types of organic ferrocene-based compounds containing biologically active pharmacophores, which show great potential for being utilised as more effective treatments. [1–3] This also includes ferrocenyl-quinoline compounds, such as those reported by Quintal *et al*. and Yousuf *et al*. [4–6]

Motivated by the work of these aforementioned researchers, this chapter focuses on the synthesis and characterisation of four ferrocenyl-quinoline compounds. The four compounds differ by the type of linker between the ferrocene and quinoline moieties, which is determined by the structural characteristics of their respective quinolinyl and/or ferrocenyl precursor compounds. Two of the ferrocenyl-quinoline compounds have been previously reported as antimalarial agents but not as antileishmanial agents, [7,8] while the other two are new compounds that have not been reported elsewhere. This chapter also discusses the *in vitro* antileishmanial activity assessment of the ferrocenyl-quinoline compounds and their precursors against *Leishmania major*, one of the causative agents of cutaneous leishmaniasis, as well as their *in vitro* cytotoxicity in murine macrophages. Finally, the selectivity of the compounds is also discussed as a measure of their suitability as potential antileishmanial agents.

3.2. Synthesis and characterisation of imino/amino-alkyl-linked ferrocenyl-quinoline compounds (2 & 3)

3.2.1. Synthesis

Scheme 3.1 shows the synthesis of the first two ferrocenyl-quinoline compounds, which contain either an imino-alkyl (**2**) or amino-alkyl linker (**3**). Compounds **2** and **3** share the same quinoline-based precursor compound (**1**), which was synthesised via a nucleophilic aromatic substitution reaction of

4,7-dichloroquinoline with 1,3-diaminopropane (**Scheme 3.1 i**), following a literature method. [9] As 1,3-diaminopropane is a liquid, the reaction was performed in the absence of a solvent. The general mechanism for this type of reaction is shown in **Figure 3.2**. In this case, 1,3-diaminopropane, which acts as the nucleophile, reacts at the 4-position of the quinoline ring bonded to the chloride. This is made possible by the high electronegativity of the quinoline nitrogen, which pulls electrons away from the 4-position to induce a partial positive charge. The nucleophile then forms a bond with the quinoline, thus displacing the chloride from the molecule. Compound **1** was obtained as an off-white solid in a moderate yield of 58%.

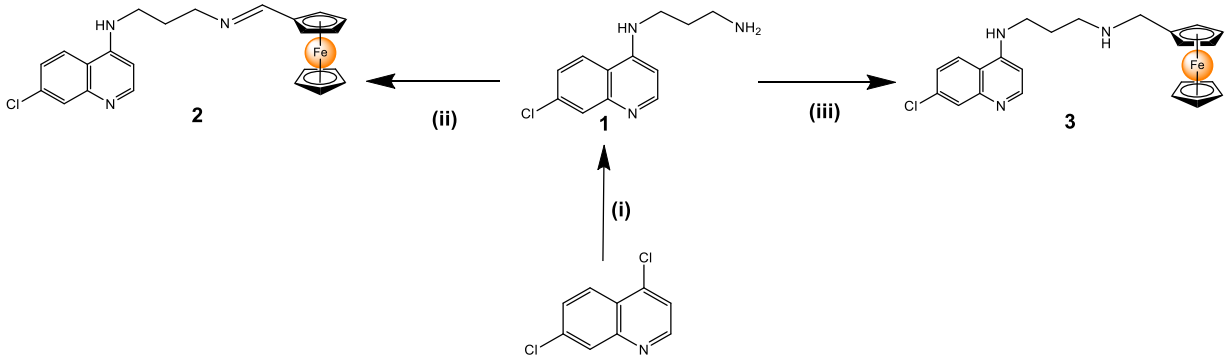

Scheme 3.1: *Synthesis of compounds **1**, **2** and **3**. Reagents and conditions: (i) 1,3-Diaminopropane, neat, 30 min, 80 °C, 22h reflux; (ii) Ferrocenecarboxaldehyde, diethyl ether, 72 h, r.t. (25 °C); (iii) Ferrocenecarboxaldehyde, anhydrous MeOH, 24 h, r.t. (25 °C), $NaBH_4$, anhydrous MeOH, 2 h, r.t. (25 °C).*

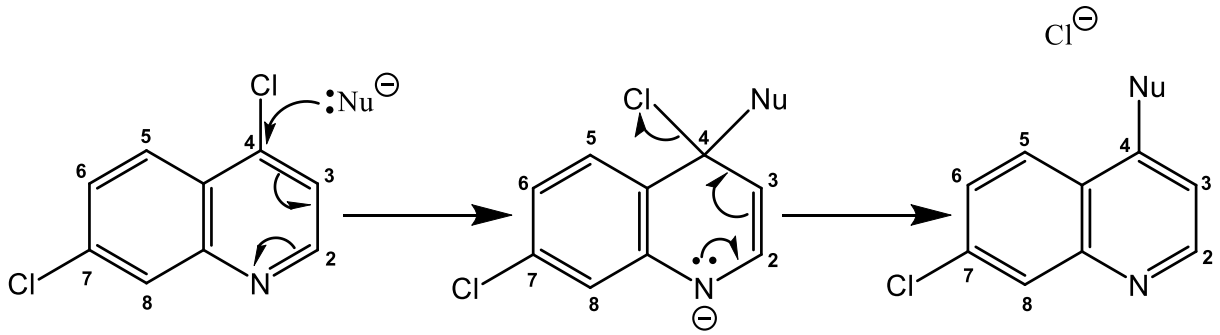

***Figure 3.2**: General mechanism of a nucleophilic aromatic substitution reaction using 4,7-dichloroquinoline. The electron-rich nucleophile (Nu^-) attacks the electron-deficient carbon on the 4-position of the quinoline ring, resulting in the displacement of the chloride ion (Cl^-).* [10]

Upon successful synthesis of compound **1**, it was then used in two separate Schiff base condensation reactions with ferrocenecarboxaldehyde to synthesise compounds **2** and **3**, which have been both previously synthesised as antimalarial agents (**Scheme 3.1 ii & iii**). [7,8] For the synthesis of **2**, the method

reported by Stringer *et al.* was used with slight modifications. [7] The first modification was specifically performing the reaction at 25 °C in an oil bath instead of relying on the ambient room temperature, and the second was extending the reaction time to 72 hours. The Schiff base condensation reaction is reversible, [11] so these modifications were made to promote the forward reaction and maximise product yield. Schiff base condensation reactions occur between primary amines and carbonyl compounds, as shown in **Figure 3.3**. The lone pair of electrons on the amine attacks the partially positive carbonyl carbon, forming a carbinolamine intermediate. The intermediate then undergoes a dehydration step, thus allowing for the formation of a C=N bond to create the Schiff base/imine. [11] Through this reaction, compound **2** was obtained as an orange-brown powder in a yield of 72%.

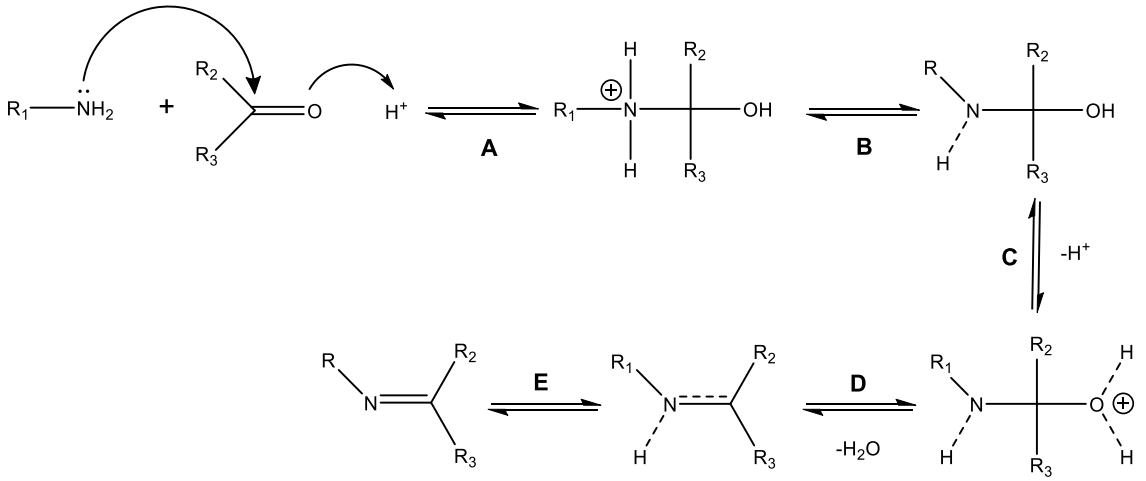

Figure 3.3*: General mechanism of a Schiff base condensation reaction, as illustrated by Subasi. (A) Formation of a carbinolamine intermediate via nucleophilic attack by a primary amine on the carbonyl carbon; (B) Loss of a proton by the amine group of the intermediate; (C) Gain of a proton by the hydroxyl group of the intermediate; (D) Loss of the protonated hydroxyl group as a water molecule; (E) Formation of an imine (C=N) bond to generate the Schiff base.* [11]

As for the synthesis of compound **3**, the method reported by Salas *et al.* was used with the temperature modifications stated earlier. [8] The Schiff base that was formed was reduced *in situ* to a secondary amine using sodium borohydride as the reducing agent (**Scheme 3.1**), making the compound more stable than compound **2** since it cannot be hydrolysed into its original starting reagents. After recrystallisation by layering dichloromethane (DCM) with hexane, an orange solid was produced in a low yield of 36%. This is significantly lower than the yield reported by Salas *et al*. (82%). [8] The difference in yield may be due to possible product loss during the purification process since conventional column chromatography was used in this study instead of flash column chromatography (which utilises pressure to accelerate sample movement), as was done by the authors. [8]

3.2.2. Characterisation

Nuclear Magnetic Resonance spectroscopy

Compounds **1**, **2** and **3** were characterised by ^{1}H and $^{13}C\{^{1}H\}$ Nuclear Magnetic Resonance (NMR) spectroscopy to confirm successful synthesis. These are standard techniques commonly used to determine the structural characteristics of organic compounds by taking advantage of the magnetic properties of hydrogen-1 and carbon-13 nuclei. [12–14] The ^{1}H NMR spectrum of the precursor compound **1** (**Figure 3.4**) shows the presence of the quinoline-associated proton signals (H_a – H_e) in the δ_H 6.51 – 8.32 ppm range. The protons of the aliphatic chain (H_f, H_g and H_h) are indicated by the triplet signals at δ_H 2.79 ppm and 3.40 ppm and the multiplet at δ_H 1.89 ppm. All the peaks observed integrate for the expected number of protons in this compound. $^{13}C\{^{1}H\}$ NMR analysis of the precursor also confirmed the expected 12 carbon atoms in the molecule.

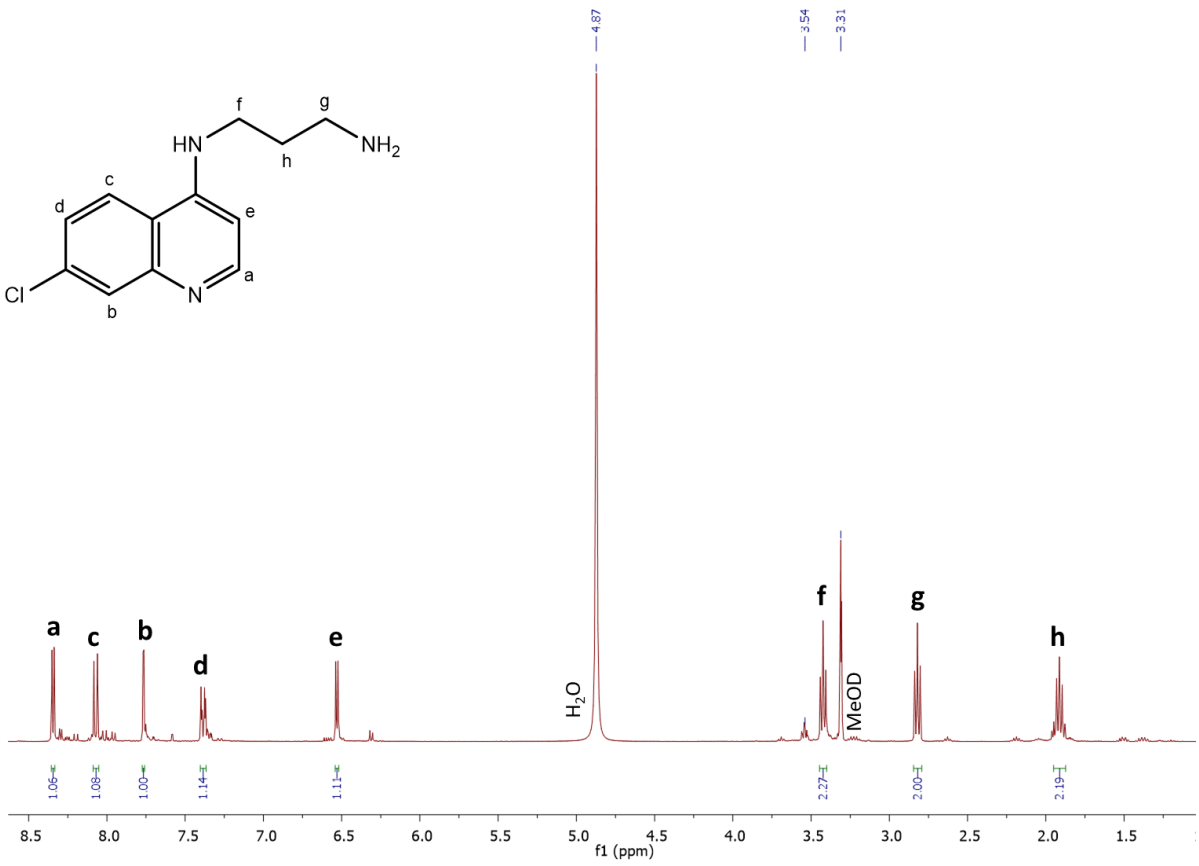

***Figure 3.4**: ^{1}H NMR spectrum of compound **1** in deuterated methanol (MeOD). The quinolinyl (**a-e**) and alkyl (**f-h**) proton signals are indicated.*

Figure 3.5 shows the stacked ^{1}H NMR spectra of compounds **2** and **3**, which are imine/amine counterparts of each other. The top spectrum (**Figure 3.5A**) shows evidence of the successful synthesis of compound **2**, indicated by the presence of the ferrocene proton signals (H_f, H_g and H_h) at δ_H 4.19 ppm, 4.48 ppm and 4.69 ppm. The largest of these, H_h, integrates for the five protons on the unsubstituted ring. There is also a singlet at δ_H 8.20 ppm, assigned to the imine proton H_I on the aliphatic chain (i, j, k). As with the precursor compound, all the signals associated with the quinoline and alkyl protons are present. The spectrum for compound **3** (Figure **B**) displays all the aforementioned peaks as well but with a noticeable overall upfield shift relative to compound **2**. Additionally, the signal for the aliphatic imine proton is absent. Instead, there is a new peak at δ_H 3.65 ppm (H_i), integrating for the two protons between the ferrocene and secondary amine functional groups. Likely, the introduction of the electron-donating CH_2 group at this position via reduction induced a shielding effect within the molecule, causing the upfield shift observed in the NMR spectrum. The integration values of the peaks with respect to both compounds are in agreement with the expected proton numbers, and the chemical shift values closely match those reported in literature. [7,8] The number of carbon atoms for compounds **2** and **3** was also verified through $^{13}C\{^{1}H\}$ NMR spectroscopy, with the chemical shift values matching the published values. [7,8]

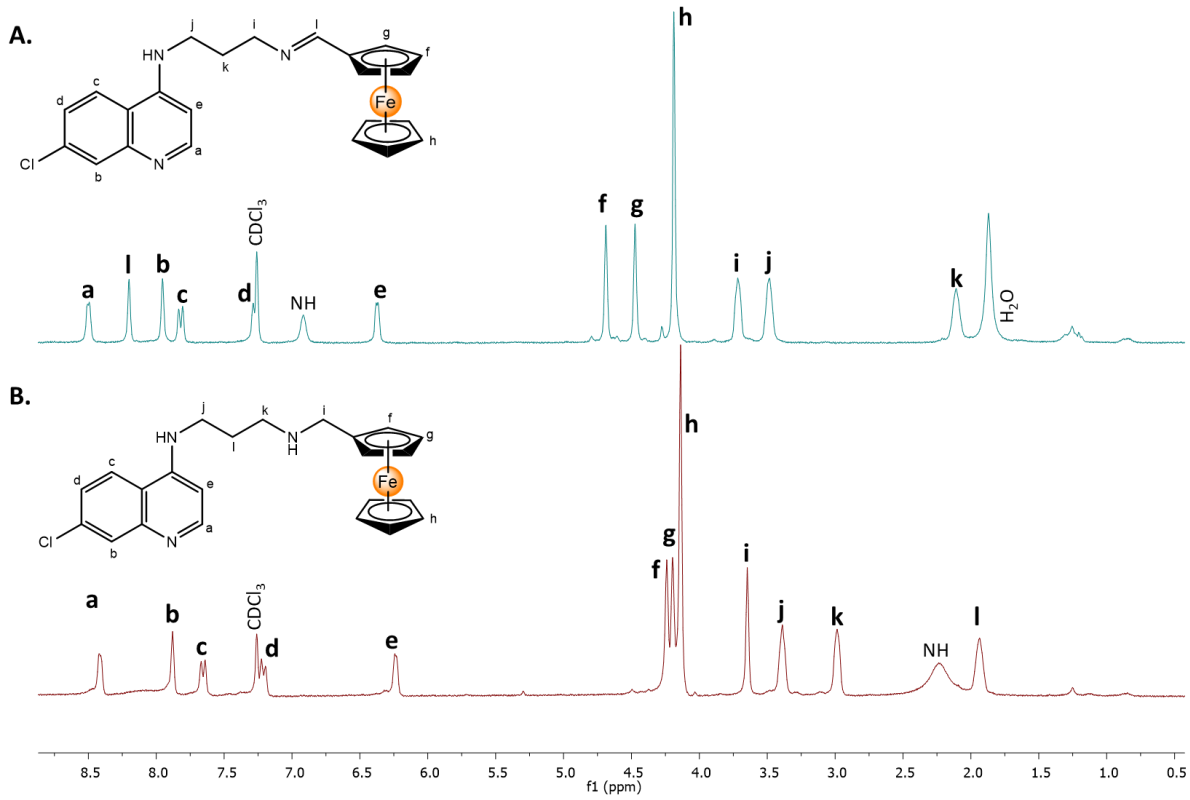

***Figure 3.5**: Stacked ^{1}H NMR spectra of compound **2** and compound **3** in deuterated chloroform ($CDCl_3$). (A) Spectrum for compound **2** with the quinolinyl (**a-e**), ferrocenyl (**f-h**), alkyl (**i-k**), imine (**l**) and amine (NH) proton signals indicated. (B) Spectrum for compound **3** with the quinolinyl (**a-e**), ferrocenyl (**f-h**), alkyl (**i-l**) and amine (NH) proton signals indicated.*

Infrared spectroscopy

All three compounds were further characterised by infrared (IR) spectroscopy, a commonly used technique for identifying functional groups in organic compounds through molecular vibrations induced by infrared radiation exposure. [15,16] In the case of compound **1**, absorption bands were observed for ν(N-H) and ν(C=N) at 3247 and 1571 cm^{-1}, respectively. Absorption bands for ν(N-H) and ν(C=N) were observed for compound **2** at 3228 and 1578 cm^{-1}, respectively. Compound **3** also shows bands corresponding to the N-H (ν = 3220 cm^{-1}) and C=N (ν = 1576 cm^{-1}) functional groups. Altogether, these findings provide further confirmation of the structural integrity of the compounds.

Mass spectrometry

The molecular mass of compound **1** was determined using Liquid Chromatography-Mass Spectrometry (LC-MS) analysis. A *m/z* value of 236.10 $[M+H]^+$ was obtained, corresponding to the calculated mass of the protonated molecular ion (236.09).

High-resolution Electrospray Ionisation Mass Spectrometry (ESI-MS) was utilised to determine the masses of the ferrocenyl-quinoline compounds **2** & **3**. For compound **2**, a base peak was observed at *m/z* 432.0930 $[M+H]^+$, which is in agreement with the calculated mass of 432.0800. The calculated protonated molecular mass of compound **3** is 434.1000, and this value correlates to that of the base peak at *m/z* 434.1088 $[M+H]^+$.

3.3. Synthesis and characterisation of triazole-amine-linked ferrocenyl-quinoline compound (6)

3.3.1. Synthesis

The synthesis of the triazole-amine-linked ferrocenyl-quinoline compound (compound **6**) required the prior formation of two precursor compounds, as illustrated in **Scheme 3.2**. The first of these was an azido-quinoline precursor (compound **4**), synthesised via a nucleophilic aromatic substitution reaction between 4,7-dichloroquinoline and an excess of sodium azide in dimethylformamide (DMF) heated to 65 °C (**Scheme 3.2 i**). [17] The mechanism resembles that of the reaction described earlier (*Section 3.2.1.*), with the N_3^- ion acting as the attacking nucleophile. Compound **4** was produced as a grey powder in a low yield of 28%. Multiple washing steps were performed to remove residual DMF during the purification of this compound, which may have reduced the yield.

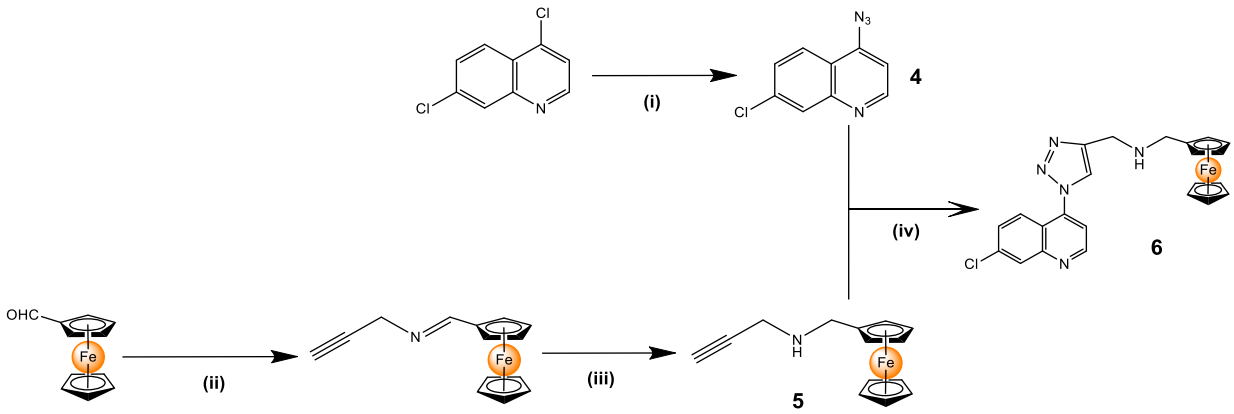

Scheme 3.2: *Synthesis of compounds **4**, **5** and **6**. Reagents and conditions: (i) NaN_3, DMF, 6 h, 65 °C; (ii) Propargylamine, anhydrous MeOH, 24 h, r.t. (25 °C); (iii) $NaBH_4$, anhydrous MeOH, 1 h, 0 °C; (iv) $CuSO_4.5H_2O$, sodium ascorbate, DCM/H_2O, 72 h, 30 °C.*

In order to generate the alkyne precursor compound (**5**), a one-pot Schiff base condensation reaction, with a sodium borohydride reduction step, was performed using ferrocenecarboxaldehyde and propargylamine in anhydrous methanol (**Scheme 3.2 ii & iii**). The reaction was performed according to the method described by Albertyn *et al*. with some modifications. [18] An orange-brown powder was obtained in good yield (84%) following this procedure.

With the two precursors in hand, the final step was to synthesise the novel compound **6** via a copper(I)-catalysed azide-alkyne cycloaddition (CuAAC) reaction, also known as a "click" reaction (**Scheme 3.2 iv**). As illustrated in **Figure 3.6**, the general mechanism is as follows: A Cu(I) cation coordinates with the participating alkyne compound to form an acetylide intermediate. The intermediate is then deprotonated by a second Cu(I) cation, leading to the formation of a dicuprate complex. Afterwards, the terminal nitrogen of the participating azide binds to the β-carbon of the acetylide/dicuprate complex to create a six-membered ring intermediate. The last step is a reductive elimination to form a five-membered Cu-intermediate, followed by protonation to regenerate the free Cu(I) cations. [19]

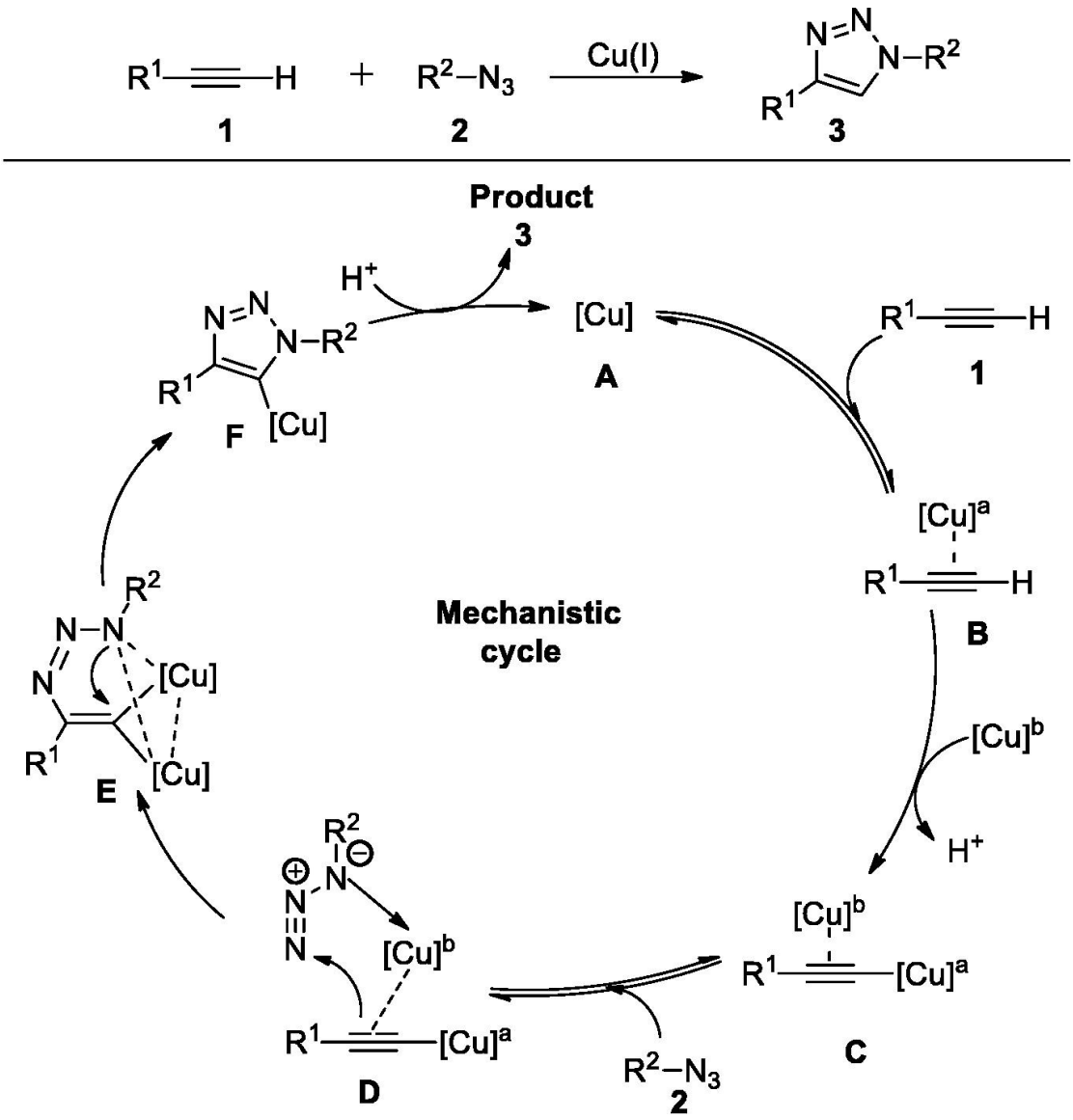

***Figure 3.6**: General mechanism of a copper(I)-catalysed azide-alkyne cycloaddition reaction, as illustrated by Anand et al. The Cu(I) cation (A) coordinates with an alkyne (1) to form an acetylide intermediate (B). Deprotonation and coordination with a second Cu(I) cation lead to the formation of a dicuprate complex (C), which binds to an azide (2) to generate a six-membered ring (D). Release of the two Cu(I) cations (E and F) results in the formation of a product with a five-membered ring (3).* [19]

For the reaction between compounds **4** and **5**, the Cu(I) catalyst was generated *in situ* by reducing copper(II) sulfate pentahydrate using an excess of sodium ascorbate. Additionally, the reaction was performed in a mixture of DCM and distilled water over 72 hours, according to the method described by Melis *et al*. [20] This produced a dark yellow oil, which was crystallised by layering ethyl acetate with hexane to afford a dark yellow solid in low yield (17%). The reason for this low yield is unclear, but the yields of click reactions in general appear to vary depending on the reactants, solvent and reaction conditions used. [5,6,19,20]

3.3.2. Characterisation

Nuclear Magnetic Resonance spectroscopy

^{1}H NMR and $^{13}C\{^{1}H\}$ NMR spectroscopic analyses were conducted to attest to the integrity of compounds **4**, **5** and **6**. The ^{1}H NMR spectrum of compound **4** is shown in **Figure 3.7**. Five signals were observed between δ_H 7.12 and 8.81 ppm in the downfield region, each assigned to the five protons on the quinoline ring system. The doublets H_c and H_d are coupled to each other with a coupling constant of 8.8 Hz. The chemical shift values also match those reported in literature. [17] Regarding the $^{13}C\{^{1}H]$ NMR analysis, nine signals were observed for the nine carbon atoms in the compound, and the chemical shifts were similar to literature values. [17]

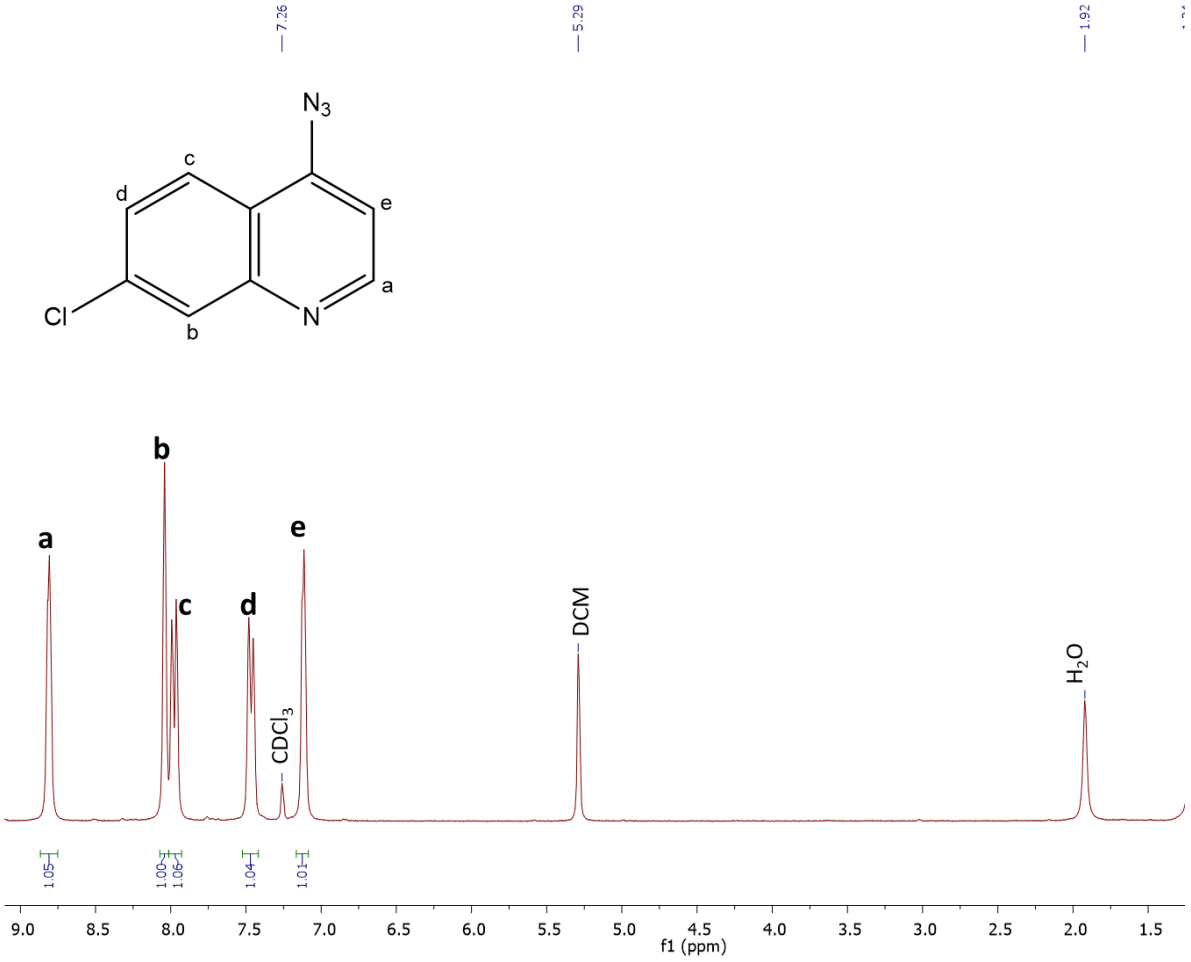

***Figure 3.7**: ^{1}H NMR spectrum of compound **4** in deuterated chloroform ($CDCl_3$). The quinolinyl proton signals (**a-e**) are indicated. DCM: residual dichloromethane.*

The ^{1}H NMR spectrum of the alkyne precursor (compound **5**) in **Figure 3.8** indicates the presence of the ferrocene peaks at δ_H 4.11, 4.14 and 4.21 ppm, integrating for two, five, and two protons, respectively. The singlets for the alkyne proton (H_f) and the two protons flanking the secondary amine group (H_d and H_e) were also found at δ_H 2.27, 3.45 & 3.60 ppm. Additional confirmation of successful synthesis was provided by the $^{13}C\{^{1}H\}$ NMR data, which showed eight signals corresponding to the eight distinct carbon environments in the compound. Both the ^{1}H and $^{13}C\{^{1}H\}$ NMR chemical shift values are in agreement with literature values. [18]

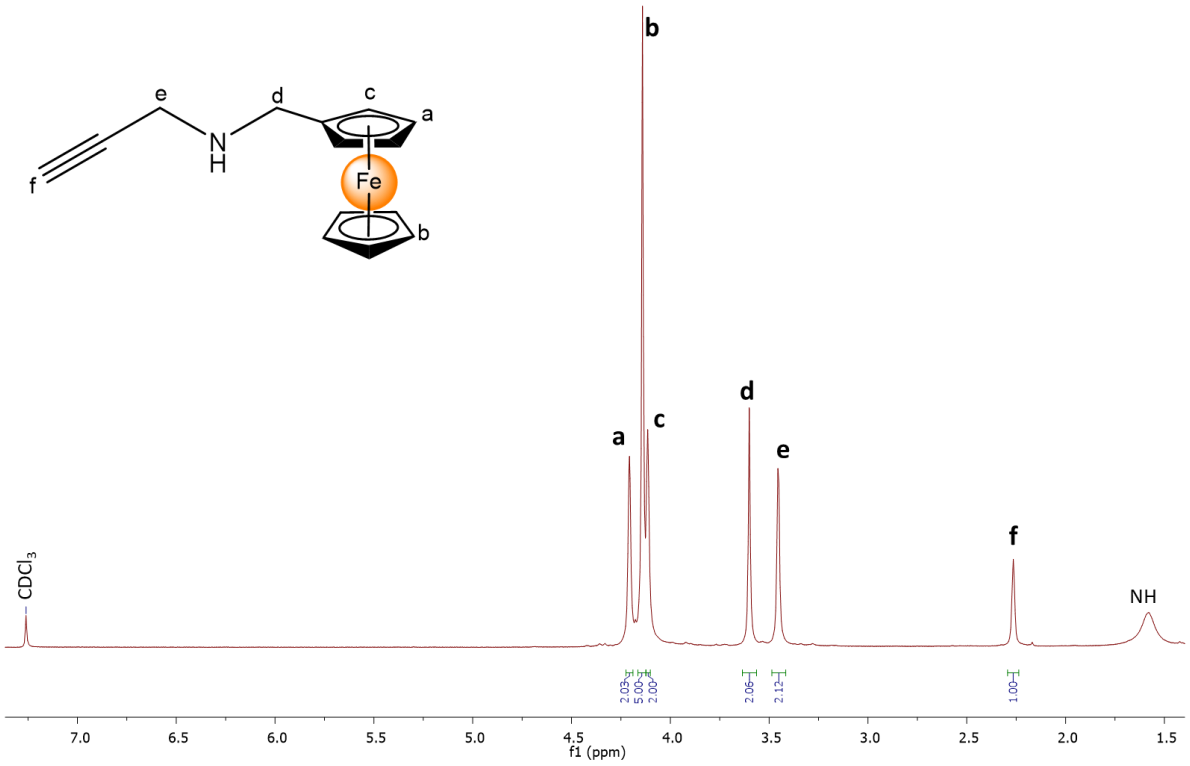

***Figure 3.8**: ^{1}H NMR spectrum of compound **5** in deuterated chloroform ($CDCl_3$). The ferrocenyl (**a-c**), alkyl (**d** & **e**), alkyne (**f**) and amine (NH) proton signals are indicated.*

^{1}H NMR analysis of compound **6** confirmed that the "click" reaction between compounds **4** and **5** was a success. In addition to the downfield quinoline ring signals for H_a, H_b, H_c, H_e and H_f, the spectrum in **Figure 3.9** shows the two triplet signals of the substituted ferrocene ring protons (H_g and H_i) on either side of the intense singlet for the unsubstituted ring protons (H_h). The diagnostic peak of the triazole proton (H_d) was also observed downfield at δ_H 7.96 ppm amidst the aromatic quinoline signals. This is likely due to the de-shielding effect of the three electron-withdrawing nitrogen atoms in the triazole ring, which also appears to have caused an overall downfield shift of the quinolinyl and alkyl proton

peaks. To confirm the identity of this peak, the compound was further analysed by homonuclear correlation spectroscopy (2D COSY), which reveals information on the coupling of protons through bonds. [21,22] The cross peaks highlighted on the 2D NMR spectrum of compound **6** in **Figure 3.10** reveal a weak correlation between the triazole proton and the two protons at H_j (δ_H 4.10 ppm), which are in close proximity to the triazole ring. All the ^{1}H NMR peaks integrate for the expected number of protons, altogether giving a total of 19 protons. This was also the case with the results of the $^{13}C\{^1H\}$ NMR analysis, which confirmed the presence of all 23 carbon atoms.

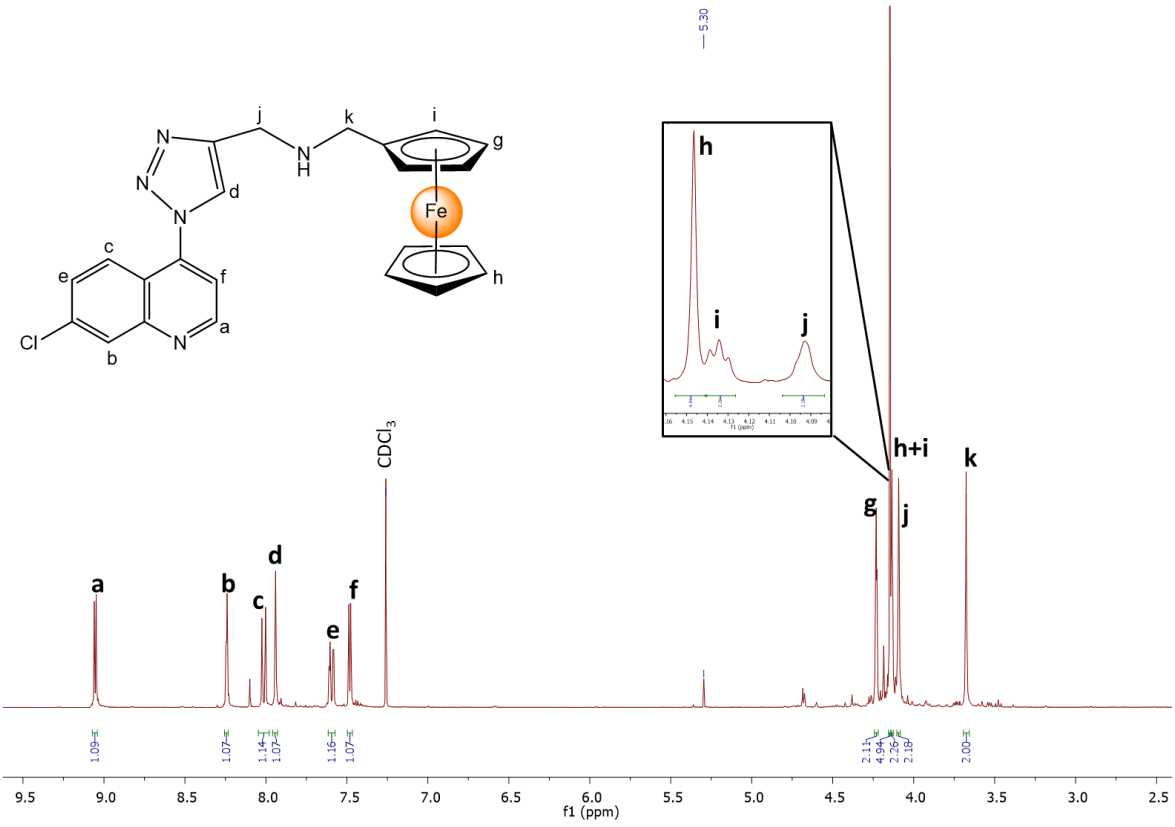

***Figure 3.9**: ^{1}H NMR spectrum of compound **6** in deuterated chloroform ($CDCl_3$). The quinolinyl (**a**, **b**, **c**, **e** & **f**), triazole (**d**), ferrocenyl (**g-i**) and alkyl (**j** & **k**) proton signals are indicated.*

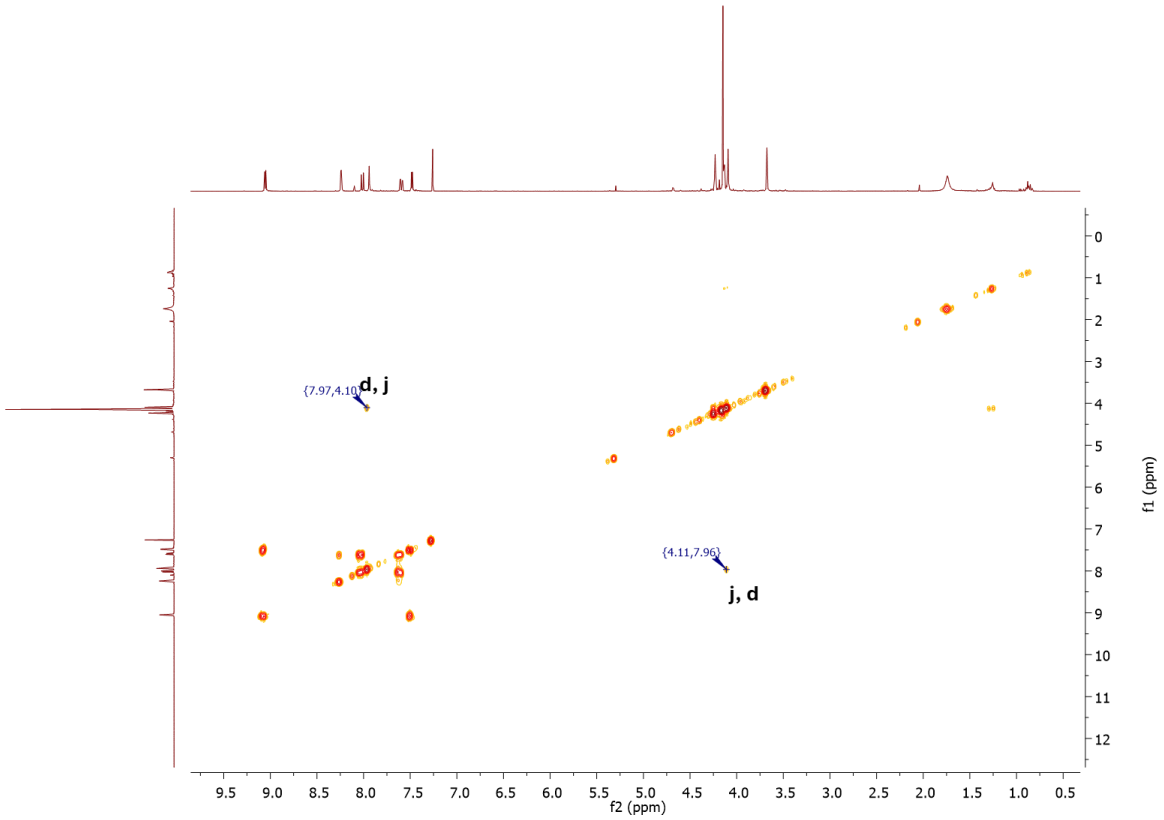

***Figure 3.10**: 2D COSY ^{1}H NMR spectrum of compound **6** in deuterated chloroform ($CDCl_3$). Cross peaks for the triazole proton (**d**) and alkyl proton (**j**) are indicated.*

Infrared spectroscopy

To further verify the successful synthesis of compounds **4**, **5** and **6,** IR spectroscopy was utilised. For compound **4**, an intense ν(N=N=N) absorption band at 2125 cm^{-1} was observed, confirming the presence of the azide functional group. The stretching frequency for the alkyne functional group (ν(C≡C)) in compound **5** was also observed at 2092 cm^{-1}, in addition to peaks for ν(N-H) at 3301 and 3092 cm^{-1}. Finally, the spectrum for compound **6** revealed absorption bands corresponding to ν(N-H) at 3330 cm^{-1} as well as ν(C=N) at 1593 cm^{-1}.

Mass spectrometry

The molecular mass of compound **4** was confirmed using LC-MS. A *m/z* value of 205.10 $[M+H]^+$ was observed, matching the calculated mass of 205.05. The molecular masses of compounds **5** and **6** were determined via high-resolution ESI-MS. Compound **5** shows a base peak at *m/z* 253.0557 $[M]^+$, which

correlates with its calculated mass of 253.0500. In the case of compound **6**, a base peak was found at *m/z* 457.0762 $[M]^+$, correlating to the calculated mass of 457.0800 for the molecular ion.

3.4. Synthesis and characterisation of phenyl-linked ferrocenyl-quinoline compound (11)

3.4.1. Attempted synthesis via Schiff base condensation (Route 1)

In order to synthesise a fourth ferrocenyl-quinoline compound with a phenyl linker, it was necessary to first synthesise a phenyl-quinoline precursor compound (compound **7**). As shown in **Scheme 3.3 i**, this was accomplished by reacting 4,7-dichloroquinoline with an excess of *p*-phenylenediamine in absolute ethanol under reflux conditions. This is also a nucleophilic aromatic substitution reaction and a published method was followed. [23] Compound **7** was obtained as a bright yellow/orange powder in excellent yield (96%).

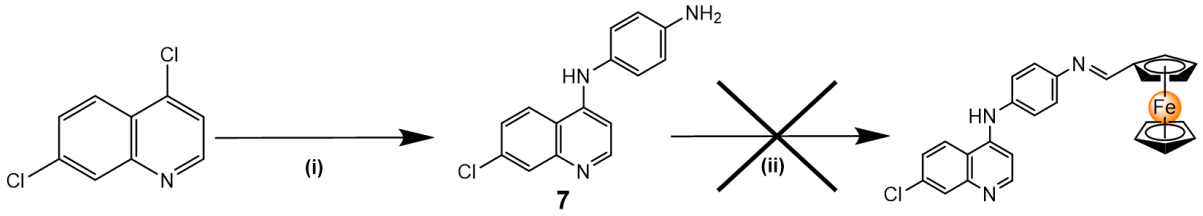

***Scheme 3.3**: Synthesis of compound **7** and attempted Schiff base condensation reaction. The cross indicates that no reaction occurred under the conditions stated. Reagents and conditions: (i) p-Phenylenediamine, absolute EtOH, 8h, reflux; (ii) Ferrocenecarboxaldehyde, anhydrous MeOH or absolute EtOH, variable time and temperature.*

Several attempts were made to synthesise a phenyl-linked ferrocenyl-quinoline compound using the precursor compound **7**. These involved a Schiff base condensation reaction between the precursor and ferrocenecarboxaldehyde in either anhydrous methanol or absolute ethanol at varying temperatures, as illustrated in **Scheme 3.3 ii**. In all the attempts, the reaction was unsuccessful as significant amounts of the unreacted starting reagents were recovered in either solid form (compound **7**) or in solution (ferrocenecarboxaldehyde). This was confirmed through ^{1}H NMR analysis of the reaction components, with the spectra showing the peaks of each unreacted reagent matching those of the recovered material (**Figures 3.11** & **3.12**). In the case of the attempts using ethanol, additional peaks were

observed in the spectrum generated by the material found in solution (δ_H 6.50 – 8.50 ppm). These peaks could not be positively identified.

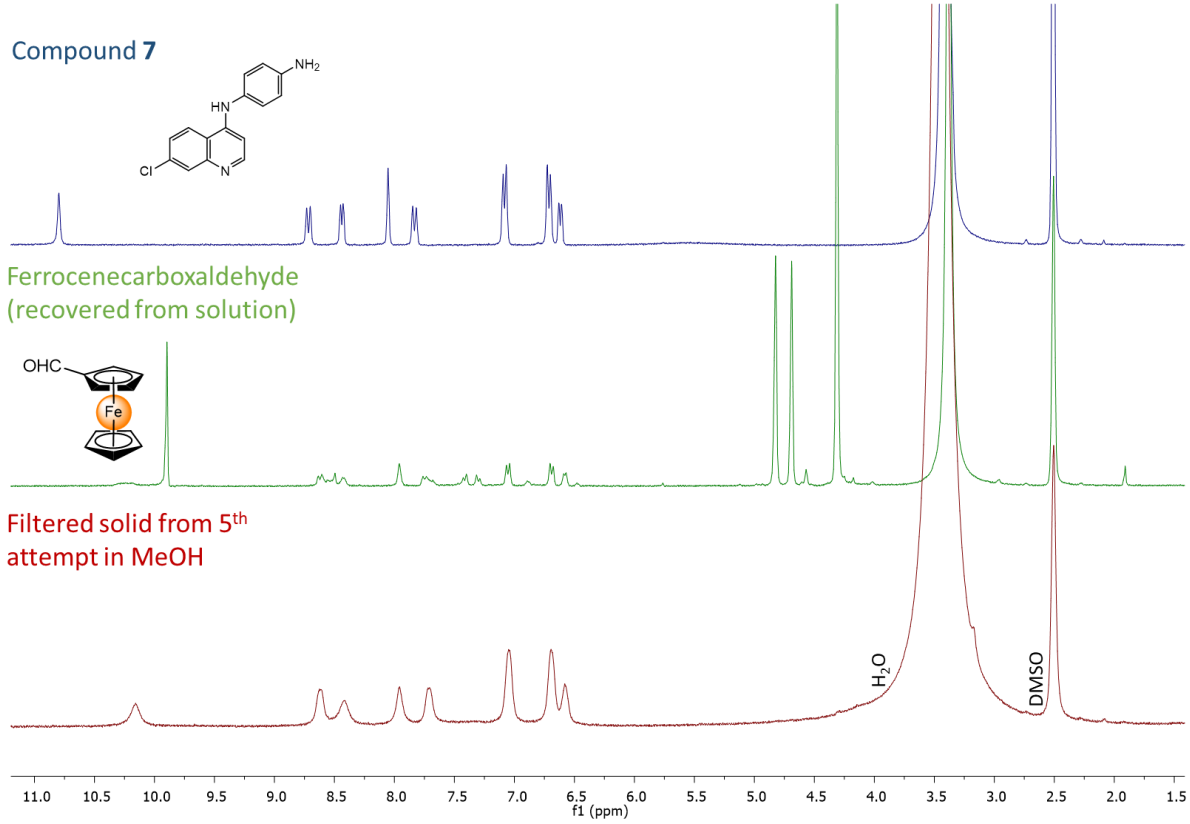

***Figure 3.11**: Stacked ^{1}H NMR spectra of compound **7**, ferrocenecarboxaldehyde and the solid obtained from the fifth synthesis attempt using anhydrous methanol. NMR solvent: deuterated dimethyl sulfoxide (DMSO-d_6).*

The failure of the Schiff base formation may be attributed to the combined inductive electron-withdrawing properties of the quinoline and aromatic diamine ring systems in the precursor molecule, making the lone pair of electrons on the free amine group less capable of nucleophilic attack on the carbonyl group of the aldehyde. In some of the synthesis attempts, glacial acetic acid was added in an effort to catalyse the reaction and encourage nucleophilic attack by the amine. This was done according to the strategy employed by Omosun and Smith, who synthesised Schiff base ligands using aromatic amines and aldehydes. [24] However, this modification to the reaction did not yield the expected results.

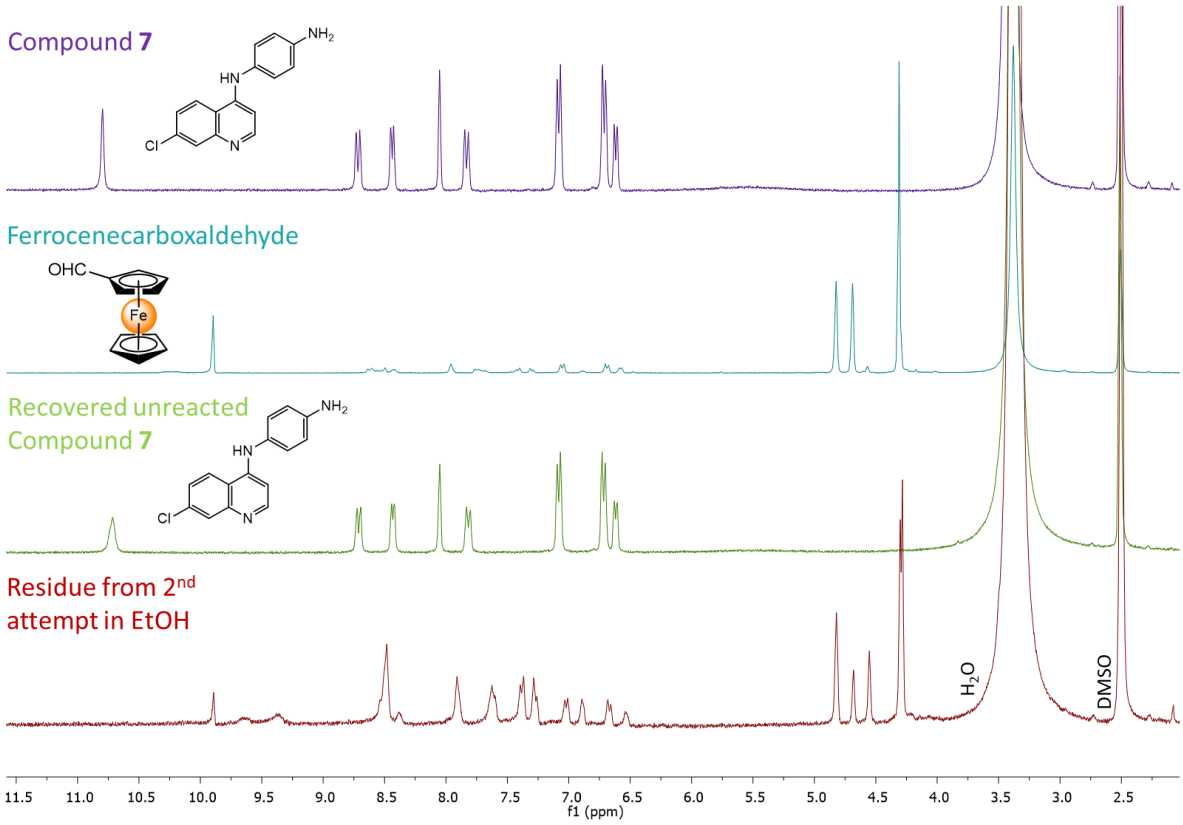

***Figure 3.12**: Stacked ^{1}H NMR spectra of compound **7**, ferrocenecarboxaldehyde, unreacted compound **7** and the residue obtained from the second synthesis attempt using absolute ethanol. NMR solvent: deuterated dimethyl sulfoxide (DMSO-d_6).*

While there is no literature describing the synthesis of this Schiff base, one article describes the synthesis of its reduced form. In this study by N'Da and Smith, the compound was made by stirring compound **7** with ferrocenecarboxaldehyde in anhydrous methanol for four hours and then adding sodium borohydride for an additional two hours at room temperature (**Scheme 3.4**). [25] This method was used in several more attempts to synthesise a phenyl-amine-linked ferrocenyl-quinoline compound, with later attempts having some modifications. Small quantities of a brown solid were obtained from each of the attempts, and this solid was analysed by ^{1}H NMR analysis to determine if it was the desired compound.

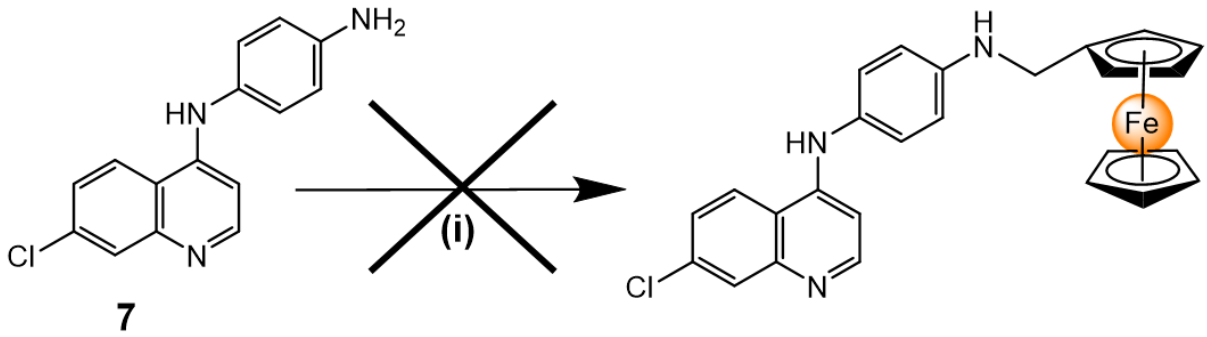

***Scheme 3.4**: Attempted synthesis of the phenyl-linked ferrocenyl-quinoline compound via a Schiff base condensation reaction followed by a reduction. The cross indicates that no reaction occurred under the conditions stated. Reagents and conditions: (i) Ferrocenecarboxaldehyde, anhydrous MeOH, variable time and temperature, $NaBH_4$, anhydrous MeOH, 2h, r.t. (25 °C).*

Figure 3.13 shows the stacked ^{1}H NMR spectra of the product from the aforementioned synthesis attempts, which all show an identical series of peaks between δ_H 6.40 and 8.80 ppm. These peaks are presumed to be associated with the quinoline and phenyl ring protons, given that a similar pattern was observed for the precursor compound **7**. However, the chemical shift values do not match those of either compound **7** or the compound reported by N'Da and Smith. [42] Moreover, there is no evidence of distinct ferrocenyl proton peaks on the spectra, which usually appear in the δ_H 4.00 to 4.50 ppm range with an integration pattern of 5-2-2 or 2-5-2. Instead, unusual multiplet signals were observed within this region. Taken together, these results imply the formation of a compound that is entirely different from what has been reported by the authors and that retains most of the precursor's structure.

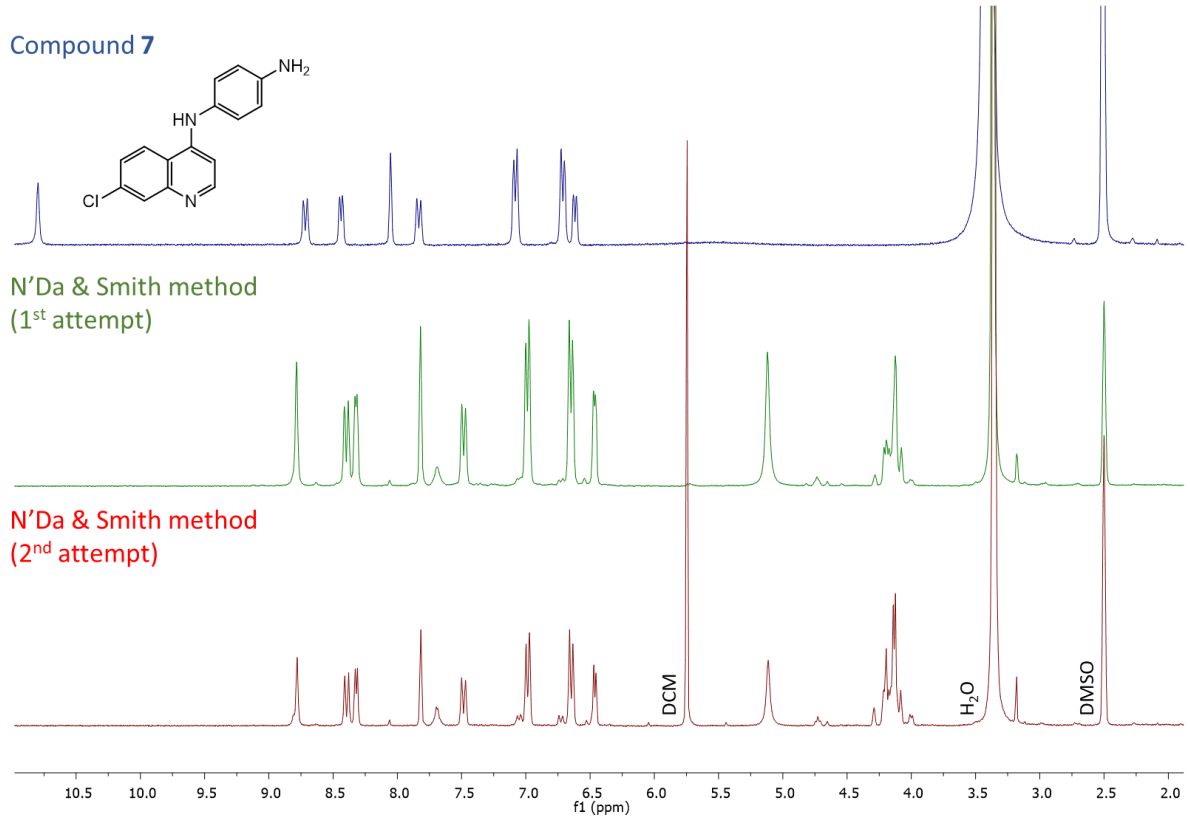

***Figure 3.13**: Stacked ^{1}H NMR spectra of compound **7** and the solid obtained from the synthesis attempts using the method reported by N'Da and Smith. NMR solvent: deuterated dimethyl sulfoxide (DMSO-d_6). DCM: residual dichloromethane.*

Characterisation

Nuclear Magnetic Resonance spectroscopy

Compound **7** was analysed by ^{1}H and $^{13}C\{^{1}H\}$ NMR spectroscopy to confirm its successful synthesis. The ^{1}H NMR spectrum of compound **7** shown in **Figure 3.14** shows signals for all five quinoline protons (H_a – H_e) within the δ_H 6.5 – 8.8 ppm range. Within that same range are the two doublets corresponding to the four phenyl ring protons (H_f and H_g) at δ_H 6.70 and 7.07 ppm, each with a coupling constant of 8.6 Hz. The chemical shift and integration values for all the peaks agree with those reported in literature. [26] Also, $^{13}C\{^{1}H\}$ NMR analysis confirmed the presence of all 15 carbons.

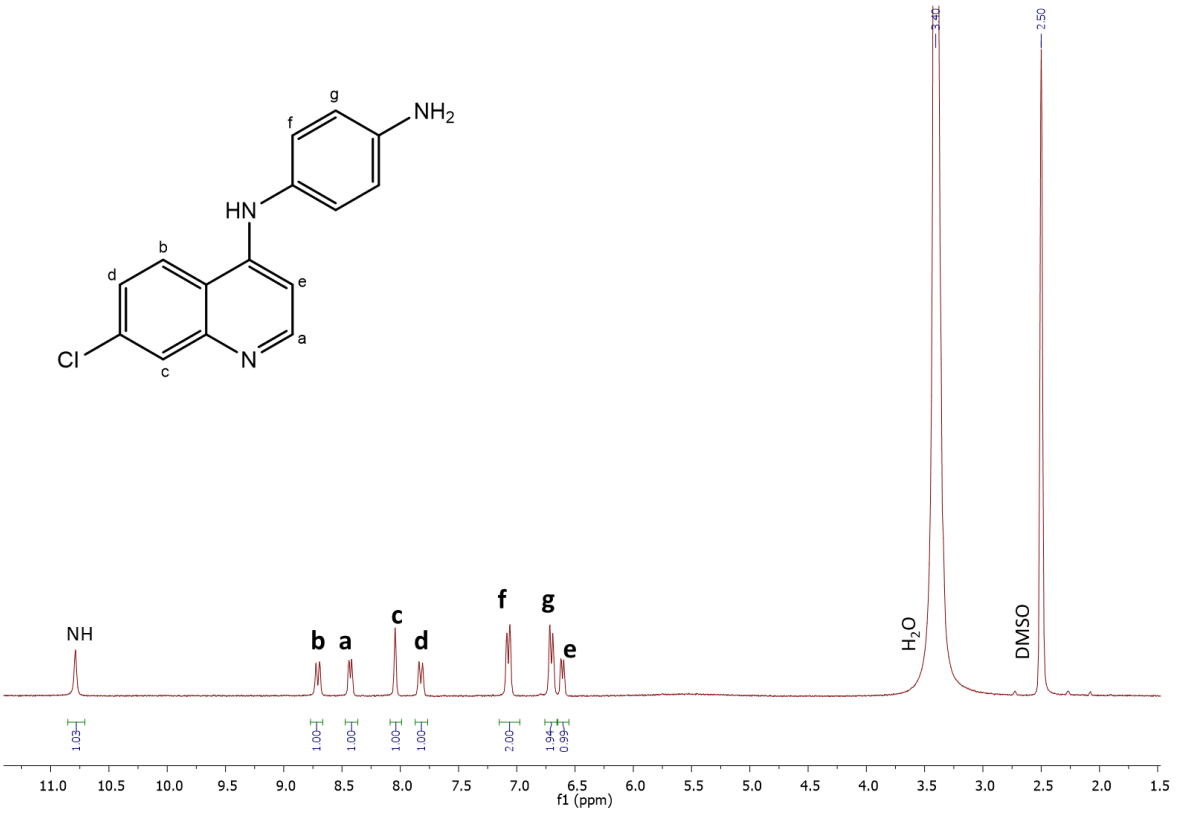

***Figure 3.14**: ^{1}H NMR spectrum of compound **7** in deuterated dimethyl sulfoxide (DMSO-d_6). The quinolinyl (**a-e**), phenyl (**f** & **g**) and amine (NH) proton signals are indicated.*

Infrared spectroscopy

IR spectroscopy was utilised to further characterise compound **7**. Absorption bands for the amine groups were found at 3429 and 3319 cm^{-1}, in addition to a ν(C=N) absorption band at 1604 cm^{-1}.

Mass spectrometry

Compound **7** was analysed by LC-MS to confirm its molecular mass. A *m/z* value of 270.10 $[M+H]^+$ was observed for the compound, which was in agreement with the calculated mass of 270.07.

3.4.2. Attempted synthesis via Schiff base condensation and nucleophilic aromatic substitution (Route 2)

Since the attempts to synthesise a phenyl-amine-linked ferrocenyl-quinoline compound using compound **7** were unsuccessful, a second precursor (compound **8**) was generated as an alternative.

Scheme 3.5 illustrates the *in situ* synthesis of compound **8** using a modified version of the method reported by Arancibia *et al*. [27] The compound was synthesised via a Schiff base condensation reaction with ferrocenecarboxaldehyde and *p*-phenylenediamine, followed by a reduction using excess sodium borohydride. The solution containing the aldehyde was added dropwise to minimise the formation of a bifunctionalised product through a reaction occurring at both NH_2 groups of the diamine. Despite this modification, crystals of the bifunctionalised product (bis-ferrocenyl methyl-phenylenediamine) were obtained in significant amounts upon purification. The result was a low yield (15%) of compound **8**, which was precipitated as either a fine dark-red powder or red granules using a DCM/hexane/pentane mixture.

The crystals of the bifunctionalised product, which were obtained from column fractions eluted with a hexane/ethyl acetate mixture, were analysed by single-crystal X-ray crystallography. The analysis revealed the molecular structure shown in **Figure 3.15**, confirming the presence of two ferrocene entities on either side of the diamino phenyl ring. The crystallographic data, parameters and selected bond lengths and angles for the compound are summarised in **Table 3.1** and **Table 3.2**.

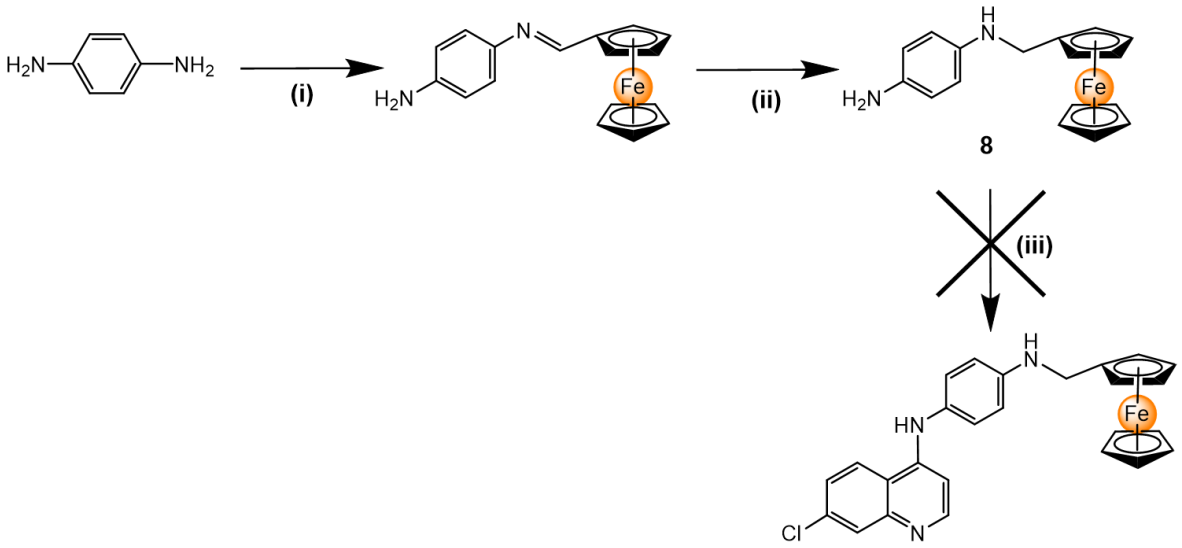

***Scheme 3.5**: Synthesis of compound **8** and attempted synthesis via nucleophilic aromatic substitution. The cross indicates that no reaction occurred under the conditions stated. Reagents and conditions: (i) Ferrocenecarboxaldehyde, anhydrous MeOH, 24 h, r.t. (25 °C); (ii) $NaBH_4$, anhydrous MeOH, 2 h, r.t. (25 °C); (iii) 4,7-Dichloroquinoline, anhydrous MeOH, 24 h, reflux.*

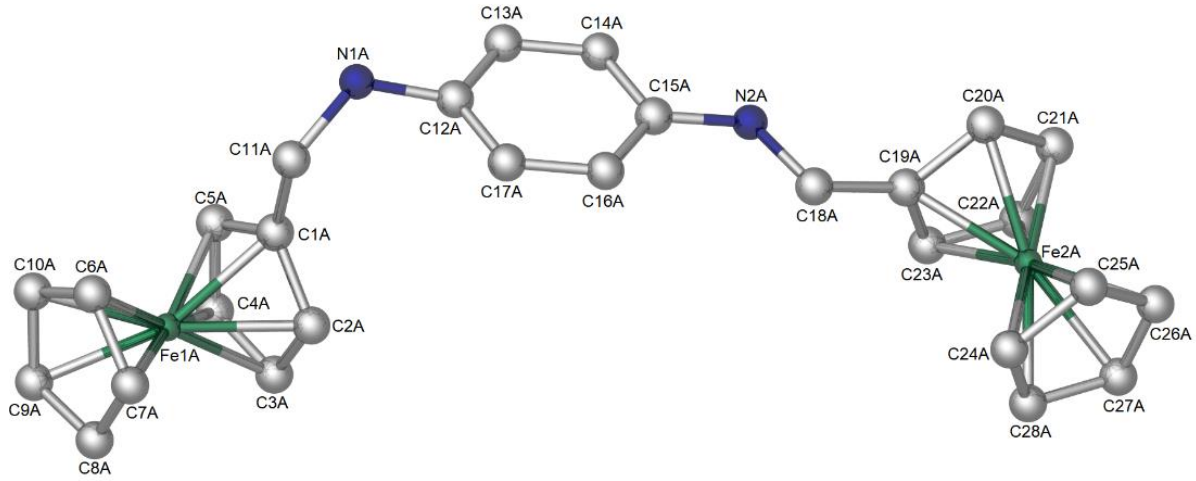

***Figure 3.15**: Single crystal X-ray molecular structure of bis-ferrocenyl methyl-phenylenediamine, showing the two ferrocenyl groups bonded to either side of the phenyl ring. Hydrogen atoms have been omitted for clarity.*

***Table 3.1**: Crystallographic data and refinement parameters for bis-ferrocenyl methyl-phenylenediamine.*

Chemical Formula	**$C_{28}H_{28}N_2Fe_2$**	***F (000)***	**4192**
Formula Weight	504.22	***Crystal Size (mm)***	0.04 x 0.10 x 0.28
Crystal System	Monoclinic	***Temperature (K)***	100
Space Group	Cc (No.9)	***Scan Range (°)***	1.8 < θ < 28.4
a, b, c (Å)	17.9132(9), 16.2767(7), 30.7257(15)	***Unique Reflections***	21921
α, β, γ (°)	90, 97.772(2), 90	R_{int}	0.046
Volume (Å^3)	8876.3(7)	***Reflections used [I>2σ(I)]***	20781
Z	16	***R, wR2***	0.0362, 0.0739
Density (g/cm^3)	1.509	***Goodness-of-Fit***	1.092
μ (mm)	1.326	***Min, Max Δρ (e Å^{-3})***	-0.52, 0.56

Table 3.2. *Selected bond lengths and angles for bis-ferrocenyl methyl-phenylenediamine.*

Bond lengths (Å)			
N_{1A} – C_{11A}	1.468 (6)	**N_{2A} – C_{15A}**	1.387 (5)
N_{1A} – C_{12A}	1.420 (5)	**N_{2A} – C_{18A}**	1.452 (6)
Fe_{1A} – C_{1A}	2.029 (4)	**Fe_{2A} – C_{19A}**	2.051 (4)
Fe_{1A} – C_{2A}	2.037 (4)	**Fe_{2A} – C_{20A}**	2.044 (4)
Fe_{1A} – C_{3A}	2.047 (5)	**Fe_{2A} – C_{21A}**	2.034 (5)
Fe_{1A} – C_{4A}	2.039 (5)	**Fe_{2A} – C_{22A}**	2.043 (5)
Fe_{1A} – C_{5A}	2.028 (5)	**Fe_{2A} – C_{23A}**	2.042 (4)
Fe_{1A} – C_{6A}	2.031 (5)	**Fe_{1A} – C_{24A}**	2.050 (5)
Fe_{1A} – C_{7A}	2.033 (5)	**Fe_{1A} – C_{25A}**	2.049 (5)
Fe_{1A} – C_{8A}	2.029 (6)	**Fe_{1A} – C_{26A}**	2.047 (5)
Fe_{1A} – C_{9A}	2.030 (6)	**Fe_{1A} – C_{27A}**	2.048 (5)
Fe_{1A} – $C1_{0A}$	2.037 (5)	**Fe_{1A} – C_{28A}**	2.032 (5)
Bond angles (°)			
C_{1A} – Fe_{1A} – C_{6A}	105.55 (18)	**C_{19A} – Fe_{2A} – C_{24A}**	108.78 (18)
Fe_{1A} – C_{1A} – C_{11A}	122.3 (3)	**Fe_{2A} – C_{19A} – C_{18A}**	130.6 (3)
C_{11A} – N_{1A} – C_{12A}	121.1 (3)	**C_{18A} – N_{2A} – C_{15A}**	124.0 (3)
Torsion angles (°)			
C_{12A} – N_{1A} – C_{11A} – C_{1A}	-66.9 (5)	**C_{15A} – N_{2A} – C_{18A} – C_{19A}**	168.0 (4)

An attempt to synthesise the desired compound was made using 4,7-dichloroquinoline and compound **8** in a nucleophilic aromatic substitution reaction, as illustrated in **Scheme 3.5 iii**. This alternative approach produced a brown solid similar to the one obtained from the previous attempts using the N'Da and Smith method. [25] Unfortunately, ^{1}H NMR analysis of the solid revealed that it was identical to the product from the previous attempts (**Figure 3.16**). The product of the alternative method also lacks the ferrocene-associated signals in the expected region of δ_H 4.00 to 4.50 ppm and has peaks seemingly corresponding to the quinoline and phenyl protons in the δ_H 6.40 to 8.80 ppm range. This result provides further confirmation of the formation of another compound different to what has been reported.

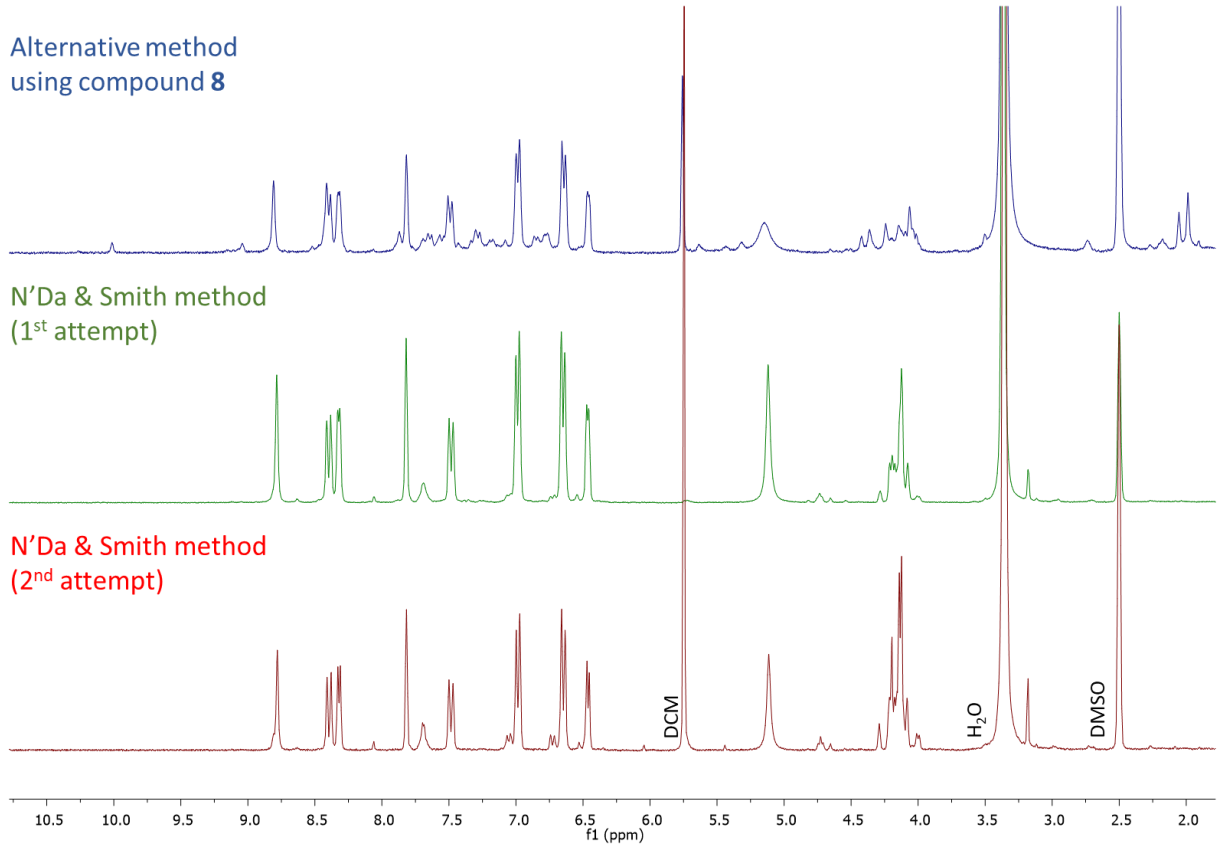

***Figure 3.16**: Stacked ^{1}H NMR spectra of the solid obtained from the synthesis attempts using the alternative and literature methods. NMR solvent: DMSO-d_6. DCM: residual dichloromethane.*

Characterisation

Nuclear Magnetic Resonance spectroscopy

NMR spectroscopic analysis of compound **8** produced the ^{1}H NMR spectrum shown in **Figure 3.17**. Two doublets, each integrating for two protons and with coupling constants of 8.6 Hz, were found at δ_H 6.64 and 6.57 ppm. These doublets are assigned to the phenyl ring protons H_a and H_b, respectively. The ferrocene proton peaks (H_c, H_d and H_e) are also present at δ_H 4.23, 4.17 and 4.13 ppm, in addition to the singlet associated with the two protons (H_f) between the ferrocene and secondary amine group. Arancibia *et al.* also reported chemical shift values similar to those observed in this study. [27] Nine signals were observed upon $^{13}C\{^{1}H\}$ NMR analysis of the compound, corresponding to the nine distinct carbon-containing chemical environments in the structure of the compound.

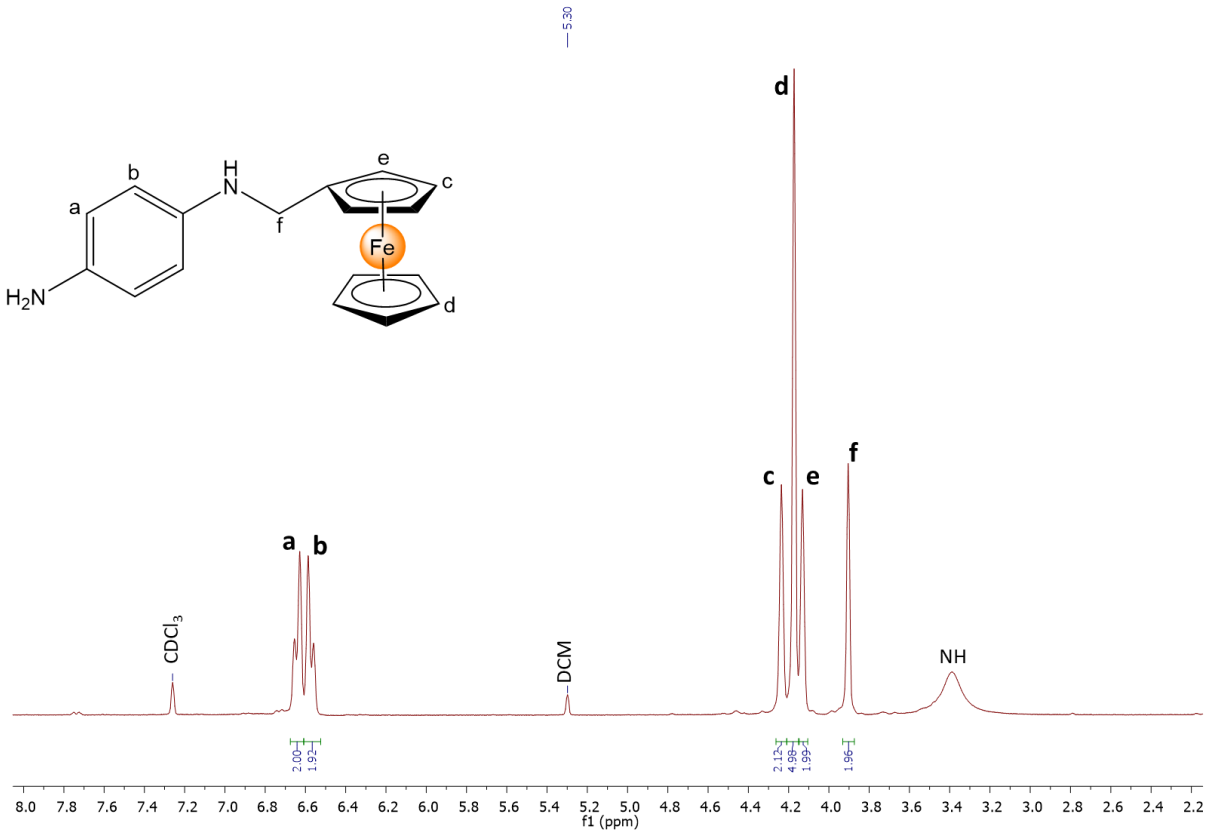

***Figure 3.17**: ^{1}H NMR spectrum of compound **8** in deuterated chloroform ($CDCl_3$). The phenyl (**a** & **b**), ferrocenyl (**c-e**), alkyl (**f**) and amine (NH) proton signals are indicated. DCM: residual dichloromethane.*

Infrared spectroscopy

IR spectroscopic analysis showed two prominent absorption bands corresponding to the N-H group were observed for compound **8**. The two bands were found at 3424 and 3347 cm^{-1}.

Mass spectrometry

ESI-MS analysis of compound **8** revealed a base peak for the molecular ion at *m/z* 306.0803 $[M]^+$, corresponding to a calculated mass of 306.0800.

3.4.3. Attempted synthesis via Mizoroki-Heck coupling (Route 3)

Following the unsuccessful synthesis attempt using precursor compound **8**, a third precursor compound (**9**) was synthesised through another nucleophilic aromatic substitution reaction almost similar to the synthesis of compound **7**. This particular compound has not been reported in literature,

but the method for its synthesis was adapted from that of compounds with similar structures, such as the previously described compound **7**. [23,28] As shown in **Scheme 3.6 i**, 4,7-dichloroquinoline was reacted with 4-iodoaniline in absolute ethanol under reflux for 24 hours. This produced a yellow-green precipitate in high yield (90%).

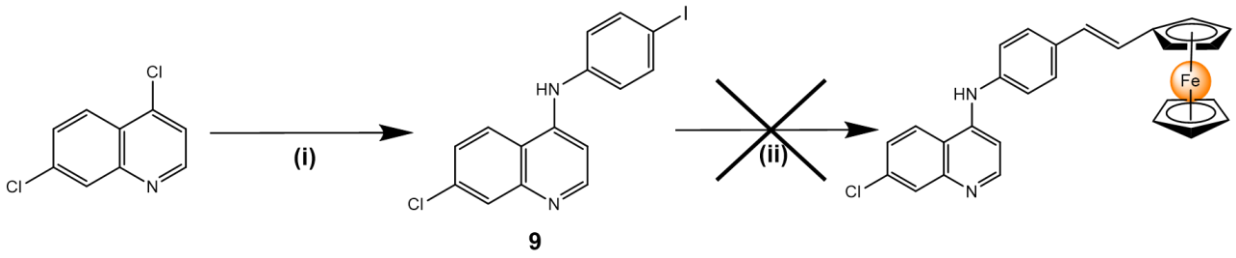

***Scheme 3.6**: Synthesis of compound **9** and attempted synthesis via Mizoroki-Heck coupling. The cross indicates that no reaction occurred under the conditions stated. Reagents and conditions: (i) 4-Iodoaniline, absolute EtOH, 24h, reflux; (ii) Vinylferrocene, $Pd(OAc)_2$, Et_3N, PPh_3, 1,4-dioxane, 72 h, reflux.*

A new attempt was made to synthesise a phenyl-alkene-linked ferrocenyl-quinoline compound through a Mizoroki-Heck coupling reaction. This type of reaction is a cross-coupling between an aryl halide and an alkene in the presence of a palladium catalyst and a base. The catalyst is typically formed from a palladium(II) precursor, and this requires a ligand to stabilise the palladium in its zero oxidation state. [29] **Figure 3.18** illustrates the general mechanism of a Mizoroki-Heck coupling reaction. Upon its formation, the palladium(0) catalyst is oxidised by inserting itself in the aryl-halide bond via oxidative addition. The next step is a complexation of the palladium(II)-aryl-halide intermediate with the alkene, which subsequently inserts itself in the palladium-aryl bond. This is then followed by a β-hydride elimination step to release the newly formed aryl alkene product and leave a palladium(II)-halide intermediate. In the final step, the base reacts with the intermediate via reductive elimination, resulting in the regeneration of the palladium(0) catalyst. [30]

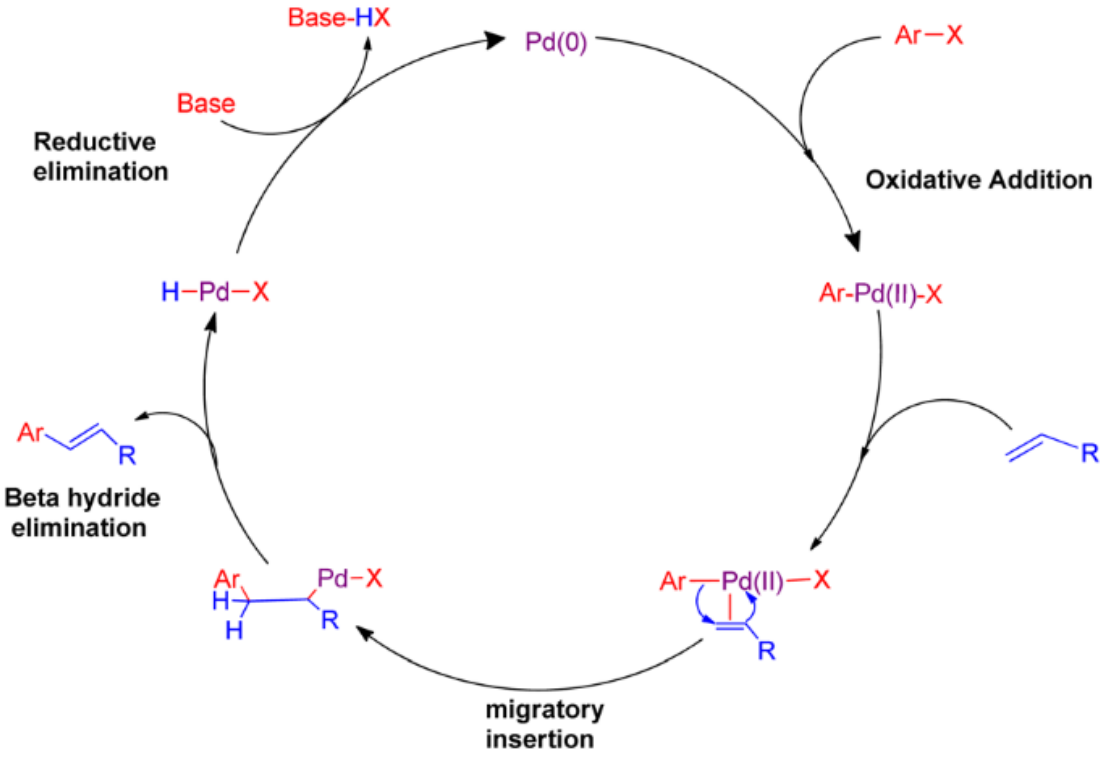

***Figure 3.18**: General mechanism of a Mizoroki-Heck coupling reaction, as illustrated by Koranne et al. The palladium(0) catalyst (purple) forms an intermediate with an aryl halide (red) via oxidative addition. An alkene (blue) then inserts itself into the palladium-aryl bond of the intermediate, and this is followed by β-hydride elimination to release the aryl alkene product. The final step is the regeneration of the catalyst by reductive elimination.* [30]

A Mizoroki-Heck coupling reaction of compound **9** with vinylferrocene was attempted, according to **Scheme 3.6 ii**. This would result in a compound in which the ferrocene moiety was linked to the rest of the molecule by a C=C bond, in contrast to the previous attempts where the linking bond was to be a C-N or C=N bond. A method reported by Govender *et al.* was used, where the chosen ligand and base were triphenylphosphine and triethylamine. [31] This method was chosen because these authors successfully performed Mizoroki-Heck reactions using vinylferrocene under the conditions indicated.

The reaction yielded a light-brown solid, but following ^{1}H NMR analysis, it was observed that this was not the anticipated product. As shown in the stacked ^{1}H NMR spectra in **Figure 3.19**, the peaks associated with the ferrocene moiety in the 4.00 – 4.50 ppm range are absent for the product. This is also substantiated by the observation that much of the vinylferrocene was recovered unconsumed after the reaction period. Moreover, when comparing the spectra of compound **9** and the product, it seems that all the quinoline and phenyl ring peaks are present but generally shifted more upfield in the product relative to the precursor. The integration values of these peaks also imply that this product

is a result of the precursor coupling to itself instead of with vinylferrocene, forming a compound with the supposed structure shown in **Figure 3.20A**. However, LC-MS analysis of this compound reported a *m/z* value of 381, which is vastly different from the calculated molecular mass of the proposed compound (506.11). It could mean that the self-coupling product instead has the structure shown in **Figure 3.20B**, whose calculated molecular mass is 381.10, but this contradicts the observed ^{1}H NMR results. Furthermore, elemental analysis indicates that the proportions of C, H and N atoms in the substance are 49.3%, 2.90% and 6.97%, respectively. However, these proportions differ greatly from the calculated atomic compositions of the proposed structures. The identity of this substance, therefore, remains inconclusive.

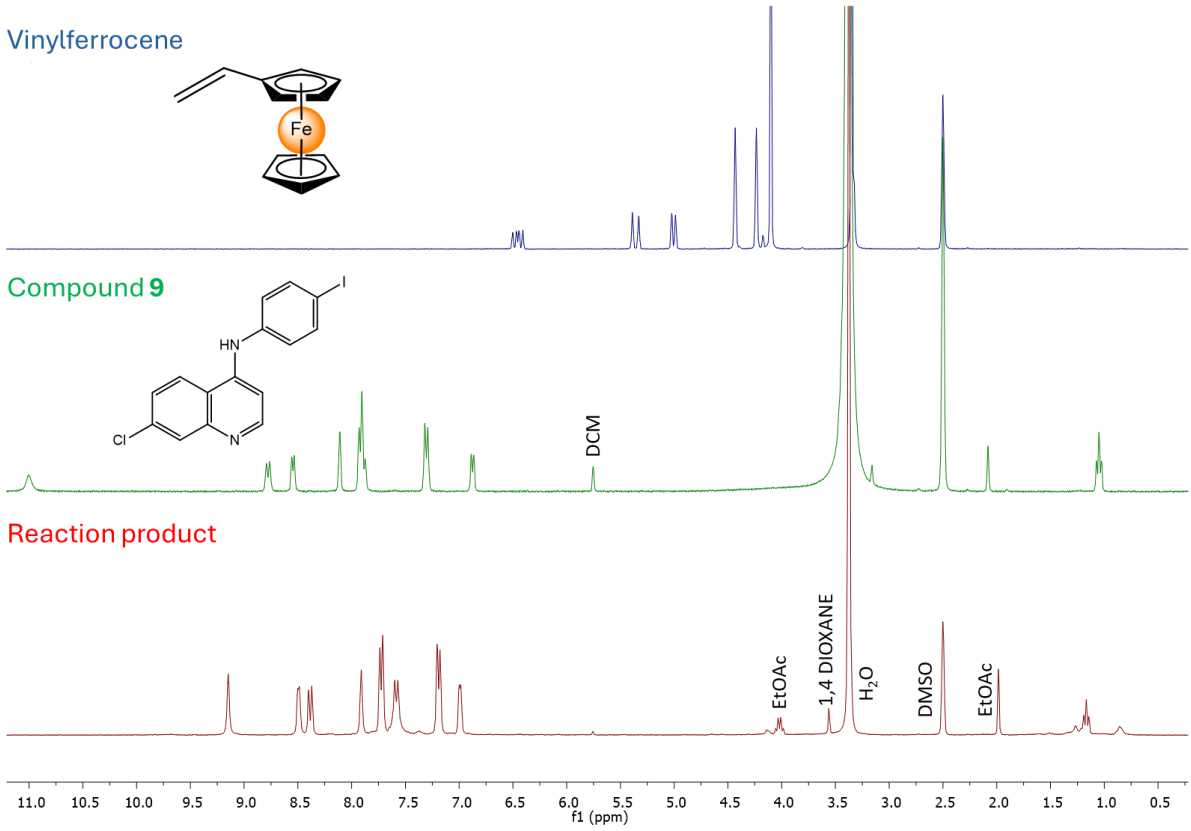

Figure 3.19: Stacked ^{1}*H NMR spectra of vinylferrocene, compound* ***9*** *and the reaction product of the attempted Mizoroki-Heck coupling reaction. NMR solvent: deuterated dimethyl sulfoxide (DMSO-*d_6*). DCM: residual dichloromethane; EtOAc: residual ethyl acetate.*

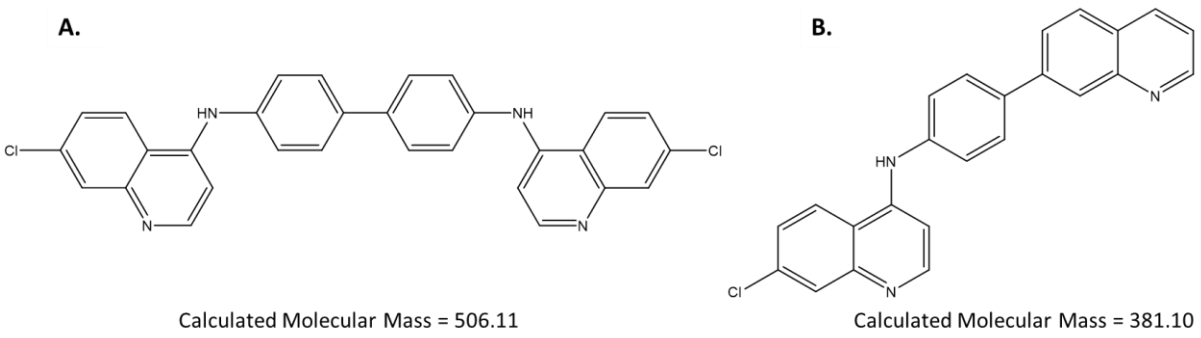

Figure 3.20*: Possible structures of the assumed self-coupling product from the synthesis attempt. The calculated molecular mass for each structure is also shown.*

Characterisation

Nuclear Magnetic Resonance spectroscopy

Figure 3.21 shows the ^{1}H NMR spectrum of compound **9**. Similar to what was observed for compound **7**, there is a pair of doublets at δ_H 7.94 and 7.28 ppm with a coupling constant of 8.6 Hz, corresponding to the phenyl ring protons (H_d and H_f). The presence of the five quinoline protons H_a, H_b, H_c H_e and H_g was confirmed as well. As with compound **7**, all 15 carbons on compound **9** were accounted for by $^{13}C\{^{1}H\}$ NMR analysis.

Infrared spectroscopy

An absorption band of stretching frequency 1607 cm^{-1} was observed for compound **9**, correlating to the C=N bond in the quinoline ring system.

Mass spectrometry

Compound **9** was analysed by LC-MS. The compound produced a base peak at *m/z* 381.10 $[M+H]^+$ for a calculated mass of 380.96.

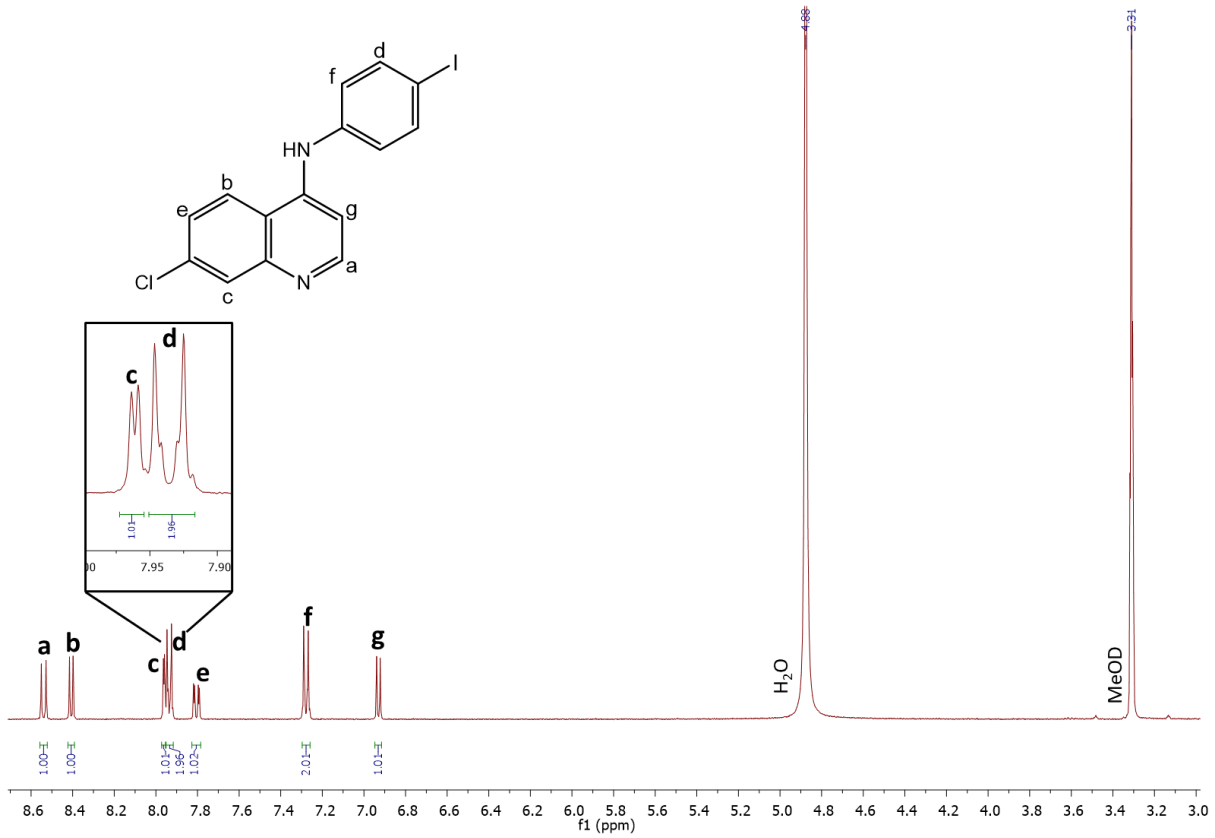

***Figure 3.21**: [1]H NMR spectrum of compound **9** in deuterated methanol (MeOD). The quinolinyl (**a**, **b**, **c**, **e** & **g**) and phenyl (**f** & **d**) proton signals are indicated.*

3.4.4. Synthesis of compound 10 and successful synthesis of phenyl-alkene-linked ferrocenyl-quinoline compound (11)

Given that the attempted synthesis using compound **9** did not yield the desired product, an alternative precursor compound (**10**) was synthesised via a Mizoroki-Heck reaction. For the synthesis of compound **10**, vinylferrocene and 4-iodoaniline were used as the reactants, while potassium carbonate, palladium(II) acetate and β-cyclodextrin were the chosen base, catalyst precursor and ligand, respectively (**Scheme 3.7 i**). The reaction was performed according to a method briefly mentioned by Kanagaraj and Pitchumani, who synthesised β-cyclodextrin derivatives for use as reusable and water-soluble ligands for Mizoroki-Heck reactions. [32] Compound **10** was produced as an orange powder in a low yield of 31%. Kanagaraj and Pitchumani reported an almost similar yield (39%) using bromobenzene and styrene as reactants, possibly indicating the limitations of using β-cyclodextrin as a ligand for this reaction. [32] It is also worth noting that compound **10** was initially synthesised in 1985 by Toma *et al*. via a reduction of 1-ferrocenyl-2-(4-nitrophenyl)ethylene using zinc

and ammonium chloride. [33] This is the only published record of its synthesis, and no other reports currently exist.

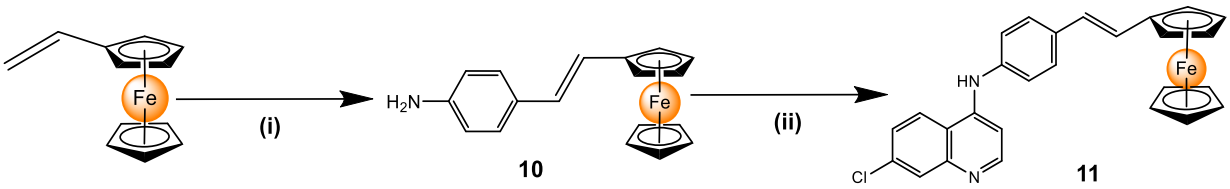

***Scheme 3.7**: Synthesis of compounds **10** and **11**. Reagents and conditions: (i) 4-Iodoaniline, $Pd(OAc)_2$, K_2CO_3, β-CD, DMF, 18 h, 110 °C; (ii) 4,7-Dichloroquinoline, anhydrous MeOH, 24h, 45 °C.*

The successful synthesis of a phenyl-alkene-linked ferrocenyl-quinoline compound was finally achieved using the precursor compound **10**. As illustrated in **Scheme 3.7 ii**, the desired novel compound (**11**) was synthesised via a nucleophilic aromatic substitution reaction involving compound **10** and 4,7-dichloroquinoline in anhydrous methanol heated to 45 °C. This produced an orange solid in a low yield of 17%, which was much lower than the yields obtained for earlier mentioned compounds synthesised via the same reaction (*i.e.*, compounds **1**, **4**, **7** and **9**). The low yield may be a consequence of the structural nature and larger molecular size of compound **10**, which possibly hinder its ability to react with 4,7-dichloroquinoline.

Characterisation

Nuclear Magnetic Resonance spectroscopy

^{1}H NMR analysis of the precursor compound **10** confirmed the presence of the ferrocene entity, indicated by the peaks at δ_H 4.10, 4.23 and 4.46 ppm with integrals accounting for five, two and two protons, respectively (**Figure 3.22**). The signals for the aromatic ring protons are also present as two doublets at δ_H 6.52 and 7.15 ppm, each with a *J*-coupling constant of 8.4 Hz and integrating for two protons. Additionally, there is a slightly broadened signal at δ_H 5.16 ppm integrating for the two protons on the alkene functional group (*i.e.*, H_c and H_d). It was anticipated that this signal would appear as two distinct doublets coupling to each other, but it seems that the expected doublets are in close proximity to one another due to the symmetry of the compound, resulting in a single peak. All the peaks corresponding to the expected 18 carbon atoms in the compound's structure were observed and identified via $^{13}C\{^1H\}$ NMR analysis.

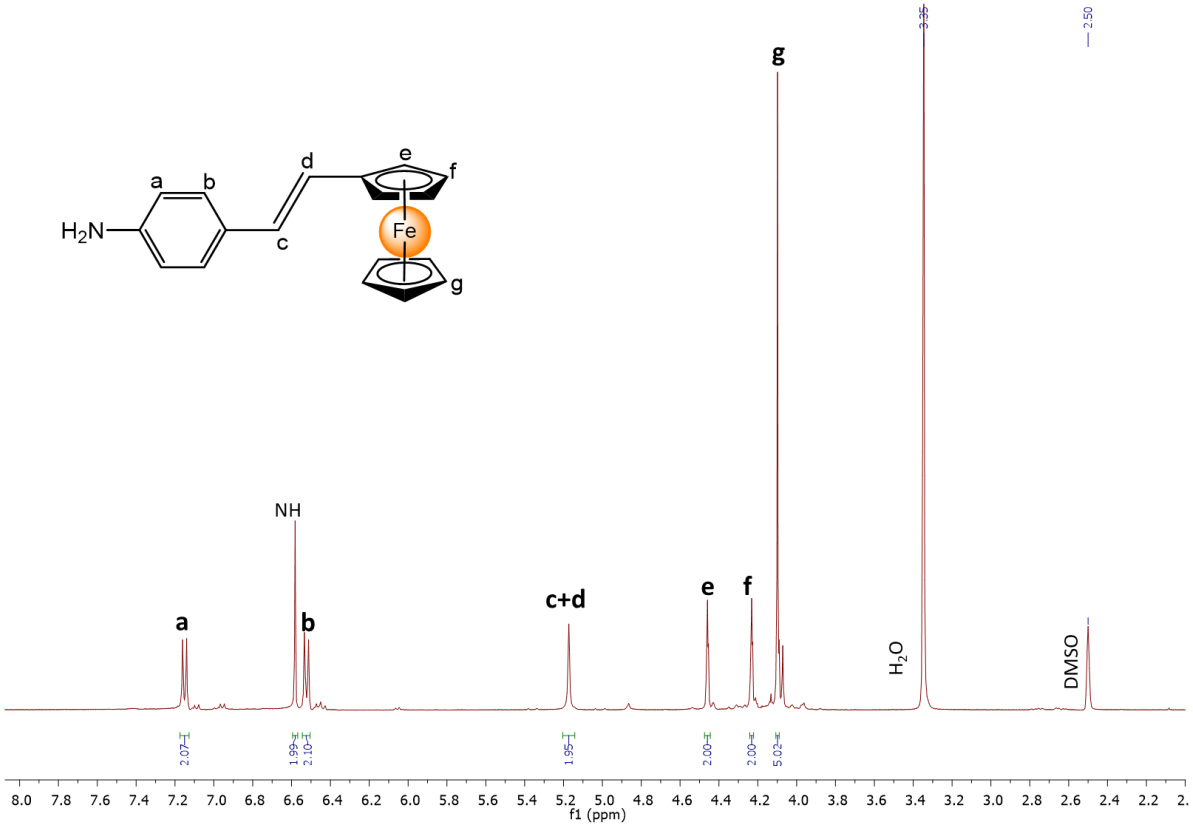

***Figure 3.22**: ^{1}H NMR spectrum of compound **10** in deuterated dimethyl sulfoxide (DMSO-d_6). The phenyl (**a** & **b**), alkene (**c** & **d**), ferrocenyl (**e-g**) and amine (NH) proton signals are indicated.*

Finally, the ^{1}H NMR spectrum of the ferrocenyl-quinoline compound **11** in **Figure 3.23** shows peaks at δ_H 4.15, 4.31 and 4.56 ppm, which are assigned to the ferrocenyl protons H_l, H_k and H_j, respectively. The downfield region of the spectrum between δ_H 6.97 and 8.48 also confirms the presence of the quinoline moiety as there are signals for the five quinolinyl protons, *i.e.*, H_a, H_b, H_c, H_d and H_g. Within that same region are the doublets corresponding to the phenyl ring protons H_e and H_f at δ_H 7.54 and 7.33 ppm, respectively. Another piece of evidence to confirm successful synthesis is that the signals for the alkene protons H_h and H_i are now visible as distinct doublets at δ_H 6.93 and 6.78 ppm, with a *J*-coupling constant of 16.2 Hz and each integrating for one proton. This points to a loss in symmetry caused by the introduction of the electron-withdrawing quinoline ring. It also confirms that the precursor compound **10**, whose spectrum displayed a broadened peak for the alkene protons (**Figure 3.22**), has a *trans*-alkene configuration. Furthermore, the observed coupling constant falls within the typical range of values for *trans*-alkene compounds (12 – 18 Hz). [34] 2D ^{1}H NMR analysis shows cross peaks at the chemical shift values of the doublets (**Figure 3.24**), thus confirming that these protons have a direct correlation with each other. Lastly, a total of 19 signals were observed after ^{13}C {^{1}H} NMR analysis, matching the expected 19 unique carbon environments in the structure of compound **11**.

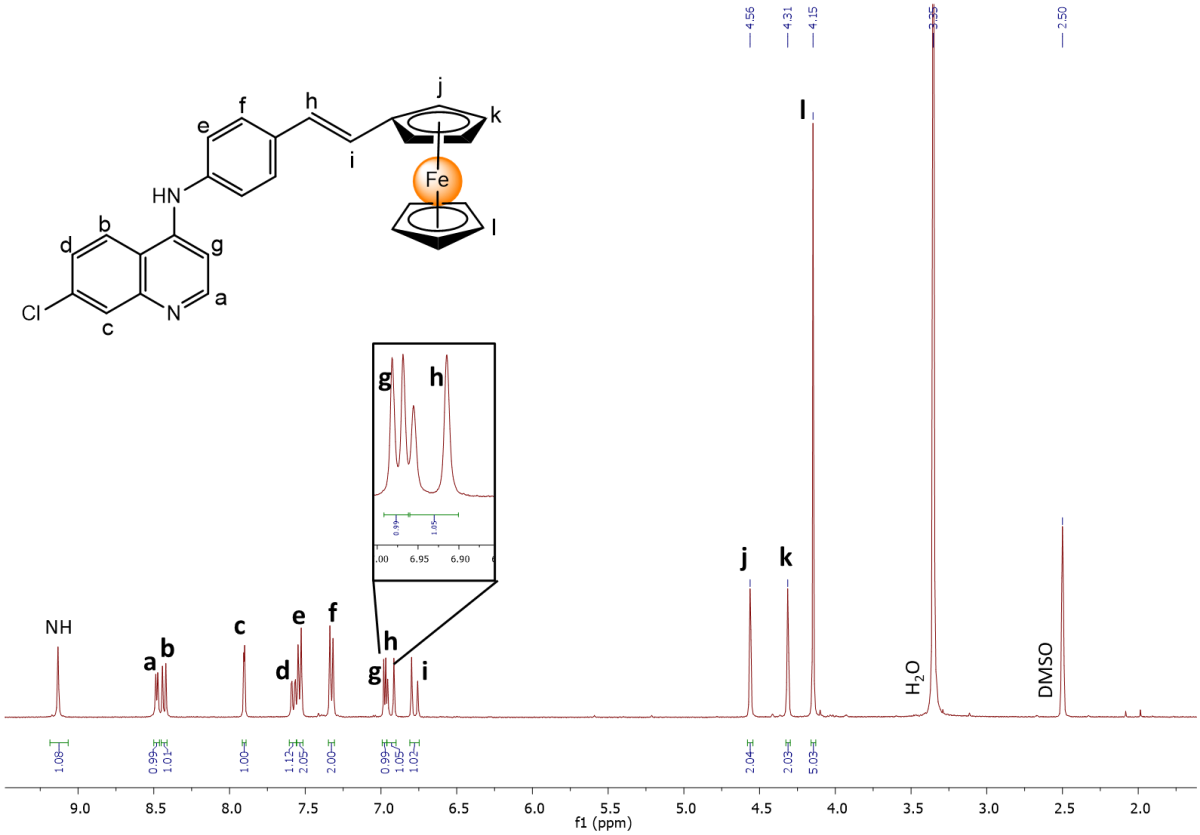

Figure 3.23: *^{1}H NMR spectrum of compound **11** in deuterated dimethyl sulfoxide (DMSO-d_6). The quinolinyl (**a**, **b**, **c**, **d** & **g**), phenyl (**e** & **f**), alkene (**h** & **i**), ferrocenyl (**j-l**) and amine (NH) proton signals are indicated.*

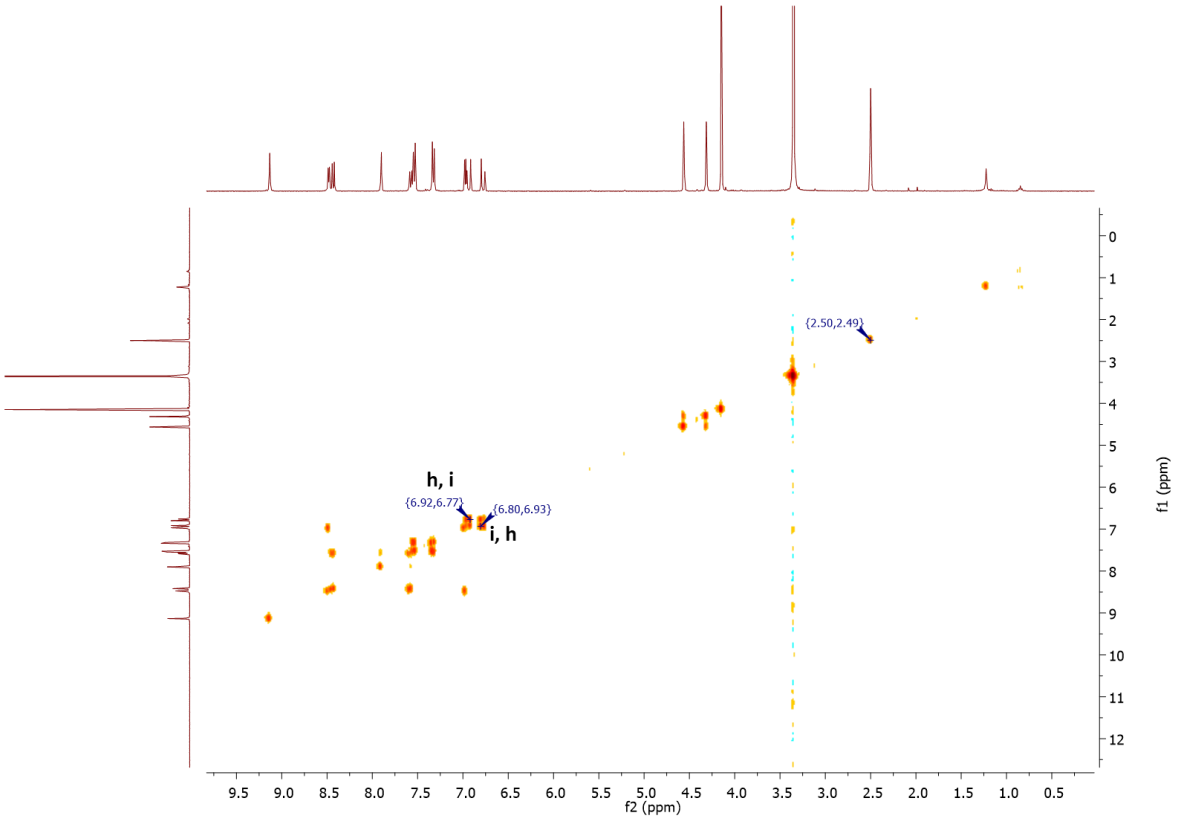

***Figure 3.24**: 2D COSY ^{1}H NMR spectrum of compound **11** in deuterated dimethyl sulfoxide (DMSO-d_6). Cross peaks for the two alkene protons (**h** & **i**) are indicated.*

Infrared spectroscopy

Additional confirmation of successful synthesis was provided via IR spectroscopic analysis. Compound **10** produced noticeable peaks for ν(N-H) and ν(C=C) at 3364 and 1606 cm^{-1}, respectively. Lastly, an intense absorption peak for the quinolinyl C=N bond at 1570 cm^{-1} was observed for compound **11**.

Mass Spectrometry

Both compounds **10** and **11**,were analysed by ESI-MS. With regard to compound **10**, a base peak of *m/z* 304.0771 $[M+H]^+$ was observed. This closely matched the calculated mass of 304.0700. Lastly, the molecular mass of compound **11** was confirmed by the presence of a base peak at *m/z* 465.0822 $[M+H]^+$, corresponding to the calculated mass of 465.0700 for the protonated molecular ion.

3.5. Antileishmanial activity assessment of compounds *in vitro*

3.5.1. Preparation of L. major LV39 promastigotes

Virulent promastigotes were obtained for biological experiments by passaging *L. major* LV39 (MRHO/SV/59/P) parasites in BALB/c mice via hind footpad infection, as described previously. [35,36] The progress of the infection was monitored weekly for eight weeks by measuring the swelling of infected footpads. As illustrated in **Figure 3.25A**, BALB/c mice showed an onset of swelling at week 3 post-infection, and the swelling continued to rise until the eighth week, in line with previous findings. [37–39] The weights of the mice also stayed consistent throughout the infection period (**Figure 3.25B**). At eight weeks post-infection, a parasite suspension was extracted from infected footpads and subsequently cultured in M199 growth medium to allow for transformation into their promastigote form.

The *in vitro* growth of *Leishmania* promastigotes is characterised by two growth phases, which are the logarithmic phase and the stationary phase. [40] In the logarithmic phase, the promastigotes divide rapidly but are not infective towards mammalian cells. This logarithmic growth continues until they reach the stationary phase, where the parasites are in their most virulent state and do not divide. [40–42] After the parasites obtained from infected mice had differentiated into promastigotes, they were then cultured in fresh growth medium to grow them to their most infective state and in sufficient numbers for further experiments. The number of parasites was counted daily to monitor their growth, and as shown in **Figure 3.26**, the parasites underwent logarithmic growth during the first four days post-culture. The growth rate slowed down on Day 5, reaching a plateau on Day 6, thus signifying that the promastigotes had reached the stationary phase. [40]

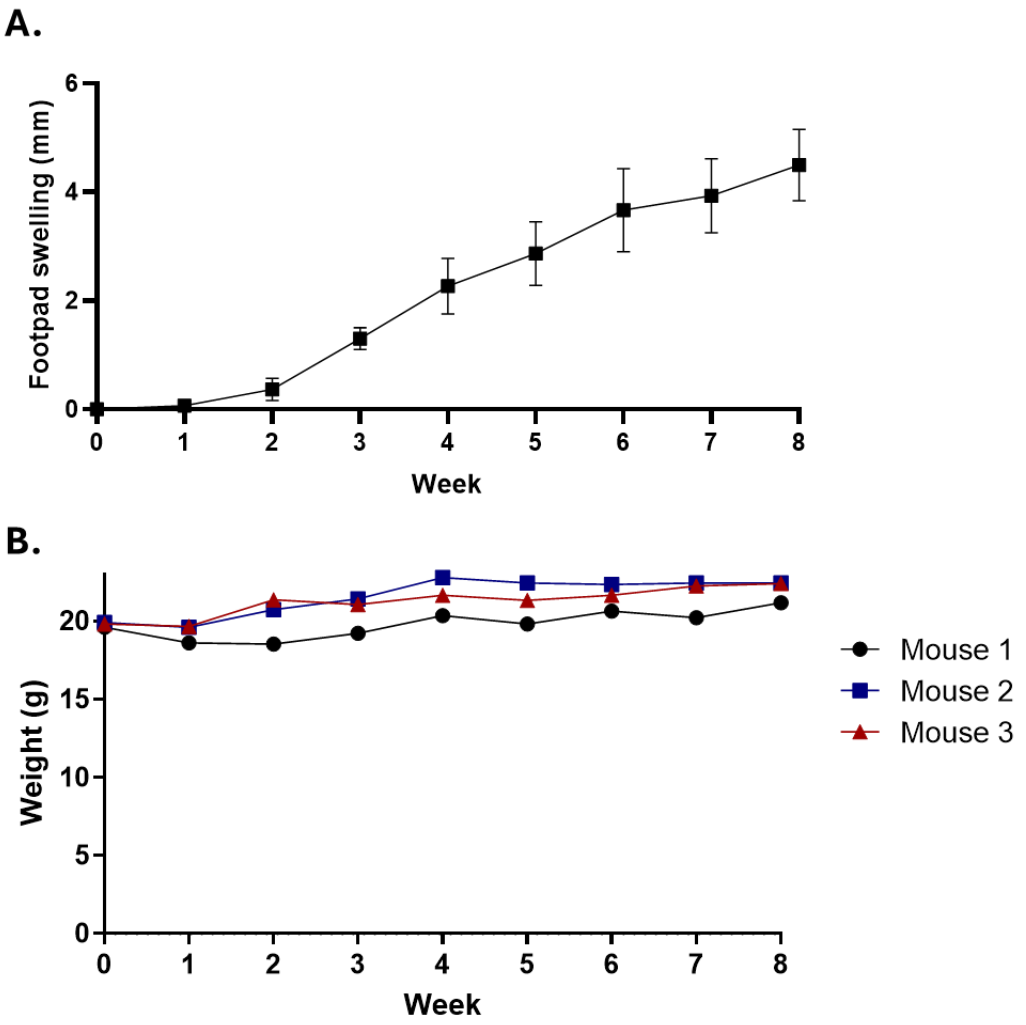

***Figure 3.25**: Progression of L. major infection in BALB/c mice. BALB/c mice were infected with 2 x 10^6 stationary phase L. major LV39 promastigotes by subcutaneous injection in the hind footpad. (A) Swelling of infected footpads measured weekly for eight weeks to monitor infection progress relative to pre-infection footpad sizes. Footpad swelling data is expressed as the mean ± SD of three animals (n=3). (B) Body weights of infected mice measured weekly for eight weeks.*

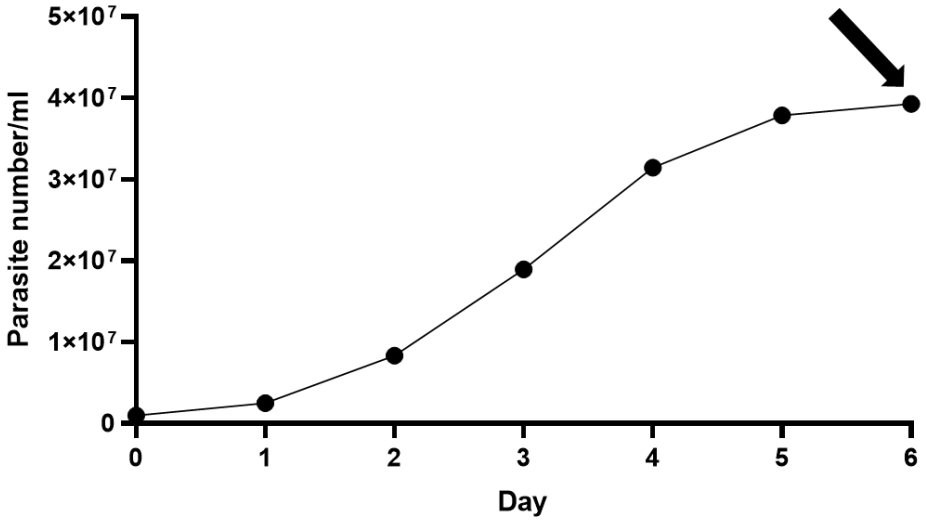

Figure 3.26: *Growth of L. major LV39 promastigotes. Promastigotes were cultured at 1 x 10^6 parasites/ml in complete M199 at 26 °C, with the number of parasites counted daily to monitor growth. The black arrow indicates the peak of the stationary phase on Day 6.*

3.5.2. Antipromastigote activity assay

The successfully synthesised ferrocenyl-quinoline compounds (**2**, **3**, **6** and **11**) and their precursors (**1**, **4**, **5**, **9** and **10**) (**Figure 3.27**) were taken forward for biological testing against *L. major* LV39 promastigotes. In order to determine the half-maximal inhibitory concentration (IC_{50}), which is the concentration of a compound required to inhibit parasite growth by 50%, [43] the compounds were solubilised in 100% DMSO and diluted in complete M199. DMSO is commonly the solvent of choice for dissolving compounds prior to biological testing to improve their solubility in water-based media, particularly the solubility of hydrophobic compounds. [44–46] All the compounds were soluble in DMSO except compound **9**. Compound **9** was partially soluble in the solvent, which led to some of it precipitating out of solution upon dilution in the culture medium. Other organic solvents like ethanol and acetone can be used as alternatives to improve the solubility of hydrophobic compounds for biological testing. [44] Unfortunately, however, compound **9** is completely insoluble in both ethanol and acetone, as evidenced by its synthesis and purification procedure (Chapter 2, *Section 2.2.9*), making it impossible to use these solvents in biological tests. This compound was, therefore, tested as a suspension, as has been done with other poorly soluble compounds in some previous studies. [7,20] Furthermore, compound **9** was included in the assay to compare it with the other quinolinyl precursors (*i.e.*, compounds **1** and **4**), even though it was ultimately not used to synthesise compound **11**.

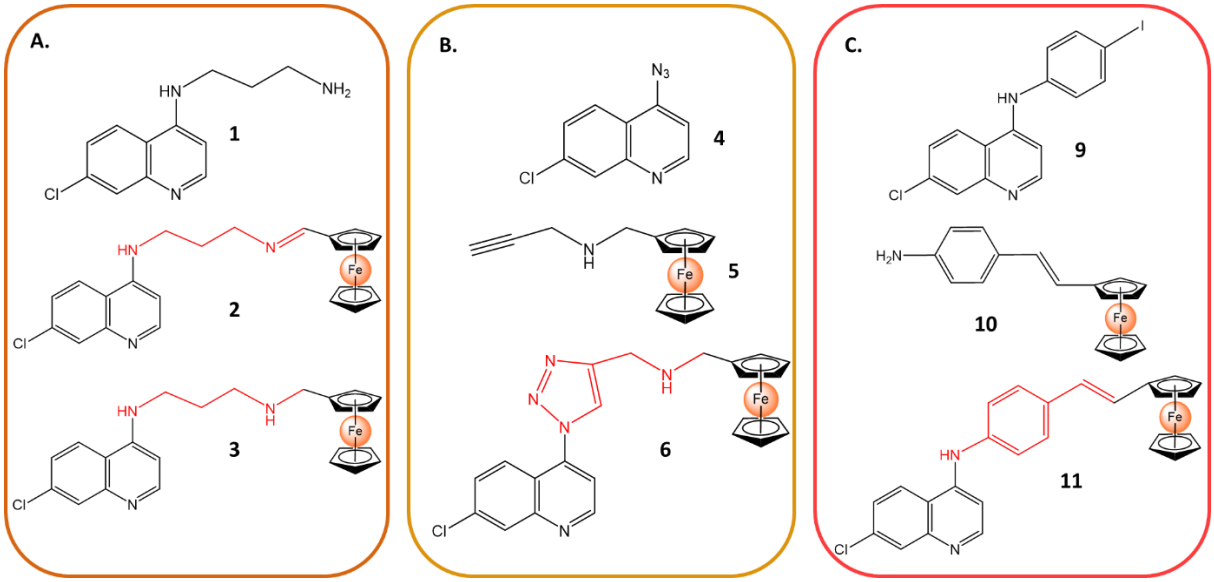

***Figure 3.27**: Structures of synthesised ferrocenyl-quinoline compounds and precursors selected for biological assessment. Compounds in each grouping were synthesised via either nucleophilic aromatic substitution, Schiff base condensation or Mizoroki-Heck coupling, ultimately leading to the formation of a ferrocenyl-quinoline compound with a distinct linker. (A) The imino-alkyl (**2**) and amino-alkyl-linked (**3**) ferrocenyl-quinoline compounds and their common amino-alkyl quinoline precursor (**1**); (B) The triazole amine-linked ferrocenyl-quinoline compound (**6**) and its azido quinoline (**4**) and ferrocenyl amino alkyne (**5**) precursors; (C) The phenyl-alkene-linked ferrocenyl-quinoline compound (**11**) and its iodo-phenyl quinoline (**9**) and ferrocenyl phenylamine (**10**) precursors. Linker regions are highlighted in red.*

Amphotericin B (AmpB), which is one of the drugs currently available as a second-line treatment for leishmaniasis, [47–49] was selected as the positive control based on previous studies that have also used the drug. [3,50,51] Pentavalent antimonials drugs and miltefosine have also been used as control drugs in similar studies. [4,52,53] The choice of control drug for studies such as this one varies across literature and appears to be determined by the availability of the drug, the parasite species/strain being studied, as well as the manifestation of leishmaniasis being investigated. DMSO was included as a vehicle control matching the percentage of DMSO in the diluted compounds.

The viability of the promastigotes was measured using a resazurin-based assay, as described in published literature. [3,54] Resazurin is a blue non-toxic dye that turns pink and fluoresces when reduced to resorufin by metabolically active cells. [54–56] The fluorescence produced by resorufin can be measured quantitatively and gives an indication of the number of viable cells. In the context of studies investigating the activity of compounds against *Leishmania* parasites, a high fluorescence relative to untreated controls signifies a high number of viable parasites (*i.e.*, low compound activity), while a low fluorescence indicates low numbers or the absence of viable parasites (*i.e.*, high compound activity).

Initial experiments were performed using a concentration range of 0.08 – 10 µg/ml for all compounds based on various reported IC_{50} values of AmpB that fall within this range. [3,50,51,57] However, as **Figure 3.28** shows, only AmpB, compound **3** and compound **6** showed activity in this range, prompting the use of a higher concentration range of 0.8 – 100 µg/ml for compounds **1**, **2**, **4**, **5**, **9**, **10** and **11** in later experiments in order to determine their IC_{50} values.

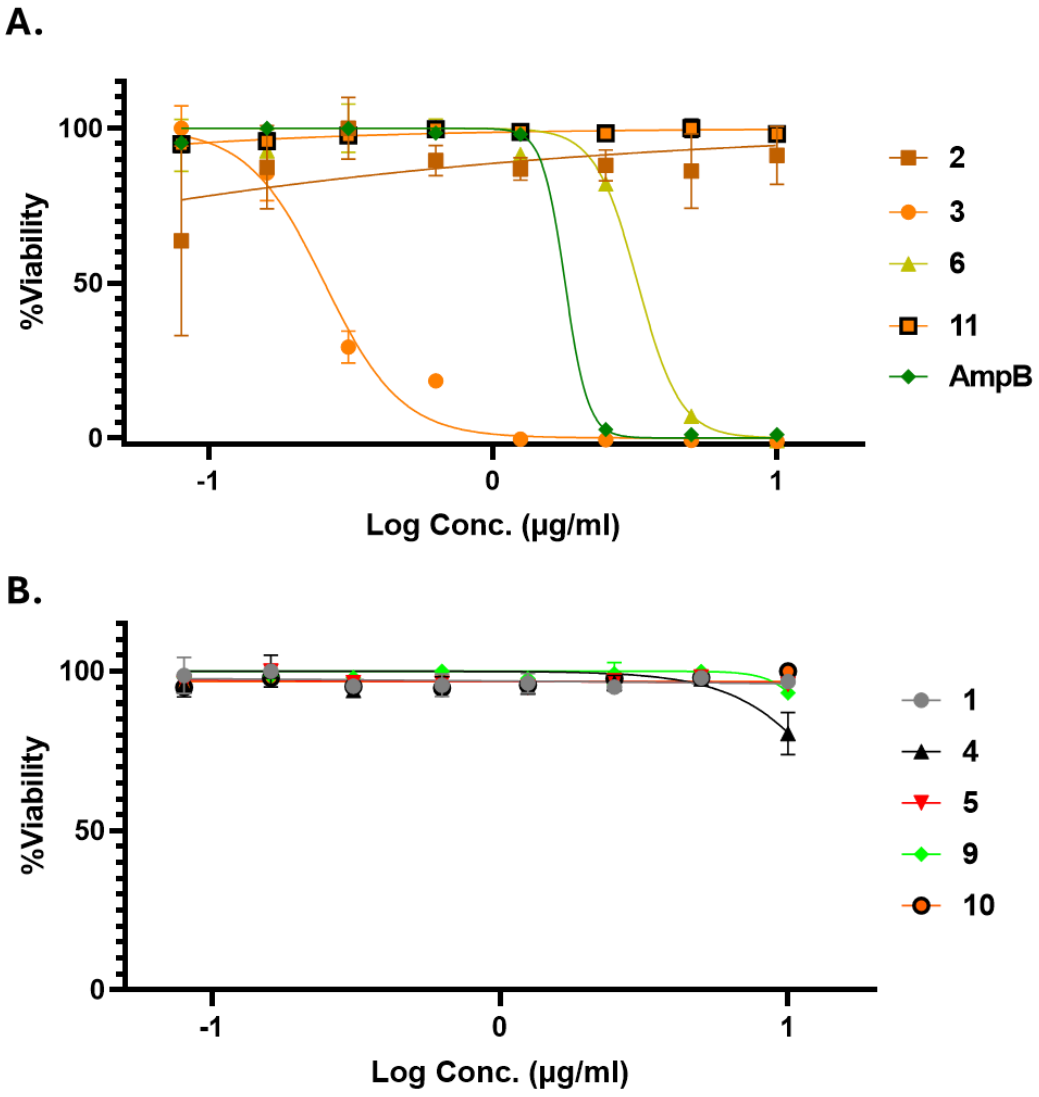

***Figure 3.28**: Antipromastigote assay dose-response curves for ferrocenyl-quinoline compounds and precursors. 2.5 x 10^6 stationary phase L. major LV39 promastigotes were treated with either the synthesised compounds or amphotericin B (AmpB) increasing concentrations over 48 hours. (A) Dose-response curves for ferrocenyl-quinoline compounds (**2**, **3**, **6** and **11**) and AmpB tested at 0.08 – 10 µg/ml; (B) Dose-response curves for precursor compounds **1**, **4**, **5**, **9** and **10** tested at 0.08 – 10 µg/ml. Parasite viability was calculated as a percentage relative to untreated controls using a resazurin-based assay. Data is representative of a single preliminary experiment that was performed in triplicate (n = 3).*

As illustrated by the dose-response curves in **Figure 3.29** and the data in **Table 3.3**, the amino-alkyl-linked ferrocenyl-quinoline compound (**3**) was the most biologically active in the series, giving an IC_{50} of 0.50 µg/ml (1.16 µM). It was more active than the control drug amphotericin B, which had an IC_{50} of 1.94 µg/ml (2.10 µM). The other ferrocenyl-quinoline compounds (**6**, **2** and **11**) followed with IC_{50} values of 4.04, 30.00 and 40.10 µg/ml (8.83, 69.49 and 86.27 µM), respectively.

***Table 3.3**: Antileishmanial activity of ferrocenyl-quinoline compounds and precursors against L. major LV39 promastigotes. IC_{50} values are expressed in both µg/ml and µM units and reported as the mean ± SD of two independent experiments that were performed in triplicate (n=6).*

Compound	IC_{50} (µg/ml)	IC_{50} (µM)
1	80.25 ± 9.69	340.45 ± 29.06
2	30.00 ± 3.82	69.49 ± 6.25
3	0.50 ± 0.35	1.16 ± 0.57
4	37.65 ± 22.42	184.00 ± 77.46
5	81.60 ± 17.82	322.37 ± 49.78
6	4.04 ± 1.13	8.83 ± 1.75
9	17.65 ± 0.35	46.37 ± 0.66
10	No activity*	No activity*
11	40.10 ± 4.81	86.27 ± 7.32
AmpB	1.94 ± 0.20	2.10 ± 0.15

**: No activity observed within the tested concentration range.*

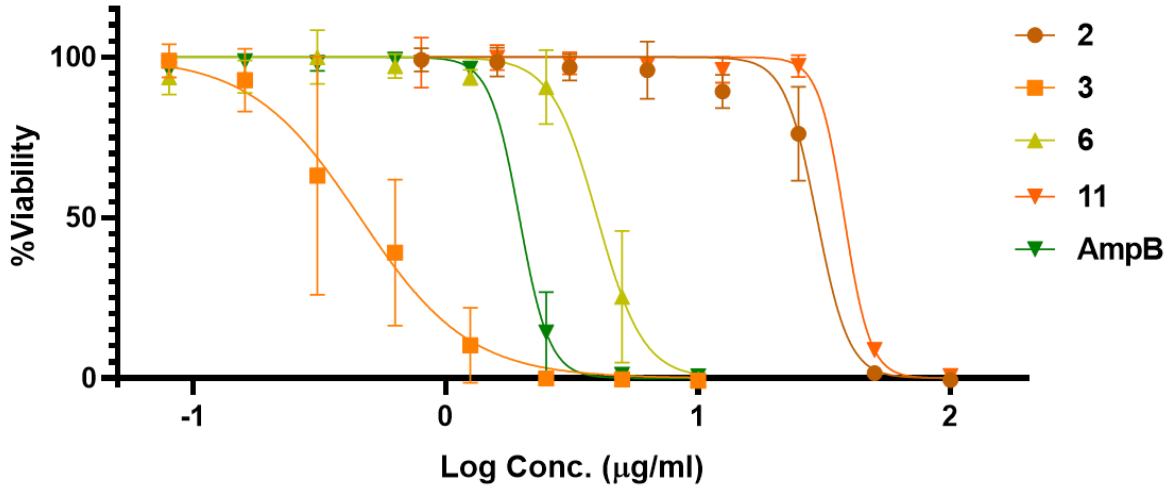

***Figure 3.29**: Antipromastigote assay dose-response curves for ferrocenyl-quinoline compounds. 2.5 x 10^6 stationary phase L. major LV39 promastigotes were treated with either the synthesised ferrocenyl-quinoline compounds (**2**, **3**, **6** and **11**) or amphotericin B (AmpB) in increasing concentrations over 48 hours. Compounds **3**, **6** and AmpB were tested at 0.08 – 10 µg/ml, while compounds **2** and **11** were tested at 0.8 – 100 µg/ml. Parasite viability was calculated as a percentage relative to untreated controls using a resazurin-based assay. Data represents a pool of two independent experiments that were each performed in triplicate (n = 6).*

Overall, these results show a structure-dependent trend in the antipromastigote activity of the four ferrocenyl-quinoline compounds (compound **3** (amino-alkyl) > compound **6** (triazole amine) > compound **2** (imino-alkyl) > compound **11** (phenyl-alkene)). Compound **3** has two secondary amines in its structure: one on the 4-position of the quinoline, and the other next to the ferrocene moiety. The secondary amine on the 4-position of the quinoline is substituted by a triazole group in compound **6**. This substitution resulted in an eight-fold difference between the IC_{50} values of the two compounds, suggesting that having a secondary amine at this position might be important for antipromastigote activity. However, there seems to be evidence indicating that the secondary amine adjacent to the ferrocene may be more important for antileishmanial activity when comparing compound **6** to a structural isomer synthesised by Yousuf *et al.*, which was also tested against *L. major* LV39 promastigotes and gave an IC_{50} of 21.80 µM. [6] The IC_{50} value of compound **6** (8.83 µM) is two and a half times lower than that of the isomer, making compound **6** the more potent of the two. When comparing the structures of the two compounds, it can be seen that the positions of the triazole group and secondary amine in their linkers are interchanged (**Figure 3.30**), and this difference in the positions of the functional groups may be responsible for the differences in their activity against *L. major* LV39 promastigotes. Yousuf *et al.* also reported on the ability of the isomer to alter promastigote morphology, disrupt mitochondrial membrane potential, reduce phospholipid content in the plasma

membrane and induce oxidative stress, all of which are factors that lead to promastigote apoptosis. [6] It may be possible that compound **6** induces the same effects as the isomer but to a greater extent. More investigations are necessary to confirm if this is the case.

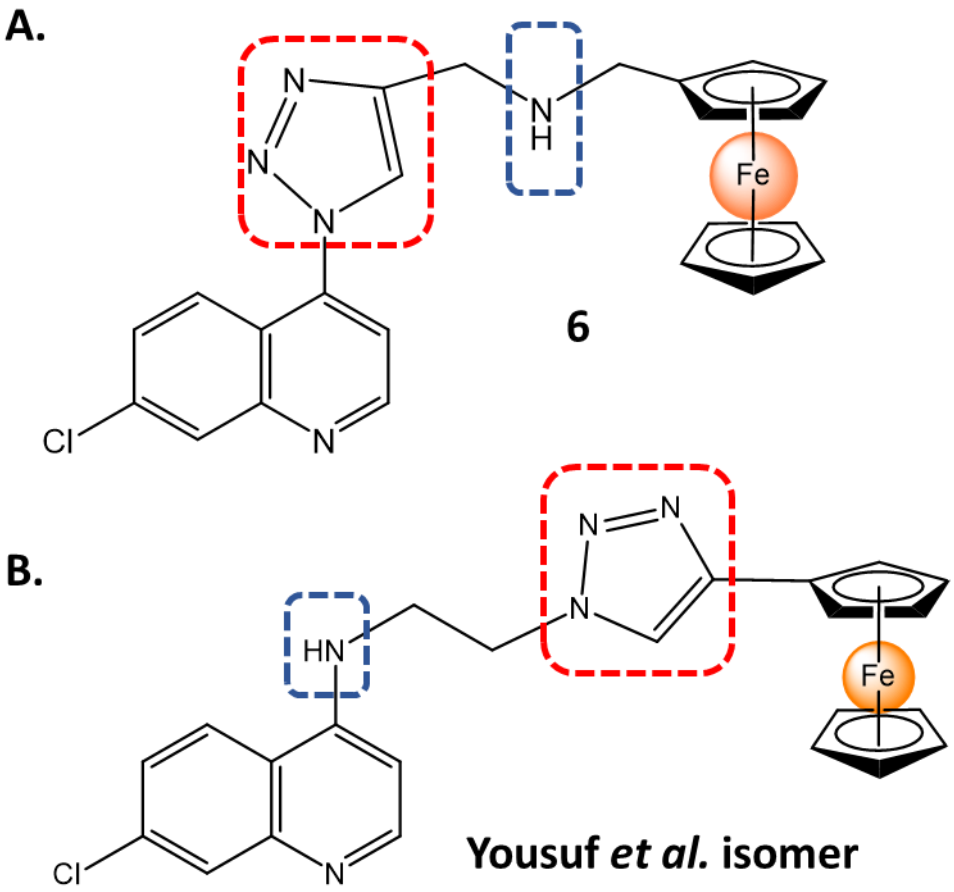

***Figure 3.30**: Structures of triazole amine-linked ferrocenyl-quinoline compounds. (A) Compound **6**, synthesised for this study; (B) The structural isomer synthesised by Yousuf et al. [6] The triazole group and secondary amine are indicated by red and blue rectangles, respectively.*

The difference in antileishmanial activity is more striking when comparing compound **3** and the third-most active compound (compound **2**). These two compounds are almost similar to each other structurally, with the sole difference being that compound **2** has an imine group instead of a secondary amine adjacent to the ferrocene moiety. Yet, this seemingly small change caused a 60-fold difference in antipromastigote activity. Both compounds were previously synthesised and reported as potential antimalarial agents by other researchers before being adopted for this study. [7,8] Stringer *et al*. reported IC_{50} values of 0.59 µM and 0.17 µM for compounds **2** and **3**, respectively, when the two compounds were tested against the K1 chloroquine-resistant strain of *P. falciparum*. [7] Similar to what has been

observed here, the substitution of the imine group for a secondary amine resulted in a 3.5-fold increase in antiparasitic activity. The authors also found that compound **3** exhibited greater growth inhibition of *T. vaginalis* parasites, the causative agents of trichomoniasis, than compound **2**. [7] However, no specific IC_{50} values were provided. Salas *et al.* reported compound **3** as being the most active against the K1 *P. falciparum* strain (IC_{50} = 0.016 µM) out of a series of various amino-alkyl-linked ferrocenyl-quinoline compounds. [8] These findings, therefore, further support the idea that having a secondary amine close to the ferrocene moiety is advantageous for improved antiparasitic activity. As this is the first study in which compounds **2** and **3** have been assessed in the context of leishmaniasis, the manner in which the compounds elicit their effects on *Leishmania* parasites remains unknown and requires additional investigation.

Compound **11** contains a secondary amine on the 4-position of the quinoline ring, like compound **3**. It also has a phenyl ring and an alkene bond linking the ferrocene moiety to the rest of the molecule. The presence of this phenyl-alkene linker in place of an amino-alkyl linker led to an 80-fold drop in activity relative to compound **3**. Earlier in this chapter (*Section 3.4.1*), the attempted synthesis of a phenyl-linked ferrocenyl-quinoline compound reported by N'Da and Smith was described. [25] This compound, which differs from compound **11** by having a secondary amine in place of the alkene, was tested for antimalarial activity by the aforementioned authors and was found to be highly active against *Plasmodium* parasites (IC_{50} = 0.96 µM). Additionally, the compound was less active than its alkyl-linked counterparts. [25] Once more, this suggests that the presence of a secondary amine adjacent to ferrocene induces high antiparasitic activity. It also supports the observation that having a phenyl linker is less favourable for antiparasitic activity.

The dose-response curves for the quinolinyl precursor compounds (**1**, **4** and **9**) and the ferrocenyl precursors (**5** and **10**) are shown in **Figure 3.31**. Compounds **1**, **4** and **9** inhibited the growth of *L. major* LV39 promastigotes, with respective IC_{50} values of 80.25, 37.65 and 17.65 µg/ml (340.45, 184.00 and 46.37 µM) (**Table 3.3**), confirming that the quinoline pharmacophore is important for antileishmanial activity, in line with previous studies. [51,52,58,59] Compound **5**, the ferrocenyl alkyne precursor of compound **6**, had an IC_{50} of 81.60 µg/ml (322.37 µM) (**Table 3.3**). In contrast to the rest of the series, compound **10**, the ferrocenyl precursor for compound **11**, had no activity in the tested concentration range.

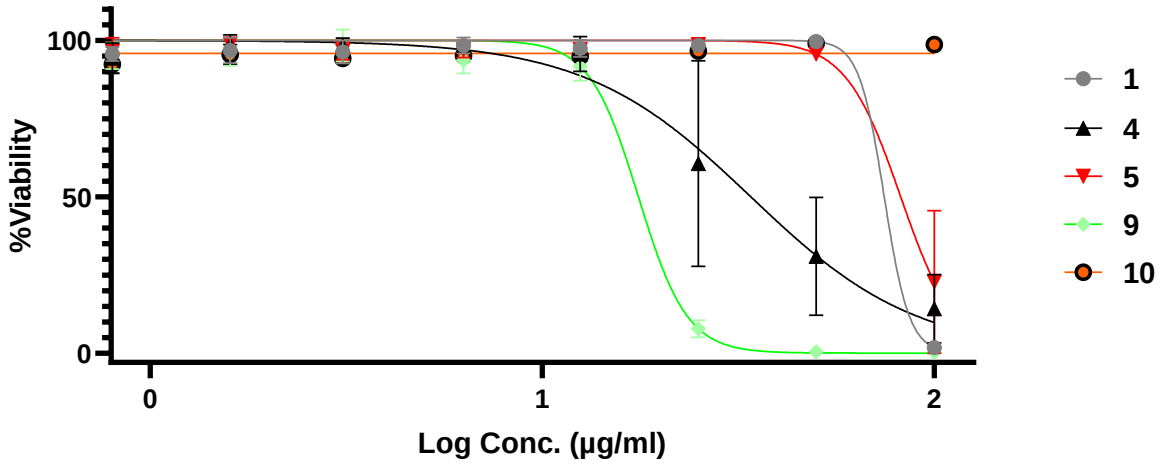

***Figure 3.31**: Antipromastigote assay dose-response curves for quinolinyl and ferrocenyl precursor compounds. 2.5 x 10^6 stationary phase L. major LV39 promastigotes were treated with either the quinolinyl precursor compounds (**1**, **4** and **9**) or the ferrocenyl precursor compounds (**5** and **10**) in increasing concentrations over 48 hours. All five compounds were tested at 0.8 – 100 µg/ml. Parasite viability was calculated as a percentage relative to untreated controls using a resazurin-based assay. Data represents a pool of two independent experiments that were each performed in triplicate (n = 6).*

The activity of the quinolinyl precursors appears to be dependent on the functional group/moiety attached to the scaffold (compound **9** (iodo-phenyl) > compound **4** (azido) > compound **1** (amino-alkyl)). Interestingly, despite its poor solubility, the iodo-phenyl compound **9** is seemingly the most active of the precursors and more potent than its derivative ferrocenyl-quinoline counterpart (*i.e.*, compound **11**). It is unclear if this high activity is due to the presence of iodine or a combination of the iodine and aromatic ring. To confirm this, it would also be worthwhile to investigate the activity of the previously described compound **7** (*Section 3.4.1*), which contains a primary amine in place of the iodine. However, it is important to note that the IC_{50} value of compound **9** may be viewed as an estimation given that the compound is partially soluble in DMSO and culture media. The azido-quinolinyl precursor (compound **4**) was the second-most active of the three, suggesting that the presence of the azide functional group induces higher antileishmanial activity than the amino-alkyl chain on compound **1**. Accordingly, compound **1** was the least active of the quinolinyl precursors. Additionally, it had an IC_{50} value much greater than that of its Schiff base derivative (compound **2**). Schiff bases/imines are prone to hydrolysis due to the Schiff base reaction being reversible. [11,60] If compound **2** was being hydrolysed into its original substituents upon dilution in aqueous media, it would have a similar IC_{50} value to that of compound **1**. As the IC_{50} values of the two compounds are vastly different from each other, this indicates that the observed activity of compound **2** is not due to its hydrolysis.

Of the two ferrocenyl precursors tested (compounds **5** and **10**), compound **5** was the only one that displayed signs of antipromastigote activity. The activity of compound **5** may be attributed to the amino alkyne chain or the ferrocene moiety itself. The latter seems more plausible given the ability of ferrocene to induce ROS production, which is known to cause cellular damage in parasites, including *Leishmania* parasites. [5,6,61–65] There are currently no reports of amino alkynes possessing antiparasitic properties. However, the activities of compound **5** and the quinolinyl precursor **4** appear to be enhanced when they react to form compound **6**, indicating a synergistic relationship between the two. There are also signs of enhanced activity when looking at the quinolinyl precursor **1**, whereby the addition of ferrocene via a reaction with the free primary amine resulted in the formation of compounds **2** and **3**, which have higher antipromastigote activity than the standalone precursor. To test if ferrocene is truly responsible for the enhanced activity of the quinolinyl precursors **1** and **4**, one could substitute the ferrocene moiety with another isosteric group, such as a phenyl group. This has been demonstrated previously in a study by Melis *et al*., who reported the enhanced antiplasmodial activity of a quinoline-based compound after substituting a phenyl group with ferrocene (phenyl compound IC_{50} = 22.73 µM; ferrocenyl compound IC_{50} = 12.30 µM). [20]

Two DMSO vehicle controls covering concentration ranges of 0.0008 – 0.1% and 0.008 – 1% were used to match the concentration of the solvent in the diluted compound solutions. These corresponded to the 0.08 – 10 µg/ml and 0.8 – 100 µg/ml compound concentration ranges, respectively. Both vehicle controls showed that DMSO had no effect on the viability of promastigotes (**Figure 3.32**). This is in line with the findings of Duran *et al.*, who determined that a DMSO concentration of up to 1% neither influences the growth of *L. tropica* and *L. infantum* promastigotes nor alters their morphology. [66] The study by Duffin and Andrews, which showed that the growth of *L. major*, *L. amazonensis* and *L. donovani* promastigotes was unaffected by 1% DMSO, also corroborates these findings. [67] The results shown here, therefore, confirm that the observed antipromastigote activity is not due to the toxic effects of DMSO.

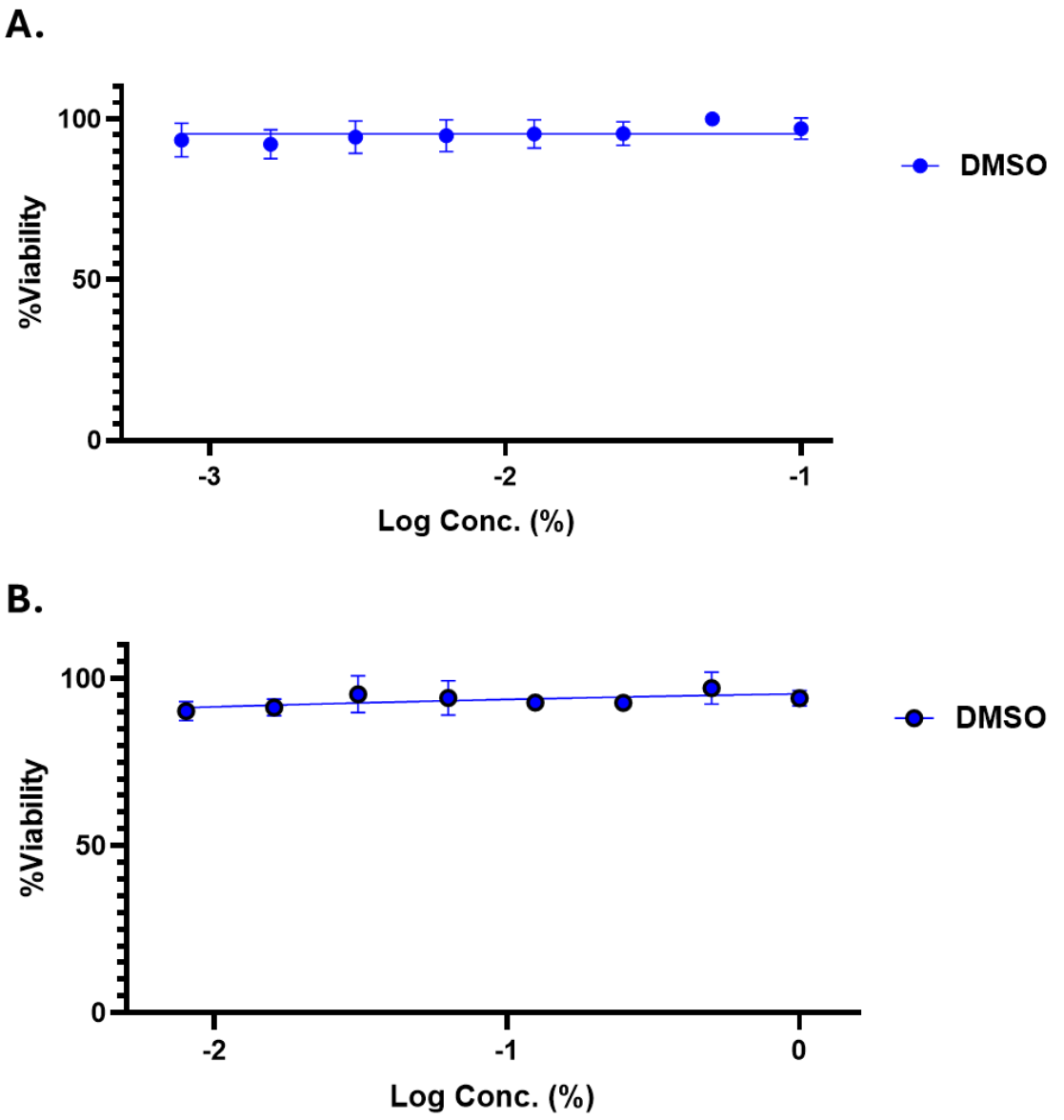

***Figure 3.32**: Antipromastigote assay dose-response curves for DMSO vehicle controls. 2.5 x 10^6 stationary phase L. major LV39 promastigotes were treated with DMSO in increasing concentrations over 48 hours. (A) DMSO vehicle control at 0.0008 – 0.1%; (B) DMSO vehicle control at 0.008 – 1%. Parasite viability was calculated as a percentage relative to untreated controls using a resazurin-based assay. Data represents a pool of two independent experiments that were each performed in triplicate (n = 6).*

3.6. *In vitro* cytotoxicity and selectivity assessment of compounds

3.6.1. Macrophage cell surface antigen expression in RAW 264.7 cell line

The RAW 264.7 macrophage cell line was selected in order to determine the cytotoxicity of the synthesised compounds *in vitro*. The *Leishmania* parasite primarily infects macrophages, which allows it to transform into its amastigote stage as part of its life cycle. [68,69] Therefore, measuring the cytotoxicity of the compounds against macrophages would give an indication of the concentration of compound required to potentially eliminate the intracellular parasite without harming the host cells.

RAW 264.7 cells are murine monocyte/macrophage-like cells derived from the Abelson leukaemia virus-transformed cell line from BALB/c mice. [70,71] They are commonly used as a reliable macrophage model for inflammation research and possess typical macrophage characteristics, such as phagocytosis, pinocytosis and nitric oxide production. [44,71,72] The cell line is also favoured for its rapid growth and ease of culture. [44] In the field of leishmaniasis research, RAW 264.7 cells have been used in infection studies. One such study by Saha *et al.* investigated the ability of *L. donovani* to suppress host oxidative burst during infection. [73] Another study investigated the apoptosis-inducing effects of microRNAs in *L. major*-infected RAW 264.7 cells. [74] The cells have also been used to determine the cytotoxicity of copper(II)-azole drug complexes and 4-quinolinyl thiosemicarbazone derivatives. [75,76] This, therefore, made RAW 264.7 cells a suitable model for this study.

RAW 264.7 cells were cultured and continuously passaged, according to previously described methods with slight modifications. [70,72] The cells were then analysed by flow cytometry to verify the expression of CD11b and F4/80, which are known murine macrophage cell surface antigens. [77–79] Populations of single cells were gated to identify cells expressing CD11b and F4/80. On average, 83.7% of the cells were double-positive for CD11b and F4/80 across three samples (**Figure 3.33A**). The geometric mean fluorescence intensity (GMFI) of $CD11b^+$ $F4/80^+$ cells was also analysed as a measure of surface antigen expression on a cell-per-cell basis relative to unstained controls, and the expression levels of CD11b were found to be slightly higher than those of F4/80 (**Figure 3.33B**). These results are consistent with those in published studies investigating cell surface antigen expression in this cell line. [80,81] Having confirmed that the RAW 264.7 cells expressed a macrophage phenotype, they were then used to assess the cytotoxicity of the ferrocenyl-quinoline compounds and their precursors.

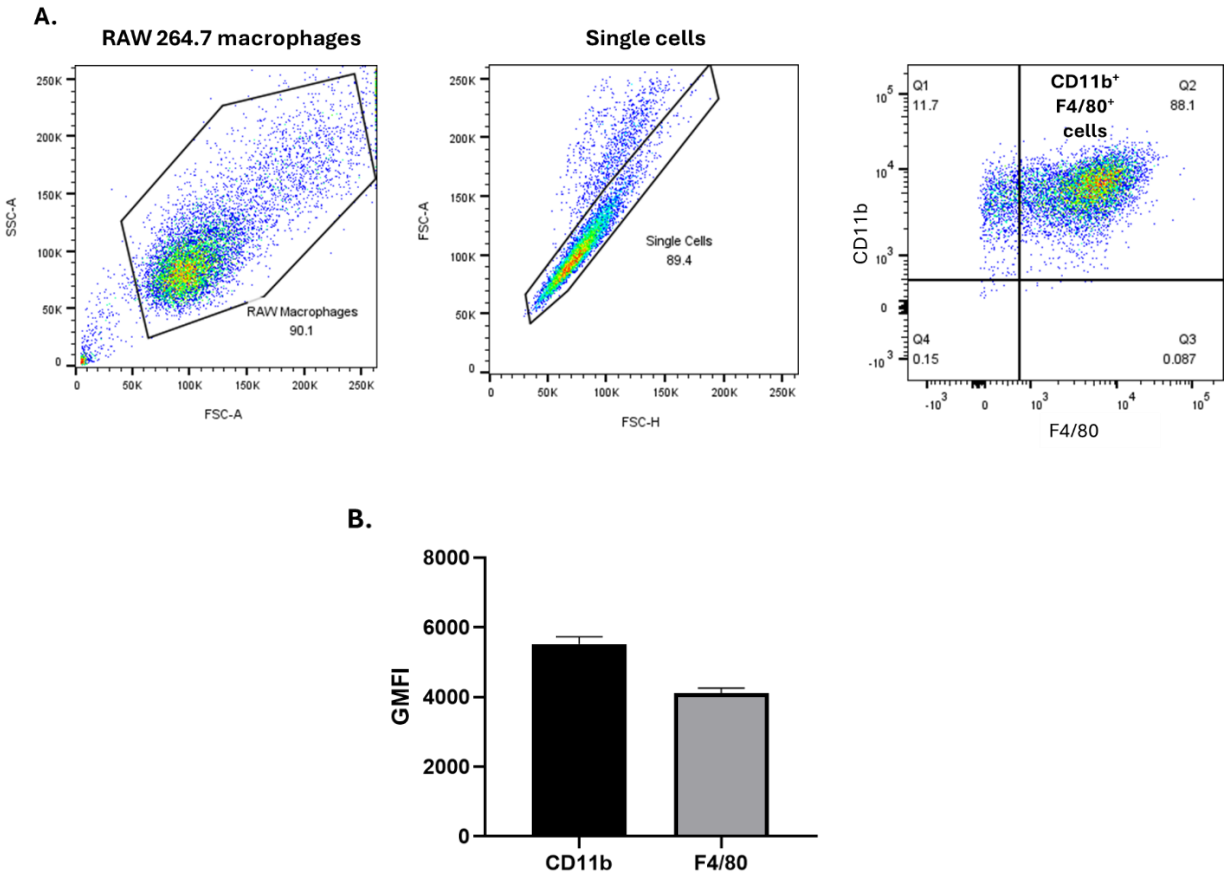

***Figure 3.33**: Flow cytometry analysis of CD11b and F4/80 expression in RAW 264.7 macrophages. RAW 264.7 cells were cultured over three days and then stained with fluorescent mouse antibodies for CD11b and F4/80 for flow cytometry analysis. (A) Cells gated for single cell populations expressing CD11b and F4/80; (B) Geometric mean fluorescence intensity (GMFI) of CD11b and F4/80 expression in CD11b⁺ F4/80⁺ populations. The analysis shown is representative of a single experiment consisting of three replicates, with the GMFI expressed as the mean ± SD.*

3.6.2. Cytotoxicity assay and compound selectivity

To test the cytotoxicity of compounds **1** – **11** in RAW 264.7 macrophages, the compounds were once again dissolved in 100% DMSO and diluted in complete DMEM, with AmpB included as the control drug. As before, all the compounds were soluble in DMSO except compound **9**, which was tested as a suspension because of its poor solubility in the culture medium. As was done for the antipromastigote assessments, a resazurin-based assay was used to measure the viability of the macrophages, following literature methods. [3,54] The compound concentration range was restricted to 0.4 – 50 µg/ml, corresponding to a DMSO concentration range of 0.004 – 0.5%. This restriction was placed to eliminate the influence of DMSO on cell viability since concentrations higher than 0.5% have been reported to be cytotoxic to RAW 264.7 cells. [44,72]

The half-maximal cytotoxic concentration (CC_{50}), which is the concentration of a compound that reduces cell viability by 50%, [82] was determined for all the tested compounds. The CC_{50} values of each compound were then used to calculate the selectivity index (SI). The SI is the ratio of the CC_{50} value to the IC_{50} value, which measures how selective a compound is toward parasitic cells rather than mammalian cells. [83] Compounds with a selectivity index of greater than 1 are considered to be more selective towards *Leishmania* parasites than mammalian cells and, therefore, can be regarded as potential antileishmanial agents. [84,85]

Figure 3.34 shows the changes in the macrophage viability in response to treatment with the four ferrocenyl-quinoline compounds (**2**, **3**, **6** and **11**) and AmpB. Compounds **3** and **6** were the most cytotoxic, giving CC_{50} values of 0.86 µg/ml (1.98 µM) and 8.55 µg/ml (18.67 µM), respectively (**Table 3.4**). These two compounds were also the most biologically active against *L. major* promastigotes (*Section 3.5.2*). Furthermore, they were the only compounds in the entire series with selectivity indices greater than 1 (compound **3** SI = 1.71; compound **6** SI = 2.11), indicating that they are more selective toward the parasites and are, therefore, candidate choices for subsequent testing in an *in vivo* model. The third-most cytotoxic ferrocenyl quinoline compound was compound **2** with a CC_{50} of 10.47 µg/ml (24.25 µM), closely followed by compound **11** with a CC_{50} of 13.00 µg/ml (27.97 µM) (**Table 3.4**). It should be noted that compound **3** was tested at a lower range of 0.2 – 25 µg/ml in order to generate a more accurate dose-response curve, as a preliminary experiment revealed that there were not enough data points in the lower end of the 0.4 – 50 µg/ml range to form a reliable curve (**Figure 3.35**).

***Table 3.4**: Cytotoxicity and selectivity of ferrocenyl-quinoline compounds and precursors. CC_{50} and IC_{50} values are expressed in both µg/ml and µM units and reported as the mean ± SD of two independent experiments that were performed in triplicate (n = 6).*

Compound	CC_{50} (RAW 264.7)		IC_{50} (*L. major* LV39 promastigote)		SI [a]
	µg/ml	µM	µg/ml	µM	
1	7.20 ± 0.16	30.55 ± 0.66	80.25 ± 9.69	340.45 ± 29.06	0.09
2	10.47 ± 5.13	24.25 ± 11.89	30.00 ± 3.82	69.49 ± 6.25	0.35
3	0.86 ± 0.06	1.98 ± 0.15	0.50 ± 0.35	1.16 ± 0.57	1.71
4	8.70 ± 0.42	42.49 ± 2.04	37.65 ± 22.42	184.00 ± 77.46	0.23
5	41.95 ± 6.43	165.73 ± 25.42	81.60 ± 17.82	322.37 ± 49.78	0.52
6	8.55 ± 0.80	18.67 ± 1.75	4.04 ± 1.13	8.83 ± 1.75	2.11
9	13.00 ± 0.14	34.15 ± 0.37	17.65 ± 0.35	46.37 ± 0.66	0.74
10	11.74 ± 3.20	38.71 ± 10.57	No activity [b]	No activity [b]	ND [c]
11	13.00 ± 1.84	27.97 ± 3.96	40.10 ± 4.81	86.27 ± 7.32	0.32
AmpB	> 50	> 54	1.94 ± 0.20	2.10 ± 0.15	> 25

[a]: Selectivity Index (CC_{50}/IC_{50}).

[b]: No activity observed within the tested concentration range.

[c]: Not determined.

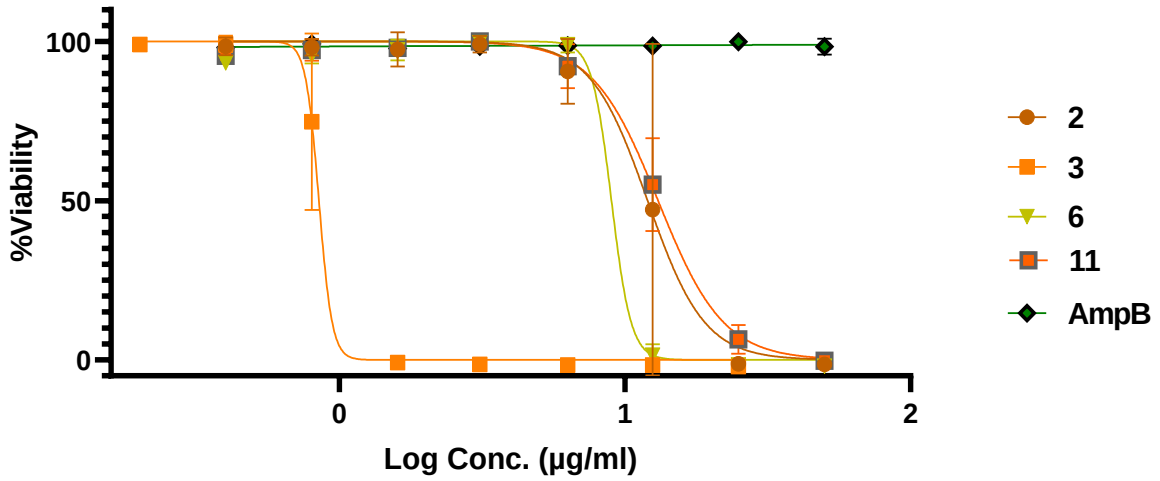

***Figure 3.34**: Cytotoxicity assay dose-response curves for ferrocenyl-quinoline compounds. 2 x 10^4 RAW 264.7 macrophages were treated with either the synthesised ferrocenyl-quinoline compounds (**2**, **3**, **6** and **11**) or amphotericin B (AmpB) in increasing concentrations over 48 hours. Compound **3** was tested at 0.2 – 25 µg/ml, while the rest of the compounds were tested at 0.4 – 50 µg/ml. Cell viability was calculated as a percentage relative to untreated controls using a resazurin-based assay. Data represents a pool of two independent experiments that were each performed in triplicate (n = 6).*

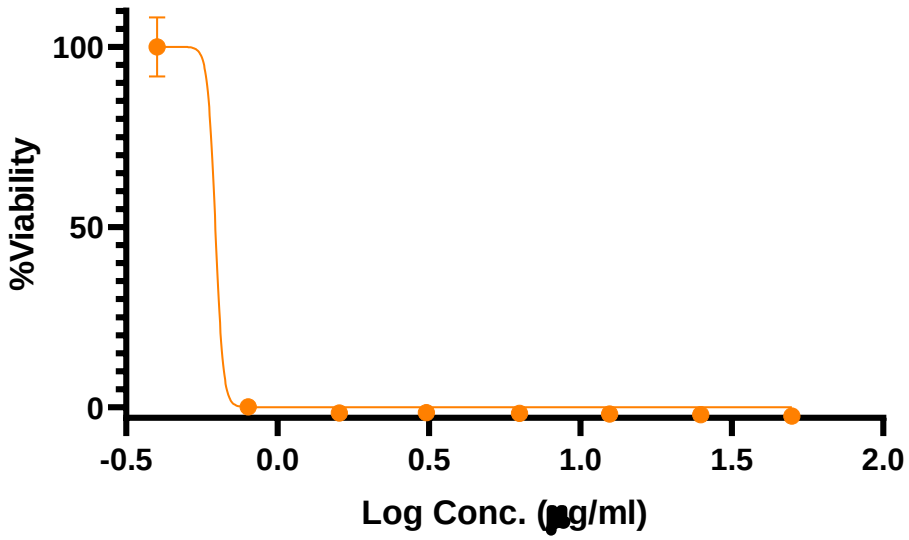

Figure 3.35: *Cytotoxicity assay dose-response curve for compound **3**. 2 x 10^4 RAW 264.7 macrophages were treated with compound **3** in increasing concentrations (0.4 – 50 µg/ml) over 48 hours. Cell viability was calculated as a percentage relative to untreated controls using a resazurin-based assay. Data represents a single preliminary experiment that was performed in triplicate (n = 3).*

As was observed for the antipromastigote activity, the cytotoxicity of the ferrocenyl-quinoline compounds (**2**, **3**, **6** and **11**) appears to be dependent on the type of linker in their structures. The cytotoxicity of these four compounds followed the same trend as the antipromastigote activity (compound **3** (amino-alkyl) > compound **6** (triazole amine) > compound **2** (imino-alkyl) > compound **11** (phenyl-alkene)). The presence of two secondary amines in compound **3**, particularly the one next to the ferrocene moiety, seems to contribute to its high cytotoxicity, considering that it was 12 times more cytotoxic than its imine counterpart (compound **2**). A similar result was observed when these two compounds were assessed for their antimalarial activity by Stringer *et al*. [7] Compound **3** was eight times more cytotoxic than compound **2** to oesophageal cancer cells (compound **3** CC_{50} = 0.74 µM; compound **2** CC_{50} = 5.80 µM). However, compound **3** had a lower selectivity than compound **2** towards both chloroquine-sensitive and chloroquine-resistant *Plasmodium* parasites (compound **3** SI = 11.56 & 4.23; compound **2** SI = 69.88 & 9.83), which is in contrast to the findings presented here. [7] In the context of this current study, however, compound **3** is more selective than compound **2**, making it a more promising antileishmanial drug candidate for further study.

Compound **6**, containing a triazole group on the 4-position of the quinoline instead of a secondary amine, was ten times less cytotoxic than compound **3**. This further supports the observation that the

secondary amine induces higher biological activity, and substitution with the triazole group at the 4-position leads to an overall drop in activity. Compound **6**, however, was more cytotoxic than the previously mentioned structural isomer synthesised by Yousuf *et al*. [6] The isomer was reported as having no observable cytotoxicity against murine splenocytes at the highest tested concentration of 22 µM. [6] This again implies that the positioning of the triazole group and secondary amine influences the biological activity of the compound. Nevertheless, compound **6** is the most selective of all the tested compounds in this present study, making it the most favourable potential antileishmanial agent.

Once again, compound **11** was the least active of the ferrocenyl-quinoline series, showing a 15-fold difference in cytotoxicity relative to compound **3**. The previously mentioned phenyl-linked compound synthesised by N'Da and Smith, which only differs from compound **11** by the presence of a secondary amine instead of an alkene, was also reported to be less cytotoxic to Chinese hamster ovarian cells than alkyl-linked compounds. [25] Therefore, similar to the observation made on the antipromastigote activity, the substitution of the amino-alkyl linker with a phenyl-alkene linker appears to reduce overall compound activity.

The cytotoxicity of amphotericin B could not be definitively determined due to the limitations imposed by the DMSO concentration stated earlier. Therefore, for this study, it was estimated to be above 50 µg/ml (54 µM), resulting in an estimated SI of above 25. However, Wu *et al*. reported a CC_{50} value of 6.18 µg/ml when they tested amphotericin B in RAW 264.7 cells. [86] In another study by Malli *et al.*, the CC_{50} value of the drug in the same cell line was reported as 16.07 µg/ml, [87] while a CC_{50} of 11.07 µg/ml was reported by Garcia *et al*. [88] Malli *et al.* state that they prepared their own amphotericin B deoxycholate suspension by mixing amphotericin B and sodium deoxycholate for their study. [87] Meanwhile, the amphotericin B used by Garcia *et al.* and Wu *et al.* was sourced commercially, and the latter specify that they used HPLC-purified amphotericin B from *Streptomyces sp*. [86,88] The amphotericin B used in this present study, which is a colloidal suspension of the drug in sodium deoxycholate, sodium chloride and sodium phosphate, was also sourced commercially. [89] Therefore, the disparity in the reported cytotoxicity of amphotericin B may be due to the differences in the preparation or formulation of the drug used in each study. Further studies will need to be conducted to determine if this is the case.

The dose-response curves for the quinolinyl precursor compounds (**1**, **4** and **9**) and ferrocenyl precursor compounds (**5** and **10**) are shown in **Figure 3.36**. The quinolinyl precursor compounds **1**, **4** and **9** had cytotoxicity values of 7.20, 8.70 and 13.00 µg/ml (30.55, 42.49 and 34.15 µM), respectively (**Table 3.4**). The least cytotoxic compound in the whole series was the ferrocenyl precursor compound **5**, giving a CC_{50} of 41.95 µg/ml (165.73 µM). Compound **10**, the other ferrocenyl precursor compound,

had a CC_{50} of 11.74 µg/ml (38.71 µM) (**Table 3.4**), which was in stark contrast to its lack of antipromastigote activity.

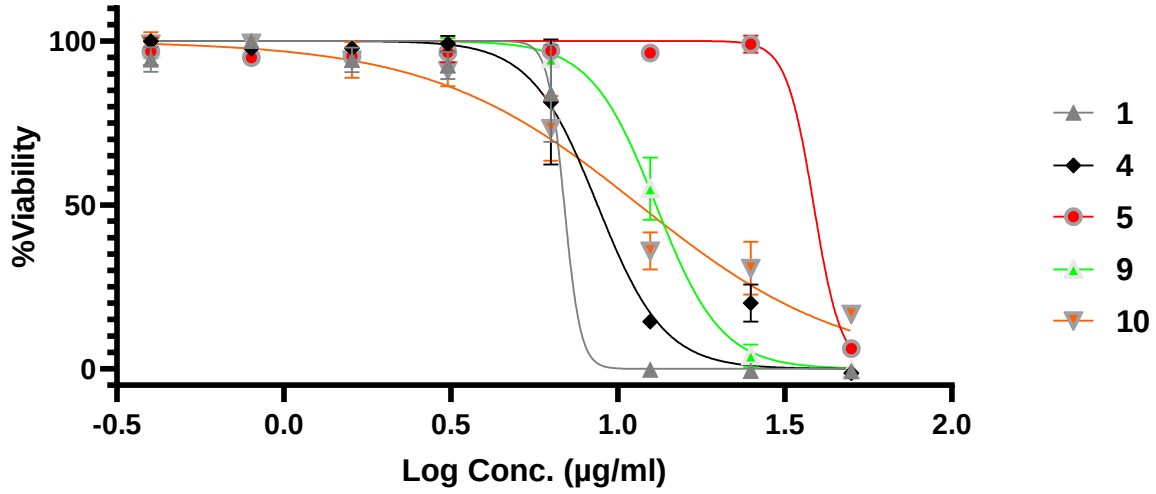

***Figure 3.36**: Cytotoxicity assay dose-response curves for quinolinyl and ferrocenyl precursor compounds. 2 x 10^4 RAW 264.7 macrophages were treated with either the quinolinyl precursor compounds (**1**, **4** and **9**) or the ferrocenyl precursor compounds (**5** and **10**) in increasing concentrations over 48 hours. All five compounds were tested at 0.4 – 50 µg/ml. Cell viability was calculated as a percentage relative to untreated controls using a resazurin-based assay. Data represents a pool of two independent experiments that were each performed in triplicate (n = 6).*

The quinolinyl precursor compounds **1**, **4** and **9** showed a different trend to that observed for their antipromastigote activity (compound **1** (amino-alkyl) > compound **9** (iodophenyl) > compound **4** (azido)). The micromolar CC_{50} values of these quinolinyl precursors were higher than those of their respective ferrocenyl-quinoline derivatives (*i.e.*, compounds **2**, **3**, **6** and **11**), implying that the incorporation of ferrocene leads to increased cytotoxicity. This is particularly noticeable with compound **6**, which is the product of a reaction between compound **4** and the ferrocenyl precursor compound **5**. Furthermore, compound **5** also had a higher CC_{50} value than compound **6**. As these two precursors form a compound with a relatively much lower CC_{50} value, this not only suggests that the incorporation of ferrocene increases cytotoxicity but also provides further evidence that the precursors have synergy with each other.

The DMSO vehicle control that was included in the cytotoxicity assay showed that macrophage viability was unaffected by DMSO concentrations between 0.004 and 0.5% (**Figure 3.37**). This confirms that the cytotoxicity data obtained in this study is solely due to the inherent properties of the tested compounds. Moreover, it validates the findings of Jamalzadeh *et al.* and Han *et al.*, who recommended concentrations lower than 0.5% for the RAW 264.7 cell line. [44,72]

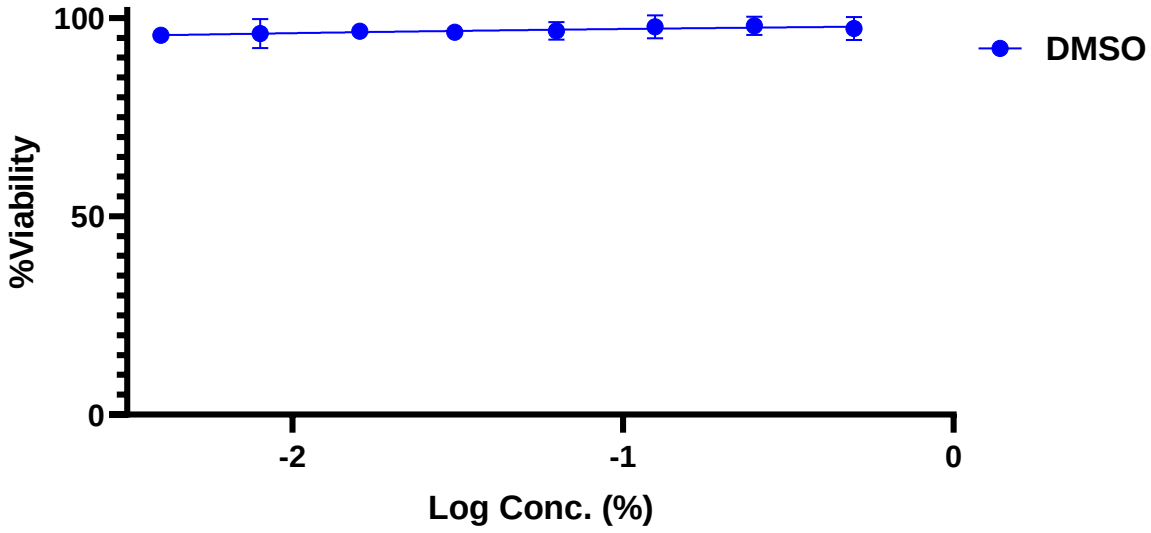

***Figure 3.37**: Cytotoxicity assay dose-response curve for DMSO vehicle control. 2 x 10^4 RAW 264.7 macrophages were treated with DMSO in increasing concentrations (0.004 – 0.5%) over 48 hours. Cell viability was calculated as a percentage relative to untreated controls using a resazurin-based assay. Data represents a pool of two independent experiments that were each performed in triplicate (n = 6).*

3.7. Summary

A series of four ferrocenyl-quinoline compounds (**2**, **3**, **6** and **11**) were synthesised for use as potential antileishmanial drug leads. Compounds **2** and **3** have been previously reported as antimalarial agents, while compounds **6** and **11** are new. These four compounds were derived from a set of various quinoline-based precursor compounds (**1**, **4** and **9**) and ferrocene-based precursor compounds (**5** and **10**), resulting in the four compounds having either an imino-alkyl, amino-alkyl, triazole amine or phenyl-alkene linker. All the compounds were fully characterised using standard spectroscopic and analytical techniques, including ^{1}H and $^{13}C\{^{1}H\}$ NMR spectroscopy, FT-IR spectroscopy and mass spectrometry.

Compound **1**, the diaminopropyl quinoline precursor compound, was synthesised via nucleophilic aromatic substitution and was subsequently used to synthesise the imino-alkyl-linked (**2**) and amino-alkyl-linked (**3**) ferrocenyl-quinoline compounds via Schiff base condensation, with an additional reduction step required to form compound **3**. The azido quinoline precursor compound (**4**) and ferrocenyl alkyne precursor compound (**5**) were synthesised via nucleophilic aromatic substitution and Schiff base condensation (followed by reduction), respectively. The triazole amine-linked ferrocenyl-quinoline compound (**6**) was then formed via a Cu(I)-catalysed azide-alkyne cycloaddition reaction using these two precursors. The iodophenyl quinoline precursor compound (**9**), generated by nucleophilic aromatic substitution, could not be used to synthesise the phenyl-alkene-linked ferrocenyl-quinoline compound (**11**). This prompted the synthesis of the ferrocenyl phenyl alkene compound (**10**) via Mizoroki-Heck coupling as an alternative precursor, which finally led to the successful synthesis of compound **11** by nucleophilic aromatic substitution.

The four ferrocenyl-quinoline compounds and their precursors were assessed for their *in vitro* biological activity against *L. major* LV39 promastigotes. The most active ferrocenyl-quinoline compound was compound **3** (IC_{50} = 0.50 µg/ml), followed by compounds **6**, **2** and **11**. Compound **3** was the only compound in the series with an IC_{50} lower than that of the control drug amphotericin B (IC_{50} = 1.94 µg/ml). The trend in the antipromastigote activities of these compounds appears to be influenced by the linker structure as well as the presence and positioning of secondary amines, with the amino-alkyl and triazole amine linkers inducing the highest activity. The quinolinyl precursor compounds (**1**, **4** and **9**) were also biologically active against the parasite, thus confirming the antiparasitic properties of the quinoline pharmacophore. Compounds **1** and **4** were less active than their ferrocenyl-quinoline derivatives, suggesting that the incorporation of ferrocene leads to enhanced antileishmanial activity. However, the opposite effect was observed for compound **9** as it showed higher activity than its derivative. The ferrocenyl precursors (**5** and **10**) had the lowest antipromastigote activity of all the synthesised compounds.

The RAW 264.7 macrophage cell line was used to determine the cytotoxicity of the synthesised compounds. The expression of CD11b and F4/80 macrophage cell surface antigens in this cell line was confirmed by flow cytometry analysis prior to cytotoxicity assessments. All the synthesised compounds were found to be more cytotoxic than amphotericin B (CC_{50} < 50 µg/ml). The cytotoxicities of the four ferrocenyl-quinoline compounds followed the same structure-dependent/functional group-dependent trend as their antipromastigote activities (compound **3** > compounds **6** > compound **2** > compound **11**) Despite being the two most cytotoxic compounds in the series, compounds **3** and **6** were determined to be the most selective toward the *Leishmania* parasite as their SI values were greater than 1 (SI = 1.71 and 2.11) . Finally, all three of the quinolinyl precursors (**1**, **4** and **9**) were less

cytotoxic than their ferrocenyl-quinoline derivatives, implying that the incorporation of ferrocene also results in increased cytotoxicity.

References

1 J. Howarth and K. Hanlon, N-ferrocenylmethyl, N'-methyl-2-substituted benzimidazolium iodide salts with in vitro activity against the Leishmania infantum parasite strain L1, *Bioorganic and Medicinal Chemistry Letters*, 2003, **13**, 2017–2020.

2 N. C. S. Costa, J. P. Piccoli, N. A. Santos-Filho, L. C. Clementino, A. M. Fusco-Almeida, S. R. De Annunzio, C. R. Fontana, J. B. M. Verga, S. F. Eto, J. M. Pizauro-Junior, M. A. S. Graminha and E. M. Cilli, Antimicrobial activity of RP-1 peptide conjugate with ferrocene group, *PLoS ONE*, 2020, **15**, 1–22.

3 J. Möller, C. Kannigadu, J. Aucamp, M. C. Joseph, A. J. Swarts and D. D. N'Da, Synthesis, electrochemistry, and in vitro antileishmanial efficacy of novel ferrocenylazines, *Applied Organometallic Chemistry*, 2023, **37**, 1–13.

4 S. Quintal, T. S. Morais, C. P. Matos, M. Paula Robalo, M. F. M. Piedade, M. J. Villa De Brito, M. Helena Garcia, M. Marques, C. Maia, L. Campino and J. Madureira, Synthesis, structural characterization and leishmanicidal activity evaluation of ferrocenyl N-heterocyclic compounds, *Journal of Organometallic Chemistry*, 2013, **745**–**746**, 299–311.

5 M. Yousuf, D. Mukherjee, S. Dey, C. Pal and S. Adhikari, Antileishmanial ferrocenylquinoline derivatives: Synthesis and biological evaluation against Leishmania donovani, *European Journal of Medicinal Chemistry*, 2016, **124**, 468–479.

6 M. Yousuf, D. Mukherjee, A. Pal, S. Dey, S. Mandal, C. Pal and S. Adhikari, Synthesis and biological evaluation of ferrocenylquinoline as a potential antileishmanial agent, *ChemMedChem*, 2015, **10**, 546–554.

7 T. Stringer, C. De Kock, H. Guzgay, J. Okombo, J. Liu, S. Kanetake, J. Kim, C. Tam, L. W. Cheng, P. J. Smith, D. T. Hendricks, K. M. Land, T. J. Egan and G. S. Smith, Mono- and multimeric ferrocene congeners of quinoline-based polyamines as potential antiparasitics, *Dalton Transactions*, 2016, **45**, 13415–13426.

8 P. F. Salas, C. Herrmann, J. F. Cawthray, C. Nimphius, A. Kenkel, J. Chen, C. de Kock, P. J. Smith, B. O. Patrick, M. J. Adam and C. Orvig, Structural Characteristics of Chloroquine-Bridged

Ferrocenophane Analogues of Ferroquine May Obviate Malaria Drug-Resistance Mechanisms, *Journal of Medicinal Chemistry*, 2013, **56**, 1596–1613.

9 C. C. Musonda, S. Little, V. Yardley and K. Chibale, Application of multicomponent reactions to antimalarial drug discovery. Part 3: Discovery of aminoxazole 4-aminoquinolines with potent antiplasmodial activity in vitro, *Bioorganic and Medicinal Chemistry Letters*, 2007, **17**, 4733–4736.

10 P. Sykes, *A Guidebook to Mechanisms in Organic Chemistry*, Longman Group, Ltd., 6th edn., 1986.

11 N. T. Subasi, in *Schiff Base in Organic, Inorganic and Physical Chemistry*, ed. T. Akitsu, IntechOpen, 2022.

12 R. Denton and I. Day, in *Organic Chemist's Desk Reference*, CRC Press, 3rd edn., 2017, p. 16.

13 A. Bainbridge and J. C. Lindon, in *Reference Module in Chemistry, Molecular Sciences and Chemical Engineering*, Elsevier, 2018, pp. 293–303.

14 M. Kaliva and M. Vamvakaki, in *Polymer Science and Nanotechnology*, Elsevier, 2020, pp. 401–433.

15 R. Ikan and B. Crammer, in *Encyclopedia of Physical Science and Technology*, Elsevier, 2003, pp. 459–496.

16 M. B. Eyring, in *Encyclopedia of Physical Science and Technology*, Elsevier, 2003, pp. 637–643.

17 E. M. Guantai, K. Ncokazi, T. J. Egan, J. Gut, P. J. Rosenthal, P. J. Smith and K. Chibale, Design, synthesis and in vitro antimalarial evaluation of triazole-linked chalcone and dienone hybrid compounds, *Bioorganic and Medicinal Chemistry*, 2010, **18**, 8243–8256.

18 C. C. Albertyn, A. van Niekerk, S. Duffy, V. M. Avery, E. Strauss and P. Chellan, Investigation of bioorganometallic artemisinins as antiplasmodials, *Journal of Organometallic Chemistry*, 2023, **987**–**988**, 122633.

19 A. Anand, R. Kumar, J. Maity and V. K. Maikhuri, Recent progress in the Cu-catalyzed multicomponent synthesis of 1,4-disubstituted 1,2,3-triazoles, *Synthetic Communications*, 2023, **53**, 345–375.

20 D. R. Melis, C. B. Barnett, L. Wiesner, E. Nordlander and G. S. Smith, Quinoline-triazole half-sandwich iridium(iii) complexes: Synthesis, antiplasmodial activity and preliminary transfer hydrogenation studies, *Dalton Transactions*, 2020, **49**, 11543–11555.

21 K. Padmalatha, D. Vijaya Durga and K. Sandhya Rani, A review on 2D NMR spectroscopy, *Indo American Journal of Pharmaceutical Sciences*, 2020, **07**, 366–371.

22 R. M. Silverstein, F. X. Webster and D. Kiemle, *Spectrometric Identification of Organic Compounds*, Wiley, 7th edn., 2005.

23 K. V. Sashidhara, M. Kumar, R. K. Modukuri, R. K. Srivastava, A. Soni, K. Srivastava, S. V. Singh, J. K. Saxena, H. M. Gauniyal and S. K. Puri, Antiplasmodial activity of novel keto-enamine chalcone-chloroquine based hybrid pharmacophores, *Bioorganic and Medicinal Chemistry*, 2012, **20**, 2971–2981.

24 N. N. Omosun and G. S. Smith, Monometallic and bimetallic sulfonated Rh(I) complexes: Synthesis and evaluation as recyclable hydroformylation catalysts, *Journal of Organometallic Chemistry*, 2021, **951**, 122022.

25 D. D. N'Da and P. J. Smith, Synthesis, in vitro antiplasmodial and antiproliferative activities of a series of quinoline-ferrocene hybrids, *Medicinal Chemistry Research*, 2014, **23**, 1214–1224.

26 A. A. El Gokha, I. M. S. Ghanim, A. El, S. A. Megeed, E. Shaban, I. El-Tantawy and E. Sayed, Synthesis and antibacterial activity of novel α-aminophosphonates bearing a quinoline moiety, *International Journal of Pharmaceutical Sciences and Research*, 2016, **7**, 181.

27 R. Arancibia, A. H. Klahn, G. E. Buono-Core, E. Gutierrez-Puebla, A. Monge, M. E. Medina, C. Olea-Azar, J. D. Maya and F. Godoy, Synthesis, characterization and anti-Trypanosoma cruzi evaluation of ferrocenyl and cyrhetrenyl imines derived from 5-nitrofurane, *Journal of Organometallic Chemistry*, 2011, **696**, 3238–3244.

28 A. S. Ressurreição, D. Gonçalves, A. R. Sitoe, I. S. Albuquerque, J. Gut, A. Góis, L. M. Gonçalves, M. R. Bronze, T. Hanscheid, G. A. Biagini, P. J. Rosenthal, M. Prudeîncio, P. O'Neill, M. M. Mota, F. Lopes and R. Moreira, Structural optimization of quinolon-4(1 H)-imines as dual-stage antimalarials: Toward increased potency and metabolic stability, *Journal of Medicinal Chemistry*, 2013, **56**, 7679–7690.

29 I. P. Beletskaya and A. V. Cheprakov, Heck reaction as a sharpening stone of palladium catalysis, *Chemical Reviews*, 2000, **100**, 3009–3066.

30 A. Koranne, S. Turakhia, V. K. Jha, S. Gupta, R. Ravi, A. Mishra, A. K. Aggarwal, C. K. Jha, N. Dheer and A. K. Jha, The Mizoroki-Heck reaction between in situ generated alkenes and aryl halides: cross-coupling route to substituted olefins, *RSC Advances*, 2023, **13**, 22512–22528.

31 P. Govender, H. Lemmerhirt, A. T. Hutton, B. Therrien, P. J. Bednarski and G. S. Smith, First- and

Second-Generation Heterometallic Dendrimers Containing Ferrocenyl–Ruthenium(II)–Arene Motifs: Synthesis, Structure, Electrochemistry, and Preliminary Cell Proliferation Studies, *Organometallics*, 2014, **33**, 5535–5545.

32 K. Kanagaraj and K. Pitchumani, The aminocyclodextrin/Pd(OAc)2 complex as an efficient catalyst for the Mizoroki-Heck cross-coupling reaction, *Chemistry - A European Journal*, 2013, **19**, 14425–14431.

33 S. Toma, A. Gaplovsky and P. Elecko, Synthesis and electronic spectra of 1-aryl-2-ferrocenylethylenes, *Chemical Papers*, 1985, **39**, 115–124.

34 M. Balci, in *Basic 1H- and 13C-NMR Spectroscopy*, Elsevier Science, 2005, pp. 87–133.

35 B. O. Osero, Z. Cele, R. T. Aruleba, R. A. Maine, M. Ozturk, M. B. Lutz, F. Brombacher and R. Hurdayal, Interleukin-4 responsive dendritic cells are dispensable to host resistance against Leishmania mexicana infection, *Frontiers in Immunology*, 2022, **12**, 1–15.

36 R. Hurdayal, N. E. Nieuwenhuizen, R. Khutlang and F. Brombacher, Inflammatory Dendritic Cells, Regulated by IL-4 Receptor Alpha Signaling, Control Replication, and Dissemination of Leishmania major in Mice, *Frontiers in Cellular and Infection Microbiology*, 2020, **9**, 1–15.

37 R. Hurdayal, N. E. Nieuwenhuizen, M. Revaz-Breton, L. Smith, J. C. Hoving, S. P. Parihar, B. Reizis and F. Brombacher, Deletion of IL-4 receptor alpha on dendritic cells renders BALB/c mice hypersusceptible to Leishmania major infection, *PLoS Pathogens*, 2013, **9**, 11–14.

38 S. P. Parihar, M. A. Hartley, R. Hurdayal, R. Guler and F. Brombacher, Topical simvastatin as host-directed therapy against severity of cutaneous leishmaniasis in mice, *Scientific Reports*, 2016, **6**, 1–10.

39 M. Mohrs, B. Ledermann, G. Köhler, A. Dorfmüller, A. Gessner and F. Brombacher, Differences between IL-4- and IL-4 receptor α-deficient mice in chronic leishmaniasis reveal a protective role for IL-13 receptor signaling, *The Journal of Immunology*, 1999, **162**, 7302–7308.

40 G. Van Zandbergen, A. Bollinger, A. Wenzel, S. Kamhawi, R. Voll, M. Klinger, A. Müller, C. Hölscher, M. Herrmann, D. Sacks, W. Solbach and T. Laskay, Leishmania disease development depends on the presence of apoptotic promastigotes in the virulent inoculum, *Proceedings of the National Academy of Sciences of the United States of America*, 2006, **103**, 13837–13842.

41 R. da Silva and D. L. Sacks, Metacyclogenesis is a major determinant of Leishmania promastigote virulence and attenuation., *Infection and immunity*, 1987, **55**, 2802–6.

42 M. Arjmand, A. Madrakian, G. Khalili, A. Najafi Dastnaee, Z. Zamani and Z. Akbari, Metabolomics-based study of logarithmic and stationary phases of promastigotes in Leishmania major by 1H NMR spectroscopy., *Iranian biomedical journal*, 2016, **20**, 77–83.

43 D. C. Swinney, in *Annual Reports in Medicinal Chemistry*, ed. J. E. Macor, Academic Press, 2011, vol. 46, pp. 301–317.

44 L. Jamalzadeh, H. Ghafoori, R. Sariri, H. Rabuti, J. Nasirzade, H. Hasani and M. R. Aghamaali, Cytotoxic effects of some common organic solvents on MCF-7, RAW-264.7 and human umbilical vein endothelial cells, *Avicenna Journal of Medical Biochemistry*, 2016, **4**, 10–33453.

45 J. Liu, H. Zhang, L. Zhang, T. Li, N. Liu and Q. Liu, Effect of various concentrations of common organic solvents on the growth and proliferation ability of Candida glabrata and their permissible limits for addition in drug susceptibility testing, *PeerJ*, 2023, **11**, e16444.

46 G. Dyrda, E. Boniewska-Bernacka, D. Man, K. Barchiewicz and R. Słota, The effect of organic solvents on selected microorganisms and model liposome membrane, *Molecular Biology Reports*, 2019, **46**, 3225–3232.

47 A. C. Pinheiro and M. V. N. de Souza, Current leishmaniasis drug discovery, *RSC Medicinal Chemistry*, 2022, **13**, 1029–1043.

48 F. Frézard, M. M. G. Aguiar, L. A. M. Ferreira, G. S. Ramos, T. T. Santos, G. S. M. Borges, V. M. R. Vallejos and H. L. O. De Morais, Liposomal Amphotericin B for Treatment of Leishmaniasis: From the Identification of Critical Physicochemical Attributes to the Design of Effective Topical and Oral Formulations, *Pharmaceutics*, 2022, **15**, 99.

49 S. Sundar and J. Chakravarty, Liposomal amphotericin B and leishmaniasis: Dose and response, *Journal of Global Infectious Diseases*, 2010, **2**, 159.

50 A. Badirzadeh, M. Heidari-Kharaji, V. Fallah-Omrani, H. Dabiri, A. Araghi and A. Salimi Chirani, Antileishmanial activity of Urtica dioica extract against zoonotic cutaneous leishmaniasis, *PLOS Neglected Tropical Diseases*, 2020, **14**, e0007843.

51 E. Torres Suarez, D. S. Granados-Falla, S. M. Robledo, J. Murillo, Y. Upegui and G. Delgado, Antileishmanial activity of synthetic analogs of the naturally occurring quinolone alkaloid N-methyl-8-methoxyflindersin, *PLOS ONE*, 2020, **15**, e0243392.

52 A. Sabt, W. M. Eldehna, T. M. Ibrahim, A. A. Bekhit and R. Z. Batran, New antileishmanial quinoline linked isatin derivatives targeting DHFR-TS and PTR1: Design, synthesis, and molecular modeling studies, *European Journal of Medicinal Chemistry*, 2023, **246**, 114959.

53 R. de M. V. Meira, S. L. da S. Gomes, E. Schaeffer, T. Da Silva, A. C. de S. Brito, L. M. Siqueira, J. D. Inácio, E. E. Almeida-Amaral, A. M. Da-Cruz, M. Bezerra-Paiva, R. H. Neves, L. S. Rodrigues, P. M. L. Dutra, P. R. R. Costa, A. J. M. da Silva and S. A. G. Da-Silva, Low doses of 3-phenyl-lawsone or meglumine antimoniate delivery by tattooing route are successful in reducing parasite load in cutaneous lesions of Leishmania (Viannia) braziliensis-infected hamsters, *Frontiers in Cellular and Infection Microbiology*, 2023, **13**, 1–14.

54 A. Kulshrestha, V. Bhandari, R. Mukhopadhyay, V. Ramesh, S. Sundar, L. Maes, J. C. Dujardin, S. Roy and P. Salotra, Validation of a simple resazurin-based promastigote assay for the routine monitoring of miltefosine susceptibility in clinical isolates of Leishmania donovani, *Parasitology Research*, 2013, **112**, 825–828.

55 J. L. Allen, S. J. Kennedy and L. N. Shaw, in *Antimicrobial Peptides*, ed. L. Hicks, Elsevier Inc., 1st edn., 2022, vol. 663, pp. 131–156.

56 D. M. Schmitt, D. M. O'Dee, B. N. Cowan, J. W. M. Birch, L. K. Mazzella, G. J. Nau and J. Horzempa, The use of resazurin as a novel antimicrobial agent against Francisella tularensis, *Frontiers in Cellular and Infection Microbiology*, 2013, **3**, 1–6.

57 V. Yardley and S. L. Croft, Activity of liposomal amphotericin B against experimental cutaneous leishmaniasis, *Antimicrobial Agents and Chemotherapy*, 1997, **41**, 752–756.

58 P. Yadav and K. Shah, Quinolines, a perpetual, multipurpose scaffold in medicinal chemistry, *Bioorganic Chemistry*, 2021, **109**, 104639.

59 S. Katiyar, K. Ramalingam, A. Kumar, A. Ansari, A. C. Bisen, G. Mishra, S. N. Sanap, R. S. Bhatta, B. Purkait, N. Goyal and K. V. Sashidhara, Design, synthesis, and biological evaluation of quinoline-piperazine/pyrrolidine derivatives as possible antileishmanial agents, *European Journal of Medicinal Chemistry*, 2023, **261**, 115863.

60 J. J. Alcázar, N. Geue, V. Valladares, A. Cañete, E. G. Pérez, L. García-Río, J. G. Santos and M. E. Aliaga, Supramolecular control of reactivity toward hydrolysis of 7-diethylaminocoumarin Schiff bases by cucurbit[7]uril encapsulation, *ACS Omega*, 2021, **6**, 10333–10342.

61 S. Peter and B. A. Aderibigbe, Ferrocene-based compounds with antimalaria/anticancer activity, *Molecules*, 2019, **24**, 3604.

62 Y. Na, J. S. Lee, J. Woo, S. Ahn, E. Lee, W. Il Choi and D. Sung, Reactive oxygen species (ROS)-responsive ferrocene-polymer-based nanoparticles for controlled release of drugs, *Journal of Materials Chemistry B*, 2020, **8**, 1906–1913.

63 M. Navarro, C. Gabbiani, L. Messori and D. Gambino, Metal-based drugs for malaria, trypanosomiasis and leishmaniasis: Recent achievements and perspectives, *Drug Discovery Today*, 2010, **15**, 1070–1078.

64 D. Gambino and L. Otero, Design of prospective antiparasitic metal-based compounds including selected organometallic cores, *Inorganica Chimica Acta*, 2018, **472**, 58–75.

65 B. S. Ludwig, S. Tomassi, S. Di Maro, F. S. Di Leva, A. Benge, F. Reichart, M. Nieberler, F. E. Kühn, H. Kessler, L. Marinelli, U. Reuning and S. Kossatz, The organometallic ferrocene exhibits amplified anti-tumor activity by targeted delivery via highly selective ligands to αvβ3, αvβ6, or α5β1 integrins, *Biomaterials*, 2021, **271**, 120754.

66 N. Duran, M. Muz, G. Culha, G. Duran and B. Ozer, GC-MS analysis and antileishmanial activities of two Turkish propolis types, *Parasitology Research*, 2011, **108**, 95–105.

67 R. N. Duffin and P. C. Andrews, Structure-activity effects in the anti-leishmanial activity of di-alkyl gallium quinolin-8-olates, *Dalton Transactions*, 2023, **52**, 15848–15858.

68 D. Liu and J. E. Uzonna, The early interaction of Leishmania with macrophages and dendritic cells and its influence on the host immune response., *Frontiers in cellular and infection microbiology*, 2012, **2**, 83.

69 M. Rossi and N. Fasel, How to master the host immune system? Leishmania parasites have the solutions!, *International Immunology*, 2018, **30**, 103–111.

70 T. T. Lucy, A. N. M. Mamun-Or-Rashid, M. Yagi and Y. Yonei, Serial passaging of RAW 264.7 cells modulates intracellular AGE formation and downregulates RANKL-induced in vitro osteoclastogenesis, *International Journal of Molecular Sciences*, 2022, **23**, 2371.

71 B. Taciak, M. Białasek, A. Braniewska, Z. Sas, P. Sawicka, Ł. Kiraga, T. Rygiel and M. Król, Evaluation of phenotypic and functional stability of RAW 264.7 cell line through serial passages, *PLoS ONE*, 2018, **13**, 1–13.

72 H. Han, J.-K. Kang, K. J. Ahn and C.-G. Hyun, DMSO alleviates LPS-induced inflammatory responses in RAW264.7 macrophages by inhibiting NF-κB and MAPK activation, *BioChem*, 2023, **3**, 91–101.

73 S. Saha, M. Basu, S. Guin, P. Gupta, A.-M. Mitterstiller, G. Weiss, K. Jana and A. Ukil, Leishmania donovani exploits macrophage heme oxygenase-1 to neutralize oxidative burst and TLR signaling–dependent host defense, *The Journal of Immunology*, 2019, **202**, 827–840.

74 M. Gholamrezaei, S. Rouhani, M. Mohebali, S. Mohammadi-Yeganeh, M. Haji Molla Hoseini, A. Haghighi, Z. Lasjerdi, F. Hamidi and M. Kazem Sharifi-Yazdi, MicroRNAs expression induces apoptosis of macrophages in response to Leishmania major (MRHO/IR/75/ER): An in-vitro and in-vivo study, *Iranian Journal of Parasitology*, 2020, **15**, 475–487.

75 J. A. de Azevedo-França, V. Feliciano dos Santos Ramos, L. Messori, F. Santanni, L. Sorace, L. Pereira Borba-Santos, S. Rozental, J. Cola Fernandes Rodrigues and M. Navarro, Synthesis, characterization, and biological evaluation of hybrid copper(ii) complexes containing azole drugs and planar ligands against neglected diseases, *New Journal of Chemistry*, 2023, **48**, 2515–2526.

76 A. G. Ribeiro, S. M. V. de Almeida, J. F. de Oliveira, T. R. C. de L. Souza, K. L. dos Santos, A. P. de B. Albuquerque, M. C. de B. L. Nogueira, L. B. de Carvalho Junior, R. O. de Moura, A. C. da Silva, V. R. A. Pereira, M. C. A. B. de Castro and M. do C. A. de Lima, Novel 4-quinoline-thiosemicarbazone derivatives: Synthesis, antiproliferative activity, in vitro and in silico biomacromolecule interaction studies and topoisomerase inhibition, *European Journal of Medicinal Chemistry*, 2019, **182**, 111592.

77 J. Nordlohne, I. Hulsmann, S. Schwafertz, J. Zgrajek, M. Grundmann, S. von Vietinghoff, F. Eitner and M. S. Becker, A flow cytometry approach reveals heterogeneity in conventional subsets of murine renal mononuclear phagocytes, *Scientific Reports*, 2021, **11**, 1–15.

78 F. Vieira, J. W. Kung and F. Bhatti, Structure, genetics and function of the pulmonary associated surfactant proteins A and D: The extra-pulmonary role of these C type lectins, *Annals of Anatomy*, 2017, **211**, 184–201.

79 B. Chen, R. Li, A. Kubota, L. Alex and N. G. Frangogiannis, Identification of macrophages in normal and injured mouse tissues using reporter lines and antibodies, *Scientific Reports*, 2022, **12**, 1–17.

80 L. J. Berghaus, J. N. Moore, D. J. Hurley, M. L. Vandenplas, B. P. Fortes, M. A. Wolfert and G. J. Boons, Innate immune responses of primary murine macrophage-lineage cells and RAW 264.7 cells to ligands of Toll-like receptors 2, 3, and 4, *Comparative Immunology, Microbiology and Infectious Diseases*, 2010, **33**, 443–454.

81 R. Ocaña-Guzmán, L. A. Ramón-Luing, M. Rodríguez-Alvarado, T. D. Voss, T. Fuchs and L. Chavez-Galan, Murine RAW macrophages are a suitable model to study the CD3 signaling in myeloid cells, *Cells*, 2022, **11**, 1–15.

82 D. I. Ugwu and J. Conradie, Anticancer properties of complexes derived from bidentate ligands, *Journal of Inorganic Biochemistry*, 2023, **246**, 112268.

83 P. Keshav, D. K. Goyal and S. Kaur, GC–MS screening and antiparasitic action of Putranjiva roxburghii leaves against sensitive and resistant strains of Leishmania donovani, *Journal of Parasitic Diseases*, 2021, **45**, 1002–1013.

84 J. A. Makwali, F. M. E. Wanjala, J. Ingonga and C. O. Anjili, In vitro studies on the antileishmanial activity of herbicides and plant extracts against leishmania major parasites, *Research Journal of Medicinal Plant*, 2015, **9**, 90–104.

85 O. Koutsoni, K. Karampetsou and E. Dotsika, In vitro screening of antileishmanial activity of natural product compounds: Determination of IC50, CC50 and SI values, *BIO-PROTOCOL*, 2019, **9**, 1–17.

86 A. Wu, E. Grela, K. Wójtowicz, N. Filipczak, Y. Hamon, R. Luchowski, W. Grudziński, O. Raducka-Jaszul, M. Gagoś, A. Szczepaniak, G. Chimini, W. I. Gruszecki and T. Trombik, ABCA1 transporter reduces amphotericin B cytotoxicity in mammalian cells, *Cellular and Molecular Life Sciences*, 2019, **76**, 4979–4994.

87 S. Malli, S. Pomel, I. Dennemont, P. M. Loiseau and K. Bouchemal, Combination of amphotericin B and chitosan platelets for the treatment of experimental cutaneous leishmaniasis: Histological and immunohistochemical examinations, *Journal of Drug Delivery Science and Technology*, 2019, **50**, 34–41.

88 A. R. Garcia, D. M. P. Oliveira, A. Claudia F. Amaral, J. B. Jesus, A. C. Rennó Sodero, A. M. T. Souza, C. T. Supuran, A. B. Vermelho, I. A. Rodrigues and A. S. Pinheiro, Leishmania infantum arginase: biochemical characterization and inhibition by naturally occurring phenolic substances, *Journal of Enzyme Inhibition and Medicinal Chemistry*, 2019, **34**, 1100–1109.

89 Sigma-Aldrich, Amphotericin B solubilized powder, g-irradiated, BioXtra, cell culture mammalian 1397-89-3, https://www.sigmaaldrich.com/ZA/en/product/sigma/a9528, (accessed 27 January 2025).

Chapter 4

Conclusion and Future Outlook

4.1. Overall conclusion

In conclusion, the findings of this study have affirmed not only the importance of quinoline as a pharmacophoric scaffold for antiparasitic drug design but also the plausibility of repurposing existing quinoline-based compounds as antileishmanial agents. Additionally, it has highlighted the possibility of enhancing the antileishmanial activity of quinoline-based compounds through the incorporation of transition metals, in this case, iron. The results of this study also clearly demonstrate the value of including secondary amines when designing drug leads with high antileishmanial activity. However, as secondary amines also appear to increase overall cytotoxicity, care must be taken when designing new drug leads to ensure that the cytotoxic effects do not outweigh their parasite-killing capabilities. The same principle may be applied when making use of iron as well since it also seems to induce cytotoxicity. While there is still room for further investigation on the efficacy and safety of the compounds described here, the findings presented in this study are promising and provide more insight into the strategies that may be employed in the development of new drugs for the treatment of cutaneous leishmaniasis.

4.2. Future outlook

4.2.1. Antiamastigote activity assessments

Since the *Leishmania* parasite exists in two forms, *i.e.*, the extracellular promastigote form and the intracellular amastigote form, there remains a need to conduct experiments to determine the potency of the most selective compounds (**3** and **6**) against the amastigote form in a suitable model. Preferably, these experiments should be in the form of a parasite rescue assay, whereby macrophages are infected with *Leishmania* parasites, treated with the test compounds and then lysed to release any surviving internalised parasites. [1–4] The viability of surviving parasites from compound-treated infected macrophages can then be compared to that of parasites from non-treated infected macrophages. This

type of assay not only mimics how the parasites infect macrophages *in vivo* but also serves as additional confirmation of the cytotoxicity of the test compounds against macrophages.

Alternatively, the antiamastigote activity could be measured through the use of axenic amastigotes, which are amastigotes obtained through the induced differentiation of promastigotes in culture media in the absence of mammalian cells. [5,6] This has been exemplified by the work of Sabt *et al*., who determined the activity of quinoline-isatin compounds against axenic *L. major* amastigotes. [7] Numerous other studies have also demonstrated that axenic amastigotes and intracellular amastigotes show no differences in drug susceptibility, indicating that cell-free and cell-based assays give similar antiamastigote activity data. [5,8] The use of axenic amastigotes in compound screening offers several advantages, including ease of culture, fast and inexpensive compound activity measurements, and eliminating the need to sacrifice laboratory animals. [5,9] However, while this approach still allows for drug screening against the medically relevant amastigote form, one should bear in mind that it does not accurately replicate the *in vivo* environment of the amastigote stage. Furthermore, it does not take into account whether the compounds can enter infected macrophages to reach their target. Therefore, for a more accurate representation of the behaviour of the parasites and compounds *in vivo*, testing the antiamastigote activity in a cell-based system is advised.

4.2.2. Cytotoxicity assessments in primary cells

The RAW 264.7 macrophage cell line was used to determine compound cytotoxicity in this study. Although these cells are a suitable macrophage model, follow-up studies are necessary to test the compounds in primary cells, such as murine bone marrow-derived macrophages, murine peritoneal macrophages or human peripheral blood monocyte-derived macrophages. These particular primary have been used to investigate antileishmanial drug activity and cytotoxicity in the past. [10–12] Testing the compounds in primary host cells is essential as a preliminary measure of their cytotoxic effects before *in vivo* testing since these cells are better representatives of cells in living tissues than cell lines. Furthermore, unlike immortalised cell lines such as the RAW 264.7 cell line, the finite lifespan of primary cells makes them less likely to undergo phenotypic and genotypic changes over time, which may influence results. [13,14] As was done in this study, a resazurin-based assay can be used to measure the viability of primary cells treated with the test compounds.

4.2.3. In vivo studies in mice

Another future objective is to test the efficacy of the most selective drug leads in *Leishmania*-susceptible BALB/c mice. Compounds **3** and **6** currently show the most promise in reaching the *in vivo* testing stage based on the selectivity data obtained in this study. However, as indicated earlier, it is necessary to test these compounds in primary cells and against intracellular *Leishmania* amastigotes to determine if they retain their selectivity. Once the antiamastigote activity of the two compounds has been determined using primary mouse cells, they could be administered in non-infected BALB/c mice, which are a commonly used *in vivo* model for leishmaniasis due to their susceptibility to *Leishmania* infection. [15–17] As these compounds have never been tested *in vivo*, this pilot experiment is necessary to determine if they have any detrimental effects on the overall health of the mice (*e.g.*, weight loss, diarrhoea, abnormal behaviour etc.) as well as to determine the maximum tolerated dose that can be administered. [18,19]

After the safety of the compounds has been confirmed and an appropriate dose has been established, the compounds can then be tested in *Leishmania*-infected BALB/c mice to investigate their effects on disease progression and parasite load. The disease progression and parasite load in compound-treated infected mice can then be compared with those of infected non-treated BALB/c mice and infected *Leishmania*-resistant C57BL/6 mice, thus giving an indication of the efficacy of the compounds. The route of administration would also need to be considered as it may influence the efficacy results. One study reported that intralesional administration of an antileishmanial drug led to a lower parasite burden than intramuscular administration. [3] Another study showed that administering a compound by either tattooing or subcutaneous injection led to reduced parasite load, with the latter route being more effective. [11] Additional routes of administration that could be explored include intraperitoneal, oral administration and topical administration. [12,20,21]

4.2.4. Mechanistic studies

Several mechanisms of action have been proposed for the antileishmanial activities of quinoline-based and ferrocene-based compounds, including inhibition of the enzyme pteridine reductase 1, ROS production, membrane disruption and altering chromatin distribution. [7,22–24] To investigate if compounds **3** and **6** bind to pteridine reductase 1, which is an essential enzyme for folate metabolism and DNA biosynthesis in *Leishmania* parasites, [7] molecular docking studies could be performed. Pteridine reductase 1 catalyses the reduction of biopterin in the presence of NADPH. [25] Therefore, one could also perform an enzymatic assay to determine if compounds **3** and **6** inhibit the catalytic activity

of this enzyme. The ability of the compounds to generate ROS, which are known to cause damage in parasitic cells, [26–28] in the presence or absence of living cells can be measured using various types of ROS detection assays. Additionally, transmission electron microscopy could be utilised to visualise parasite cell membrane damage and changes in chromatin distribution after treatment with the compounds.

The effects of the compounds on the immune system can also be investigated as part of their mechanism of action. A few studies have reported that quinoline-based and ferrocene-based compounds can induce expression of T helper 1 (Th1) cytokines (IFN-γ, IL-12, IL-2 and TNFα) and production of nitric oxide (NO) in macrophages, which signify a parasite-killing immune profile in infected cells. [21,24,28] Th1 cytokines are known to be produced by CD4 T cells, which are found in lymph nodes. [29–31] These cells could be isolated from the lymph nodes of *Leishmania*-infected BALB/c mice treated with compounds **3** and **6** and then cultured to obtain supernatant containing secreted Th1 cytokines. The secreted cytokines can be quantified using an enzyme-linked immunosorbent assay (ELISA) as a measure of expression levels. [32–34] The NO levels in infected macrophages treated with the compounds can be determined *in vitro* using several types of NO detection assays, such as the commonly used Griess assay. [3,17,28]

References

1 C. A. N. Njanpa, S. C. N. Wouamba, L. R. T. Yamthe, D. Dize, B. M. T. Tchatat, P. V. F. Tsouh, M. N. Pouofo, J. B. Jouda, B. L. Ndjakou, N. Sewald, S. F. Kouam and F. F. Boyom, Bio-guided isolation of anti-leishmanial natural products from Diospyros gracilescens L. (Ebenaceae), *BMC Complementary Medicine and Therapies*, 2021, **21**, 1–12.

2 J. Möller, C. Kannigadu, J. Aucamp, M. C. Joseph, A. J. Swarts and D. D. N'Da, Synthesis, electrochemistry, and in vitro antileishmanial efficacy of novel ferrocenylazines, *Applied Organometallic Chemistry*, 2023, **37**, 1–13.

3 A. Badirzadeh, M. Heidari-Kharaji, V. Fallah-Omrani, H. Dabiri, A. Araghi and A. Salimi Chirani, Antileishmanial activity of Urtica dioica extract against zoonotic cutaneous leishmaniasis, *PLOS Neglected Tropical Diseases*, 2020, **14**, e0007843.

4 S. K. Jain, R. Sahu, L. A. Walker and B. L. Tekwani, A parasite rescue and transformation assay for antileishmanial screening against intracellular Leishmania donovani amastigotes in THP1 human acute monocytic leukemia cell line., *Journal of visualized experiments : JoVE*, 2012, **70**,

1–14.

5 G. Dias-Lopes, A. Zabala-Peñafiel, B. C. de Albuquerque-Melo, F. Souza-Silva, L. Menaguali do Canto, L. Cysne-Finkelstein and C. R. Alves, Axenic amastigotes of Leishmania species as a suitable model for in vitro studies, *Acta Tropica*, 2021, **220**, 105956.

6 M. Teixeira, R. De Jesus Santos, R. Sampaio, L. Pontes-de-Carvalho and W. L. Dos-Santos, A simple and reproducible method to obtain large numbers of axenic amastigotes of different Leishmania species, *Parasitology Research*, 2002, **88**, 963–968.

7 A. Sabt, W. M. Eldehna, T. M. Ibrahim, A. A. Bekhit and R. Z. Batran, New antileishmanial quinoline linked isatin derivatives targeting DHFR-TS and PTR1: Design, synthesis, and molecular modeling studies, *European Journal of Medicinal Chemistry*, 2023, **246**, 114959.

8 H. L. Callahan, A. C. Portal, R. Devereaux and M. Grogl, An axenic amastigote system for drug screening, *Antimicrobial Agents and Chemotherapy*, 1997, **41**, 818–822.

9 S. Gupta and Nishi, Visceral leishmaniasis: experimental models for drug discovery., *The Indian journal of medical research*, 2011, **133**, 27–39.

10 K. Seifert, P. Escobar and S. L. Croft, In vitro activity of anti-leishmanial drugs against Leishmania donovani is host cell dependent, *Journal of Antimicrobial Chemotherapy*, 2010, **65**, 508–511.

11 R. de M. V. Meira, S. L. da S. Gomes, E. Schaeffer, T. Da Silva, A. C. de S. Brito, L. M. Siqueira, J. D. Inácio, E. E. Almeida-Amaral, A. M. Da-Cruz, M. Bezerra-Paiva, R. H. Neves, L. S. Rodrigues, P. M. L. Dutra, P. R. R. Costa, A. J. M. da Silva and S. A. G. Da-Silva, Low doses of 3-phenyl-lawsone or meglumine antimoniate delivery by tattooing route are successful in reducing parasite load in cutaneous lesions of Leishmania (Viannia) braziliensis-infected hamsters, *Frontiers in Cellular and Infection Microbiology*, 2023, **13**, 1–14.

12 V. Yardley, F. Gamarro and S. L. Croft, Antileishmanial and antitrypanosomal activities of the 8-aminoquinoline tafenoquine, *Antimicrobial Agents and Chemotherapy*, 2010, **54**, 5356–5358.

13 B. Taciak, M. Białasek, A. Braniewska, Z. Sas, P. Sawicka, Ł. Kiraga, T. Rygiel and M. Król, Evaluation of phenotypic and functional stability of RAW 264.7 cell line through serial passages, *PLoS ONE*, 2018, **13**, 1–13.

14 G. Kaur and J. M. Dufour, Cell lines: Valuable tools or useless artefacts, *Spermatogenesis*, 2012, **2**, 1–5.

15 C. M. Restrepo, A. Llanes, L. Herrera, E. Ellis, R. Lleonart and P. L. Fernández, Gene expression

patterns associated with leishmania panamensis infection in macrophages from BALB/c and C57BL/6 mice, *PLoS Neglected Tropical Diseases*, 2021, **15**, 1–20.

16 E. N. Loría-Cervera and F. J. Andrade-Narváez, Review: Animal models for the study of leishmaniasis immunology, *Revista do Instituto de Medicina Tropical de Sao Paulo*, 2014, **56**, 1–11.

17 M. Amini, H. Nahrevanian, M. Farahmand, S. Khatami, S. Javadian and F. Mirkhani, Immuno-biochemical variation in susceptible BALB/c and resistant C57BL/6 mice infected with Iranian strain of cutaneous leishmaniasis; Leishmania major MRHO/IR/75/ER, *Internet Journal of Infectious Diseases*, 2009, **7**, 1–4.

18 T. Burkholder, C. Foltz, E. Karlsson, C. G. Linton and J. M. Smith, Health evaluation of experimental laboratory mice, *Current Protocols in Mouse Biology*, 2012, **2**, 145–165.

19 S. C. Gad, in *Encyclopedia of Toxicology*, Elsevier, 4th edn., 2024, pp. 43–44.

20 S. P. Parihar, M. A. Hartley, R. Hurdayal, R. Guler and F. Brombacher, Topical simvastatin as host-directed therapy against severity of cutaneous leishmaniasis in mice, *Scientific Reports*, 2016, **6**, 1–10.

21 S. P. Chowdhuri, S. Dhiman, S. K. Das, N. Meena, S. Das, A. Kumar and B. B. Das, Novel Pyrido[2′,1′:2,3]imidazo[4,5-c]quinoline Derivative Selectively Poisons Leishmania donovani Bisubunit Topoisomerase 1 to Inhibit the Antimony-Resistant Leishmania Infection in Vivo, *Journal of Medicinal Chemistry*, 2023, **66**, 3411–3430.

22 G. de S. V. Tavares, D. V. C. Mendonça, D. P. Lage, J. da T. Granato, F. M. Ottoni, F. Ludolf, M. A. Chávez-Fumagalli, M. C. Duarte, C. A. P. Tavares, R. J. Alves, E. S. Coimbra and E. A. F. Coelho, Antileishmanial Activity, Cytotoxicity and Mechanism of Action of Clioquinol Against Leishmania infantum and Leishmania amazonensis Species, *Basic and Clinical Pharmacology and Toxicology*, 2018, **123**, 236–246.

23 E. Torres Suarez, D. S. Granados-Falla, S. M. Robledo, J. Murillo, Y. Upegui and G. Delgado, Antileishmanial activity of synthetic analogs of the naturally occurring quinolone alkaloid N-methyl-8-methoxyflindersin, *PLOS ONE*, 2020, **15**, e0243392.

24 M. Yousuf, D. Mukherjee, A. Pal, S. Dey, S. Mandal, C. Pal and S. Adhikari, Synthesis and biological evaluation of ferrocenylquinoline as a potential antileishmanial agent, *ChemMedChem*, 2015, **10**, 546–554.

25 B. Nare, L. W. Hardy and S. M. Beverley, The roles of pteridine reductase 1 and dihydrofolate

reductase- thymidylate synthase in pteridine metabolism in the protozoan parasite Leishmania major, *Journal of Biological Chemistry*, 1997, **272**, 13883–13891.

26 D. Gambino and L. Otero, Design of prospective antiparasitic metal-based compounds including selected organometallic cores, *Inorganica Chimica Acta*, 2018, **472**, 58–75.

27 M. Navarro, C. Gabbiani, L. Messori and D. Gambino, Metal-based drugs for malaria, trypanosomiasis and leishmaniasis: Recent achievements and perspectives, *Drug Discovery Today*, 2010, **15**, 1070–1078.

28 M. Yousuf, D. Mukherjee, S. Dey, C. Pal and S. Adhikari, Antileishmanial ferrocenylquinoline derivatives: Synthesis and biological evaluation against Leishmania donovani, *European Journal of Medicinal Chemistry*, 2016, **124**, 468–479.

29 G. Volpedo, T. Pacheco-Fernandez, E. A. Holcomb, N. Cipriano, B. Cox and A. R. Satoskar, Mechanisms of immunopathogenesis in cutaneous leishmaniasis and post Kala-azar dermal leishmaniasis (PKDL), *Frontiers in Cellular and Infection Microbiology*, 2021, **11**, 1–16.

30 E. K. Elmahallawy, A. A. M. Alkhaldi and A. A. Saleh, Host immune response against leishmaniasis and parasite persistence strategies: A review and assessment of recent research, *Biomedicine and Pharmacotherapy*, 2021, **139**, 111671.

31 Á. Gabriel, A. Valério-Bolas, J. Palma-Marques, P. Mourata-Gonçalves, P. Ruas, T. Dias-Guerreiro and G. Santos-Gomes, Cutaneous leishmaniasis: The complexity of host's effective immune response against a polymorphic parasitic disease, *Journal of Immunology Research*, 2019, **2019**, 1–16.

32 B. O. Osero, Z. Cele, R. T. Aruleba, R. A. Maine, M. Ozturk, M. B. Lutz, F. Brombacher and R. Hurdayal, Interleukin-4 responsive dendritic cells are dispensable to host resistance against Leishmania mexicana infection, *Frontiers in Immunology*, 2022, **12**, 1–15.

33 R. Hurdayal, H. H. Ndlovu, M. Revaz-Breton, S. P. Parihar, J. K. Nono, M. Govender and F. Brombacher, IL-4–producing B cells regulate T helper cell dichotomy in type 1- and type 2-controlled diseases, *Proceedings of the National Academy of Sciences of the United States of America*, 2017, **114**, E8430–E8439.

34 M. Mohrs, B. Ledermann, G. Köhler, A. Dorfmüller, A. Gessner and F. Brombacher, Differences between IL-4- and IL-4 receptor α-deficient mice in chronic leishmaniasis reveal a protective role for IL-13 receptor signaling, *The Journal of Immunology*, 1999, **162**, 7302–7308.

Appendix

Spectroscopic data for compounds 1 – 11

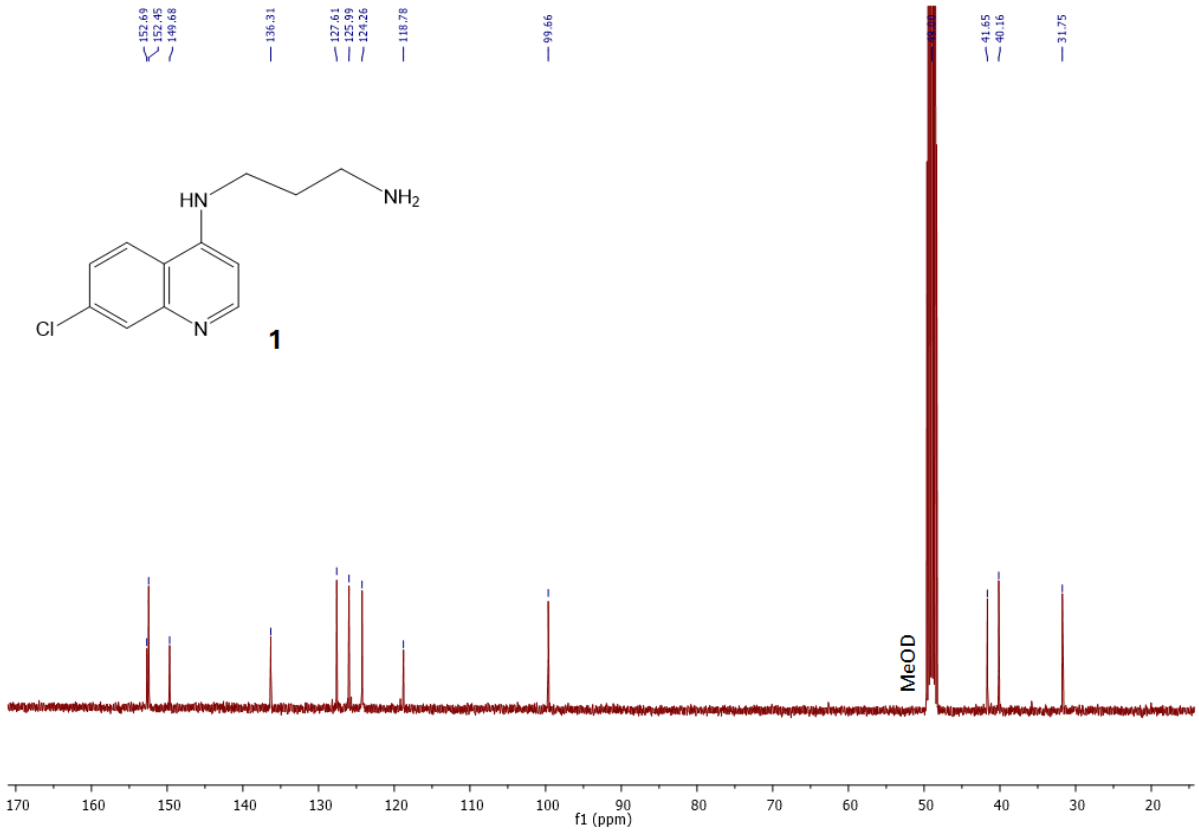

***Figure A1**: $^{13}C\{^{1}H\}$ NMR spectrum of compound **1** in deuterated methanol (MeOD).*

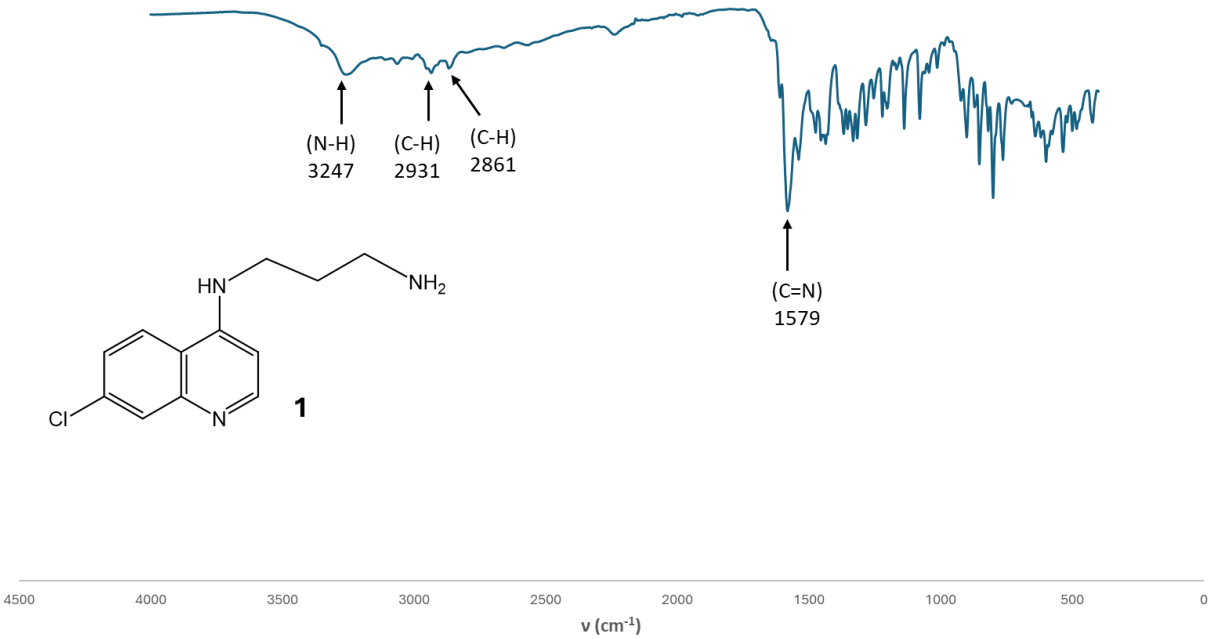

***Figure A2**: Infrared spectrum of compound **1**.*

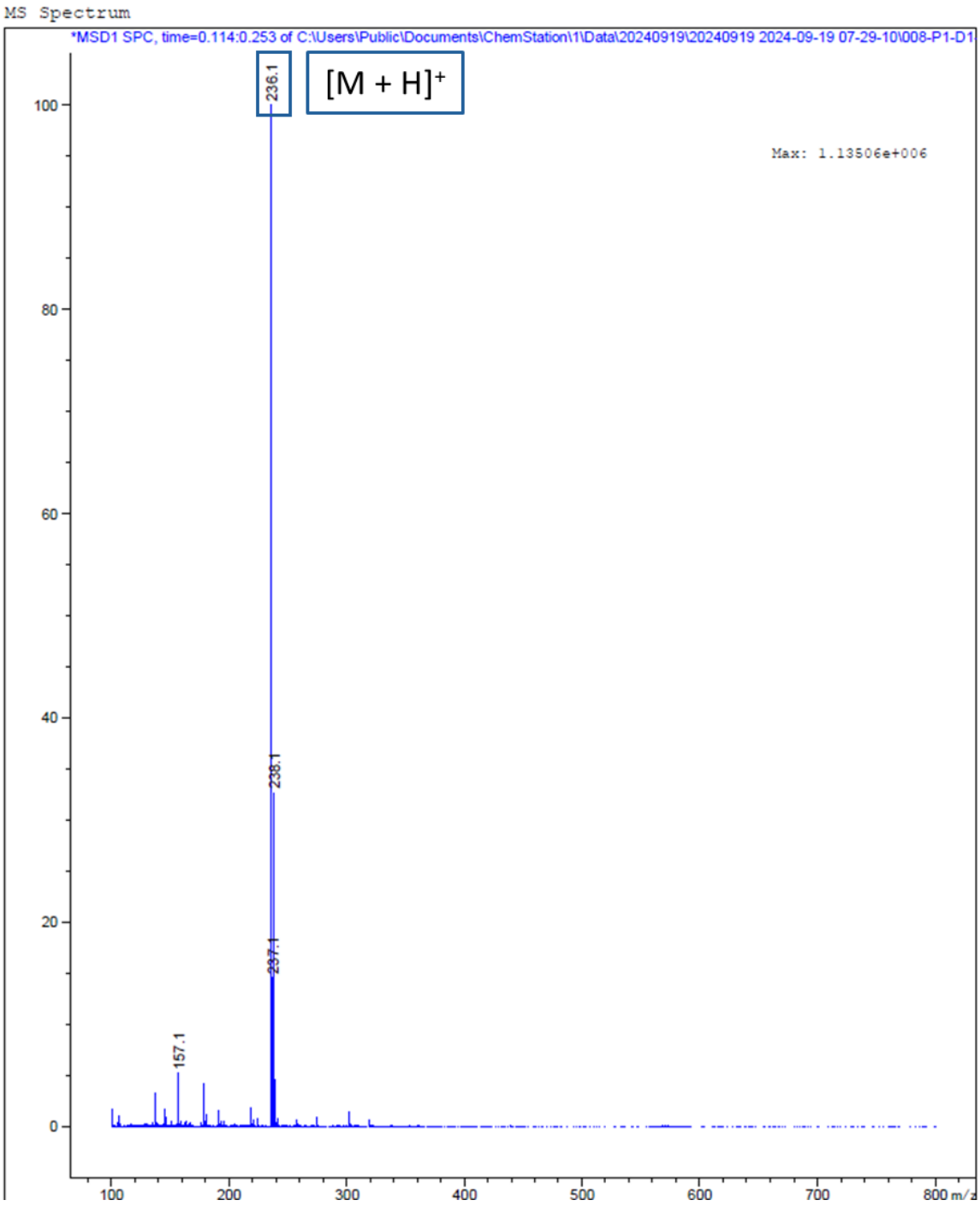

***Figure A3**: Liquid chromatography mass spectrum of compound **1**.*

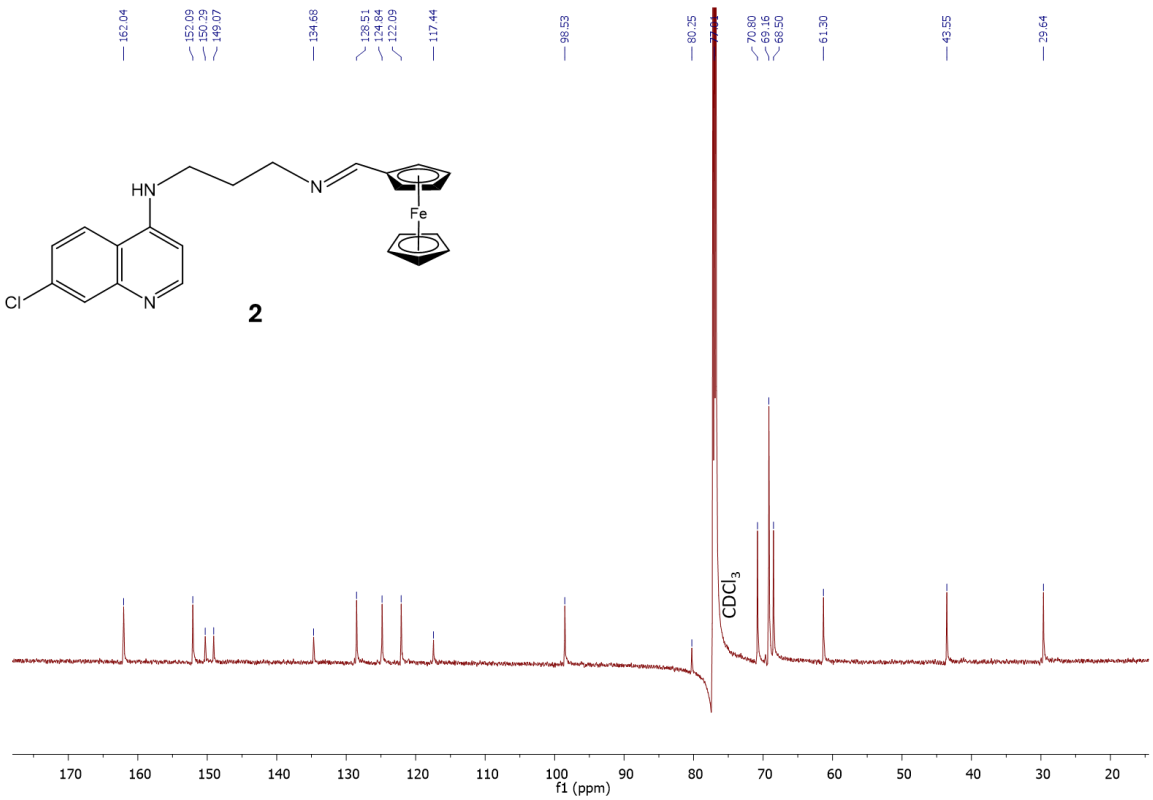

***Figure A4**: $^{13}C\{^{1}H\}$ NMR spectrum of compound **2** in deuterated chloroform ($CDCl_3$).*

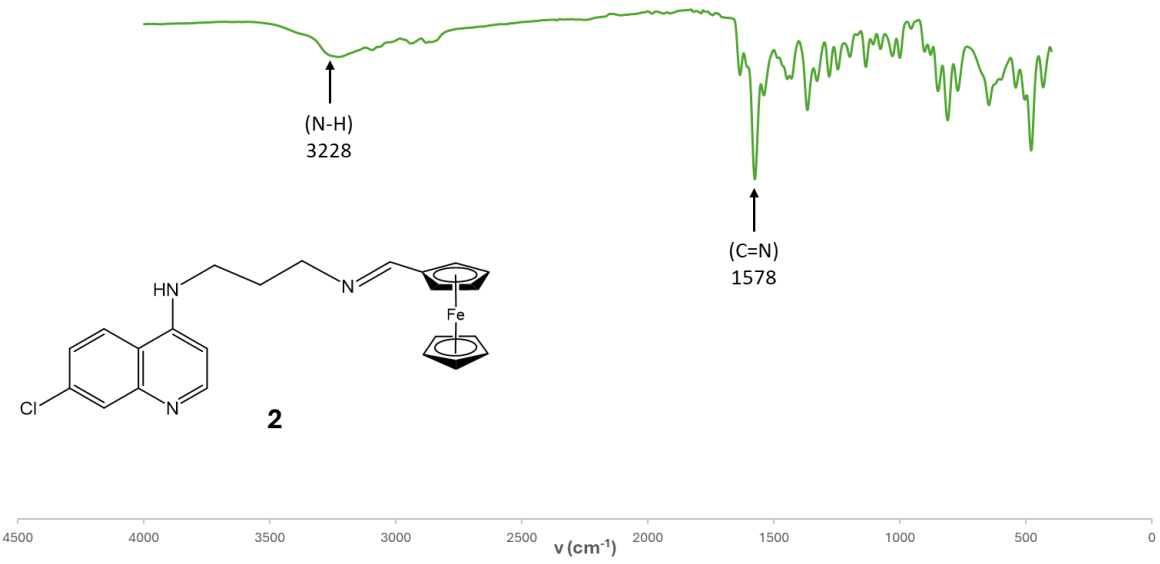

***Figure A5**: Infrared spectrum of compound **2**.*

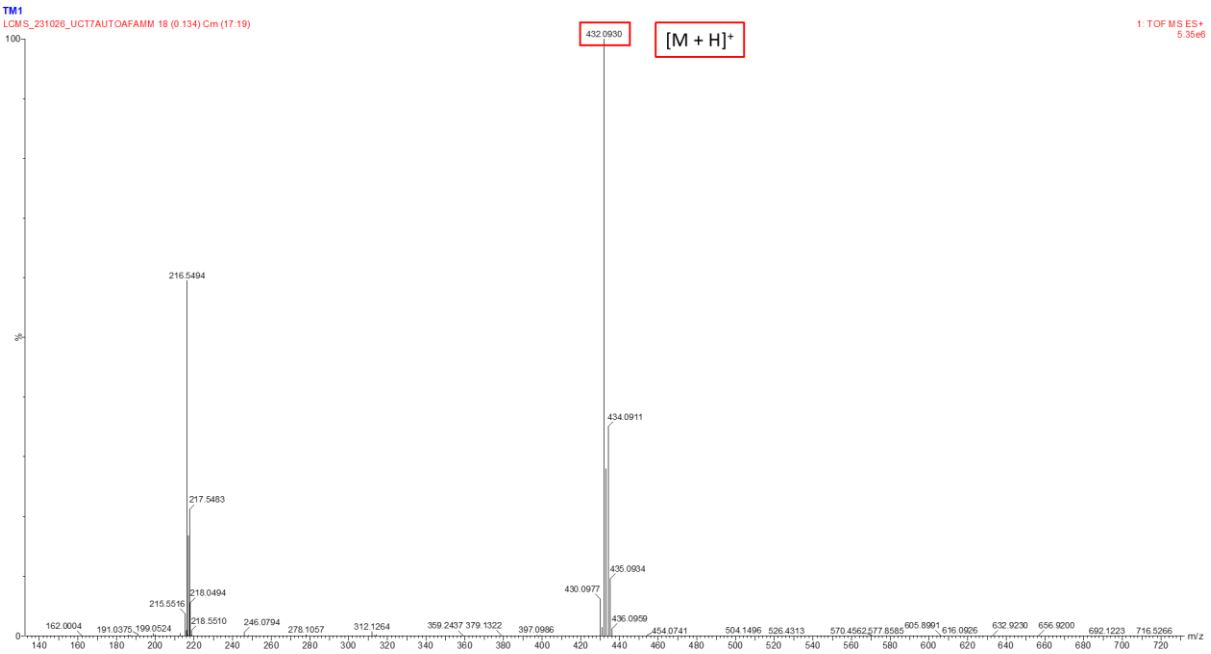

***Figure A6**: High resolution ESI mass spectrum of compound **2**.*

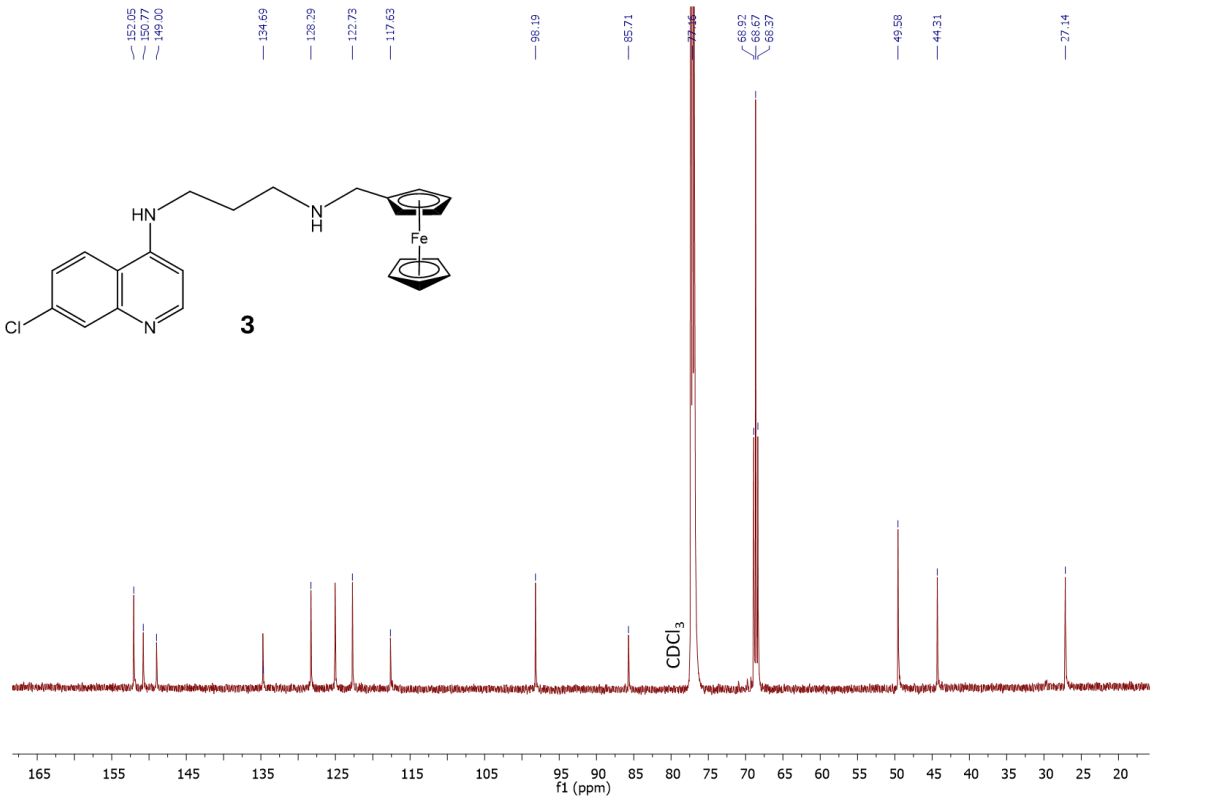

***Figure A7**: $^{13}C\{^{1}H\}$ NMR spectrum of compound **3** in deuterated chloroform ($CDCl_3$).*

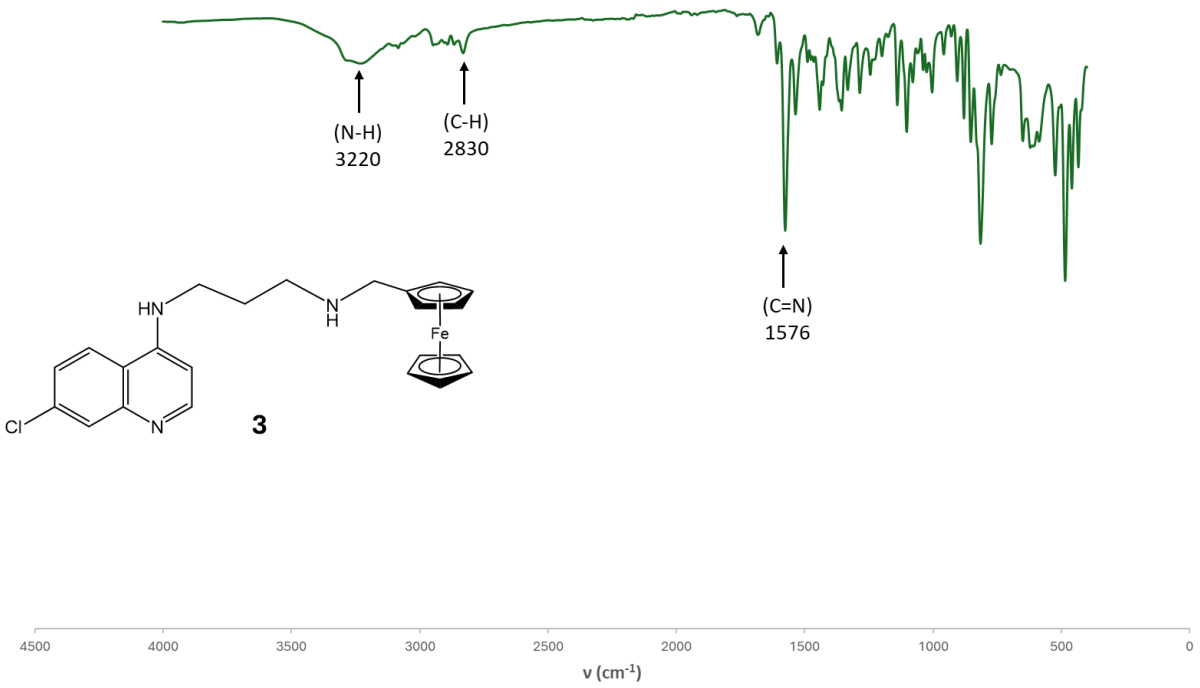

***Figure A8**: Infrared spectrum of compound **3**.*

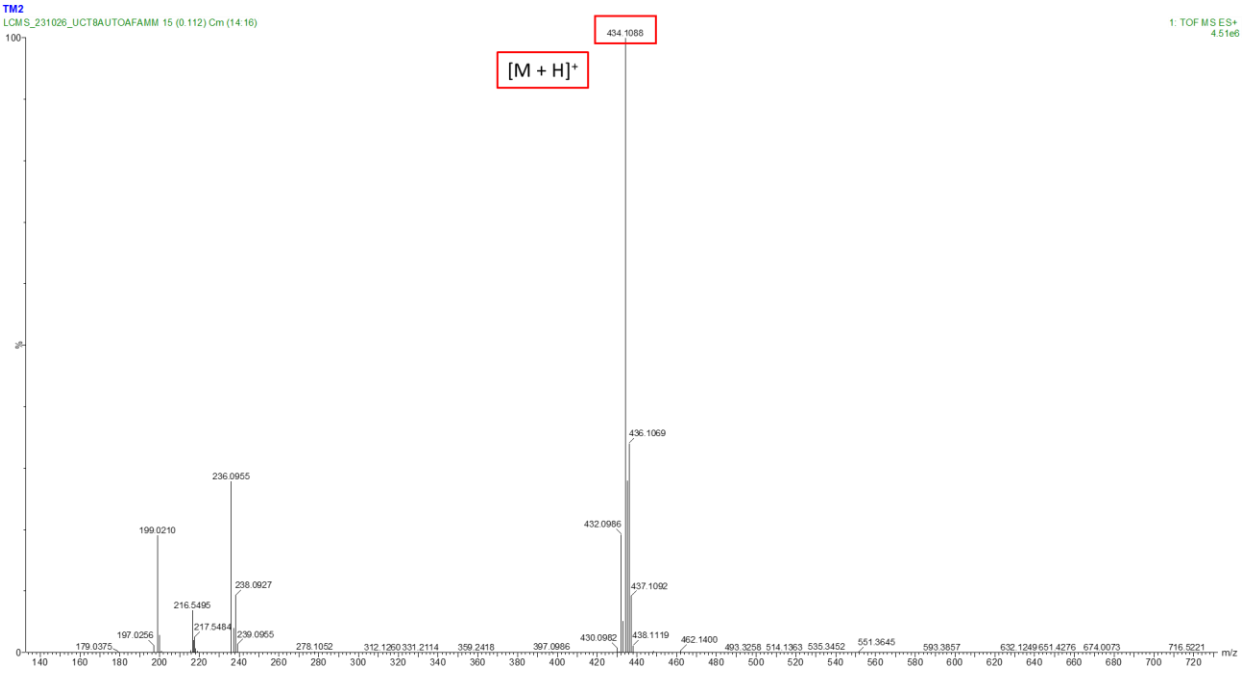

***Figure A9**: High resolution ESI mass spectrum of compound **3**.*

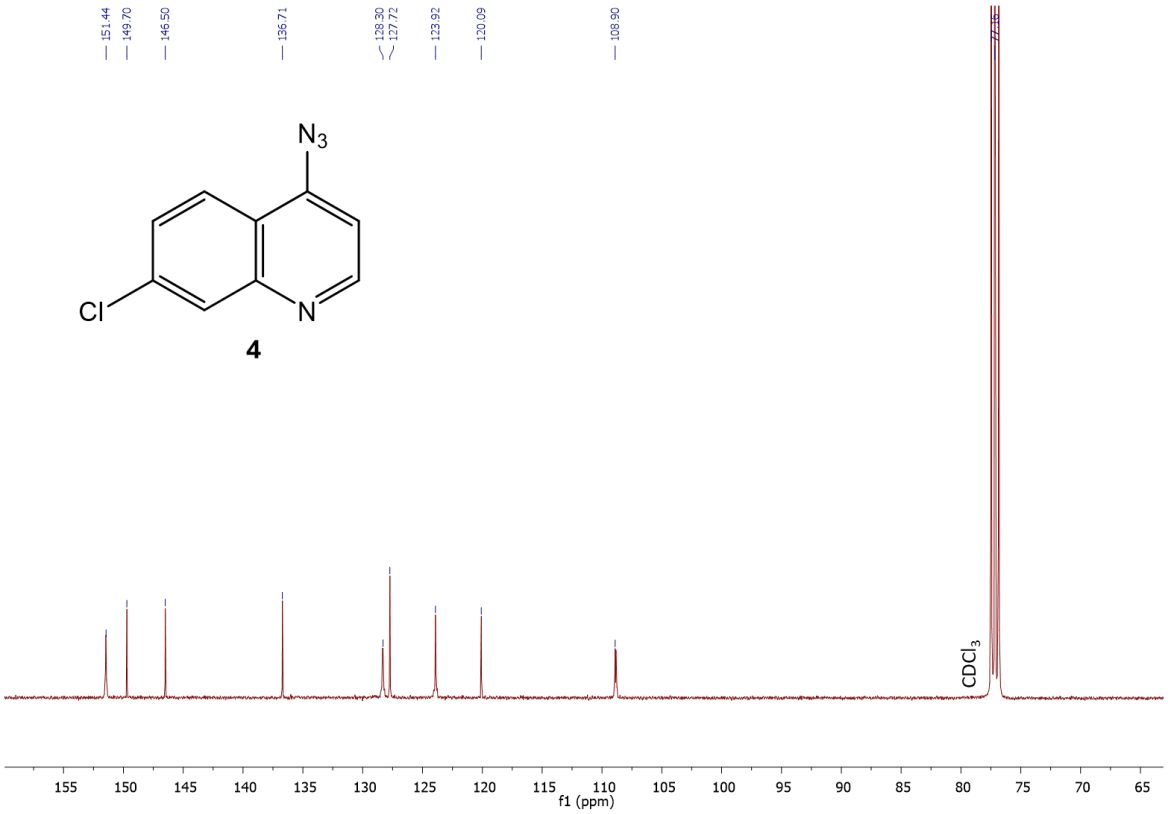

***Figure A10**: $^{13}C\{^{1}H\}$ NMR spectrum of compound **4** in deuterated chloroform ($CDCl_3$).*

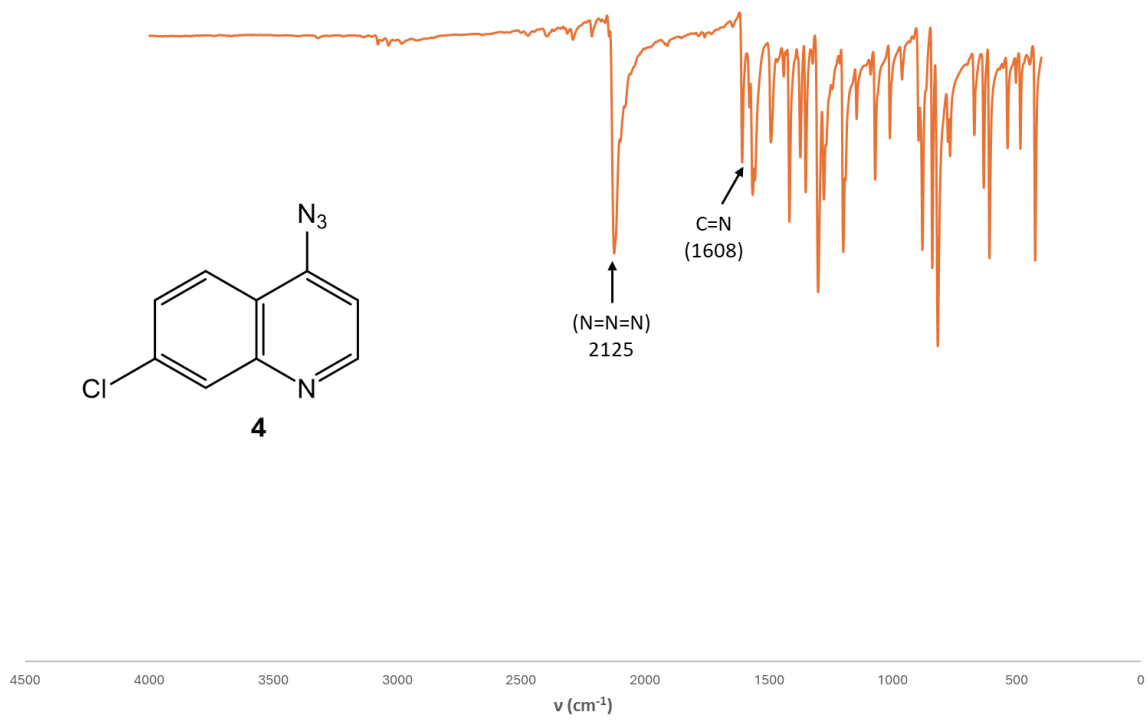

***Figure A11**: Infrared spectrum of compound **4**.*

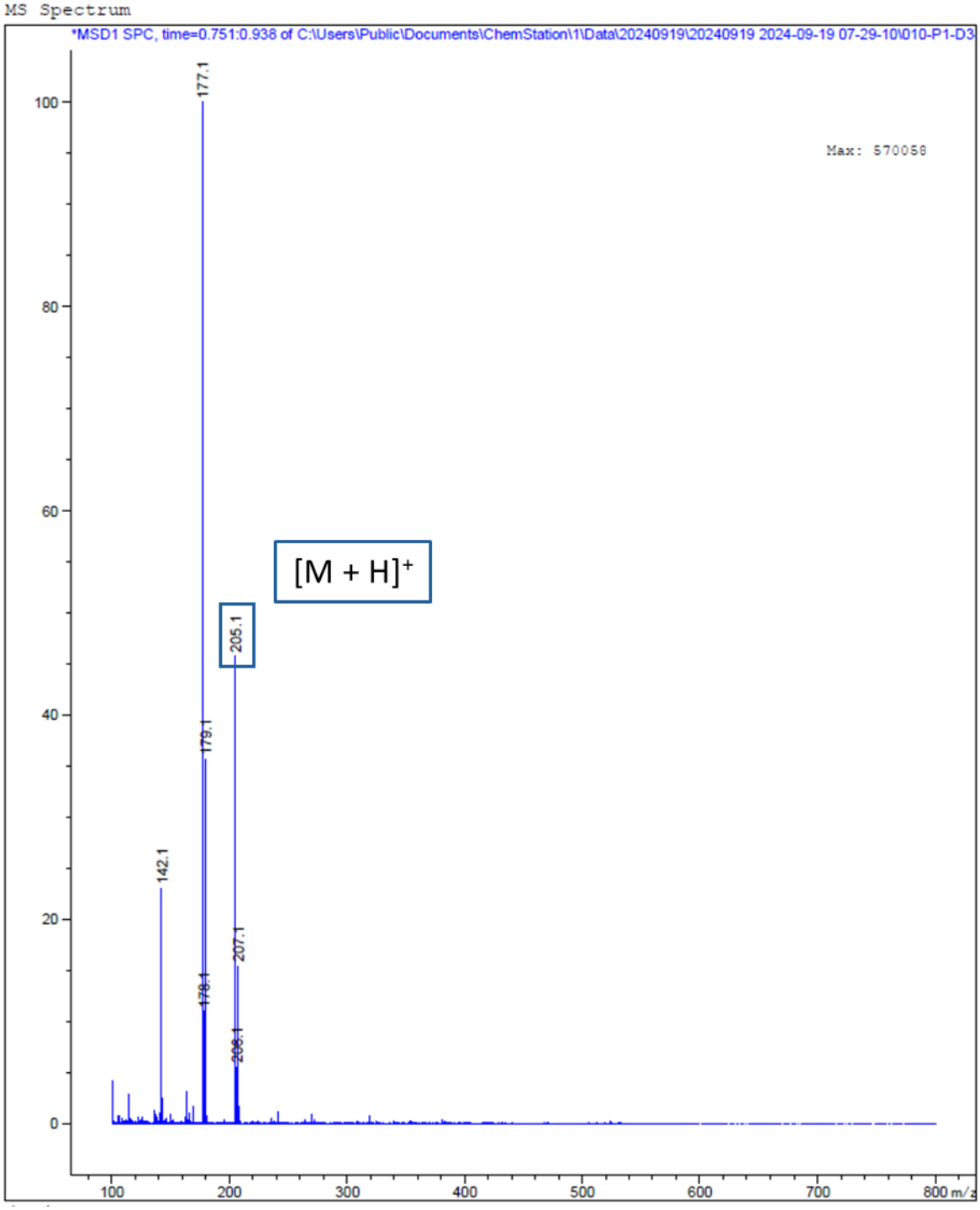

***Figure A12**: Liquid chromatography mass spectrum of compound **4**.*

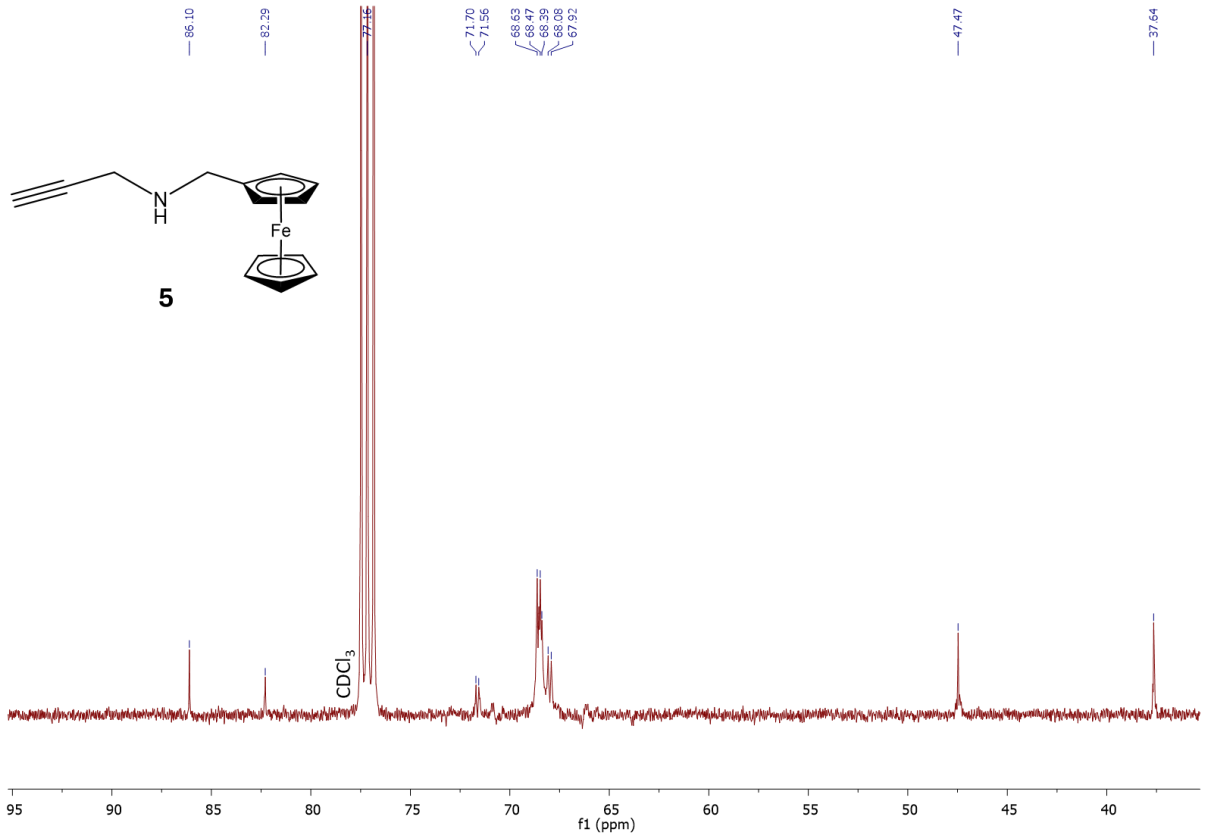

***Figure A13**: $^{13}C\{^{1}H\}$ NMR spectrum of compound **5** in deuterated chloroform ($CDCl_3$).*

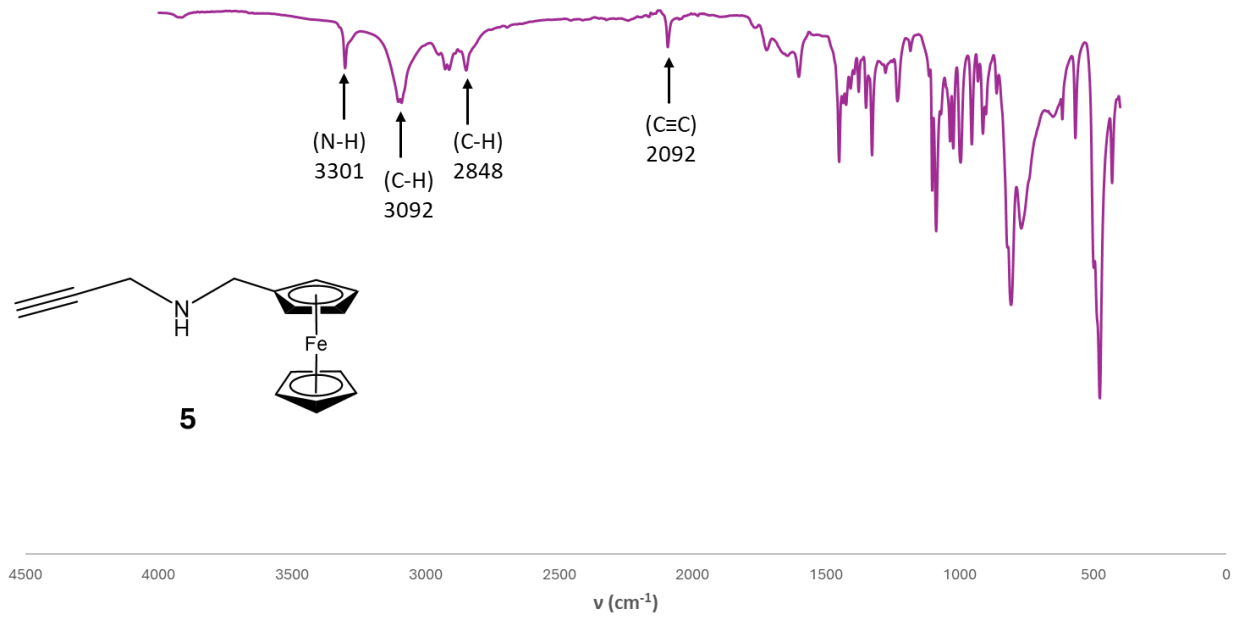

***Figure A14**: Infrared spectrum of compound **5**.*

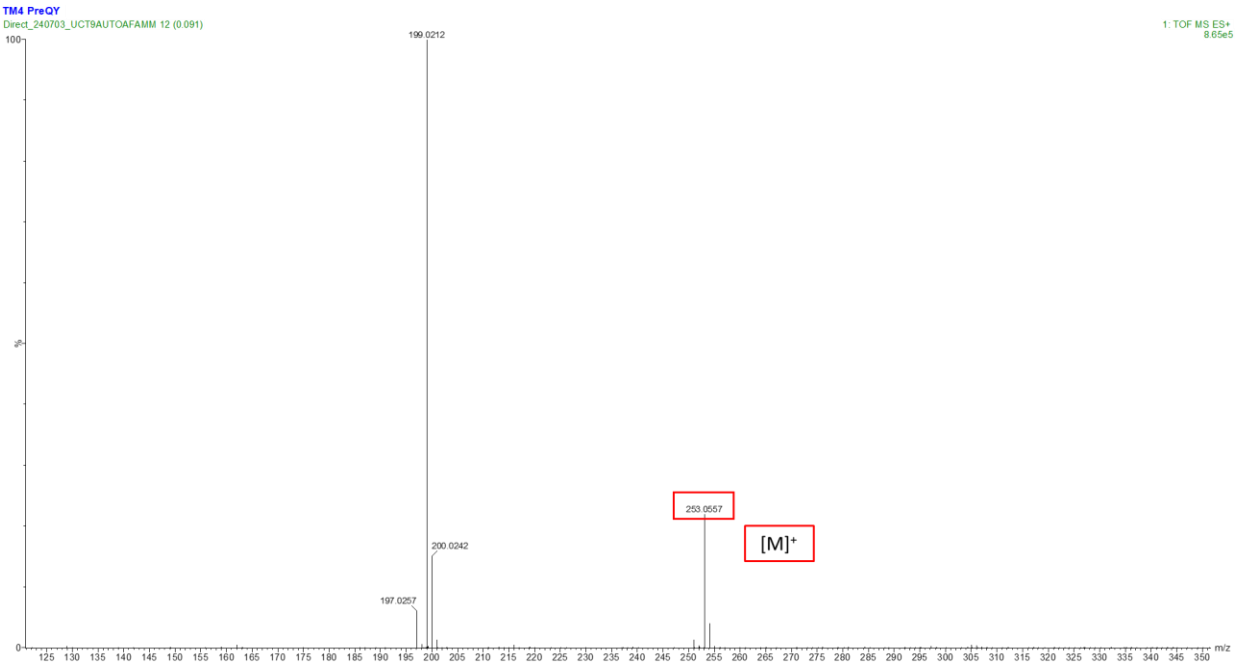

***Figure A15**: High resolution ESI mass spectrum of compound **5**.*

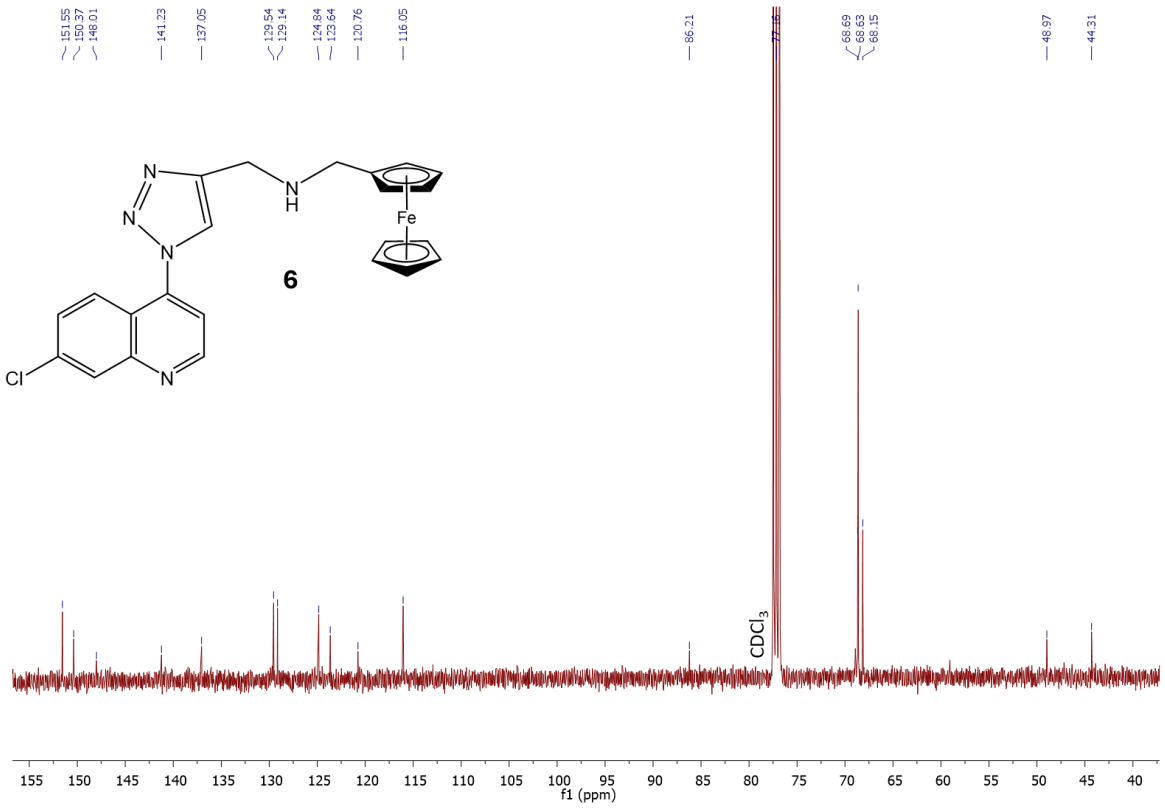

***Figure A16**: $^{13}C\{^{1}H\}$ NMR spectrum of compound **6** in deuterated chloroform ($CDCl_3$).*

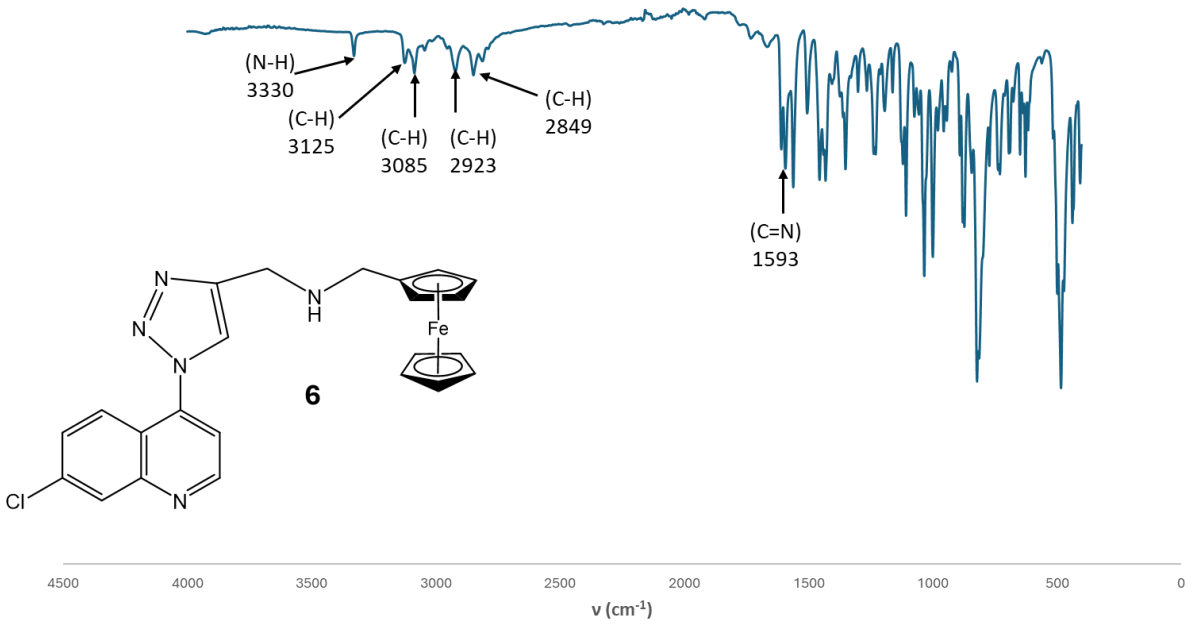

***Figure A17**: Infrared spectrum of compound **6**.*

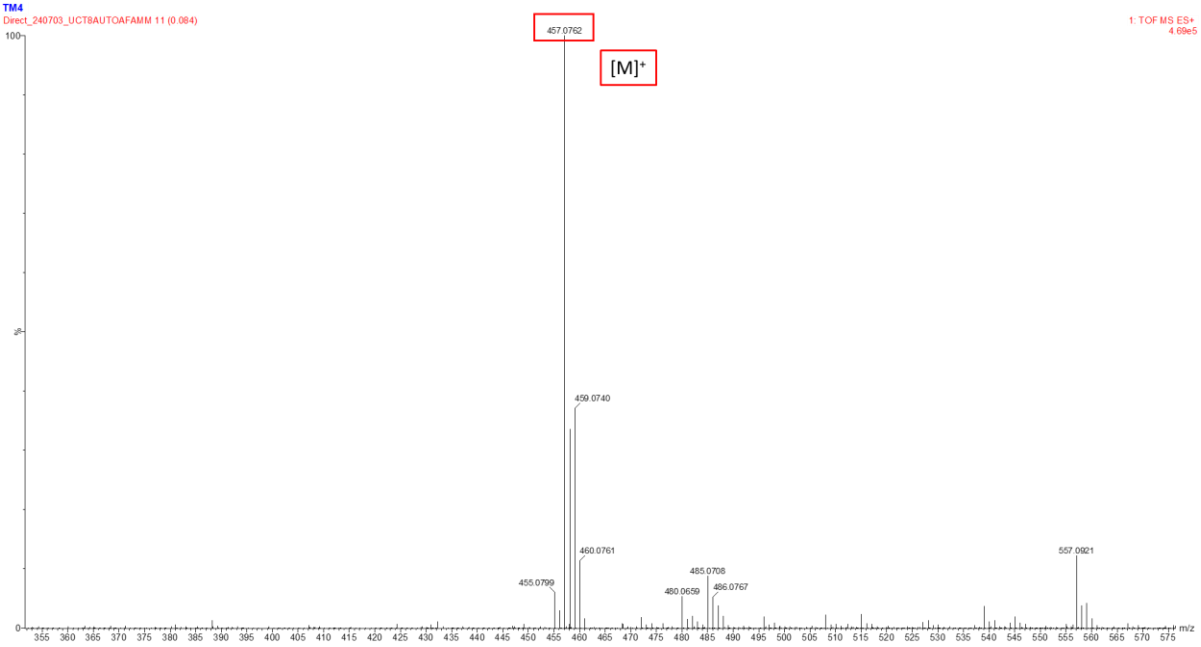

***Figure A18**: High resolution ESI mass spectrum of compound **6**.*

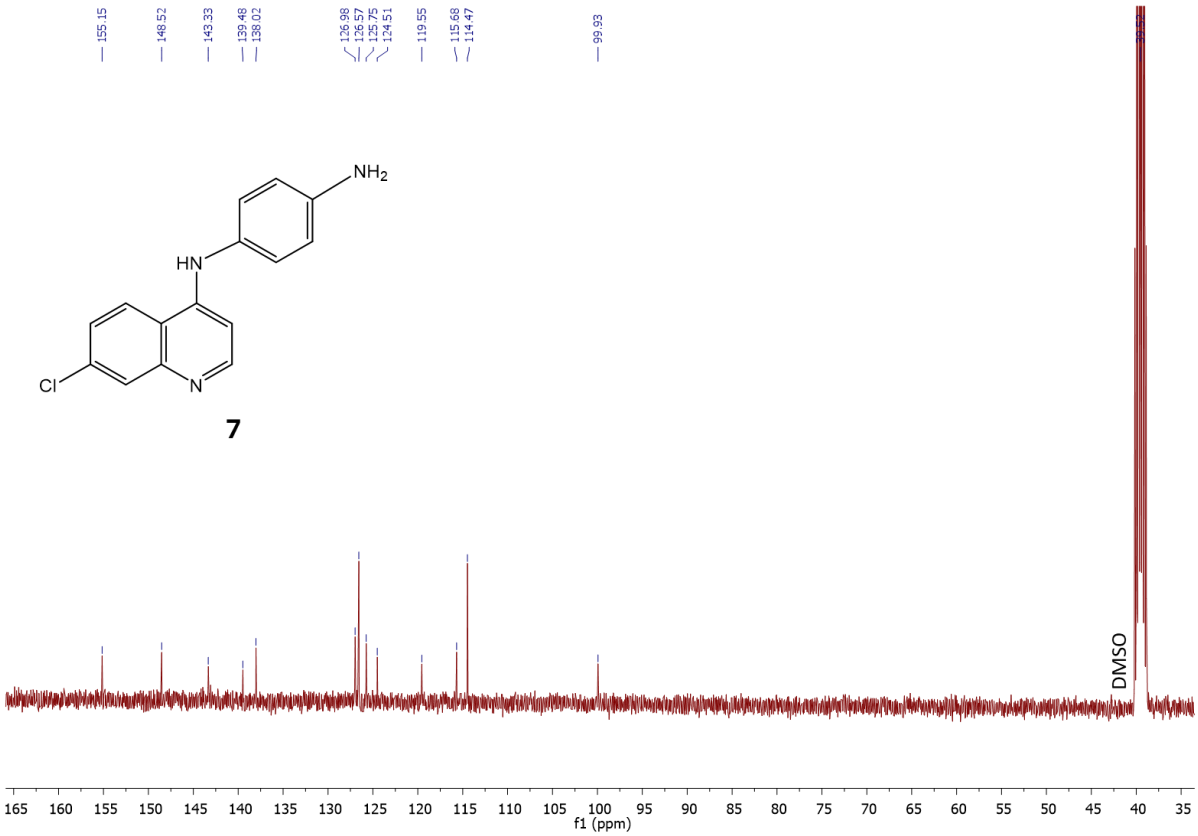

***Figure A19**: $^{13}C\{^{1}H\}$ NMR spectrum of compound **7** in deuterated dimethyl sulfoxide (DMSO-d_6).*

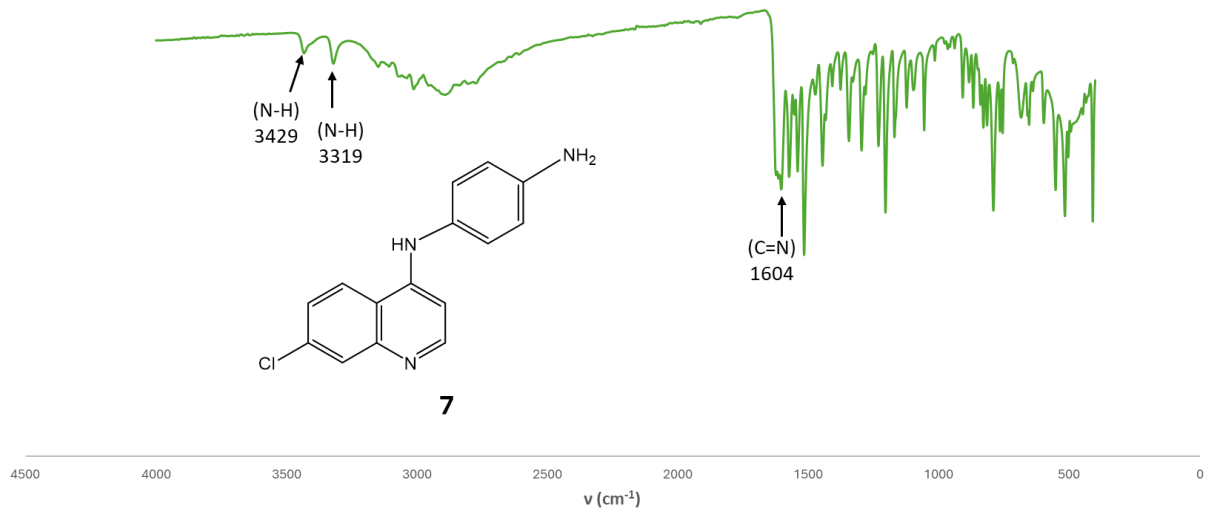

***Figure A20**: Infrared spectrum of compound **7**.*

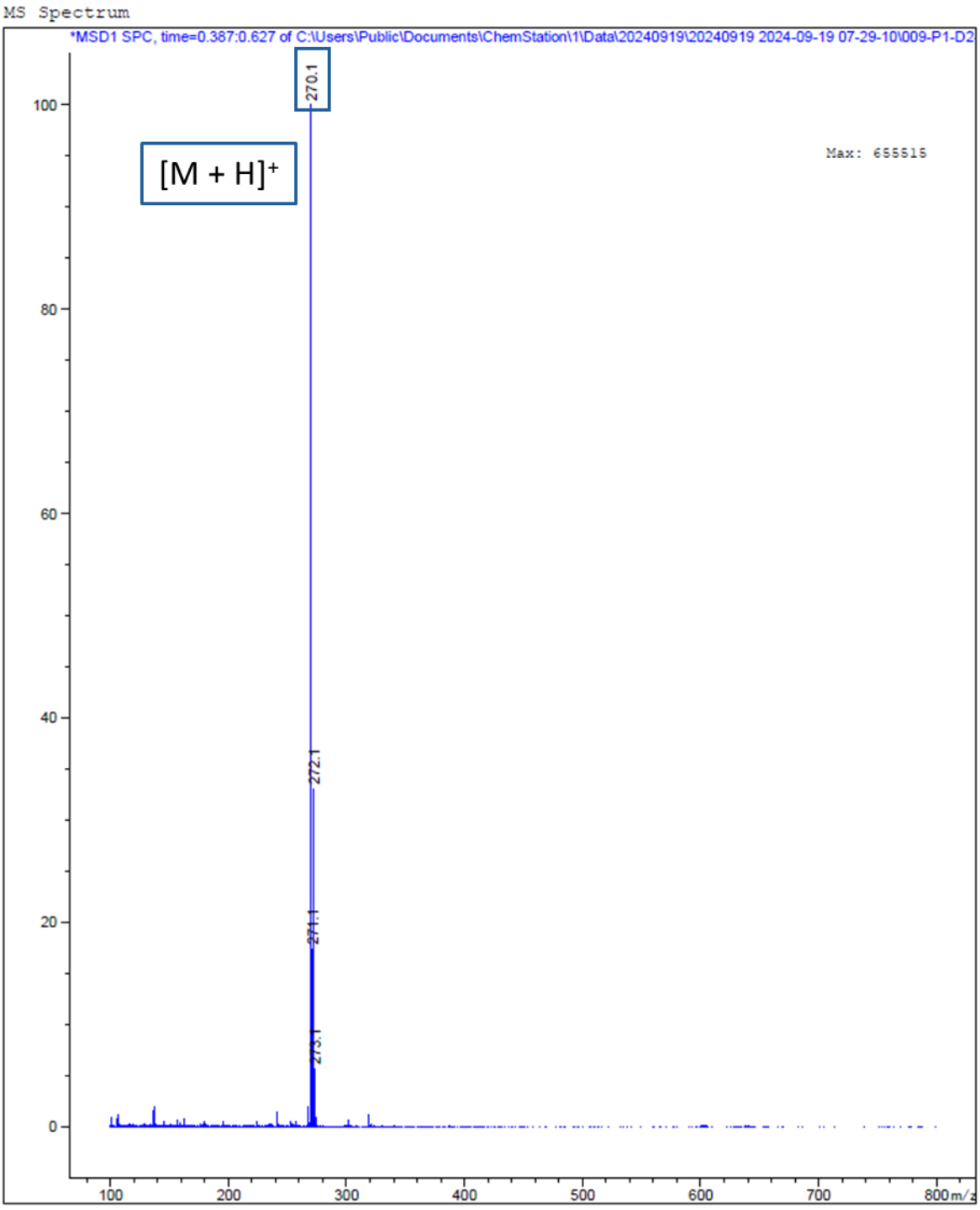

***Figure A21**: Liquid chromatography mass spectrum of compound **7**.*

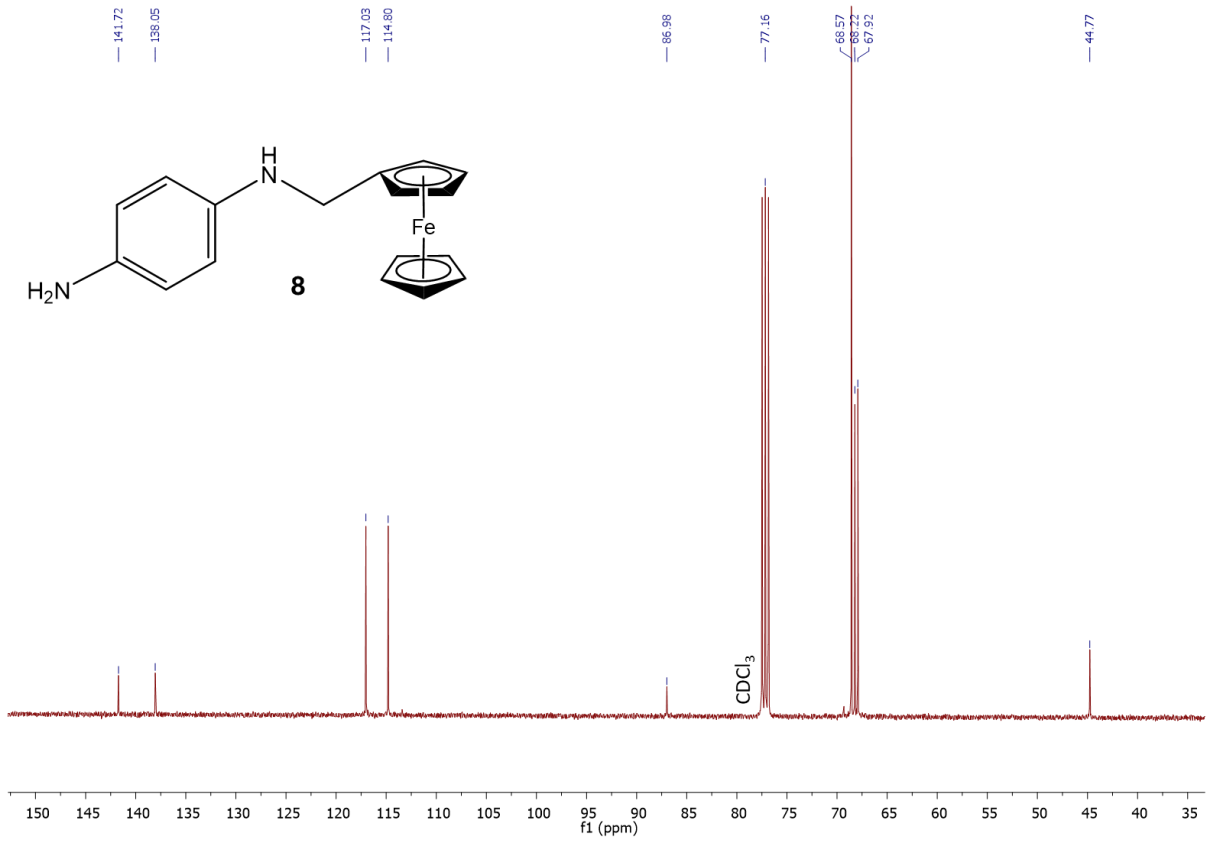

***Figure A22**: $^{13}C\{^{1}H\}$ NMR spectrum of compound **8** in deuterated chloroform ($CDCl_3$).*

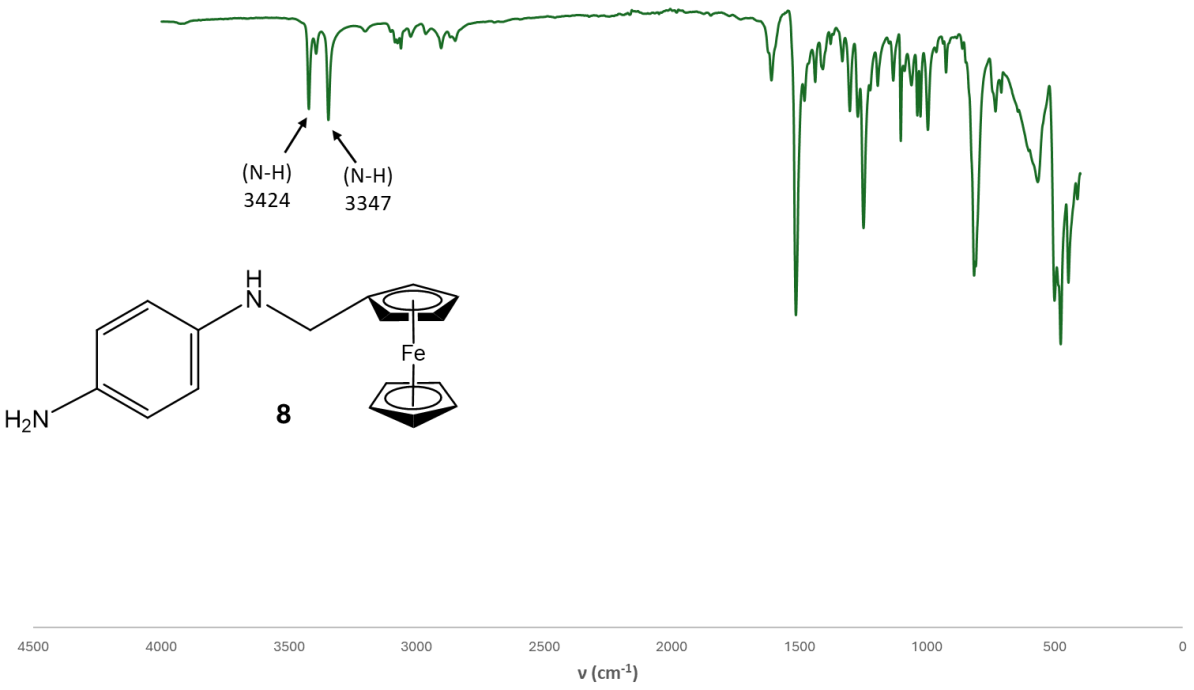

***Figure A23**: Infrared spectrum of compound **8**.*

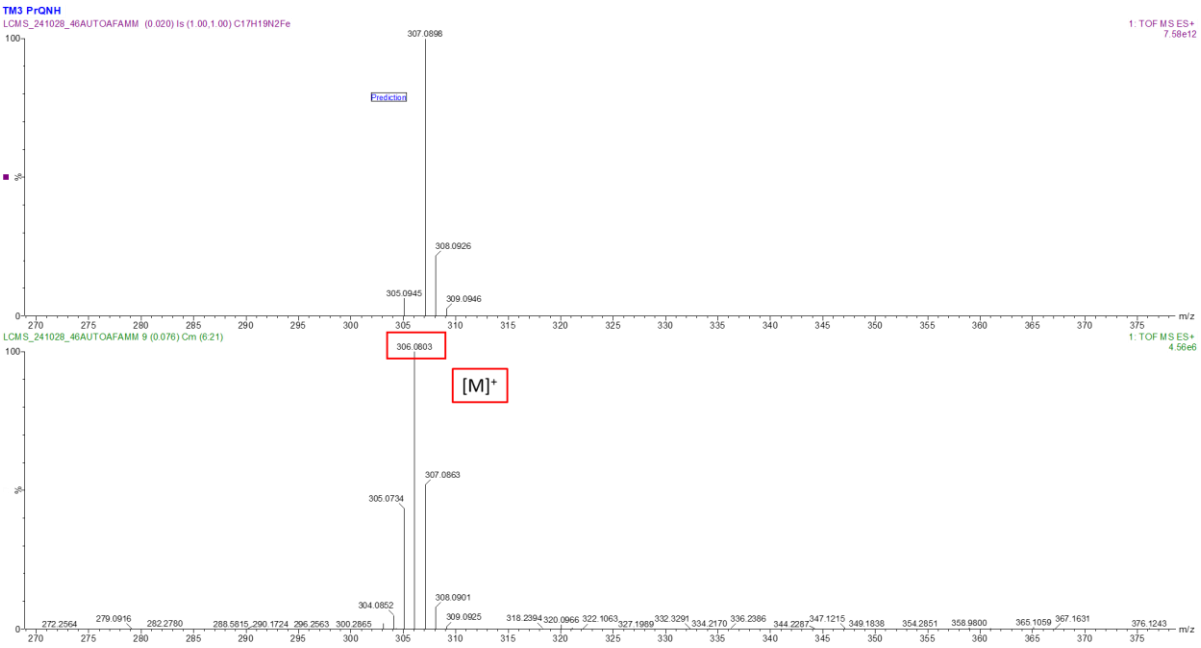

***Figure A24**: High resolution ESI mass spectrum of compound **8**.*

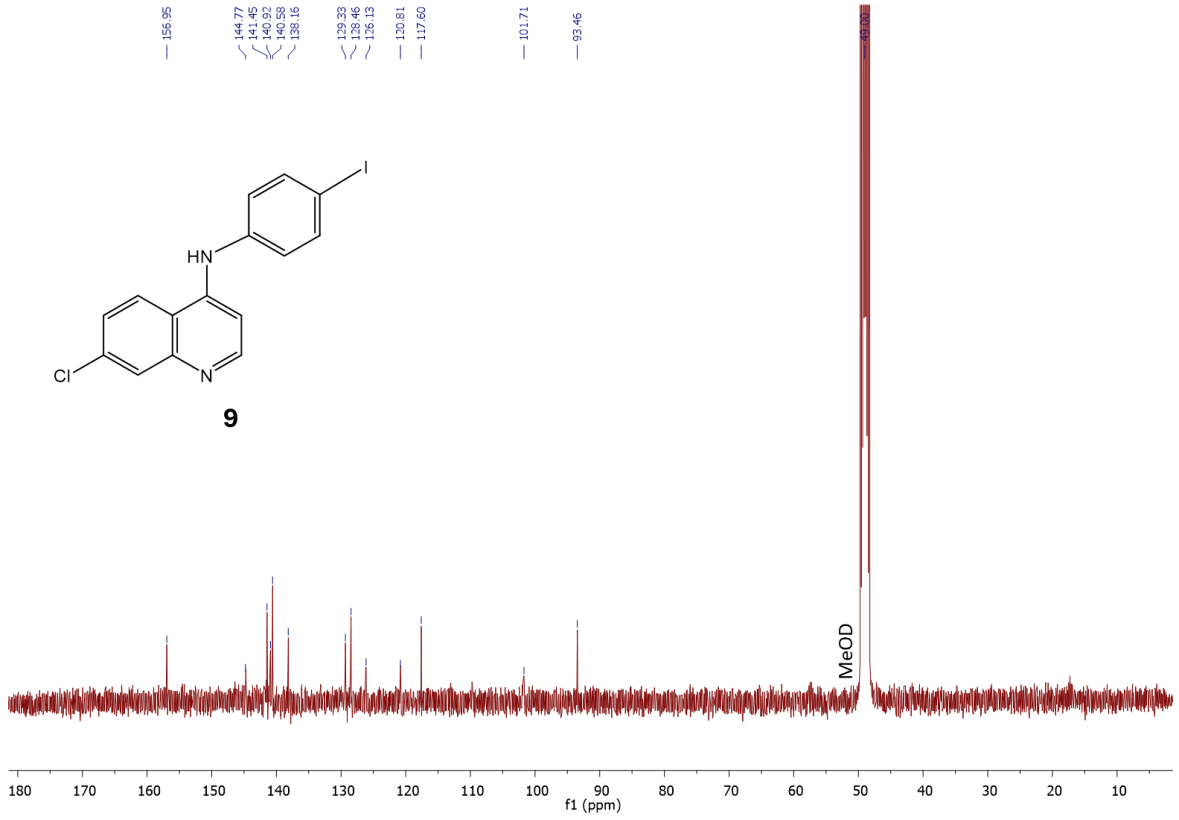

***Figure A25**: $^{13}C\{^{1}H\}$ NMR spectrum of compound **9** in deuterated methanol (MeOD).*

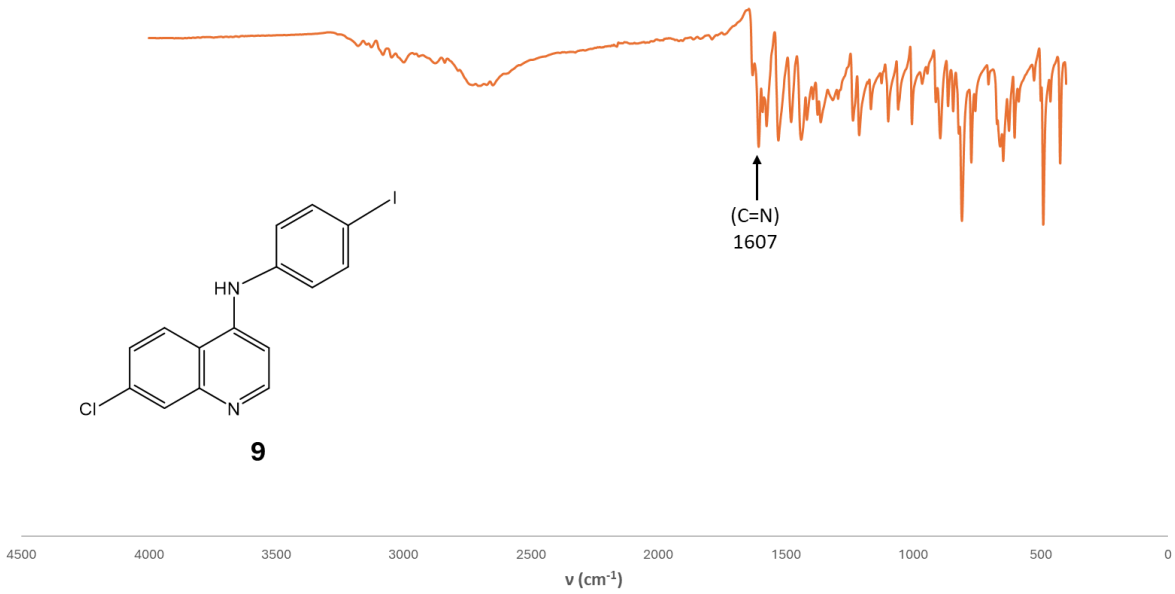

***Figure A26**: Infrared spectrum of compound **9**.*

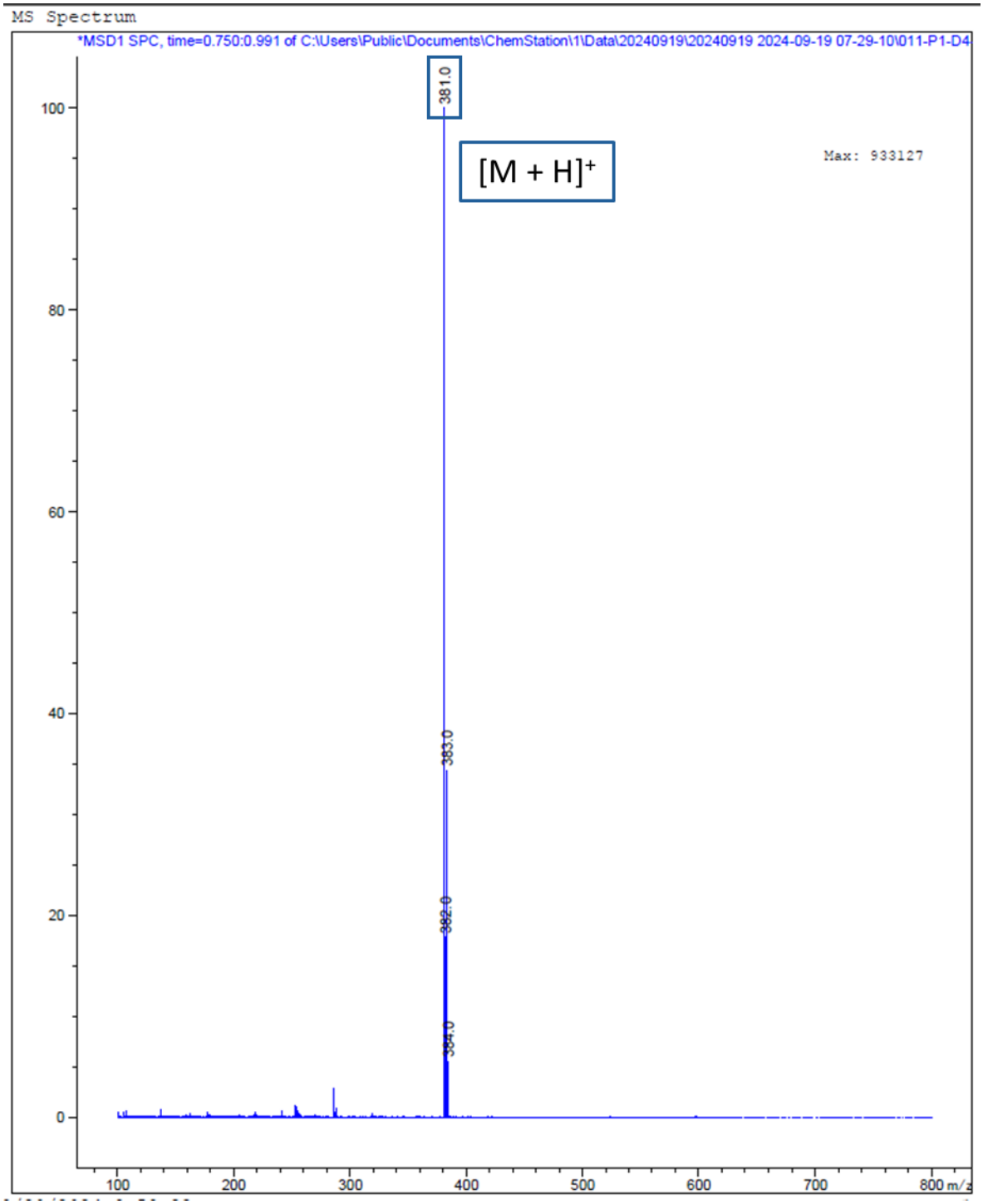

***Figure A27**: Liquid chromatography mass spectrum of compound **9**.*

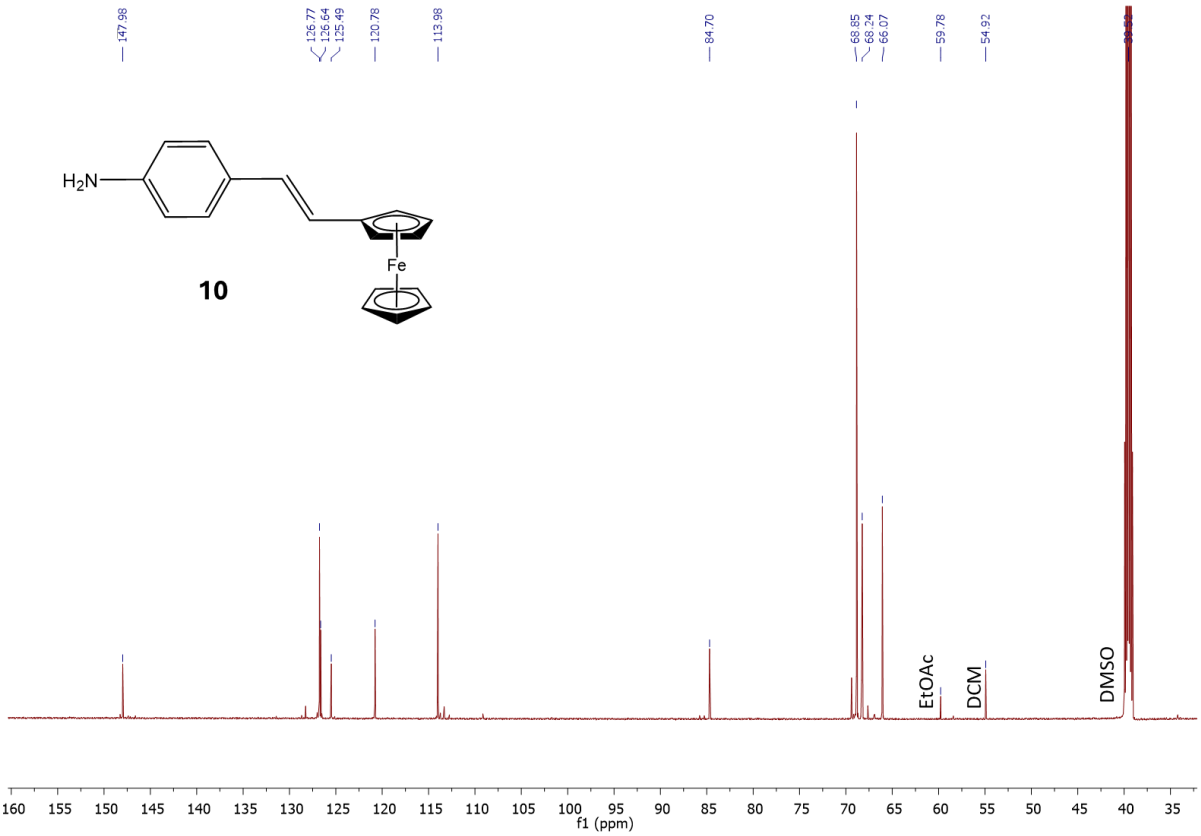

***Figure A28**: $^{13}C\{^{1}H\}$ NMR spectrum of compound **10** in deuterated dimethyl sulfoxide (DMSO-d_6).*

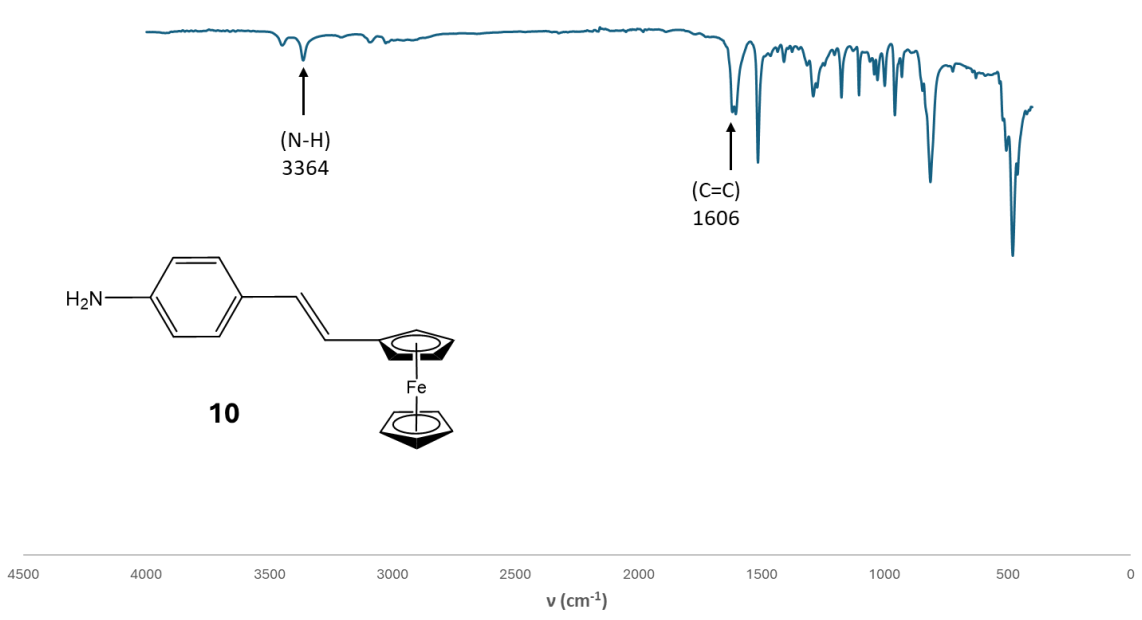

***Figure A29**: Infrared spectrum of compound **10**.*

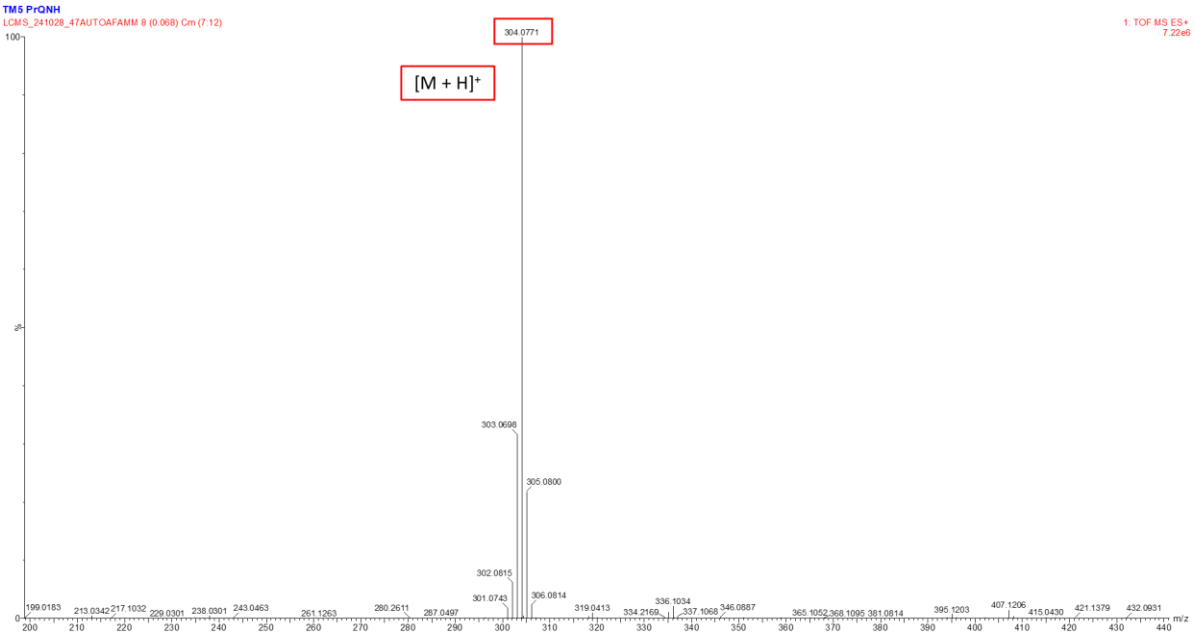

***Figure A30**: High resolution ESI mass spectrum of compound **10**.*

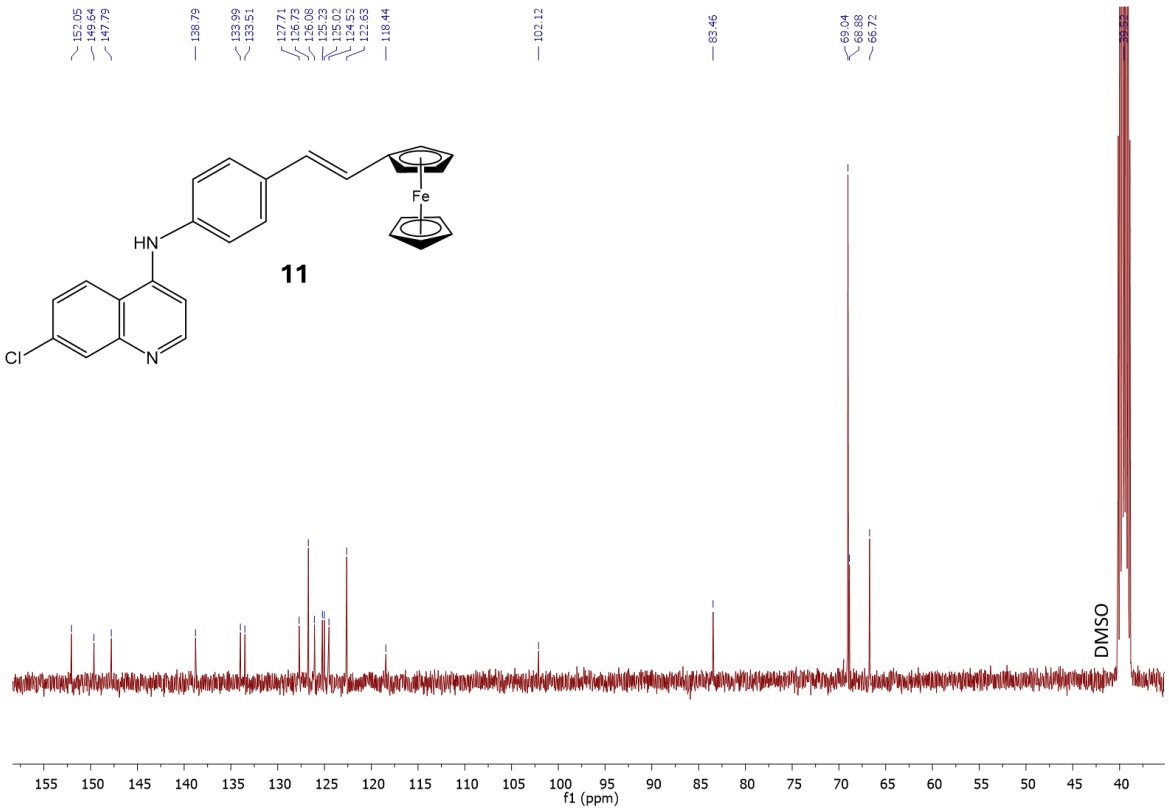

***Figure A31**: $^{13}C\{^{1}H\}$ NMR spectrum of compound **11** in deuterated dimethyl sulfoxide (DMSO-d_6).*

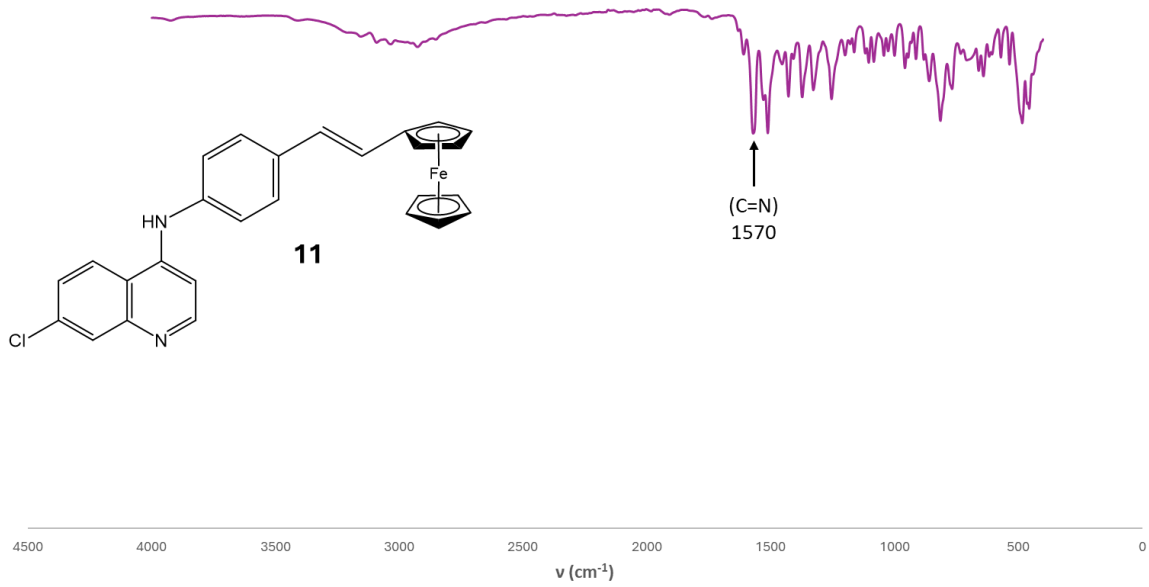

***Figure A32**: Infrared spectrum of compound **11**.*

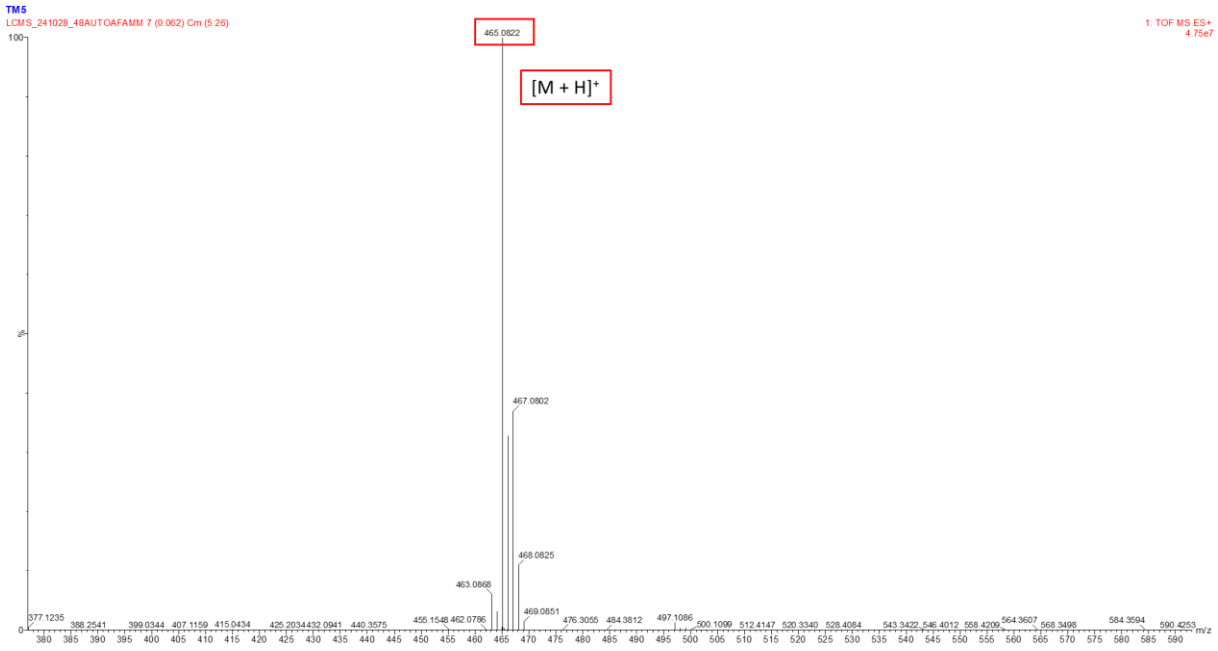

***Figure A33**: High resolution ESI mass spectrum of compound **11**.*